LEABHARLANN CHOLÁISTE NA TRÍONÓIDE, BAILE ÁTHA CLIATH | TRINITY COLLEGE LIBRARY DUBLIN
Ollscoil Átha Cliath | The University of Dublin

Terms and Conditions of Use of Digitised Theses from Trinity College Library Dublin

Copyright statement

All material supplied by Trinity College Library is protected by copyright (under the Copyright and Related Rights Act, 2000 as amended) and other relevant Intellectual Property Rights. By accessing and using a Digitised Thesis from Trinity College Library you acknowledge that all Intellectual Property Rights in any Works supplied are the sole and exclusive property of the copyright and/or other IPR holder. Specific copyright holders may not be explicitly identified. Use of materials from other sources within a thesis should not be construed as a claim over them.

A non-exclusive, non-transferable licence is hereby granted to those using or reproducing, in whole or in part, the material for valid purposes, providing the copyright owners are acknowledged using the normal conventions. Where specific permission to use material is required, this is identified and such permission must be sought from the copyright holder or agency cited.

Liability statement

By using a Digitised Thesis, I accept that Trinity College Dublin bears no legal responsibility for the accuracy, legality or comprehensiveness of materials contained within the thesis, and that Trinity College Dublin accepts no liability for indirect, consequential, or incidental, damages or losses arising from use of the thesis for whatever reason. Information located in a thesis may be subject to specific use constraints, details of which may not be explicitly described. It is the responsibility of potential and actual users to be aware of such constraints and to abide by them. By making use of material from a digitised thesis, you accept these copyright and disclaimer provisions. Where it is brought to the attention of Trinity College Library that there may be a breach of copyright or other restraint, it is the policy to withdraw or take down access to a thesis while the issue is being resolved.

Access Agreement

By using a Digitised Thesis from Trinity College Library you are bound by the following Terms & Conditions. Please read them carefully.

I have read and I understand the following statement: All material supplied via a Digitised Thesis from Trinity College Library is protected by copyright and other intellectual property rights, and duplication or sale of all or part of any of a thesis is not permitted, except that material may be duplicated by you for your research use or for educational purposes in electronic or print form providing the copyright owners are acknowledged using the normal conventions. You must obtain permission for any other use. Electronic or print copies may not be offered, whether for sale or otherwise to anyone. This copy has been supplied on the understanding that it is copyright material and that no quotation from the thesis may be published without proper acknowledgement.

Bolus-Tracking Arterial Spin Labeling: A New Approach to Quantifying Cerebral Perfusion with Magnetic Resonance Imaging

A thesis submitted for the degree of

Doctor of Philosophy

Presented to:

The School of Medicine, Faculty of Health Sciences, Trinity College Dublin

September 2009

Author

Michael Kelly

M. Sc.

Supervisor

Dr. Christian Kerskens

9417

Declaration of Authorship

This thesis is the sole work of the author and has not been submitted in whole or in part to this or any other university for any other degree. The author gives permission for the library to lend or copy this work upon request.

Michael Kelly

Abstract

The body of work presented herein describes the development a new technique for the quantification of cerebral perfusion, termed bolus-tracking arterial spin labeling (btASL). The technique uses a novel non-compartmental model of cerebral perfusion in combination with ASL magnetic resonance imaging (MRI) experiments to quantify the changes in the perfusion state of the rat brain under the following conditions: increased neural activity, normal ageing and methylenedioxymethamphetamine (MDMA) administration.

An ASL sequence was implemented on a 7 Tesla MRI system. The sequence employs the principle of flow-induced adiabatic inversion to provide a bolus of labeled arterial water at the labeling plane in the neck, proximal to the imaging plane in the brain. The fast low-angle shot (FLASH) imaging sequence was used to acquire perfusion-weighted images. Region of interest (ROI) specific concentration-time curves, representing the passage of the bolus through a selected ROI, were generated from the perfusion-weighted images. The non-compartmental model of cerebral perfusion is based on a Fokker-Planck equation that incorporates three factors that affect the concentration of labeled water within the brain: bulk flow, diffusion and T_1 longitudinal relaxation. A least squares fit of the non-compartmental model to the ASL concentration-time curves allows the following perfusion parameters to be quantified: mean transit time (MTT), capillary transit time (CTT), relative volume of labeled water (rVLW), relative flow of labeled water (rFLW) and relative perfusion coefficient of labeled water, rPLW. The latter describes the dispersion of the bolus due to diffusion effects and the exchange of water between vascular and extravascular spaces.

A validation study of the btASL technique was performed in which data was acquired from male Wistar rats (n=3) for three ROIs (cortex, hippocampus and whole brain) and three bolus durations (1.5 s, 2.0 s and 3.0 s). The MTT, CTT and rVLW were quantified for each animal for varying ROI and bolus length. No significant differences were found in the MTT, CTT, rVLW, rFLW and rPLW within each animal for varying bolus duration.

In the functional MRI (fMRI) study of the effects of increased neural activity on cerebral perfusion, electrical stimulation of the rat forepaw resul-

ted in increased neural activity in the somatosensory cortex forelimb (S1FL) region in two groups of female Wistar rats: a group under sedation by medetomidine (n=5)and a group under anaesthesia by propofol (n=5). In both groups, the MTT and CTT were found to decrease significantly during neuronal activation. The rVLW increased significantly and a corresponding increase in rFLW and rPLW was also calculated. The MTT and CTT were not significantly different for the two anaesthetic agents but the increases in rVLW, rFLW and rPLW were significantly higher in the propofol group. The results demonstrate the sensitivity of btASL to subtle changes in the haemodynamic response to neural activity.

The study of the effects of normal ageing on cerebral perfusion revealed a significant increase in MTT and CTT in aged rats (n=5) compared to young (n=9) and middle aged (n=5) rats, while no significant change in rVLW was found. This finding corresponds to a decrease in rFLW and rPLW in the aged group. In the study of the acute effects of MDMA usage on cerebral perfusion, the MTT and CTT were found to decrease significantly in a group of rats imaged 3 hours post MDMA administration (n=5) compared to a control group (n=4). In the absence of a significant change in rVLW, this corresponds to a transient increase in rFLW and rPLW due to the MDMA challenge. The perfusion parameters were found to trend towards a return to baseline values in a third group of rats imaged 24 hours post MDMA administration.

In summary, the btASL technique provides a quantitative assessment of the changes in cerebral perfusion under varying physiological conditions in terms of a unique set of perfusion parameters (MTT, CTT, rVLW, rFLW, rPLW). The findings presented demonstrate the potential of btASL to provide interesting results in future applications in the field of neuroscience.

To Car and to my parents

Acknowledgements

First and foremost, I would like to thank Dr. Christian Kerskens, my PhD supervisor, for giving me the opportunity to work on an interesting and rewarding project over the past three years. His constant willingness to lend assistance and offer constructive advice whenever problems arose were fundamental to the progression of the project. I would also like to express my sincerest gratitude to Prof. Marina Lynch, Dr. James Jones and Dr. Andrew Harkin for the interest they displayed in my project and for all the invaluable advice and support they have given me.

I have been lucky enough to work closely with some extremely helpful and dedicated people during my PhD. I would like to thank Christoph, who I worked with extensively in the lab and was always prepared to lend a hand with experiments and help with interpreting the results. Thanks to Karen for her impressive persistence with the fMRI experiments when many people may have given up. Thanks also to Jennifer, Joe, Matt, Jennie, Larry and Oli. It has been a pleasure working with all of you and hopefully we will work together again in the future.

To Jennie, Joe, Christoph and Ronan in the office, thanks for making the day-to-day experiences so enjoyable. I always enjoyed our chats over coffee, our occasional outings for "one pint" and most of all, our conference trips (Hawaii, Chicago and Valencia... some good times!). I would also like to collectively thank all the other PhD students and post docs at TCIN (past and present) for creating a great social and working environment that was at all times enjoyable to be a part of. I have enjoyed getting to know you all over the past few years and I wish you all the best in your future endeavours. Sincere thanks also to all of the staff at TCIN. In particular, I would like to thank Barbara for her patience with my many funding-related requests and Colm for his help with all things LaTeX and Unix-related.

Of course I also want to say thank you to all my friends and family and in particular, my parents. Your support has been invaluable, particularly over the last few months of my PhD when the pressure was on. Finally, I want to thank Car for listening to my "occasional" rants, for keeping me sane and calm and for always giving me nothing but the soundest of advice.

List of Abbreviations

aBV	Arterial blood volume
AD	Alzheimer's disease
AFP	Adiabatic fast passage
AIF	Arterial input function
ANOVA	Analysis of variance
ASL	Arterial spin labeling
ATP	Adenosine triphosphate
BBB	Blood brain barrier
BFV	Blood flow volume
BOLD	Blood oxygenation level dependent
BP	Blood pressure
btASL	Bolus-tracking arterial spin labeling
CASL	Continuous arterial spin labeling
CBF	Cerebral blood flow
CBV	Cerebral blood volume
CeCT	Contrast enhanced computed tomography
$CMRO_2$	Metabolic rate of oxygen comsimption
CSF	Cerebrospinal fluid
CTT	Capillary transit time
DAI	Double adiabatic inversion
DSC	Dynamic susceptibility contrast
ECG	Electrocardiograph
EPI	Echo-planar imaging
EPISTAR	EPI and signal targeting with alternating radiofrequency
FAIR	Flow-sensitive alternating inversion recovery
FAIRER	FAIR with an extra RF pulse
FLASH	Fast low-angle shot
fMRI	Functional magnetic resonance imaging
GE-EPI	Gradient-echo EPI
GM	Grey matter
IR	Inversion recovery
LASCA	Laser speckle contrast analysis
LCBF	Local cerebral blood flow

LCMRglu	Local cerebral glucose utilization
LDF	Laser Doppler flowmetry
LMCA	Left middle cerebral artery
MDMA	Methylenedioxymethamphetamine
MRI	Magnetic resonance imaging
MT	Magnetization transfer
MTC	Magnetization transfer contrast
MTT	Mean transit time
NSA	Number of signal averages
OEF	Oxygen extraction fraction
PASL	Pulsed arterial spin labeling
pCO_2	Partial pressure of carbon dioxide
PCT	Perfusion-computed tomography
PET	Positron emission tomography
PICORE	Proximal inversion with control for off-resonance effects
PS	Permeability surface-area product
PULSAR	Pulsed STAR labeling of arterial regions
QUASAR	Quantitative STAR labeling of arterial regions
QUIPSS	Quantitative imaging of perfusion using a single subtraction
RARE	Rapid acquisition with relaxation enhancement
rCBF	Relative cerebral blood flow
rCBV	Relative cerebral blood volume
RF	Radiofrequency
rFLW	Relative flow of labeled water
RMCA	Right middle cerebral artery
ROI	Region of interest
rPLW	Relative perfusion coefficient of labeled water
rVLW	Relative volume of labeled water
S1FL	Left forelimb primary somatosensory cortex
SAR	Specific absorption rate
SE-EPI	Spin-echo EPI
SNR	Signal-to-noise ratio
SPECT	Single photon emission computed tomography
STAR	Signal targeting with alternating RF
STAR-HASTE	STAR and half Fourier single shot turbo spin-echo

TE	Echo time
TILT	Transfer insensitive labeling technique
TR	Repetition time
UNFAIR	Uninverted flow-sensitive alternating inversion recovery
VSASL	Velocity-selective arterial spin labeling
VTR	Variable repetition time
WM	White matter

List of Figures

1.1 Kety and Schmidt tracer curves 4
1.2 Meier and Zierler method 7
1.3 ASL perfusion weighted image formation 11
1.4 The effective magnetic field 12
1.5 Flow-induced adiabatic inversion 15
1.6 Magnetization transfer schematic 19
1.7 Magnetization transfer asymmetry 20
1.8 Two-coil CASL 21
1.9 CASL perfusion territory imaging 23
1.10 EPISTAR pulse sequence 25
1.11 FAIR pulse sequence 28
1.12 PASL arterial transit time 29
1.13 QUIPSS pulse sequence 30
1.14 Velocity selective ASL schematic 31
1.15 Velocity selective ASL sequence 32
1.16 Bi-exponential single compartment model 36
1.17 One-barrier distributed parameter model 40
1.18 Two-compartment model of restricted water exchange 41
1.19 Two-compartment model with finite capillary permeability . . 42
1.20 Neurovascular coupling 48
1.21 The BOLD signal 50

2.1 Bolus dispersion schematic 63

3.1 Bruker Biospec 7T animal MRI scanner 78
3.2 Experimental setup 79
3.3 Bolus-tracking ASL sequence 80
3.4 High resolution anatomical image 81

3.5 Sample ASL images 83
3.6 FLASH pulse sequence 84
3.7 Region of interest selection 86
3.8 Concentration-time curves for varying bolus length 87
3.9 Curve fitting robustness 90
3.10 Location of middle cerebral arteries 92

4.1 ASL maps with 1.5 s bolus duration 102
4.2 ASL maps with 2.0 s bolus duration 102
4.3 ASL maps with 3.0 s bolus duration 102
4.4 Curve fitting results for animal 1 103
4.5 Curve fitting results for animal 2 104
4.6 Curve fitting results for animal 3 105
4.7 Validation study transit time histograms 106
4.8 Validation study rVLW histograms 107

5.1 Somatosensory cortex activation maps (medetomidine) 116
5.2 Curve fitting results (medetomidine) 117
5.3 Transit time histogram (medetomidine) 118
5.4 rVLW histogram (medetomidine) 118
5.5 Somatosensory cortex activation maps (propofol) 119
5.6 Curve fitting results (propofol) 120
5.7 Transit time histogram (propofol) 121
5.8 rVLW histogram (propofol) 121
5.9 Comparison of medetomidine and propofol MTT 122
5.10 Comparison of medetomidine and propofol CTT 122
5.11 Comparison of medetomidine and propofol rVLW 123
5.12 Comparison of medetomidine and propofol change in rVLW . 123

6.1 Ageing study MTT histogram 127
6.2 Ageing study CTT histogram 128
6.3 Ageing study rVLW histogram 129
6.4 MDMA study MTT histogram 135
6.5 MDMA study CTT histogram 136
6.6 MDMA study rVLW histogram 137
6.7 MDMA related temperature variation 139

7.1 Linear correlation between change in MTT and CTT 148

List of Tables

3.1 Bolus-tracking ASL time points 82

4.1 Variation in rFLW and rPLW for 2.0 s v 1.5 s bolus 98
4.2 Variation in rFLW and rPLW for 3.0 s and 1.5 s bolus 98
4.3 Variation in rFLW and rPLW for 3.0 s and 2.0 s bolus 98

5.1 rFLW and rPLW calculation (medetomidine) 110
5.2 rFLW and rPLW calculation (propofol) 112

6.1 Variation in rFLW and rPLW for aged v young animals 130
6.2 Variation in rFLW and rPLW for aged v middle aged animals . 130
6.3 rFLW and rPLW calculation (MDMA 3hr v control) 138
6.4 rFLW and rPLW calculation (MDMA 3hr v 24 hr) 138

A.1 Validation study MTT and CTT 153
A.2 Validation study rVLW 154
A.3 Transit time results (medetomidine) 155
A.4 rVLW results (medetomidine) 155
A.5 Transit time results (propofol) 156
A.6 rVLW results (propofol) 156
A.7 Ageing study MTT, CTT and rVLW results (cerebral cortex) . 157
A.8 Ageing study MTT, CTT and rVLW results (hippocampus) . . 158
A.9 Ageing study MTT, CTT and rVLW results (whole brain) . . . 159
A.10 MDMA study MTT, CTT and rVLW (right cortex) 160
A.11 MDMA study MTT, CTT and rVLW (left cortex) 160
A.12 MDMA study MTT, CTT and rVLW (right striatum) 161
A.13 MDMA study MTT, CTT and rVLW (left striatum) 161

Contents

1 Cerebral Perfusion Quantification **1**

1.1 Cerebral Perfusion 1

1.2 Seminal Approaches for the Quantification of Cerebral Perfusion 3

1.2.1 The Kety and Schmidt Method 4

1.2.2 The Meier and Zierler Indicator-Dilution Method . . . 6

1.3 Arterial Spin Labeling: Sequences 9

1.3.1 Continuous Arterial Spin Labeling 10

1.3.2 Pulsed Arterial Spin Labeling 23

1.3.3 Velocity Selective Arterial Spin Labeling 31

1.4 Arterial Spin Labeling: Perfusion Quantification 33

1.4.1 Single-Compartment Models 33

1.4.2 Two-Compartment Models 39

1.4.3 Model-Free Arterial Spin Labeling Quantification . . . 43

1.4.4 Arterial Spin Labeling Quantification Errors 45

1.5 Mechanisms that Alter Cerebral Perfusion 47

1.5.1 Neural Activity 47

1.5.2 Normal Ageing 55

1.5.3 MDMA Intake 57

2 Theoeretical Results: A Non-Compartmental Model of Cerebral Perfusion **61**

2.1 Introduction 61

2.2 Derivation of Fokker-Planck Equation 63

2.2.1 The Bloch Equation for Longitudinal Relaxation 63

2.2.2 The Langevin Equation 64

2.2.3 Combining the Langevin and Bloch Equations 65

2.2.4 Transfer to the Fokker-Planck Equation 65
2.3 Bolus-Tracking Arterial Spin Labeling Solution 67
2.4 Physical Interpretation of Transit Times 69
2.5 Comparison of the Bolus-Tracking ASL Solution to Existing Theories 71
2.6 Additional Solution for a Saturation Experiment 72
2.7 Discussion of Theoretical Results 73
2.8 Appendix: Solution to the Fokker-Planck Equation for the Bolus-Tracking Arterial Spin Labeling Boundary Conditions . 75

3 Materials and Methods **77**
3.1 Magnetic Resonance Imaging Hardware 77
3.2 Animal Preparation 77
3.2.1 Animal Setup for Non-Functional Studies 78
3.2.2 Animal Setup for Functional Studies 79
3.3 Imaging Slice Location 81
3.4 Bolus-Tracking Arterial Spin Labeling 81
3.4.1 Arterial Spin Labeling Preparation 82
3.4.2 Fast Low Angle Shot Image Acquisition 83
3.5 T1 Measurement 84
3.6 Data Analysis 85
3.6.1 Regions of Interest and Concentration-Time Curves . . 85
3.6.2 Curve Fitting 86
3.6.3 Quantification of Perfusion Parameters from Curve Fitting Parameters 90
3.6.4 Calculation of Error in Perfusion parameters 93

4 Experimental Validation of Non-Compartmental Model of Cerebral Perfusion **95**
4.1 Introduction 95
4.2 Results 96
4.2.1 Bolus-Tracking Arterial Spin Labeling Datasets 96
4.2.2 Transit Time Results 97
4.2.3 rVLW, rFLW and rPLW Results 97
4.3 Discussion 99

5 Functional MRI with Bolus-Tracking Arterial Spin Labeling 108
5.1 Introduction . . . 108
5.2 Results . . . 109
5.2.1 Medetomidine Results . . . 109
5.2.2 Propofol Results . . . 111
5.2.3 Comparison of Medetmoidine and Propofol Results . . 111
5.3 Discussion . . . 112

6 Additional Bolus-Tracking Arterial Spin Labeling Results 124
6.1 Ageing Study . . . 124
6.1.1 Introduction . . . 124
6.1.2 Results . . . 125
6.1.3 Discussion . . . 126
6.2 MDMA Study . . . 132
6.2.1 Introduction . . . 132
6.2.2 Results . . . 133
6.2.3 Discussion . . . 139

7 Discussion 142
7.1 Summary . . . 142
7.1.1 Further Validation and Testing . . . 147
7.2 Conclusions and perspectives . . . 150

A Data Tables 152

Chapter 1

Cerebral Perfusion Quantification

1.1 Cerebral Perfusion

The term cerebral perfusion refers to the process involved in the delivery of nutritive blood to the brain tissues capillary bed [1, 2]. Accurate perfusion measurement can provide an important insight into the perfusion state of the brain under various physiological and pathophysiological conditions. As a result, numerous imaging techniques have been developed specifically to evaluate cerebral perfusion and brain haemodynamics [3]. Optical techniques such as laser-Doppler flowmetry (LDF), two-photon microscopy and laser speckle contrast analysis (LASCA) [4, 5, 6] are capable of imaging cerebral perfusion with very high spatial resolution. However, disadvantages such as low penetration depth, scattering effects, the need to inject fluorescent dyes and the need to create a cranial window limits the practicality of these techniques in the clinical setting. As a result, the main imaging techniques dedicated to assessing the global perfusion state of the brain are positron emission tomography (PET), single photon emission computed tomography (SPECT), contrast-enhanced computed tomography (CeCT), dynamic perfusion-computed tomography (PCT), Doppler Ultrasound, dynamic susceptibility contrast magnetic resonance imaging (DSC-MRI), and arterial spin labeling (ASL) MRI (for a review of these techniques see [3]).

PET techniques use intravenously injected positron emitting radioisotopes such as ^{15}oxygen water ($H_2{}^{15}O$) in combination with arterial blood sampling to provide quantitative cerebral perfusion maps [7]. In SPECT

imaging, radiopharmaceuticals such as ^{133}Xenon (^{133}Xe) are injected and subsequent tomographic images based on the tracer distribution are indicative of regional cerebral haemodynamics [8]. CeCT and dynamic PCT use computed tomography (CT) imaging in combination with Xenon tracers [9] and iodinated contrast agents [10] respectively to assess cerebral perfusion. Doppler ultrasound can measures the blood flow volume (BFV) in the internal carotid arteries noninvasively and the BFV can be used as a correlate for cerebral perfusion [11]. DSC-MRI assesses cerebral perfusion by tracking the first pass of an exogenous contrast agent, typically chelated gadolinium, through the capillary bed [12]. ASL is a MRI technique that does not require the use of an exogenous contrast agent but uses magnetically labeled water protons as an endogenous tracer for the measurement of cerebral perfusion [13, 14].

Each of these techniques relies on inherently different contrast mechanisms and consequently the delivery of blood to the capillary bed is described by many different parameters. The results of perfusion imaging studies are commonly expressed in terms of cerebral blood flow (CBF), which has a typical unit of ml/100ml/min. This unit is a rate (per unit time) rather than a volume-flux (volume per unit time) measurement and therefore describes an average flow rate within a voxel of arbitrary volume [1]. For historical reasons, CBF is often stated as ml/100g/min. However, in practise no information can be obtained about the tissue mass of individual voxels and a mean brain density of 1 g/ml is assigned to all voxels. Cerebral perfusion can also be expressed in terms of cerebral blood volume (CBV), which describes the fraction of a voxel that contains blood vessels. It is therefore dimensionless and is usually expressed either as a percentage or in ml/100g. Finally, the mean transit time (MTT) is usually defined as the average time it takes a particle to traverse the vasculature and is measured in seconds. These are the main parameters in general use in perfusion imaging studies.

Most of the techniques above rely upon the injection of contrast agents and or the use of ionizing radiation, with the exception of Doppler ultrasound which can be regarded as entirely noninvasive but suffers from limited spatial resolution [15]. The ASL technique (section 1.3) is noninvasive and can provide global, quantitative cerebral perfusion maps with acceptable spatial and temporal resolutions. The non-invasiveness of ASL makes

it very suitable for perfusion measurements both in healthy volunteers and in patient groups requiring repetitive follow-ups.

As a result, the various ASL approaches (section 1.3.1 and Section 1.3.2) have been applied to many studies investigating healthy brain function, pathophysiologies and treatment outcomes. For example, visual stimulation ASL functional MRI (fMRI) studies have measured CBF changes in the occipital cortex [16] and motor studies have measured CBF changes in the primary motor cortex [17]. ASL studies in stroke patients have helped to ascertain that the cessation of CBF to brain tissue can lead to permanent brain damage if the cessation persists for approximately 3 min [18]. CBF alterations in patients suffering from cardiovascular disease such as carotid stenosis [19], age related disease such as Alzheimer's disease (AD) [20] and psychiatric conditions such as depression [21] have been measured using ASL. The assessment of brain tumor types is also possible as ASL perfusion shows consistently higher CBF values in high-grade than low-grade gliomas [22].

In each of these applications, perfusion-weighted images are acquired using one of the many ASL acquisition strategies (section 1.3.1 and section 1.3.2). In order to quantify cerebral perfusion, a theory that takes into account physiological mass transport of blood into and out of the brain and the exchange mechanisms within the brain tissue must be applied to the ASL data.

1.2 Seminal Approaches for the Quantification of Cerebral Perfusion

All present-day perfusion measurements, both MRI and non-MRI, are essentially based on the theory behind two seminal approaches: the freely-diffusible tracer theory of Kety and Schmidt [23] and the indicator-dilution theory of Meier and Zierler [24]. These two approaches will now be described in detail.

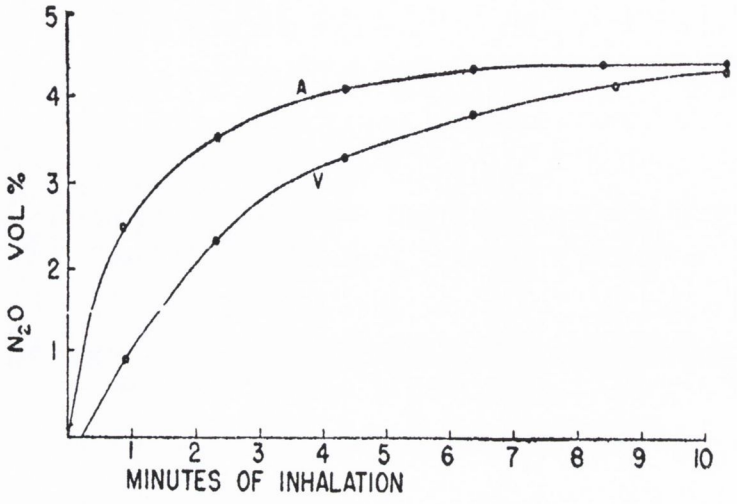

Figure 1.1: Arterial (A) and venous (V) N_2O concentrations ($c_a(t)$ and $c_v(t)$) during the inhalation of O_2 and N_2O mixture. Adapted from [23].

1.2.1 The Kety and Schmidt Method

The original Kety and Schmidt experiments used the inhalation of freely diffusible nitrous oxide (N_2O) as a tracer to estimate CBF. Freely diffusible tracers can leave the intravascular space without restriction and be distributed throughout the entire tissue volume. A theory based on Fick's principle was developed by Kety and Schmidt. Fick's principle for metabolically inert tracers states that the change in the the mean tracer concentration in tissue, $c_t(t)$, equals the flow rate multiplied by the arterio-venous concentration difference of the tracer. This can be expressed as follows:

$$\frac{\partial c_t(t)}{\partial t} = -F\frac{\partial c}{\partial V} = -F\frac{c(x+\Delta x) - c(x)}{\Delta x}, \tag{1.1}$$

where F is the flow rate defined as the flow velocity multiplied by the flow cross-sectional area and $c(x+\Delta x)$ and $c(x)$ denote the contrast agent concentrations at locations in space corresponding to the venous and arterial compartments respectively. When $c_a(t)$ and $c_v(t)$ (the arterital and venous tracer concentrations) are substituted for these two terms, Fick's principle can be written in the form commonly used in tracer kinetic studies [1]:

$$\frac{dc_t(t)}{dt} = CBF(c_a(t) - c_v(t)). \tag{1.2}$$

where CBF is expressed as flow per unit volume here. The Fick formula in

equation 1.2 was written as follows in the theoretical formulation of Kety and Schmidt to describe the delivery of oxygen to the brain [23]:

$$CBF = \frac{100(dc_t(t)/dt)}{(c_a(t) - c_v(t))T} \tag{1.3}$$

where CBF is in units of cc./100 grams of tissue/minute and dc_t/dt represents the quantity of tracer consumed by the tissue in the time interval t, in minutes and T is the time at which equilibrium is reached. The theoretical formulation needs to be modified for the case of an inhaled tracer where $c_a(t)$ and $c_v(t)$ both start at zero and increase over time, with $c_a(t)$ increasing more rapidly than $c_v(t)$, as shown in figure 1.1[1]. Equation 1.2 can be rearranged as follows:

$$CBF = \frac{dc_t(t)/dt}{c_a(t) - c_v(t)}. \tag{1.4}$$

In the case of two curves such as A and V, the quantity of tracer removed from the blood by the brain cannot be calculated from $c_a(t)$ - $c_v(t)$ but is calculated from the total area between the curves A and V. As a result the denominator in equation 1.4 must be integrated from t=0 to t=T. Finally, introducing a factor of 100 to ensure consistency of the units, equation 1.4 becomes:

$$CBF = \frac{100(dc_t(t)/dt)}{\int_0^T (c_a(t) - c_v(t))dt} \tag{1.5}$$

A solution to the integral in equation 1.5 was found. Following the assumption that the quantity of N_2O taken up by the brain in the time interval t is equal to the venous concentration, c_v, multiplied by a partition coefficient for N_2O between brain tissue and blood (i.e. the ratio of the concentration of N_2O in brain tissue to that in the blood), the CBF was obtained from a set of curves such as those in figure 1.1. This assumption implies that the N_2O tracer is freely diffusible (i.e. N_2O is exchanged freely across the capillary walls) and that equilibrium has been reached between the brain and blood N_2O concentrations after the time interval, t. The theory of Kety and Schmidt forms the basis for the first quantitative arterial spin labeling

[1]In the original experiments, the curves A and V were measured by sampling blood from the femoral artery and right internal jugular vein over time respectively

methods that used Fick's principle to describe the dynamics of in-flowing magnetically labeled water molecules (section 1.4.1).

1.2.2 The Meier and Zierler Indicator-Dilution Method

When a freely diffusible tracer is used, the blood volume cannot be assessed and an intravascular tracer would be needed in order to quantify CBV, whereas the distribution volume of purely intravascular tracer is equal to the CBV. The Meier and Zierler approach considers the basic relationship of the central volume theorem [25]:

$$CBV = MTT \times CBF. \tag{1.6}$$

The internal structure of the vascular system is assumed to consist of many branchings and interlacings of blood vessels and consequently, particles of an indicator entering the vascular system at point P in figure 1.2(a) will require varying amounts of time to reach Q and a distribution of traversal times is considered instead of a single traversal time. A closed flow system, that is, one with a single in-flow orifice, P, and a single outflow orifice, Q, is assumed. For an instantaneous injection of indicator (Evan's blue dye) injected into the systemic venous circulation and sampled from a systemic artery, all of the indicator injected at P must eventually leave the system at Q, if non-leaky capillaries are assumed. As a result, a concentration versus time curve such as the curve shown in figure 1.2(b) can be sampled at Q.

The system contains a volume, V, of fluid which enters and exits at a constant rate of flow, F (where F is in units of volume per unit time). If F is high, the injected indicator is mixed with a large amount of blood and the concentration at Q in figure 1.2(a) will be low. This inverse relationship between flow and sampled indicator concentration forms the basis of the quantification of flow by the Meier and Zierler method. If q units of indicator are injected at P at $t=0$ and $c(t)$ is the measured concentration at Q in figure 1.2(b), then the amount of indicator that leaves the system in a small time interval, t to $t+dt$ is equal to $c(t)\times Fdt$. Since all the indicator injected at P leaves the system at Q, the total amount injected is given by the integral [24]:

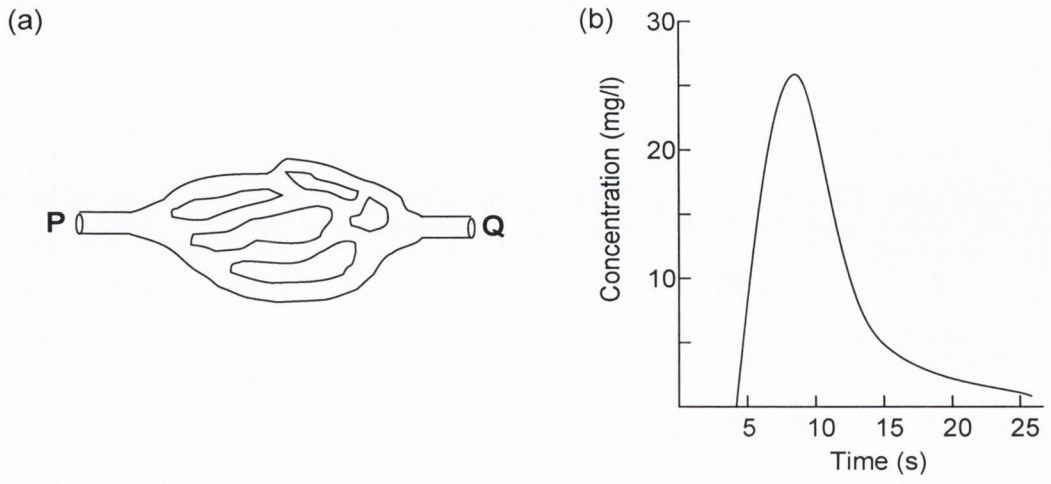

Figure 1.2: (a) Schematic diagram of vascular bed with injection site at P and asmpling site at Q. (b) Concentration of indicator as a function of time for an instantaneous, time-domain impulse function injection of indicator (recirculation of the indicator is neglected for simplicity) [24].

$$q = F \int_0^\infty c(t)dt. \tag{1.7}$$

It follows that the area under the concentration-time curve is equal to q/F and solving for F we get:

$$F = \frac{q}{\int_0^\infty c(t)dt}. \tag{1.8}$$

The product $Fc(t)$ is the rate at which indicator is leaving the system at time t. In order to establish the fundamental relationship of the central volume theorem, CBV = MTT$\times$CBF, the following function was introduced:

$$h(t) = \frac{Fc(t)}{q}. \tag{1.9}$$

This is the fraction of the injected indicator that leaves the system per unit time. The assumption is made that the distribution of transit times for the indicator particles is indicative of the distribution for all fluid particles. Therefore, for all particles entering the system at $t=0$, $h(t)$ is the fraction of those particles leaving per unit time. Combining equation 1.8 and equation 1.9 gives the following:

$$\int_0^\infty h(t)dt = 1, \tag{1.10}$$

where *h(t)* is now the frequency function of the traversal times (i.e. the frequency with which each transit time occurs or the distribution of transit times). All particles within the fluid can be distinguished by the time it takes the particles to travel from P to Q. The volume of the system can be found by establishing the volume of particles with traversal times in the time interval t to $t+dt$ and summing these volume elements for all traversal time intervals as follows [24]:

$$V = \int_0^\infty tFh(t)dt \qquad \text{or} \qquad V = F\int_0^\infty th(t)dt. \tag{1.11}$$

The function *h(t)* has been defined in equation 1.10 as the frequency of traversal times, so the integral in equation 1.11 is simply the mean of the traversal times or the MTT, which is conventionally denoted by, $\bar{t}$:

$$\bar{t} = \int_0^\infty th(t)dt \tag{1.12}$$

If we recall the definition of *h(t)* in equation 1.9 and substitute the equation for F in equation 1.8, the following formulation for $\bar{t}$ in terms of the concentration-time curve, *c(t)*, measured at Q:

$$\bar{t} = \frac{\int_0^\infty tc(t)dt}{\int_0^\infty c(t)dt}. \tag{1.13}$$

Equation 1.13 states that the MTT for a purely intravascular tracer can be calculated from the first statistical moment of the concentration-time curve, *c(t)*. Finally, the central volume theorem can be written as:

$$V = \bar{t}F, \tag{1.14}$$

where V is the total intravascular volume from P to Q in figure 1.2, F is the constant rate of flow at which fluid enters and exits the system and $\bar{t}$ is the mean traversal time of fluid particles in the system, or MTT. It should be noted that this model is based on the fundamental assumption that the system has no stagnant pools (i.e. fluid anywhere in the system must be eventually eliminated). This assumption limits the application of the theory

to purely intravascular tracers. As a result, the Meier and Zierler method forms the basis of quantitative DSC-MRI bolus tracking experiments, in which the first pass of a bolus of intravascular contrast agent is monitored and a model-independent perfusion estimation is obtained [26].

1.3 Arterial Spin Labeling: Sequences

In ASL, the water molecules of flowing blood are used as an endogenous freely diffusible tracer and the injection of an exogenous contrast agent is not necessary. As arterial water flows into the capillary bed, water exchange between blood and tissue occurs through the blood brain barrier (BBB). When the magnetization of the flowing water molecules is labeled (or tagged), a MRI signal change arises as the arterial blood perfuses into the tissue and both the apparent tissue T_1 and the tissue magnetization are altered. These changes can be used to quantify cerebral perfusion.

Labeling is achieved by introducing a radiofrequency (RF) saturation [13, 14] or inversion pulse [27] proximal (upstream) to the tissue of interest. The location of the labeling plane is determined by the carrier frequency of the pulse. Following a time delay that allows the magnetically labeled water molecules to reach the tissue capillary bed and exchange with water molecules in the tissue, an imaging sequence is acquired in the brain, distal (upstream) to the tagging location. It should be noted that the water exchange involves both physical molecular exchange and magnetization exchange and the consequences of the latter will be discussed in section 1.3.1 (magnetization transfer effects).

There exist two main classes of ASL techniques: continuous ASL (CASL) and pulsed ASL (PASL). Both classes contain many variations of the basic ASL approach described above and have been thoroughly review in the literature [1, 28, 29]. A summary of the main ASL sequences and the principles behind them will follow in sections 1.3.1 and 1.3.2. A third and more recent ASL technique known as velocity selective ASL (VSASL) will be briefly discussed in section 1.3.3.

1.3.1 Continuous Arterial Spin Labeling

CASL, also known as steady-state ASL was the first ASL technique to be developed [14, 13]. The inversion of inflowing spins is achieved by applying a 2 - 4 s RF pulse while applying a magnetic field gradient in the direction of arterial flow. Moving arterial spins experience a slow variation in the resonance frequency, which ultimately results in their inversion, while static spins located in the tissue are saturated. The inversion slice, or labeling plane must be located proximal to the imaging plane and is generally at the common carotid artery. Spins flowing through this plane are inverted by the principle of flow-driven adiabatic inversion, a method previously used in angiography [30], where the theory of adiabatic fast passage (AFP) [31] is applied to the specific case of the inversion of flowing spins. The degree of the inversion achieved by the flow-driven adiabatic inversion scheme depends on the velocity of the blood, the orientation of the vessels to relative to the labeling plane and the RF power and gradient strength and is typically in the range of 80 - 95% [32, 33, 34]. The degree of inversion, α_0, describes the labeling efficiency at the inversion plane and is given by the following [28, 35]:

$$\alpha_0 = \frac{M_a^0 - M_a^{inv}}{2M_a^0}, \tag{1.15}$$

where ${M_a}^0$ is the equilibrium longitudinal magnetization of arterial spins and ${M_a}^{inv}$ is the longitudinal magnetization of arterial spins after they move through the inversion plane. Due to the longitudinal relaxation that occurs during the transit time from the labeling plane to the ROI, the inversion state of labeled spins at the perfusion site should be corrected for T_1 relaxation time of the arterial water, T_{1a} as follows [36]:

$$\alpha(t) = \alpha_0 \exp\left(\frac{-t}{T_{1a}}\right). \tag{1.16}$$

At least two images, a labeled and control image (figure 1.3), are acquired by a CASL sequence. The pulse sequence to acquire the labeled image begins with a flow-driven adiabatic inversion pulse and an accompanying magnetic field gradient, G along the direction of arterial flow. RF pulse durations of several seconds are needed to achieve CASL, which can results

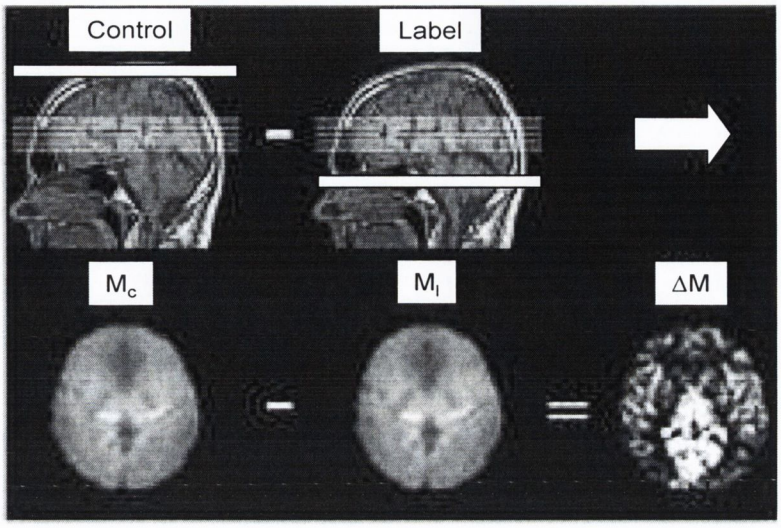

Figure 1.3: Schematic representation of the formation of a qualitative perfusion weighted image from the subtraction of a labeled image from a control image. The horizontal white bars on the control and label images represent the RF inversion pulse in a CASL experiment (section 1.3.1). Adapted from [1].

in the regulatory limits on specific absorption rate (SAR) being reached and or the capability of the RF amplifier being exceeded. As a result, a rectangular pulse of several second duration is typically approximated by a series of shorter pulses separated by an interpulse interval, with a duty cycle in the range of 70-90%.

The carrier frequency of the labeling pulse is offset to provide a labeling location a few centimeters from the imaging plane. For a given labeling frequency, f_l the gradient strength, G determines the position of the labeling plane, Δr as follows [37]:

$$f_l = \frac{\gamma}{2\pi} G \Delta r, \tag{1.17}$$

where f_l is the frequency offset with respect to the Larmor frequency, Δr is the separation between the labeling plane and the imaging plane and γ is the gyromagnetic ratio. Following the long labeling pulse, a spoiler gradient is often introduced to remove any transverse magnetization formed by imperfections in the inversion pulse. After a time delay, a host imaging sequence is played at the image location. A number of pulse sequences can be used as the imaging sequence, including SE [13], GE [38], echo-planar imaging (EPI) [39] and fast low-angle shot (FLASH) [40]. In order to remove

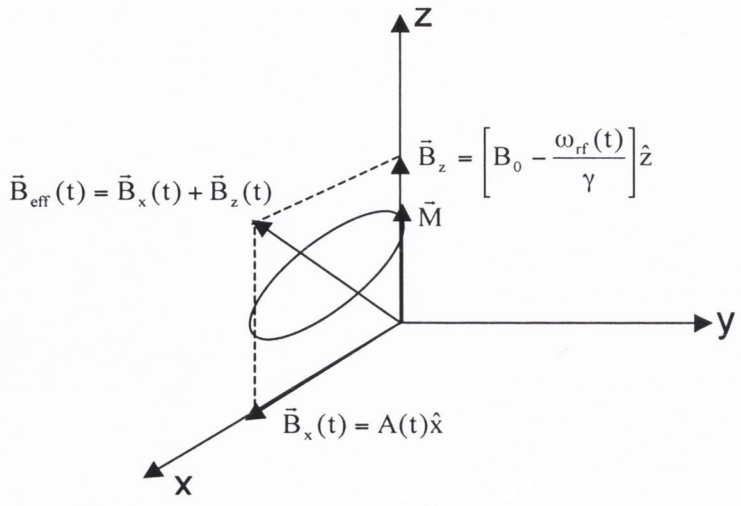

Figure 1.4: The effective magnetic field $\vec{B}_{eff}$, is the resultant vector of the z component of the magnetic field in the rotating frame that arises due to $\omega_{rf}(t)$ modulations and the x component of the magnetic field in the rotating frame that arises due to the application of a B_1 field with amplitude $A(t)$ [37].

the static tissue signal and provide a purely perfusion-weighted map at the ROI, a control image is acquired. For the control image, the offset frequency of the labeling pulse, f_l in Eqn. 1.17 is generally reversed to -f_l to place the inversion or saturation plane distal to the imaging plane and an identical host imaging sequence is played at the imaging plane. Alternatively, the gradient G in equation 1.17 is reversed and the frequency offset remains unchanged. When the labeled image M_l, is subtracted from the control image M_c, the difference image $\Delta M = |M_c\text{-}M_l|$ can be viewed directly as a qualitative perfusion-weighted image, as illustrated in figure 1.3.

Adiabatic Inversion Radiofrequency Pulses

In order to understand the application of the principle of AFP to the inversion of flowing spins to the CASL approach, a brief introduction to adiabatic inversion pulses is required. A transverse RF magnetic field with a time-dependent amplitude A(t) and carrier frequency $\omega_{rf}(t)$ can be described as follows [37]:

$$B_1(t) = A(t)e^{-i\omega_{rf}(t)t}. \tag{1.18}$$

In the frame of reference rotating with a frequency of ω_{rf} the effective mag-

netic field will have two orthogonal components, one in the transverse plane and one along the z axis (B_0) direction, as shown in figure 1.4. The component in the transverse plane is equal to the amplitude of the RF magnetic field and is given by:

$$B_x(t) = A(t), \tag{1.19}$$

where, without loss of generality, it is assumed that the B_1 field is applied along the x axis of the rotating frame of reference. The component of the effective magnetic field along the z axis is defined by the frequency difference between the Larmor frequency (ω=γB_0):

$$B_z(t) = \frac{1}{\gamma}[\omega - \omega_{rf}(t)] = B_0 - \frac{\omega_{rf}(t)}{\gamma}. \tag{1.20}$$

The effective magnetic field is the vector sum of these two orthogonal components and is given by:

$$\vec{B}_{eff}(t) = B_x\hat{x} + B_z\hat{z}, \tag{1.21}$$

where $\hat{x}$ and $\hat{z}$ are unit vectors along the x and z axes of the rotating frame of reference, respectively. The magnitude and direction of $\vec{B}_{eff}$ are given by:

$$|\vec{B}_{eff}| = \sqrt{B_x^2(t) + B_z^2(t)} \tag{1.22}$$

$$\psi = \arctan\left(\frac{B_x(t)}{B_z(t)}\right) \tag{1.23}$$

The magnetization vector $\vec{M}$, shown in figure 1.4, precesses around $\vec{B}_{eff}$ in the rotating frame of reference. In general, $\vec{B}_{eff}$ is tilted towards the z axis except exactly at resonance, when ω_{rf}=ω and the z component of $\vec{B}_{eff}$ is zero.

The principle of AFP states that for an adiabatic pulse $\vec{M}$ follows the direction of $\vec{B}_{eff}$ for a given spin system, provided that the direction of the effective magnetic field does not vary too much during one precession of $\vec{M}$ about $\vec{B}_{eff}$ [41]. This condition is known as the *adiabatic condition* and is described by [37]:

$$\left|\frac{d\psi}{dt}\right| \ll \gamma|\vec{B}_{eff}|, \tag{1.24}$$

where ψ, in radians, is defined by equation 1.23. When the adiabatic condition is satisfied, a magnetization vector that is initially collinear with $\vec{B}_{eff}$ will remain collinear with $\vec{B}_{eff}$ during an inversion. The condition is important when applying the theory of adiabatic inversion to the specific case of flow-driven adiabatic inversion, where the magnetization of moving spins is inverted adiabatically.

Flow-Driven Adiabatic Inversion

An arbitrary RF pulse that has neither amplitude nor frequency modulation can be defined by the following equation [42]:

$$B_1(t) = Ae^{-i\omega_{rf}t}, \tag{1.25}$$

where the amplitude A and frequency ω_{rf} of the pulse are constants and B_1 is the transverse magnetic field from the RF pulse. Consideration of the principles involved in adiabatic inversion outlined above, leads to the conclusion that this pulse will not behave as an adiabatic inversion pulse for stationary (tissue) spins as neither the amplitude or frequency are modulated in time. However, for moving spins, when a magnetic field gradient G is applied along the direction of motion, the pulse described in equation 1.25 can produce an adiabatic inversion. While the RF is held constant, the $\vec{B}_0$ field is swept due to G and spins moving with a constant velocity will consequently experience a sweep of the resonant frequency.

Figure 1.5(a) defines a co-ordinate system in terms of the location of the inversion plane (r=r_0), where r_0=$\omega_{rf}/(\gamma G)$ and γ is the gyromagnetic ratio. Spins located at r_0 are on resonance. A group of spins moving towards the labeling plane from a remote location $r(t) \gg r_0$ towards the labeling plane at r_0, passing through the labeling plane and flowing away from the labeling plane experience a time-varying frequency offset defined by the following equation [37]:

$$\Delta\omega(t) = \gamma G r(t) - \omega_{rf} = \gamma G[r(t) - r_0]. \tag{1.26}$$

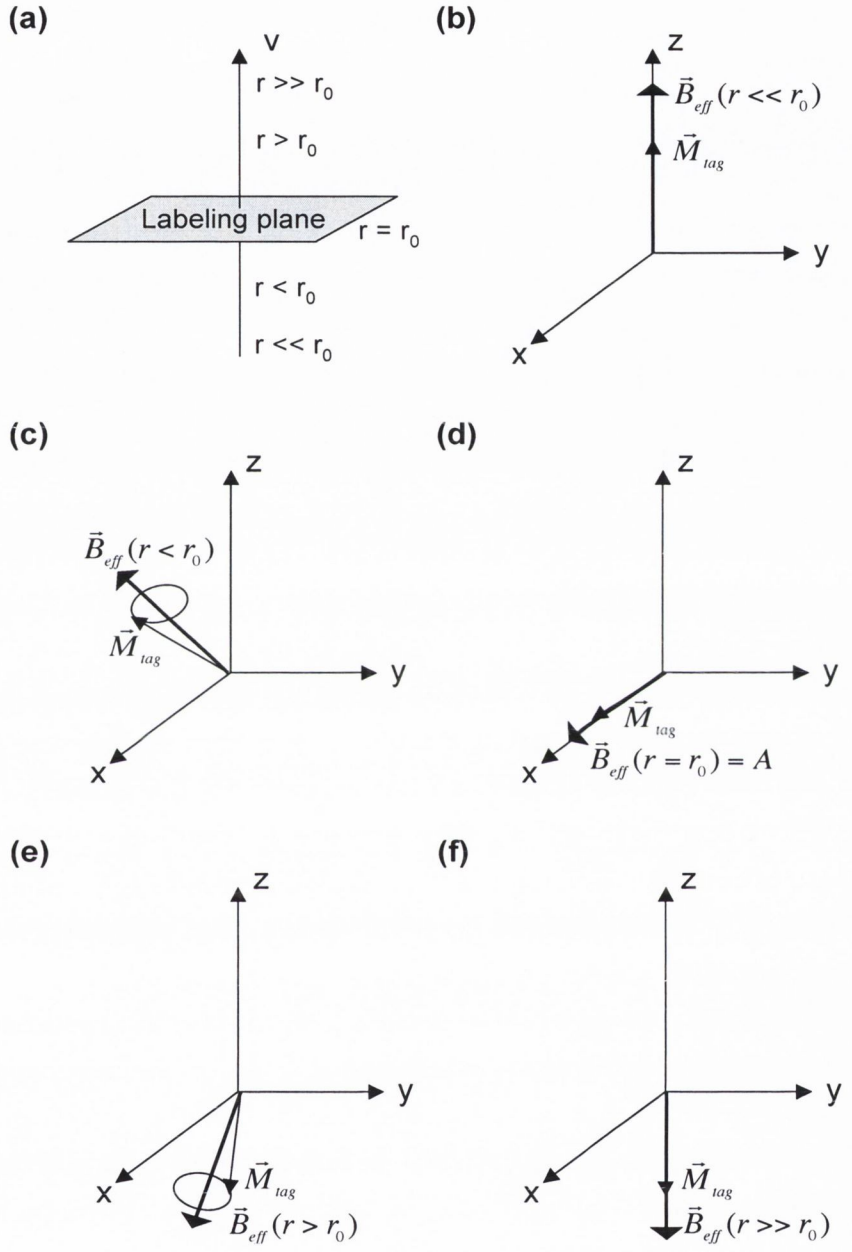

Figure 1.5: Flow-induced adiabatic inversion. (a) Arterial blood flowing from a location remote from the tagging plane ($r << r_0$), passing through the tagging plane ($r = r_0$) and eventually moving away from the tagging plane toward the imaging location ($r >> r_0$). (b)-(f) Change in direction of the effective magnetic field $\vec{B}_{eff}$ together with the magnetization vector $\vec{M}_{tag}$ during the course of the arterial blood flow in (a). Under the adiabatic condition, the magnetization of arterial spins $\vec{M}_{tag}$ follows $\vec{B}_{eff}$ [37].

This offset in the precession frequency of the moving spins due to their position relative to the labeling plane leads to a z component of the effective magnetic field, $\vec{B}_{eff}$ defined as [37]:

$$\vec{B}_{eff} = \frac{\Delta\omega(t)}{\gamma}\hat{z} + A\hat{x}. \tag{1.27}$$

From equation 1.27 it can be deduced that the RF pulse is in this case applied along the x axis with a frequency of ω_{rf}. When the moving spins are a relatively large distance from the labeling plane (i.e. $r(t) \gg r_0$), the effective magnetic field, $\vec{B}_{eff}$ is approximately parallel to the z axis of the rotating frame of reference because $|\Delta\omega(t) \gg \gamma A|$, as shown in figure 1.5(b). As the spins approach the tagging plane at r_0, $\vec{B}_{eff}$ rotates to the transverse plane. Equation 1.24 gives the condition that must be satisfied for adiabatic inversion to occur. As long as this condition is satisfied for the moving spins, the magnetization $\vec{M}_{tag}$ of these spins will follow $\vec{B}_{eff}$ and nutate towards the x axis, as shown in figure 1.5(c). At the labeling plane ($r(t)=r_0$), the moving spins are on resonance and $\vec{B}_{eff}$ and $\vec{M}_{tag}$ lie in the transverse plane, as shown in figure 1.5(d). As the spins move away from the labeling plane, the frequency offset $|\Delta\omega(t)|$ begins to increase, causing $\vec{B}_{eff}$ and $\vec{M}_{tag}$ to nutate towards the longitudinal axis, as shown in Fig.1.5(e) until ultimately, $\vec{B}_{eff}$ is antiparallel to the z. As long as the adiabatic condition in equation 1.24 is satisfied, $\vec{M}_{tag}$ follows $\vec{B}_{eff}$ and is inverted from the $+z$ axis to the $-z$ axis, as shown in figure1.5(f).

The adiabatic condition in equation 1.24 needs to be modified for the specific case of moving spins where the success of the inversion scheme depends also on the strength of G, the velocity of the moving spins, v and the T_2 relaxation time of the arterial blood, T_{2b}. For spins moving with a velocity component v parallel to G, the velocity-dependent frequency offset that forms the z component of $\vec{B}_{eff}$ is given by [41]:

$$\Delta\omega = \gamma G v t. \tag{1.28}$$

When the definition of Ψ in equation 1.23 is taken into account, equation 1.24 can be rewritten as:

$$\frac{Gv}{|\vec{B}_{eff}|} \ll \frac{\gamma}{2\pi}\left|\vec{B}_{eff}\right|. \tag{1.29}$$

The inversion must also be faster than T_{2b}, the T_2 relaxation time of the blood. When this dependency is combined with equation 1.29 we arrive at the adiabatic condition for flow-driven adiabatic inversion [13, 41, 37]:

$$\frac{1}{T_{2b}} \ll \frac{Gv}{|\vec{B}_{eff}|} \ll \frac{\gamma}{2\pi} \left|\vec{B}_{eff}\right|. \tag{1.30}$$

Equation 1.30 forms the basis for all CASL experiments. Contravention of this condition can occur for slow moving spins if relaxation occurs during the transition of the spins through the labeling plane (left hand inequality) or if the velocity of the moving spins is so great that the fundamental adiabatic condition of equation 1.24 is contravened.

Quantum Mechanical Description of Adiabatic Inversion

A quantum mechanical description of the change in the orientation of the net magnetization vector following an adiabatic version is given by Zhernovoy [43]. In this description, the z axis component of $\vec{M}_{tag}$ following an inversion is given by:

$$M_z = M_0 P - M_0(1-P) = M_0(2P-1), \tag{1.31}$$

where P is the probability of keeping the orientation of a spin constant with respect to the applied external magnetic field, $\vec{B}_1$ and is given by [43]:

$$P = \exp\left(\frac{-\pi s^2}{2r\hbar}\right) \tag{1.32}$$

where $s{=}\hbar\gamma \mathrm{B}_1$ and $r{=}\hbar\gamma \mathrm{dB}_1/\mathrm{dt}$. This leads to the following expression for M_z in terms of the $\vec{B}_1$ field [43]:

$$M_z = M_0\left(2\exp\left(\frac{-\pi\gamma B_1^2}{2\mathrm{d}B_1/\mathrm{d}t}\right) - 1\right). \tag{1.33}$$

If we consider that the term $\mathrm{d}B_1\mathrm{d}t$ can be described as follows:

$$\frac{dB_1}{dt} = \frac{\partial B_1}{\partial x} \cdot \frac{dx}{dt}, \tag{1.34}$$

then equation 1.33 can be rewritten as [44]:

$$M_z = M_0\left(2\exp\left(\frac{-\pi\gamma B_1^2}{2\vec{G}\cdot\vec{v}}\right) - 1\right). \tag{1.35}$$

Equation 1.35 describes M_z in terms of the amplitude of the $\vec{B}_1$ field, the gradient strength $\vec{G}$ used to achieve the inversion and the velocity $\vec{v}$ of the flowing spins.

Magnetization Transfer Effects

In magnetization transfer contrast (MTC) imaging, magnetization transfer (MT) effects are used as the basis of a positive contrast mechanism that can be used to assess tissue and specifically tumor type [45, 46]. However, in the case of CASL, MT effects are problematic as they cause reduced inversion efficiency at the inversion plane and faster relaxation of the arterial label [35]. These effects cause signal loss in the perfusion-weighted images that leads to errors in the subsequent quantification step (section 1.4). This confounding factor is particularly evident in one-coil CASL, where the volume RF transmit coil is used to provide the ASL inversion.

The MT effects arise due to the application of long lasting RF inversion pulses, which acts as a powerful MT pulse in a way similar to an MT-weighted technique. Water molecules (protons) in the arterial blood (free water protons) have long T_2 relaxation times and therefore satisfy the adiabatic condition for flow-driven adiabatic inversion (equation 1.30). As a result, the MT effect on water molecules in blood is small. However, Protons that are bound to macromolecules in static tissue have much sorter T_2 relaxation times and therefore do not meet the adiabatic condition. These protons are saturated over the entire duration of the ASL pulse due to their broad RF absorption spectrum, while free water protons are largely unaffected at the imaging plane due to their narrow RF absorption spectrum (figure 1.6). Subsequent chemical exchange between the two proton pools results in magnetization transfer. The resultant reduction in signal from the free water pool at the imaging plane leads to an overestimation of perfusion [47].

The basic CASL approach discussed so far attempts to compensate for these MT effects by acquiring distal labeling during the acquisition of the control image (i.e. the offset frequency of the labeling pulse, f_l in equation 1.17 is reversed to $-f_l$ for the control image). This approach assumes that the MT effect is symmetrical about the Larmor frequency. However, it has been shown that different MT effects are observed for corresponding

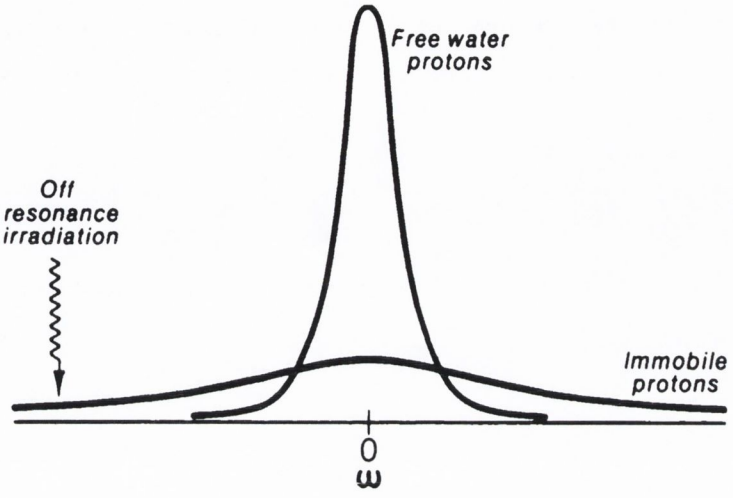

Figure 1.6: Schematic representation of the free water (arterial) and immobile (tissue) proton pools. The tightly bound immobile protons at the imaging plane are selectively saturated or inverted by an off-resonance ASL pulse, while the free water protons are unaffected due to their narrow RF absorption spectrum. Asymmetries in the immobile proton spectrum are thought to contribute to MT effects (ω = Larmor frequency). Adapted from [46].

f_l and -f_l values ($\delta\omega_2$ and -$\delta\omega_2$ in figure 1.7). The asymmetry is thought to arise from a number of contributing factors such as intrinsic asymmetry in the MT spectrum, asymmetry of the RF coil response or imperfections in the gradient used during off-resonance RF irradiation [48].

Several schemes that compensate for the MT asymmetry have been proposed.For example, a four-step acquisition strategy was proposed by Pekar et al [48]. This approach requires $4N$ averages, where N is a positive integer. The frequency offset of the inversion pulse toggles between f_l and -f_l as usual but at each offset frequency, the labeling gradient alternates between +G and - G, resulting in a total of four acquisitions. A difference image between (f_l, G) and (f_l, -G) compensates for the asymmetry of the MT effects. Also, eddy current effects that arise due to gradient switching are compensated in a difference image between (-f_l, G) and (f_l, G). By combining multiple difference images acquired in this manner, both the asymmetric MT effect and eddy current effect are limited.

Alsop and Detre [49] proposed a novel labeling scheme to compensate for the asymmetric MT effects, particularly when multislice imaging is required. In this approach, a typical proximal inversion plane is used to pro-

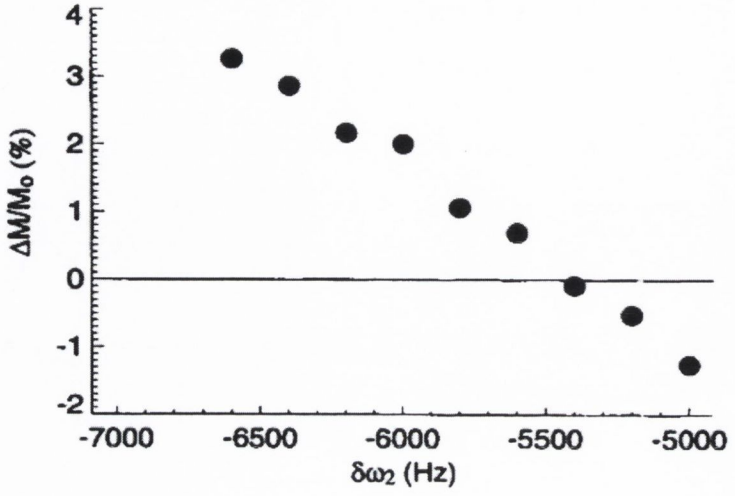

Figure 1.7: Variation in $\Delta M/M_0$ for various offset frequencies, $\delta\omega_2$, as measured in [48]. $\Delta M/M_0$ is the fractional difference in signal intensity between an image acquired with a frequency offset of $\delta\omega_2$ and an image acquired with a frequency offset of $-\delta\omega_2$

duce the labeled image. For the control image, two closely spaced inversion planes are created by applying a sinusoidal modulation to the RF waveform. This creates two closely spaced inversion planes, which is also referred to as double adiabatic inversion (DAI). Flowing arterial spins are inverted while traversing the first inversion plane and then theoretically returned to the original equilibrium state on traversing the second inversion plane. There is therefore no net effect on the arterial labeling, while the spatially dependent off-resonance effects of the labeling pulse are precisely reproduced.

Two-Coil CASL

The use of a small dedicated labeling coil, which is actively decoupled from the receive coil, provides a hardware-based solution to the MT problem in ASL [50, 51]. In this approach, the small labeling coil is typically placed over either the left or right carotid artery, which facilitates selective labeling and mapping of the respective perfusion territories of the carotid arteries [52, 53, 54]. Due to the small sensitive region of the labeling coil, almost no saturation of macromolecules at the imaging plane occurs and this proves particularly useful when multislice perfusion imaging is required. A distal RF inversion pulse is not required for the control image, as shown in figure 1.8. This reduces the RF power deposition and SAR, which is import-

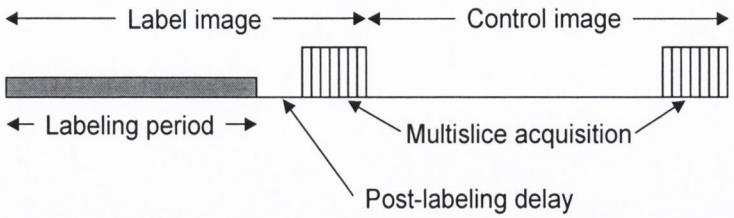

Figure 1.8: Two-coil CASL pulse sequence. The labeling pulse is applied at the neck and can be followed by a multislice image set at the ROI without the need to correct for MT effects. A RF inversion pulse is not required for the control image. Adapted from [52].

ant for human studies [52].

The main disadvantage of the two-coil CASL approach is the need for non-standard hardware, such as a second transmit channel and a detunable RF coil, which typically need to be built in-house as they are not readily available with commercial clinical scanners. Furthermore, as the labeling coil needs to be sufficiently close to the carotid artery to provide adequate signal-to-noise ratio (SNR), the labeling generally takes place further from the imaging plane than with the conventional one-coil approach. This leads to increased relaxation of the label before it enters the imaging slices and leads to longer post-labeling delays between the labeling and imaging phases (figure 1.8). As a result, the two-coil approach does not always provide superior SNR to the one-coil approach [28].

Pseudo CASL

The CASL sequences described so far require a post-labeling delay to allow labeled spins to travel into the ROI and exchange with tissue spins, thereby providing true perfusion contrast. In addition, two images are acquired, usually in an interleaved manner: one with spin labeling and another as a control. As a result, the method suffers from poor time resolution, typically on the order of a few seconds, which can be prohibitively long for applications where superior time resolution is required, such as the functional mapping of brain activation [27, 55].

These limitations have been largely addressed by a form of CASL, known as pseudo-CASL [56, 57]. This approach uses repeated RF pulses to acquire labeled and control images instead of the continuous RF wave used by tra-

ditional CASL approaches and is based on the principle that the repeated application of RF pulses creates a steady state in the absebce of T_1 and T_2 decay [58]. This principle implies that magnetization oriented along the steady state direction at the midpoint between two pulses will return to the same direction following subsequent RF pulses. The angle of the steady state orientation is determined by two factors: the phase shift accumulated between subsequent RF pulses, ϕ, and the flip angle of the RF pulses, α. The longitudinal magnetization, M_z of the steady state magnetization is determined by these two parameters as follows [59]:

$$M_z = \frac{\pm M_0 \sin\alpha \sin\frac{\phi}{2}}{\sqrt{(1-\cos\alpha)^2 + \sin^2\alpha \sin^2\frac{\phi}{2}}} \tag{1.36}$$

From this equation it can be seen that magnetization with near zero phase shift will be in the transverse plane ($M_z \rightarrow 0$), whereas magnetization with 180^0 will be approximately aligned along the z axis. Therefore, by gradually changing the phase shift from -180° to 180°, the magnetization will be inverted in a manner similar to the flow-driven adiabatic inversion of CASL. The psuedo-CASL approach uses this principle to perform two experiments: one with spin labeling and the other as a control. The temporal resolution of the perfusion measurements is enhanced by using short RF pulses in conjunction with an ultra-fast imaging sequence.

This approach has been used to measure the haemodynamic response to neuronal activity in the rat brain with a temporal resolution of approximately 100 ms [56]. This temporal resolution enabled the onset of the perfusion response to be measured approximately half a second after the onset of stimulation, which would not be possible with traditional CASL approaches. The technique has also been shown to permit the acquisition of a multislice subtraction pair (label and control) of perfusion weighted images in less than three seconds [57].

CASL Perfusion Territory Imaging

As discussed above, CASL with a separate labeling coil can be used to image the perfusion territories of the major cerebral arteries. However, perfusion territory CASL has also been demonstrated without the use of a separate coil

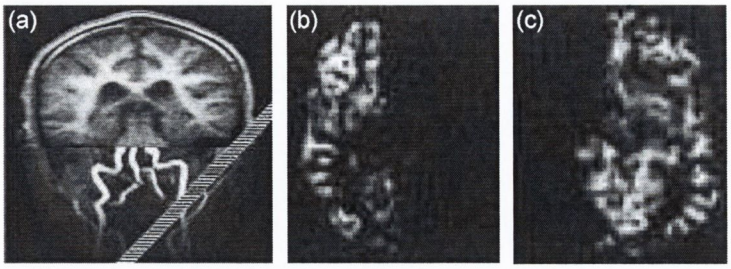

Figure 1.9: CASL perfusion territory imaging. (a) Schematic representation of oblique labeling plane that allows individual carotid arteries to be labeled. (b) Perfusion territory image for left carotid artery. (c) Perfusion territory image for right carotid artery. Adapted from [60].

by Werner et al [60]. A multisclice CASL labeling strategy first presented by Alsop and Detre [49] that uses amplitude-modulated RF irradiation to perform a double inversion on inflowing spins for the control experiment was combined with a method that provides an oblique labeling plane at the carotid arteries [61]. This combination allows a send/receive head coil to be used for the selective labeling of either the left or right carotid artery, and the use of a separate labeling coil is not necessary. A schematic representation of the oblique labeling plane and sample perfusion territory images are shown in figure 1.9

1.3.2 Pulsed Arterial Spin Labeling

The PASL technique relies on the labeling of a large volume of blood with a short RF pulse, instead of labeling blood as it flows through a thin inversion plane (CASL). Adiabatic RF pulses are normally used to obtain thick inversion slabs with sharp edges. The labeled volume (or bolus) then flows from the arterial bed to the capillary bed and exchanges the labeled magnetization in the blood with the unlabeled magnetization of the tissue water. The labeled magnetization in the tissue experiences T_1 relaxation and eventually becomes indistinguishable. As a result, the PASL signal is transient.

PASL sequences can be broadly grouped into two categories: those based on the echo-planar imaging and signal targeting with alternating radiofrequency (EPISTAR) approach and those based on the flow-sensitive alternating inversion recovery approach (FAIR). These two categories will be described in detail. A further sequence known as quantitative imaging of

perfusion using a single subtraction (QUIPSS) [62] aimed at reducing the transit time sensitivity of the EPISTAR and FAIR approaches (section 1.4.4) will also be described.

EPISTAR-based PASL Sequences

The original EPISTAR sequence was introduced by Edleman et al [55] and is illustrated in figure 1.10. The labeling sequence (figure 1.10(a)) begins with a 90° saturation pulse that, due to the presence of the slice-selective gradient, saturates the spins at the ROI. A spoiler gradient is then played to dephase any transverse magnetization before the labeling phase. A spatially selective inversion pulse, typically a hyperbolic secant adiabatic inversion pulse(see above), inverts spins within a thick slab proximal to the imaging slice (figure 1.10(c)). To reduce the effect of the nonideal labeling profile, a spatial gap is placed between the inversion slab and the imaging slice. Consequently, a long time delay of the order of 1 s is introduced to allow the inverted spins to travel from the labeling slab to the imaging plane and exchange with the uninverted tissue spins. The inverted magnetization causes a signal reduction when the host sequence is played. The host sequence for EIPSTAR is either spin-echo EPI (SE-EPI) or gradient-echo EPI (GRE-EPI).

In the original implementation of EPISTAR, the control image was acquired by simply repeating the sequence with the labeling pulse switched off [55]. This approach fails to take into account the MT effects of an inversion pulse, described in section 1.3.1. To allow for this source of error, an inversion pulse identical to that in the labeling image is played prior to the acquisition of the control image (figure 1.10(b)), except that its carrier frequency is chosen to place the labeling slab distal to the imaging plane (figure 1.10(d)). The spatial location of the labeling slab is determined by the frequency of the labeling pulse, $f_{epistar}$, and the labeling gradient, G, in a similar manner to the CASL case in equation 1.17.

However, as discussed above, the MT effects are not symmetrical about the resonance frequency. To counteract this, Edelman et al developed an improvement of the EPISTAR method, in which the 180° inversion pulse in the labeling phase is replaced by a 360° adiabatic RF pulse and the control pulse is replaced by two 180° adiabatic pulses at the same location as the labeling pulse [63]. The bandwidth of the labeling pulse determines the width of the

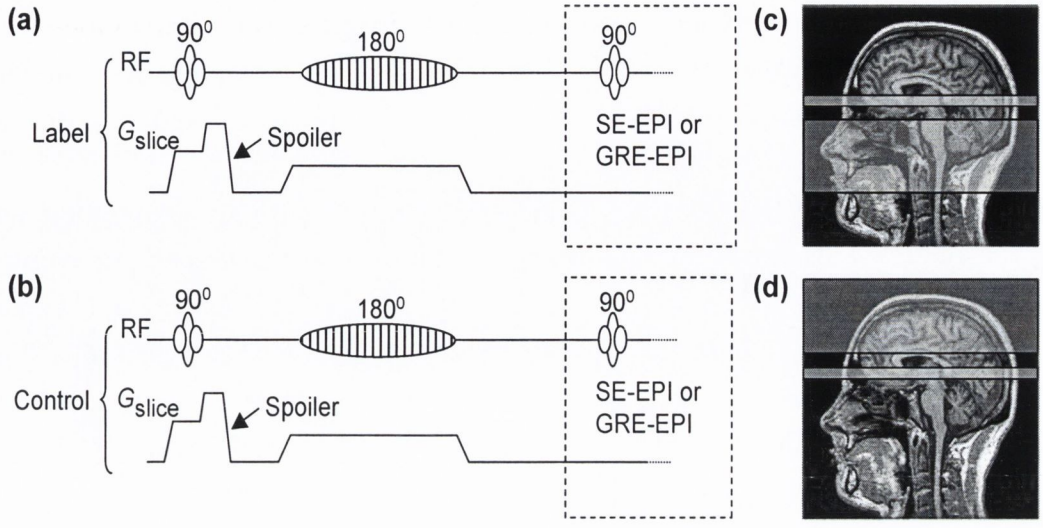

Figure 1.10: EPISTAR pulse sequence. The 90° spatially selective saturation pulses at the beginning of the sequences in (a) and (b) saturate spins at the imaging location (light blue shaded area in (c) and (d)) and the spoiler gradient dephases any residual transverse magnetization. The frequency offset, labeling gradient and offset frequency determine the location and width of the inversion slabs (grey shaded areas) for the label and control image in (c) and (d). Adapted from [37].

inversion slab. The RF irradiation, frequency shift and bandwidth of the labeling and control pulses are identical and consequently the magnetization transfer effects are exactly cancelled by image subtraction.This improved EPISTAR sequence is often simply referred to as signal targeting with alternating radiofrequency (STAR). In both cases, the subtracted signal for EPISTAR is $\Delta M_{epistar}$=M_c-M_l and is a positive quantity.

A number of variations of the EPISTAR sequence for PASL have been developed. Due to the sensitivity of the EPI acquisition to susceptibility effects [64], Chen et al replaced the EPI host sequence by a single-shot rapid acquisition with relaxation enhancement (RARE) sequence (sections 3.5 and 3.6.1), and developed the signal targeting with alternating RF and half-Fourier single shot turbo spin-echo (STAR-HASTE) method [65]. This sequence permitted perfusion imaging to be performed without many of the artifacts encountered when using EPI acquisition.

The transfer insensitive labeling technique (TILT), also based on EPISTAR, replaces the inversion pulse by two consecutive 90° RF Pulses of the same phase for the label image and by two 90° RF Pulses of opposite phase for the control image [66, 67]. The RF pulses with opposite phase have no

net effect on the magnetization and thereby provide the control image, while the net RF effect on the macromolecular spins is the same for both the label and control image and the MT-related signal in the static tissue is canceled out by the subtraction procedure.

Another variation of the EPISTAR approach, proximal inversion with a control for off-resonance effects (PICORE) was introduced by Wong et al [68]. The labeling scheme is identical to EPISTAR, with the inversion pulse providing a labeled slab proximal to the imaging slice (figure 1.10(a)). However, the control image is acquired using the same RF inversion pulse offset as the labeling scheme, with the omission of the labeling gradient to prevent the inversion of inflowing spins. Typically, an offset frequency of approximately 5 kHz is chosen to leave the magnetization at the imaging slice unperturbed. The MT effects, present in the EPISTAR sequence, are alleviated by the PICORE sequence. Furthermore, the use of a distal inversion slab in the EPISTAR sequence causes a reduction in the perfusion weighted signal due to inflow from the distal slab into the imaging slice. The PICORE sequence is not sensitive to inflow as a distal inversion slab is not needed. However, the use of different gradient waveforms in the acquisition of the labeled and control images make the PICORE sequence more sensitive to eddy-current effects than the EPISTAR sequence [37].

The pulsed STAR labeling of arterial regions (PULSAR) technique developed by Golay et al [69] consists of a multi-slice EPISTAR sequence that is preceded by a four-pulse saturation preparation, known as water suppression enhanced through T_1 effects (WET) [70]. The WET saturation technique saturates the entire volume of interest with superior uniformity to traditional 90° spatially selective saturation pulses. The STAR labeling phase of the PULSAR sequence is followed by an additional 90° saturation pulse at the labeling plane, to provide sharp definition of the start of the labeled bolus in a manner similar to the QUIPPS I sequence [62] (see QUIPSS sequences section below).

FAIR-based PASL Sequences

The original FAIR sequence was proposed by Kwong et al [71] and independently by Kim [72] and is illustrated in figure 1.11. This sequence uses a frequency-selective pulse with and without an accompanying slice-selction

gradient to produce the labeled and control images respectively as shown in figure 1.11(a) and (b). For the labeled image, the slice selective pulse inverts spins at the imaging slice while leaving spins elsewhere unperturbed, as illustrated in figure 1.11(c)). As with the EPISTAR sequence, a time delay follows this inversion pulse to allow uninverted arterial spins to move into the imaging slice and exchange with tissue water. For the control image, spins within the entire sensitive region are inverted (figure 1.11(d)), due to the absence of the slice-selective gradient. Thus, the perfusion contrast in FAIR is a positive quantity for the following subtraction: ΔM_{fair}=M_l-M_c.

The inversion pulse in figure 1.11(a) and (b) is typically adiabatic with a bandwidth of approximately 1-5 kHz [37]. The spatial profile of the inversion pulse for the labeled image is generally made wider than the imaging slice thickness to allow for imperfect RF pulse profile and therefore ensure uniform inversion of the entire imaging slice. A spoiler gradient is often applied after the inversion pulse as in EPISTAR. In the original implementations of FAIR, the EPI sequence was used to acquire the label and control images [71, 72] but a variety of host sequences such as FLASH and RARE can also be used.

FAIR is less sensitive to MT effects than EPISTAR as it does not require the use of off-resonance RF pulses with respect to the imaging slice. This facilitates multisclice perfusion weighted imaging. Furthermore, because the tissue and arterial blood experience the same inversion and recover at similar rates due to the fact that the T_1 of blood is only slightly longer than that of grey matter, arterial inflow in the control image is less of a problem with FAIR than EPISTAR [73]. An additional advantage of the FAIR sequence is its sensitivity to both proximal and distal inflowing blood since uninverted spins from either side of the imaging slice are effectively tagged. This reduces the underestimation of perfusion that arises in EPISTAR-based experiments. However, if the control image is acquired with the slice-selective gradient set to zero, the FAIR sequence is sensitive to eddy-current errors. This error can be alleviated by playing the same slice-selective gradient as the label sequence at a different time, away from the inversion pulse [71].

A variation of the FAIR sequence known as uninverted flow-sensitive alternating inversion recovery (UNFAIR) was developed to reduce the sensitivity of FAIR to differences in T_1 between blood and tissue. This sequence

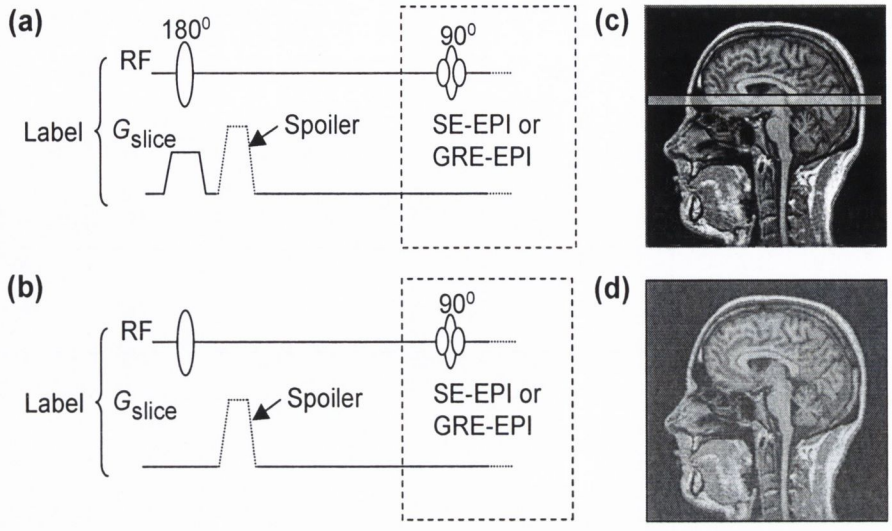

Figure 1.11: FAIR pulse sequence. The selective 180° inversion pulse in (a) is applied to the imaging slice (light blue shaded area in (c)). The non-selective inversion pulse in (b) inverts all spins within the sensitive region (grey shaded area in (d)). Adapted from [37].

uses two inversion pulses for both the labeled and control images. For the labeled image, one of the inversion pulses is played with a slice selective gradient while the other inversion pulse is nonselective. Therefore the magnetization at the imaging slice experiences a 360° rotation while elsewhere, spins are inverted. For the control image, both inversion pulses are non-selective, resulting in an uninverted image. In this case, the following subtraction ensures the perfusion weighted magnetization difference is a positive quantity: M_{unfair}=M_c-M_l.

A further variation of FAIR, known as BASE, uses basis (BA) image with no spin preparation as the control image and a selective (SE) inversion pulse at the imaging slice for the labeled image [74]. This sequence compensates for errors in FAIR perfusion quantification arising from the imaging slice profile, as the control image does not employ a non-selective inversion pulse. When using the FAIR or UNFAIR sequences, if the selective inversion pulse does not invert the entire image slice, uninverted spins at the extremes of the imaging slice will contribute to the perfusion-weighted signal. This problem is alleviated with the BASE sequence.

Mai et al [75] developed the flow-sensitive alternating inversion recovery with an extra RF pulse (FAIRER) sequence to reduce the inversion time

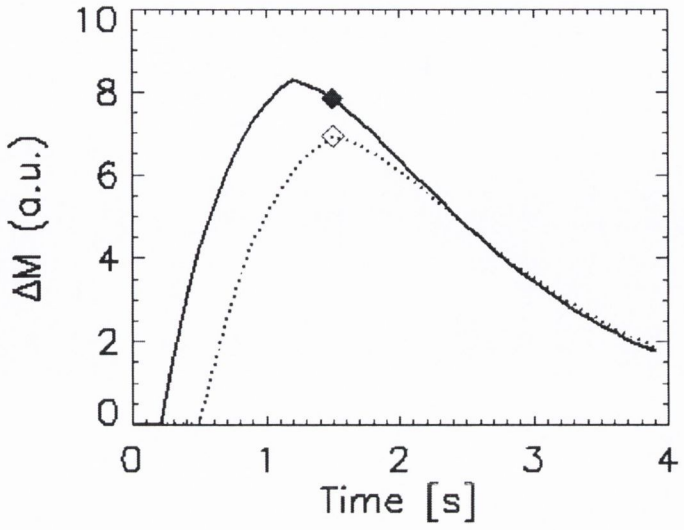

Figure 1.12: Diagram of PASL time course for two voxels having the same CBF and relaxation characteristics but different arrival times of the labeled magnetization. Measurement at one inversion time (1.5 s) would lead to a lower ΔM signal in a voxel with an arrival time of 500 ms (open square) compared with a voxel with an arrival time of 200 ms (closed square) [1].

sensitivity of the subtracted image from FAIR. FAIRER uses an additional slice-selective 90° saturation pulse immediately after the preparatory FAIR inversion pulse. Image acquisition is performed after an inversion time, TI. The control image is acquired using a nonselective inversion pulse, as in FAIR. The technique was used to track the pulmonary perfusion time-course by varying the TI and demonstrated sensitivity to the perfusion-weighted signal, even at TI's between the null points of different tissue types [76].

QUIPSS Sequences

A major source of error in perfusion quantification with PASL techniques is the variation in the arterial transit time across the imaging slice, as illustrated in figure 1.12. In most PASL approaches, perfusion is quantified by assessing the perfusion-weighted signal at a single inversion time point, and therefore variation in the arterial transit time is not taken into account. Also, when perfusion quantification is based on PASL images for one inversion time, CBF quantification is not possible and relative perfusion values between regions are not valid [1].

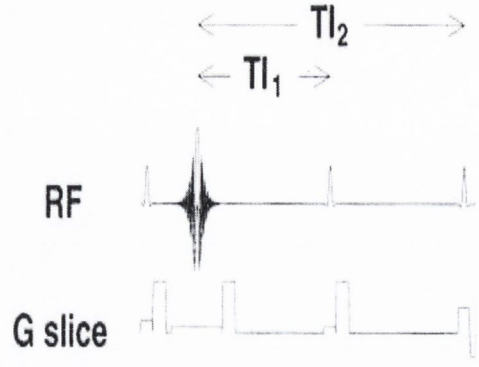

Figure 1.13: ASL preparation for the QUIPSS/QUIPSS II sequence.RF pulses from left to right are: An inplane presaturation pulse, followed by the inversion pulse. A saturation pulse is then applied at the imaging location for QUIPSS or at the labeling location for QUIPSS II. The 90° pulse for the subsequent image acquisition is also shown. Adapted from [68].

Wong et al introduced two quantitative ASL methods, quantitative imaging of perfusion using a single subtraction (QUIPSS) and QUIPSS II, to reduce the sensitivity of FAIR and EPISTAR techniques to transit time [62]. In QUIPSS, a saturation pulse is applied to the imaging slice at a time TI_1 after the both the labeling and control inversion pulses (figure 1.13). This has the effect of removing the contribution to the final difference signal of blood that arrives at the imaging location before TI_1. The image is then acquired at time TI_2 (figure 1.13) and only labeled blood that enters the imaging slice between TI_1 and TI_2 contributes to the perfusion-weighted image.

In QUIPSS II , the saturation pulse is applied to the labeling location rather than the imaging location. In this regime, only labeled blood that leaves the labeling region in the time TI_1 contributes to the difference signal. This produces a well-defined bolus of labeled blood, which facilitates CBF quantification [62, 77]. Luh et al developed the QUIPSS II sequence further by using a train of thin-slice saturation pulses, applied periodically, instead of the single, thick slice saturation pulse used in QUIPSS [77]. Since thin-slice sinc saturation pulses provide superior B_1 homogeneity over than slice and sharper edges than a single thick-slice saturation pulse, the new method (QUIPPS II with thin-slice TI periodic saturation or Q2TIPS) is capable of more accurate CBF quantification than the original QUIPSS methods.

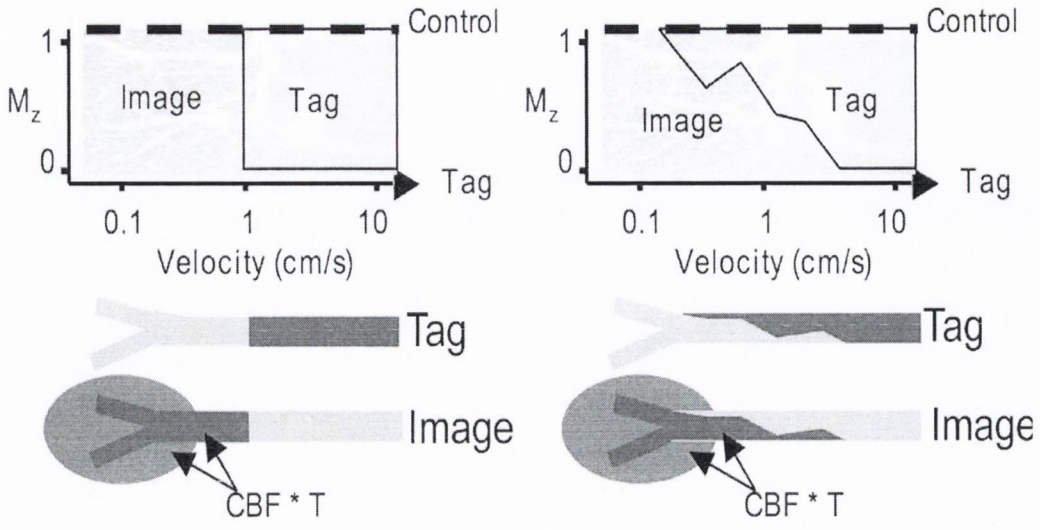

Figure 1.14: Schematic representation of the VS-ASL technique. Left: VS-ASL with ideal velocity cutoff. Right: VS-ASL with imperfect velocity cutoff. The label before and after flowing into the capillary bed is represented below in each case. In both cases, the total amount of labeled blood appearing in the VS-ASL image is TI·CBF [78].

1.3.3 Velocity Selective Arterial Spin Labeling

The CASL and PASL techniques label spins based on their location (i.e. with spatial selectivity). The VS-ASL technique [78] uses a velocity selective (VS) labeling scheme that modulates the longitudinal magnetization of blood traveling with a velocity V greater than a sharp cutoff velocity, V_c (figure 1.14). The image acquisition is restricted to include only spins with $V < V_c$ and consequently, only spins that have decelerated during from above to below V_c during the inversion time, TI, are included in the labeled image. This setup ensures that venous blood, which in general accelerates, is excluded from the labeled image.

As with conventional ASL approaches, static tissue is also labeled by the VS-ASL labeling scheme and control images are required to remove this static tissue component. Control images in VS-ASL are again setup to only include spins with $V < V_c$. The difference image between the labeled and control images removes the static tissue component and the final VS-ASL image is sensitive only to magnetization that was above V_c at the time of labeling and below V_c at the time of imaging.

The use of velocity encoding gradient pulses in combination with RF

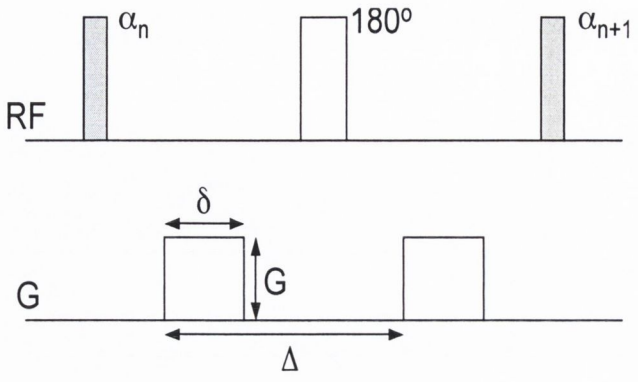

Figure 1.15: Basic elements of a VS sequence. Two elements of the RF pulse train, with an arbitrary flip angle α are shown, with a 180° refocusing pulse midway between them. The gradient pulses of strength G, duration δ and separation Δ, provide the velocity encoding [79].

pulse trains to provide velocity selectivity was initially proposed by Norris and Schwarzbauer [79]. The key components of a VS sequence are shown in figure 1.15. The two RF pulses of flip angle α are part of the RF pulse train. The 180° pulse in combination with the two gradient pulses provides the velocity encoding. The gradient pulses induce a velocity-dependent phase shift between each pair of pulse train elements given by [79]:

$$\phi = \gamma G v \delta \Delta, \tag{1.37}$$

where γ is the gyromagnetic ratio, G is the gradient strength, v is the velocity of the flowing spins, δ is the duration of the gradient pulses and Δ is the time delay separating the gradient pulses. These gradient parameters determine the cutoff velocity, V_c, in VS-ASL and the RF pulse train saturates spins with velocities above V_c (RF pulse trains capable of *inverting* spins across a range of velocities have not yet been developed).

Ideally, only inflowing blood spins contribute to the VS-ASL signal. However, in reality both diffusion and motion unrelated to blood flow contributes to the signal. The sequence in figure 1.15 is sensitive to diffusing spins due to the b-value of the velocity encoding gradients. Furthermore, CSF motion in the brain can produce large subtraction errors as the velocity of CSF motion can often be above V_c. The importance of carefully selecting both the inflow time and the V_c has also been highlighted [80], where a large and undesirable contribution to the VS-ASL signal was measured from large

vessels in humans if V_c is greater than 4 cm/s. However, the ability of the VSASL technique to accurately quantify CBF in diseased subjects with slow and or collateral flow conditions [78] and its potential to separate the intravascular signal from the extravascular signal in fMRI experiments [81] hold much promise for future developments of the VSASL technique.

1.4 Arterial Spin Labeling: Perfusion Quantification

Data acquired using any of the ASL techniques outlined in section 1.3 will be perfusion weighted. The relationship between the ΔM signal and the CBF depends mainly on many factors such as proton density, the T_1 relaxation rates of the brain tissue and inflowing blood and the transit time from the labeling plane to the imaging plane. Traditionally, CBF is quantified using the Kety and Schmidt approach, described in section 1.2.1, where the time for a freely diffusible tracer to reach equilibrium is directly related to Fick's principle [82]:

$$\frac{dC_t(t)}{dt} = CBF(c_a(t) - c_v(t)), \tag{1.38}$$

where $C_t(t)$,$c_a(t)$ and $c_v(t)$ are the concentrations of tracer in the tissue, arterial and venous blood respectively (it should be noted that equation 1.38 can be obtained directly from equation 1.3). The first quantitative ASL measurements used a model that adapted this theoretical approach to ASL experiments [13, 14]. This model and other single compartment kinetics models (i.e. models based on Fick's principle) will now be described in detail.

1.4.1 Single-Compartment Models

Modified Bloch Equation Model

The modified Bloch equation of Detre and Williams assums that labelled arterial blood water is a freely diffusible tracer. This implies that the exchange of blood water with tissue water happens instantaneously on its arrival to the parenchyma. With this assumption, a mono-exponential decay

is used to describe the tissue response function. The modified Bloch equation, which includes the flow dependent exchange term for labeled blood spins is as follows [13]:

$$\frac{dM_t(t)}{dt} = \frac{M_b^0 - M_b(t)}{T_1} + fM_a(t) - \frac{f}{\lambda}M_b(t), \tag{1.39}$$

where f is defined as the brain blood flow (ml/g/s), λ is the brain/blood partition coefficient for water (the ratio of the quantity of water/g of brain to the quantity of water/g of blood), T_1 is the spin-lattice relaxation time of blood water, M_b is the longitudinal magnetization per gram of brain tissue, $M_b{}^0$ is M_b under fully relaxed conditions and M_a is the longitudinal magnetization per ml of arterial blood.

In order to derive equation 1.39 it was assumed that the brain behaves as a well-mixed compartment such that the magnetization of labeled spins in the venous outflow is equal to that in the brain tissue ($fM_v = fM_b/\lambda$). It is also assumed that in a steady state (i.e. when spins are continuously inverted using the CASL approach) the inflowing magnetization is equal to the outflowing magnetization and $M_a(t) = -M_a{}^0$ at all times. Based on these assumptions, a solution for f in terms of measurable quantities was found [13]:

$$f = \frac{\lambda}{T_{1app}} \cdot \frac{M_b^{ctrl} - M_b^{lab}}{2M_b^{ctrl}}, \tag{1.40}$$

where T_{1app} is the relaxation time that describes the exponential decrease in M_b due to the T_1 relaxation time of brain water and a flow and exchange term ($1/T_{1app}=1/T_1+f/\lambda$), $M_b{}^{ctrl}$ is the image intensity in the control image and $M_b{}^{lab}$ is the image intensity in the labeled image. Using this theoretical formulation, an average brain flow of approximately 1.4 ml/g/min was measured in normocarbic rats. This finding was comparable to CBF values measured by existing tracer techniques [83] and demonstrated that quantitative ASL could become a useful, non-invasive tool for the quantification of cerebral perfusion. Many subsequent derivatives and improvements of this seminal quantitative ASL approach have been developed.

Modified Bloch Equation Model Accounting For Relaxation Time Differences

Calamante et al developed the original modified Bloch equation theory to incorporate the difference in the T_1 relaxation time for tissue and arterial blood [84]. The T_{1app} term in the original model does not take into account the relaxation of labeled spins while in the arterial blood and since the spins initially relax with this relaxation time, T_{1a}, the mono-exponential model leads to $1/T_1$ related errors in perfusion quantification (CBF is overestimated, particularly in white matter, which has the shortest T_1 value).

It is assumed that T_{1a} is constant throughout the inverted slice and therefore, equation 1.39 is solved with the following initial conditions [84]:

$$M_{ctrl}(t) = M_a^0(1 - 2\alpha_0 e^{-t/T_{1a}}) \quad \text{and} \quad M(t=0) = 0, \tag{1.41}$$

where α_0 is the degree of inversion at the labeling planed defined by equation 1.15. Under these conditions, the difference between the magnetization for the control and inversion image as a function of time is [84]:

$$\Delta M(t) = M_{ctrl} - M(t) = 2\alpha_0 M_0 \frac{f}{\lambda} \frac{(e^{-t/T_{1app}} - e^{-t/T_{1a}})}{\left(\frac{1}{T_{1a}} - \frac{1}{T_{1app}}\right)}. \tag{1.42}$$

The bi-exponential function in equation 1.42 was fitted to experimental data acquired using the EPISTAR PASL technique (section 1.3.2) and CBF was quantified from the fitting parameters. Sample curves obtained in this way using various values for T_{1a} are shown in figure. 1.16. This approach is also capable of taking the trailing edge, τ_d, of the bolus into account. This is necessary as a bolus of a defined duration will cease to supply inverted blood to the imaging location after a time τ_d and if this time is less than TI, the model must take into account the fact that univerted or fresh blood will be supplied to the imaging location.

A similar approach was taken by Kwong et al [71], where data acquired using the FAIR PASL technique (section 1.3.2) was fitted to a bi-exponential model. In this model, the arterial transit time, τ_a, is also taken into account. However, this model assumes that in the selective inversion phase of the FAIR acquisition the thickness of the inversion slice is the same as the imaging slice. In practice this is not the case and the inverted slab is generally

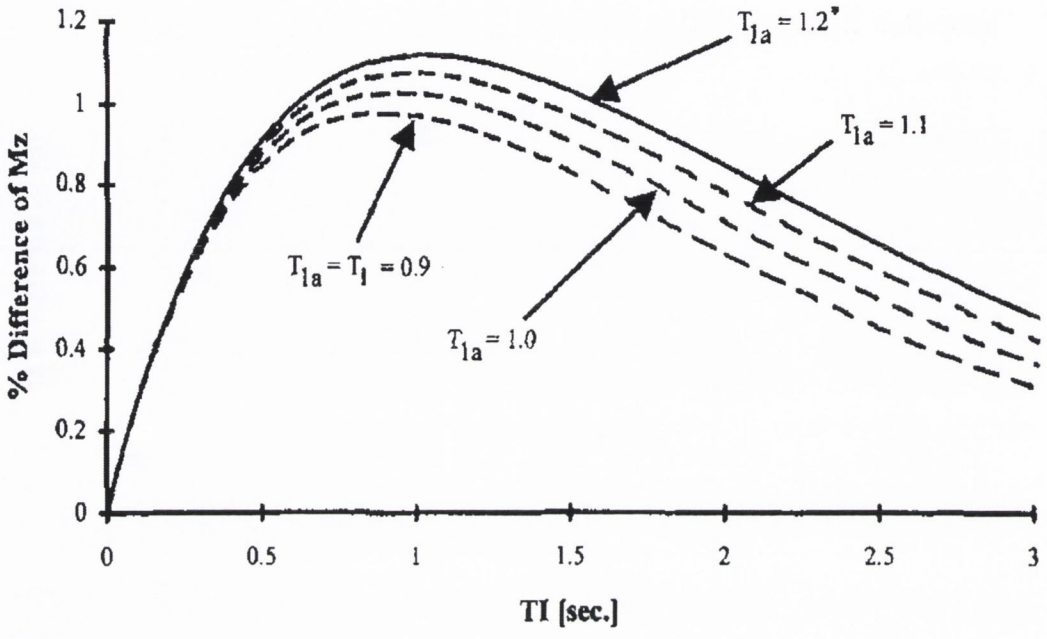

Figure 1.16: Magnetization difference in grey matter as a function of the inversion time, TI, for different T_{1a} values. The curves were obtained using the single compartment model that allows for differences in the T_1 of tissue and blood. Adapted from [84].

wider to reduce the effects of an imperfect inversion pulse profile. This assumption leads to an overestimation of α_0 and a consequent error in the perfusion quantification.

General Kinetic Model

The general kinetic model, where the magnetization difference between the labeled and control images is described using a convolution integral, was proposed by Buxton et al [85]. The magnetization difference between the control and the labeled image, $\Delta M(t)$ is constructed as a sum over time of the delivery of magnetization to the tissue, weighted by the fraction of that magnetization that remains in the tissue voxel. The various physical processes involved are described in terms of three time-dependent functions; (i) the delivery function (or fractional (AIF)) $c(t)$, which is the normalized concentration of labeled water arriving at the ROI at time t, (ii) the residue function $r(t,t')$, which is the fraction of labeled water that arrives at the ROI at a time t' and is still present at time t and (iii) the magnetization relaxation function $m(t,t')$, which is the fraction of the original longitudinal magnetiz-

ation associated with labeled water molecules that arrived at time t' and is still present at time t.

The arterial magnetization at the labeling plane after an inversion pulse is $2\alpha M_{0,b}$, where $M_{0,b}$ is the equilibrium magnetization of arterial blood and α is the degree of inversion achieved by the inversion pulse. The amount of the labeled magnetization delivered to the imaging slice between τ and $\tau+d\tau$ is $2\alpha M_{0,b} f c(t')$, where f is again the CBF. The fraction of that labeled magnetization that remains at the ROI at time t is $r(t-t')m(t-t')$. It follows that the change in the magnetization over time due to the inflowing labeled water is given by [85]:

$$\begin{aligned} \Delta M &= 2 \cdot M_{0,b} \cdot CBF \cdot \int_0^t c(\tau) \cdot r(t-\tau) \cdot m(t-\tau) d\tau \\ &= 2 M_{0,b} f \{ c(t) \star [r(t) m(t)] \}, \end{aligned} \tag{1.43}$$

where $\star$ denotes convolution. This model allows greater flexibility than the modified Bloch equation approaches for the analysis of ASL experiments (both CASL and PASL). The choice of delivery function, $c(t)$, residue function, $r(t)$ and magnetization relaxation function, $m(t)$, allows transit delays from the labeling plane to the imaging plane, magnetization decay, exchange of water between blood and tissue, clearance by venous flow and the different forms of ASL to be modeled.

The general kinetic model is based on a number of assumptions. Firstly, it is assumed that the labeled blood arrives at the imaging plane via uniform plug glow (i.e. before τ_a no labeled blood arrives and after $\tau_a+\tau_d$, unlabeled blood is once again delivered to the imaging slice). Secondly, single-compartment kinetics are assumed, whereby the exchange of water between any existing compartments within the tissue is assumed to be rapid enough to ensure that the concentration ratio between these compartments is constant, even though the total concentration is a function of time. With this assumption, the residue function is of the form, $r(t) = \exp[-ft/\lambda]$.

Summary of Single-Compartment Models

The modified Bloch equation models and the general kinetic model have been shown to be equivalent [86]. Consequently, the assumption of the gen-

eral kinetic model that $r(t) = \exp[-ft/\lambda]$ is equivalent to the assumption of the modified Bloch model that $m_v = M(t)/\lambda$, i.e. the fundamental assumption of single-compartment models that water undergoes rapid exchange across the capillary walls. In reality, labeled blood water remains in the vessel for a given time before exchanging across the capillary wall into the extravascular water and thus relaxes with T_{1a} before the exchange. Single-compartment models that only account for T_{1app} will therefore overestimate perfusion as T_{1a} is longer than T_{1app} [86]. Ewing et al [87] demonstrated this overestimation by the single-compartment model by varying the effective T_1 of single-coil ASL experiments.

Furthermore, the assumption that $m_v = M(t)/\lambda$ also leads to inaccuracies in perfusion quantification as the exchange of water between the capillary bed and the brain tissue will not necessarily have reached equilibrium at the time of measurement and some labeled spins may pass through the vasculature without undergoing exchange. This potential underestimation of the venous outflow magnetization can lead to an underestimation of perfusion [86].

Petersen et al explains the equivalence of all single-compartment models by defining a "standard model" that summarizes the individual single-compartment approaches. In this standard model, the delivery function, or arterial input function, $c(t)$, is given by [1] :

$$\begin{aligned} c(t) &= \begin{cases} 0 & t < \tau_a \\ \alpha \cdot \mathrm{e}^{-R_{1a} \cdot t}, \text{(PASL)} & \tau_a \leq t < \tau_d \\ \alpha \cdot \mathrm{e}^{-R_{1a} \cdot \tau_a}, \text{(CASL)} & \tau_a \leq t < \tau_d \\ 0 & t \geq \tau_d \end{cases} \\ r(t) &= \mathrm{e}^{-\frac{CBF \cdot t}{\lambda}} \\ m(t) &= \mathrm{e}^{-R_{1t} \cdot t} \end{aligned} \tag{1.44}$$

where R_{1a} and R_{1t} are the relaxation rates for arterial blood abd tissue respectively. Again, the assumptions of equation 1.44 are uniform plug flow and the repaid exchange of single-cpmartment kinetics. As can be seen, various parameters such as the transit times τ_a and τ_d, the brain/blood partition coefficient, λ, ${M_a}^0$ and R_{1a} and R_{1t} need to be estimated or measured

in order to quantify CBF.

1.4.2 Two-Compartment Models

The errors arising from single-comparment models lead many investigators to develop alternative models that do not assume a well-mixed blood compartment. The model of Alsop and Detre [88] included an additional arterial blood compartment in addition to the well-mixed tissue compartment. Separate T_1 relaxation times were used for each compartment and labeled water was assumed to cross from the blood to the tissue compartment after a predefined exchange time, T_{ex}. While the signal curves obtained using this model were in better agreement with ASL data than those from single-compartment models, the time T_{ex} was difficult to measure or define.

Restricted Capillary Permeability Models

A subsequent model developed by St. Lawrence et al [89] introduced the concept of the capillary permeability surface-area (PS) product, that had previously been measured in both injected tracer [90] and PET studies [91], to the ASL modeling problem. PS is interpreted as a measure of the permeability of the capillary wall to water. The capillary-tissue system is described by the one-barrier distributed parameter (1BDP) model, where two concentric cylinders are separated by an infinitely thin barrier (figure 1.17). The inner cylinder represents the capillary space and the outer cylinder represents the tissue space. The barrier represents the blood-brain barrier (BBB). A set of differential equations describing this model were obtained by including separate terms in the residue function of the general kinetic model [85] (secion 1.4.1) for the capillary and tissue compartments [89]:

$$A_c \frac{\partial C_c(x,t)}{\partial t} = -F \frac{\partial C_c(x,t)}{\partial x} - \frac{PS}{L} C_c(x,t) + \frac{PS}{\lambda L} C_b(x,t) - A_c R_{1c} C_c(x,t), \quad (1.45)$$

$$A_b \frac{\partial C_b(x,t)}{\partial t} = \frac{PS}{L} C_b(x,t) - A_b R_{1b} C_b(x,t). \quad (1.46)$$

Each of the parameters in equations 1.45 and 1.46 are defined in figure 1.17. When solved for a bolus input function, the model predicts an overestima-

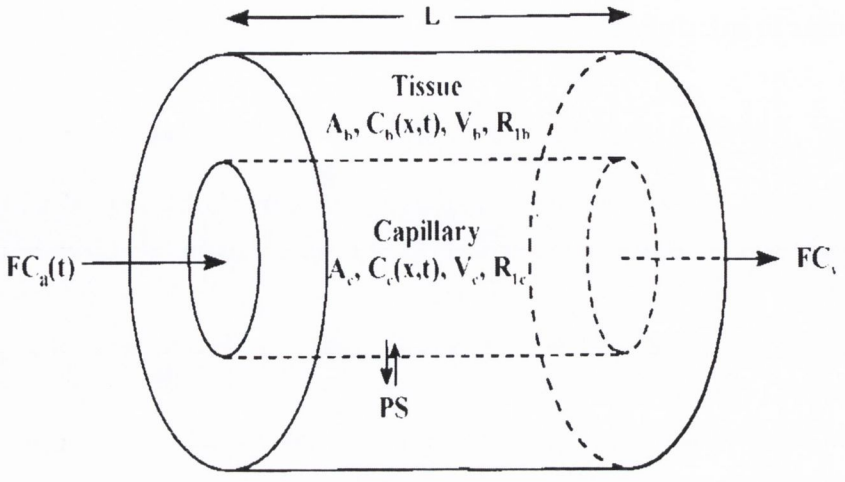

Figure 1.17: The one-barrier distributed parameter (1BDP) model for the capillary-tissue system. The inner and outer cylinders represent the capillary and tissue spaces respectively. The barrier represents the blood brain barrier. The variables in the figure are defined as follows: A_c = capillary space cross-sectional area, V_c = capillary space volume, $C_c(x,t)$ is the time and spatially dependent capillary tracer concentration (the subscript b refers to these parameters for the brain tissue), $C_a(t)$ and $C_v(t)$ are the arterial and venous blood concentrations of the tracer, F is the rate of blood flow into the capillary space, L is the length of the capillary tissue unit, R_{1c} and R_{1b} are the capillary and blood relaxation rates respectively and PS is the capillary permeability surface area product. λ is the blood/brain partition coefficient [89].

tion of perfusion at low perfusion rates and an underestimation of at high perfusion rates if the single-compartment model is used.

Another two-compartment model that allows for restricted water exchange between the capillary bed and the surrounding tissue space was introduced by Zhou et al [92]. As well as dealing with vascular and extravascular compartments, the vascular system itself is divided into two sections: a macrovascular section that includes arteries and veins and a microvascular section that includes arterioles, capillaries and venules (figure 1.18). The model is an extension of the modified Bloch equation model (secion 1.4.1). The following Bloch equations are used to describe the microvascular magnetization, M_m, and the extravascular magnetization, M_e [92]:

$$\begin{aligned} \frac{d[\lambda M_m(t)]}{dt} = & - R_{1m}[\lambda M_m(t) - \lambda M_{m0}] - k_{in}\lambda M_m(t) \\ & + k_{out}M_e(t) + f[M_a(t) - M_v(t)], \end{aligned} \tag{1.47}$$

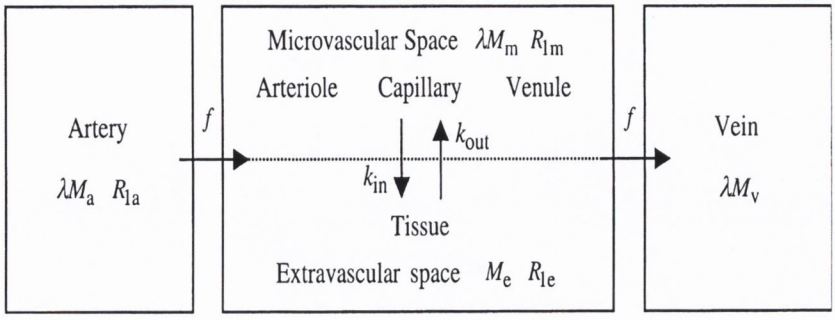

Figure 1.18: Schematic diagram of the two-compartment model of Zhou et al [92]. Two exchange rates, k_{in} and k_{out} are used to describe restricted water exchange. The subscripts (m), (e), (a) and (v) represent the microvascular, extravascular, arterial and venous compartments respectively, M refers to the magnetization and R to the relaxation rate. λ is the blood/brain partition coefficient.

$$\frac{dM_e(t)}{dt} = -R_{1e}[M_e(t) - M_{e0}] + k_{in}\lambda M_m(t) - k_{out}M_e(t). \tag{1.48}$$

Each of the parameters in equations 1.47 and 1.48 are defined in figure 1.18. The exchange rates k_{in} and k_{out} describe the exchange of water from the microvasculature to the extravascular space and vise versa. Both rates dependent on PS: k_{in}=PS/CBV and k_{out}=$PS/(\lambda\text{-}CBV)$. The model assumes that the blood compartment is well-mixed, i.e. labeled water in the blood compartment equilibrates throughout the compartment instantaneously. An underestimation of perfusion at high flow rates is predicted.

The restricted capillary models of Lawrence et al [89] and Zhou et al [92] consider two separate compartments and restricted water exchange between these compartments. However, due to the theoretical complexities of these models and the number of free parameters that must be measured or estimated, there has been limited experimental validation of these approaches.

A two-compartment model with fewer free parameters was introduced and validated with in vivo data by Parkes and Tofts [93]. As with previous models, the blood-brain system is described in terms of a vascular and an extravascular compartment, separated by a semipermeable membrane, as shown in figure 1.19. The following modified Bloch equations with an inflow, outflow, relaxation and exchange term are used to describe the volume-weighted magnetization in each compartment [93]:

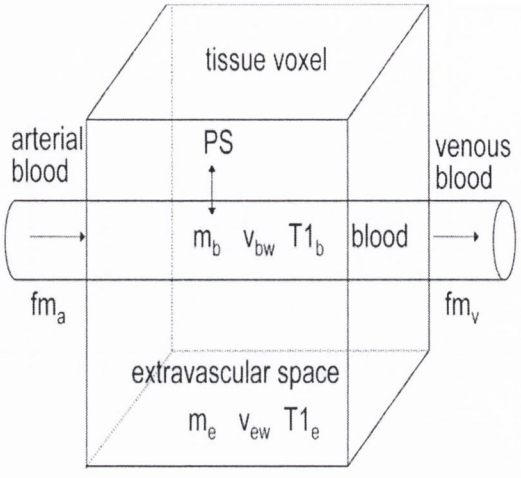

Figure 1.19: Schematic diagram of two-compartment model of Parkes and Tofts [93]. The magnetization m, longitudinal relaxation time, T_1 and water volume v_w are given the subscripts b and e for the blood and extravascular compartments respectively. m_a and m_v represent the arterial and venous magnetization respectively.

$$\frac{d(v_{bw}m_b)}{dt} = -\frac{v_{bw}m_b}{T1_b} + f(m_a - m_v) - PSm_b \tag{1.49}$$

$$\frac{d(v_{ew}m_e)}{dt} = -\frac{v_{ew}m_e}{T1_e} + PSm_b \tag{1.50}$$

A number of possible strategies are suggested for solving equations. 1.49 and 1.50, based on the assumptions taken about m_v. The "slow solution" assumes labeled spins do not leave the tissue voxel during the measurement time, i.e. m_v=0. It is suggested that this strategy is suitable in the normal human brain as the MTT is generally longer than the ASL measurement time. The "fast solution" assumes the tissue voxel and the venous blood have equal magnetization, i.e. m_v=$m_b v_{bw}$ and is thought to be more suited to small animal imaging where the MTT can be shorter than the measurement time. A third strategy , referred to as the "distributed solution", combines the other two strategies by setting m_v=0 for $t <$ MTT and m_v= $m_b v_{bw}$ for $t >$ MTT. Solutions for equations 1.49 and 1.50 are provided for both the CASL and FAIR techniques. The solutions are fitted to data from the human brain to quantify grey and white matter perfusion.

The model was applied to a primate ASL study by Zappe et al [94]. In this study, the "fast solution" was chosen because significant venous out-

flow was observed in the anesthetized primate. The CBF values measured were noted to be higher than CBF values obtained using PET imaging. Carr et al [95] assessed the experimental limitations PS places on this model and concluded that acceptable levels of precision in PS quantification, which are required prior to interpreting measured differences between patient and healthy groups for example, are at present unattainable.

1.4.3 Model-Free Arterial Spin Labeling Quantification

The model-based approaches described in sections 1.4.1 and 1.4.2 each require assumptions on parameters such as bolus duration, spatial variability of the blood-brain partition-coefficient λ or the permeability surface-area product PS, or the number of compartments necessary to fully explain the measured perfusion-weighted signal. Petersen et al [96] proposed a model-free ASL quantification approach that quantifies CBF by deconvolving the tissue response curve by the AIF. The model-free ASL quantification approach proposes that if the exact form of the fractional AIF, *c(t)*, is known, equation 1.43 of the general kinetic model can be deconvolved to provide a measure for CBF that does not require any assumptions about the underlying mechanisms of perfusion. The AIF for voxel filled with arterial blood is obtained by multiplying *c(t)* by the magetization difference $2 \cdot M_{0,b}$ [96]:

$$AIF(t) = 2 \cdot M_{0,b} \cdot c(t). \tag{1.51}$$

where $M_{0,b}$ is the equilibrium magnetization of a blood filled voxel. When the magnetization difference between labeled and control ASL measurements, $\Delta M(t)$, is deconvolved by this AIF, the result is the residue function, $r(t\text{-}\tau)$, multiplied by the relaxation function, $m(t\text{-}\tau)$ and the CBF [96]:

$$CBF \cdot r(t-\tau) \cdot m(t-\tau) = CBF \cdot R(t-\tau). \tag{1.52}$$

, where $r(t\text{-}\tau)$ describes the fraction of labeled spins arriving at a voxel at time τ that still remains within the voxel at time t and $m(t\text{-}\tau)$ quantifies the longitudinal magnetization fraction of labeled spins arriving at the voxel at time τ that remains at time t. The total residue function, $R(t\text{-}\tau)$, is obtained by combining $m(t\text{-}\tau)$ and $r(t\text{-}\tau)$ and is a positive, decreasing function with $R(0)$=1 by definition. As a result, the CBF can estimated from the maximum

of R. Therefore, the only remaining unknown that must be determined in order to obtain R and thereby obtain a model-free assessment of perfusion is the AIF.

The method proposed by Ye et al [97] in which velocity encoding bipolar crusher gradients (section 1.14) are used to dephase moving spins with a mean velocity above a specified cut-off, was used by Petersen et al to measure the AIF locally. ASL images at multiple time-points post-labeling were acquired in a single slice of the human brain with and without crusher gradients. The ASL sequence, named quantitative STAR labeling of arterial regions (QUASAR) combines the PULSAR sequence (section 1.3.2) with a technique for sampling rapidly at multiple time points known as the Look-Locker method [98].

The signal from the large arteries, which is representative of the shape of the AIF, is obtained by subtracting the crushed signal curve from the non-crushed curve. This signal must be weighted by the local arterial blood volume (aBV) to correct for partial volume effects that are always present at the spatial resolutions employed in ASL. The aBV is estimated by dividing the area under the AIF curve at each voxel by the area of the labeled bolus with duration τ_b and also taking into account the longitudinal relaxation of the bolus that occurs during its transit time, τ_a, from the labeling plane to the imaging plane [96, 99]:

$$aBV = \frac{\int_{-\infty}^{\infty}(\Delta M_{ncr}(t) - \Delta M_{cr}(t))e^{1/T_{1b}}dt}{2 \cdot M_{0,b} \cdot \tau_b \cdot \alpha}. \tag{1.53}$$

where ΔM_{ncr} and ΔM_{cr} are the noncrushed and crushed data, respectively, α is the degree of inversion and T_{1b} is the longitudinal relaxation time of arterial blood. Once the measured AIF has been corrected, the CBF can be quantified by deconvolution. The average CBF in 13 normal subjects was found to be approximately 10% smaller than the values obtained using the single-compartment general kinetic model (section 1.4.1). The authors suggest that this difference may be indicative of the underestimation of the true CBF by the deconvolution process [26]. A recent validation study compared the CBF measured in both tumors and normal grey matter by the model-free ASL approach and DSC-MRI [100]. The CBF estimates from both techniques were found to be in good agreement. The model-free ASL technique

was also recently applied to an fMRI study [101], with a description of this study given below in section 1.5.1.

1.4.4 Arterial Spin Labeling Quantification Errors

The main source of error in the quantification of perfusion with ASL is variation in the arterial transit time, τ_a across the imaging slice. τ_a is typically longer in distal tortuous regions of the capillary bed. The potential for underestimating perfusion in such regions, particularly when perfusion is assessed at a single inversion time point, is illustrated in figure 1.12. While ASL sequences such as QUIPSS and QUIPSS II [62, 77] (section 1.3.2) have been developed to decrease the sensitivity of ASL to transit time effects, the error can still be significant in vascularly compromised patients with conditions such as atherosclerosis [102]. Transit time errors are more prevalent when using PASL techniques as the steady-state nature of CASL techniques. The use of a pre-delay of approximately 1 s between the continuous labeling and the image acquisition renders CASL methods almost insensitive to transit time errors [103].

Another error source in ASL arises due to the presence of large arteries in the ΔM signal used for perfusion quantification. The inflow of labeled blood into these arteries during the measurement can lead to an overestimation of perfusion. The use of crusher gradients to remove the contribution of large, high blood velocity vessels from the signal was introduced by Ye et al [97] and discussed above in section 1.4.3. These gradients can effectively eliminate the inflow error from CASL measurements and has also been adapted for PASL sequences. An alternative approach is to choose a long inversion time that ensures no labeled blood is present in the large arteries at the time of measurement [97].

When a spatially defined bolus is labeled, ideally the profile of the RF inversion pulse should be perfectly rectangular. However, this is not realizable in practice due to the finite duration of the RF pulse and hardware limitations. The resultant non-rectangular bolus can contaminate the imaging slice, as illustrated in figure 1.14. This source of error is particularly relevant in PASL sequences and consequently techniques such as TILT (section 1.3.2) have been developed to improve the profile of the labeled bolus [66]. Again, due to the steady-state nature of the CASL technique, imperfect bolus shape

is less of an issue. However, the efficiency of the labeling achievable when applying the principle of flow-driven adiabatic inversion (section 1.3.1) is problematic when CASL techniques are used [49].

The ΔM signal change in ASL at normal perfusion rates is typically in the range 0.5-1.5% of the full signal [1]. This necessitates signal averaging to ensure adequate SNR is achieved. As a result, scanning times can run to 3 to 4 minutes and issues such as patient motion, scanner stability and SAR become relevant. As a result, there is a constant trade-off between resolution, scan time and SNR, particularly when applying ASL to patient groups.

When a bolus is labeled in ASL, the bolus shape is initially close to rectangular. By the time it reaches the imaging plane, the bolus will have dispersed due to the tortuosity of the microvasculature, friction with the vessel walls, resistance and pulsatile flow. This results in a parabolic bolus shape at the imaging plane, as opposed to the ideal plug flow profile. Hrabe et al proposed a physiological PASL model with analytical solutions that allows for a distribution of arrival times at the imaging slice [104]. The distribution of velocities and path lengths taken by individual water molecules is considered. Such approaches may be sensitive to varying dispersion effects in patients with vascular disease or in aged patients [1].

Many of the quantitative models described above (section 1.4.1) rely on the definition of the blood-brain partition coefficient, λ, first defined by Kety [105]. Values of $\lambda = 0.9$ ml/g, 0.98 ml/g and 0.82 ml/g are assumed for whole brain, grey and white matter respectively. It has been demonstrated that this parameter varies not only for different tissues but is also ROI dependent [106] and quantification errors due to inaccurate λ values are likely.

Despite these potential sources of quantification errors, it should be noted that similar issues arise when using other imaging techniques and modalities such as DSC-MRI, CT and PET to quantify cerebral perfusion. Due to its noninvasive nature and high potential for further development, ASL is currently used in numerous research and clinical applications [1].

1.5 Mechanisms that Alter Cerebral Perfusion

As discussed above in section 1.1, the various ASL techniques and quantitative models have been used to quantify the changes in cerebral perfusion arising from a wide range of physiological and pathophsyiological conditions. For the purpose of the results presented in chapter 5 and sections 6.1 and 6.2, the variations in cerebral perfusion due to three specific conditions will now be introduced: localized neural activity, normal ageing and methylenedioxymethamphetamine (MDMA, "ecstacy") administration. The focus of these introductions will be the existing knowledge on the changes in the cerebral perfusion parameters under these three conditions.

1.5.1 Neural Activity

Neurovascular Coupling

The principle of neurovascular coupling, defined as the close spatial and temporal relationship between neural activity and CBF, was first proposed by Roy and Sherrington [107]. The regulation of CBF during brain activity involves the coordinated interaction of neurons, glia (astrocytes, microglia, oligodendrocytes) and vascular cells (endothelium, smooth muscle cells and adventitial cells) [108, 109]. The signals generated by the neurons and glia during a period of activation are interpreted by the vascular cells and transduced into vascular changes that lead to CBF increases at the activated region (figure 1.20). Energy, in the form of adenosine triphosphate (ATP), is required for various cellular processes of neurons, such as the restoration of ionic gradients following depolarization and the recycling of neurotransmitters. ATP is formed by either glycolysis (anaerobic) or oxidative glucose metabolism (aerobic). A continuous supply of glucose and oxygen is provided by CBF to maintain cerebral metabolism.

It has been suggested that the increased requirement for oxygen and glucose at the activated region causes the subsequent increase in CBF [110]. However, the prevailing view is that the CBF increase is in fact mediated by neurotransmitter release and not by the local energy needs of the brain [111]. For example, Mathiesen et al [112] demonstrated that AMPA receptor[2] block-

[2]AMPA receptors are glutamate receptors that mediate fast synaptic transmission in the

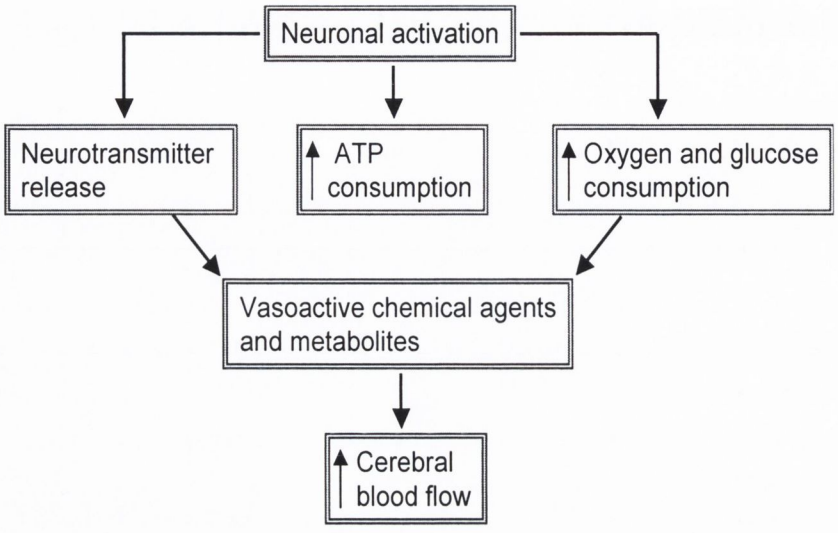

Figure 1.20: Summary of neurovascular coupling physiological mechanism. Adapted from [115].

ade resulted in attenuated CBF increases during activation. This suggests that CBF responses are of neuronal origin. Furthermore, Logothetis et al [113] simultaneously measured cortical local field potenetials (LFPs) and BOLD fMRI (see below) responses and demonstrated that only LFPs were significantly correlated with the haemodynamic response to activation. The role of astrocytes in neurovascular coupling has only recently been established. Xu et al [114] discovered that astrocytes play an active role in transferring signals from the neurons to that vasculature that result in upstream vasodilation during physiological increases in neuronal activity.

The haemodynamic changes that accompany increased neural activity, such as CBF, CBV and $CMRO_2$ changes, are linked spatially and temporally to the location and duration of the activation. As a result, these transient changes form the basis of neuroimaging techniques that use the haemodynamic response to neural activity to map regional changes in function in the brain.

Blood Oxygenation Level Dependent fMRI

The most commonly used fMRI technique is the blood oxygenation level dependent (BOLD) technique. The seminal work of Ogawa et al [116, 117]

central nervous system

on the use of the BOLD technique in the rat brain established that the BOLD contrast was altered by changes in blood oxygen demand or flow due to increased neural activity. This work was followed by a series of BOLD fMRI studies in humans [27, 118, 119] and since then, BOLD fMRI has emerged as the foremost method for visualizing the vascular correlates of brain activation.

The BOLD contrast is produced by magnetic field inhomogeneities induced by deoxyhemoglobin (dHb), which is contained within red blood cells that are in turn restricted to blood vessels [120]. The paramagnetism of dHb causes a reduction predominantly in the $T2^*$ relaxation time due to the magnetic susceptibility differences that arise between the dHb-containing blood vessels and the surrounding space. The effects of dHb on the $T2^*$ relaxation time can be imaged by a suitable MRI protocol [116, 27].

An increase in dHb following neural activity would be expected to cause a decrease in the BOLD signal. However, due to overcompensation by CBF, oxygen is oversupplied and the BOLD signal actually increases during activation [121], as shown in figure 1.21. Figure 1.21 also shows the initial dip and poststimulus undershoot in the BOLD signal. The initial dip has been attributed to the early increase in oxygen consumption that precedes the CBF response [122]. The poststimulus undershoot has been linked to the mismatch between changes in CBF and CBV [123]. At these late time points in the response, the CBF and metabolic rate of oxygen consumption ($CMRO_2$) are predicted to have returned to baseline while the CBV is still elevated. More recently, an alternative explanation for the post-stimulus undershoot was proposed following a multimodality fMRI study of visual activation in the human brain [124]. A post-activation period of approximately 30 s was observed, during which $CMRO_2$ remained elevated while CBF and CBV had returned to baseline levels. This finding also demonstrates that increased metabolic demand does not necessarily result in increased blood flow.

Due to the complexities of the physiological basis of the BOLD contrast mechanism, the quantification of changes in parameters such as CBF, CBV and the $CMRO_2$ during increased neural activity has proven difficult. However, a number of quantitative approaches for the BOLD technique have been proposed. Buxton and Frank proposed a mathematical model for the

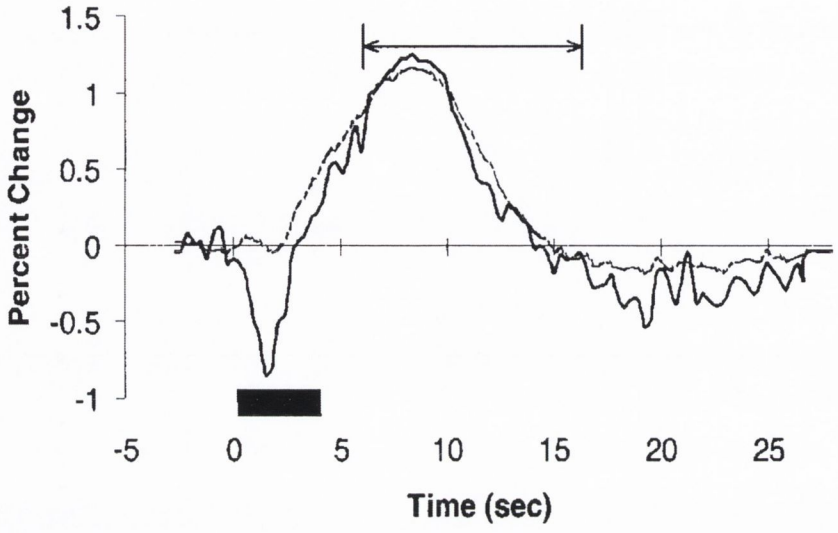

Figure 1.21: The BOLD signal time course (experimental pixel time course fitted to theoretical model [122]). The initial dip occurs during the stimulus (black rectangle). The maximum in the positive BOLD signal occurs approximately 5 s poststimulus. This is followed by the poststimulus undershoot before returning to equilibrium.

delivery of oxygen to the brain [125]. The model is based on two assumptions: (a) there is no capillary recruitment during activation (i.e. all capillaries are continuously perfused, even in the resting state [126]) and (b) oxygen metabolism is perfectly efficient (i.e. all of the oxygen made available to the tissue is metabolized). An expression is derived for a flow-dependent oxygen extraction fraction, $E(f)$, that describes the fraction of oxygen in the blood extracted by the tissue. The required change in CBF to increase $CMRO_2$ is characterized in terms of $E(f)$. The relationship between fMRI signal changes and changes in CBF and $CMRO_2$ is examined with the conclusion being that flow and oxygen consumption are tightly coupled and fMRI signal changes can provide a robust quantitative measure of the flow change. However, the assumptions that the tissue concentration of oxygen follows a simple exponential decay and that all capillaries have the same transit time may not be accurate [127].

A similar approach to modeling cerebral oxygen delivery was taken by Hyder et al [128]. In this case, the model describes the link between $CMRO_2$ and CBF in terms of an effective diffusivity, D, for oxygen in the capillary bed. The parameter D is assumed to be CBF-dependent as changes in the

capillary concentration of oxygen, hematocrit (proportion of blood volume occupied by red blood cells), and/or blood volume can effect D. As a result of the CBF-dependency of D, this model predicts a linear relationship between CBF and $CMRO_2$ for certain physiological ranges. This prediction is in conflict with the non-linear relationship predicted by the Buxton and Frank model [125],

A calibrated BOLD technique has also been proposed to quantify the $CMRO_2$ from the BOLD signal [129, 130]. This approach estimates the maximum possible change in the BOLD signal by inducing hypercapnia (the state of excess carbon dioxide concentration in the blood). This state causes an increase in CBF without increasing $CMRO_2$ and thereby allows the BOLD signal to be normalized by a calibration factor related purely to CBF heterogeneity. The resultant normalized BOLD signal is only dependent on $CMRO_2$ and can therefore by used for $CMRO_2$ quantification. A recent review of calibrated BOLD techniques [131] suggests that the inspiration of a carbon dioxide/oxygen mixture should not be used for calibration as the stimuli can produce BOLD signal changes that cannot be accounted for by a model based purely on $CMRO_2$ consumption. This coupled with the invasiveness of the technique, particularly in aged or diseased subjects, is a significant disadvantage of the calibrated BOLD technique.

Alterations in the mechanisms behind neurovascular coupling due to ageing and/or disease progression pose another problem for the interpretation of BOLD fMRI studies. For example, it is well known that Alzheimer's disease (AD) is associated with a decrease in microvessel density, flattening of endothelial cells and smooth muscle cell degradation [132]. Each of these effects plays a role in reducing both the resting CBF and the increase in CBF following neural activity [133]. Furthermore, structural changes in the vasculature such as decreased vascular reactivity, atherosclerosis, increased tortuosity of cerebral vessels, reduced resting CBF and $CMRO_2$, that are known to occur with ageing, may result in a reduced CBF response that is not indicative of an actual reduction in neural activity [132]. It follows that if the BOLD fMRI technique is insensitive to altered vascular structure, it may not be the optimum method to assess neural activity in cohorts of aged and/or diseased subjects.

Arterial Spin Labeling fMRI

ASL fMRI approaches can provide an alternative to the BOLD technique. ASL was first applied to a human fMRI study by Edelman et al [55]. The EPISTAR sequence (section 1.3.2) was used to provide qualitative perfusion-weighted maps of sensorimotor activation. Kerskens et al carried out the first ASL fMRI study in rats, where the CASL adiabatic inversion preparation (section 1.3.1) was used in combination with snapshot FLASH imaging (section 3.4) to measure perfusion increases in the somatosensory cortex of anaesthetized rats during forepaw stimulation [40].

Activation imaging using ASL has several potential advantages over the BOLD fMRI technique. ASL is insensitive to magnetic susceptibility effects that can degrade the BOLD signal. By interleaving labeled images with control images, long-term instabilities in the image intensity can be alleviated [134]. This long-term stability of ASL fMRI was tested by Aguirre et al [16] with the conclusion being that ASL fMRI is more sensitive to slow changes in neural activity that evolve over long periods of time (>24 hours) than BOLD fMRI. This makes ASL more suitable for longitudinal studies where changes in the perfusion response to neural activity are tracked over time. There have also been indications that the ASL signal is better localized at the site of neural activity than the BOLD signal [135, 136], as the BOLD signal is affected by additional signal from deoxygenated blood in the draining venous vessels, downstream from the activation site. However, the primary advantage of ASL fMRI over BOLD fMRI is the fact that the signal is directly related to blood flow, not blood oxygenation and therefore contains information that can be extracted to quantify the perfusion parameters of active brain regions. Changes in physiological parameters such as CBF and CBV during neural activity can be accurately quantified and tracked over time.

The quantification of CBF during activation is commonly achieved with ASL by applying the modified Bloch equation approach (section 1.4.1). The first such quantitative ASL study was carried out by Kwong et al [27]. A spin-echo inversion recovery (IR) sequence provided T_1 sensitive perfusion-weighted images during stimulation of the visual and primary motor cortex of humans. The change in CBF during activation was then estimated from the measured T_1 difference, by applying the theory of Detre et al [14]:

$$\frac{1}{T_{1app}} = \frac{1}{T_1} + \frac{f}{\lambda}, \tag{1.54}$$

where T_{1app} is the observed (apparent) longitudinal relaxation time with flow effects included, T_1 is the true longitudinal relaxation time in the absence of flow, f is the flow in milliliters per gram of brain tissue per unit time and λ is the blood-brain partition coefficient. As stated before (section 1.4.1), this theory assumes that the exchange of water molecules between the capillaries and the extravascular water is rapid. This assumption of near perfect capillary permeability to water is considered acceptable at normal flow rates in healthy subjects but fails at higher flow rates [137], which are typically found during neuronal activation. Additionally, a constant value for λ is chosen for the quantification of CBF but it is possible that this parameter varies with age or under disease conditions.

A quantitative fMRI method, based on the QUIPSS II sequence (section 1.3.2), was described by Wong et al [68]. A single-compartment kinetic model that describes the inflow of labeled blood in a similar manner to the subsequent general kinetic model [85] (section 1.4.1) was used to quantify CBF. A finger-tapping fMRI paradigm resulted in increase neural activity in the motor cortex. The typical fractional change in CBF with activation was in the order of 50%. The authors also describe the capability of ASL fMRI to simultaneously acquire BOLD contrast data. A gradient echo (GE) EPI sequence was used for image acquisition and when an in-plane presaturation pulse is applied, the BOLD signal can be extracted. A comparison of the results from both contrast mechanisms revealed that the BOLD signal changes occur both in the brain parenchyma (capillary bed) and in large veins, while the ASL signal is more closely localized to the parenchyma. The possibility of extracting the BOLD signal from ASL fMRI data has also been reported by Kim et al through the use of a quantitative multi-slice FAIR technique [138].

Another quantitative ASL fMRI method that simultaneously acquires BOLD contrast through the use of a GE-EPI acquisition is described by Wang et al [139]. The modified Bloch equation single-compartment model in equation 1.42 (section 1.4.1) was applied to PASL data from a modified FAIR sequence [140] to quantify changes in CBF in the motor cortex due to a finger-tapping fMRI paradigm and a mean CBF increase of approximately 25% during activation was reported.

The model-free ASL approach described in section 1.4.3 was recently applied to an fMRI study [101]. Stimulation of the visual cortex was achieved through the use of an 8 Hz checkerboard pattern with three levels of visual contrast (25%,50% and 100%). Using both the model free approach and the general kinetic model described in section 1.4.1, significant changes in CBF were detected in the visual cortex. The percentage increase in CBF for the three visual contrast levels were found to be in good agreement for both quantitative approaches. The arrival time of the ASL bolus at the microvasculature (small arterioles and capillaries), referred to as τ_m, was also quantified by both approaches and was found to decrease during visual stimulation. The magnitude of the decrease in τ_m was larger for the 50% visual contrast level than for the 25% level. This decrease was attributed to flow velocity increases during stimulation. There was a slight tendency for the arterial blood volume (aBV), calculated by equation 1.53, to increase during visual stimulation. The authors conclude that the microvasculature, as opposed the larger arteries on which the aBV depends, plays an important role in regulating changes in flow and volume in response to neuronal activation.

The CBF changes measured by ASL fMRI were recently validated by PET data in a comparitive fMRI study [141]. The $H_2{}^{15}O$ PET tracer technique is regarded as the current gold standard for in vivo imaging of CBF and has previously been used to validate DSC-MRI CBF measurements [142]. An interleaved FAIR-BOLD sequence, previously implemented by Hoge et al [130] was used in combination with visual stimulation with a checkerboard, with contrast levels varying from 25% to 100%. The change in CBF in the visual cortex was between 11.4% and 22.5% for the various stimulation intensities, while the BOLD signal changes ranged from 1.0% to 1.9%. The changes in CBF measured by CBF and PET were not significantly different. Furthermore, the CBF measurements made using PET had a much lower SNR than those made using ASL-fMRI. When coupled with the non-invasiveness of the ASL fMRI technique, it was concluded that ASL-fMRI is a viable alternative to the gold standard PET technique.

1.5.2 Normal Ageing

The Cerebrovascular Correlates of Ageing

Disruption of the cerebrovasculature is found in many neurological and psychiatric disorders. However, extensive research has shown that normal, physiological ageing also causes both structural and functional changes in the cerebrovascular system throughout the human lifespan that can begin as early as the fourth decade [143]. These vascular changes are the basis for alterations in both resting cerebral perfusion and neurovascular coupling [132].

The alteration of the structure of the cerebral vasculature in ageing is largely attributed to atherosclerosis, which involves thickening of vessel walls, necrosis (cell death) of the smooth muscle and endothelial cells that line the vessels and thickening of the sub-endothelial membrane. These age-realted vascular changes have been well characterized in both humans [144, 145] and rats [146] and are known to cause reductions in cerebral perfusion and vessel reactivity, redistribution of blood flow and in some cases can lead to thrombotic occlusion. The density of microvessels (number of vessels per unit tissue volume) is also known to decrease with ageing in certain cerebral regions, with deficits reported in the hypothalamus [147], hippocampus [148] and frontal and visual cortices [149]. There is also an increase in the tortuosity of some vessels with ageing, which is thought to be due to loss of longitudinal stiffness in the aged vessel wall [150].

Cerebral vessels react to various chemical modulators, particularly carbon dioxide (CO_2) concentration. Normally, increased CO_2 concentrations result in dilation of the cerebral vessels. However, an age-associated decrease in the reactivity of cerebral vessels has been established by studies investigating the cerebral perfusion response to hypercapnia (the state of elevated CO_2 in the blood) in the rat brain. As well as regional deficits in cerebral perfusion due to ageing, a significant and homogenous reduction in the ability of cerebral vessels to dilate has been reported [151, 152, 153].

Vasodilation is the main mechanism of the haemodynamic response to neural activity (neurovascular coupling, section 1.5.1). As a result, decreases in cerebral vessel reactivity with ageing limit the responsiveness of vessels to increased neural activity [109]. Other mechanisms such as a reduction

in the number of neurotransmitter receptors on astrocytes also affect neurovascular coupling in aged subjects [132].

The Measurement of Age-Related Alterations in Cerebral Perfusion

Each of the cerebrovascular correlates of ageing outlined above are thought to contribute to the decline of cerebral perfusion with age. A large number of MRI and non-MRI quantitative perfusion studies have measured these age-related cerebral perfusion deficits.

Pantano et al [154] applied $^{15}O_2$ PET to a study of young and aged humans and measured an 18% average decrease in CBF in grey matter (GM) cortical regions. Leenders et al [155] used the same PET technique to measure CBF and CBV decreases with age and concluded that both decreased by approximately 0.50% per year. Subsequent PET studies have reported similar deficits in cerebral perfusion due to ageing in cortical and cerebellar regions [156, 152]. Grey matter perfusion deficits have also been measured by SPECT imaging [157, 158]. Transcranial Doppler has produced similar findings for compromised flow and reduced blood flow velocities in the larger cerebral arteries with advancing age [159]. However, the limited spatial resolution of these non-MRI techniques renders them less capable of resolving CBF differences in smaller sub-regions, particularly in rodent studies [153].

For imaging studies involving aged subjects and/or repeat scanning of either humans or rodents, ASL offers the advantage of longitudinal signal stability [134] without the use of tracer compounds. In a study aimed at establishing the reproducibility and stability of ASL as well as the effects of gender and ageing, Parkes et al [160] applied a multislice CASL technique [49] (section 1.3.1) to 34 human subjects with an age range of 20 - 67 years. A significant decrease in the ratio of GM to WM perfusion was detected. This finding suggested that cerebral perfusion deficits were most profound in GM regions. GM perfusion was found to decrease by 0.45% per year with regional analysis suggesting that the decrease was mainly due to changes in the frontal cortex.

The age dependence of cerebral perfusion was also investigated by Biagi et al [161], using the same multislice CASL sequence [49], in 44 subjects with an age range of 4 - 78 years. A similar decrease in CBF was reported, this time both in GM and WM, with the decrease being greater in GM. The use of

very young subjects in this study facilitated the quantification of CBF over a broader age range than previous ageing studies. The results suggest a non-linear decline in CBF from childhood to adulthood, rather than a constant rate of decline.

More recently, a study by Mitschelen et al [153] applied the FAIR technique [72] (section 1.3.2) to an ageing study in rats. A decrease in baseline perfusion in an aged group (26 months) compared to an adult group (9.5 months) was reported for the dorsal hippocampus. The study also included a hypercapnia challenge in which cerebral perfusion was measured during administration of CO_2 in the inspired gas mixture to establish if the reactivity of the vasculature decreases in the aged group. An attenuated response to hypercapnia was detected in several ROIs. The aged rats were also classified, using a water maze, as memory impaired or memory intact. An increase in perfusion in the hippocampus of the memory impaired aged rats compared to the adult rats was detected, indicating that a hippocampal increase in CBF may be an early indicator for cognitive diseases such as mild cognitive impairment (MCI).

1.5.3 MDMA Intake

The Cerebrovascular Consequences of MDMA Intake

The recreational drug 3,4-methylenedioxymethamphetamine (MDMA, or "ecstasy") is known to produce both short term (acute) and long term (chronic) changes in brain function. Acute MDMA effects in both rats and humans include hyperthermia, tachycardia and hypertension (elevated temperature, heart rate and blood pressure respectively) [162, 163, 164], which gives rise to increases in the incidence of cerebrovascular accidents and morbidity [165, 166]. These acute effects of MDMA are mediated by enhanced release and reduced uptake of monoamine neurotransmitters such as noradrenaline and serotonin with the net effect being an increase in the synaptic availability of these neurotransmitters. Monoamine oxidase activity, which is responsible for metabolism within brain cells, is reduced [167]. These acute effects are short-lived, lasting for approximately 24 hours [168].

In the longer-term, the effect of MDMA on serotonin (5-HT) levels in the brain is thought to play a major adverse role, resulting in impaired brain

function and cerebrovascular disease [165, 169]. The involvement of 5-HT in the regulation of brain microcirculation is well established [170, 171]. Intracerebrally released 5-HT causes vasoconstriction and a resultant reduction in CBF in many brain regions. Vasodilation and variations in blood brain barrier (BBB) permeability due to 5-HT have also been observed [171]. Furthermore, a number of studies have shown that changes in CBF and local cerebral glucose utilization ($LCMR_{glu}$), a measure of metabolism, do not exhibit the expected correlation when 5-HT levels are varied [162, 172, 168]. This indicates that 5-HT plays a direct and not a secondary role in controlling the microvasculature. MDMA initially causes an increase in 5-HT release and 5-HT-induced effects in the brain but repeated use over time leads to a loss of serotonergic neurons, a reduction in 5-HT levels and a consequent upregulation of $5\text{-}HT_2$ receptors [165, 173]. A number of studies have aimed to establish the short and long-term effects of these variations in 5-HT on cerebral perfusion.

The measurement of Acute MDMA-Related Alterations in Cerebral Perfusion

Ferrington et al [168] performed a MDMA study to establish the relationship between local CBF (LCBF) and $LCMR_{glu}$ in three groups of rats. The [^{14}C]-iodoantipyrine autoradiographic technique was used for CBF quantification [174]. Group one were administered a single dose of MDMA or saline (controls) 25 minutes prior to LCBF and $LCMR_{glu}$ measurement, group two were given the same treatments three weeks prior to measurements and group three were given both the three week and 25 minutes prior treatments. LCBF was found to be uncoupled from $LCMR_{glu}$ in the MDMA-treated rats. The group one rats showed regions of focal hyperaemia (increased blood flow) that indicated a loss of autoregulatory capacity in response to hypertension. Autoregulation is the process by which the brain maintains constant CBF over a wide range of blood pressures [175]. However, if hypertension is pronounced, cerebral blood vessels can suffer lasting physical disruption and CBF can remain elevated [162]. The authors suggest this mechanism as a possible explanation for the measured focal hyperaemia. The findings from groups two and three suggest that prior exposure to MDMA, which causes a significant depletion in 5-HT, does not

alter the cerebrovascular regulatory dysfunction associated with acute exposure to MDMA.

A previous study by Quate et al [172] using the same quantitative autoradiographic CBF technique and a similar animal model to Ferrington et al, measured significant decreases in LCBF in the superior colliculus and anterior thalamus of rats studied 25 minutes post-MDMA administration. The LCBF was again found to be uncoupled from $LCMR_{glu}$, suggesting a direct relationship between 5-HT and changes in LCBF. The vasoconstrictor action of 5-HT was suggested as a possible explanation for focal decreases in CBF.

The Measurement of Chronic MDMA-Related Alterations in Cerebral Perfusion

Reneman et al [165] used ^{123}Iodine SPECT (section 1.1) to measure 5-HT_2 receptor densities in three groups: abstinent recent MDMA users, former MDMA users and healthy control subjects. Bolus-tracking DSC-MRI with intravenous injection of Gd was used to generate CBV maps in two groups: chronic MDMA users and control subjects. A down-regulation of 5-HT_2 receptors due to MDMA-induced 5-HT release was observed. Furthermore, local 5-HT_2 receptor levels and CBV were found to be correlated in MDMA users. In regions with reduced 5-HT_2 receptor levels, an associated decrease in CBV thought to be linked to the vasoconstriction effects of 5-HT was measured. Conversely, an increase in 5-HT_2 receptor levels was found in abstinent users and was associated with an increase in CBV, implicating vasodilation in specific brain regions. These results indicate that the 5-HT_2 receptor levels are involved in acute and long-term cerebrovascular changes in MDMA users.

Another combined SPECT-MRI study investigating the long-term effects of MDMA on CBF was carried out by Chang et al [176]. Abstinent MDMA users were compared to an age and gender-matched control group. A subgroup of the abstinent MDMA users had MDMA doses administered prior to scanning. High resolution ^{99m}Technetium SPECT scans were calibrated by ^{133}Xenon SPECT images that provided a measure of absolute regional CBF (rCBF). The calibrated SPECT images were then overlaid on inversion recovery (IR) EPI images, for optimal ROI selection. No significant long-

term change in rCBF was measured in the abstinent MDMA group compared to the control group, although a trend towards reduced rCBF was detected in most ROIs. An acute decrease in rCBF in the globus pallidus and caudate was detected in the subjects that were administered MDMA prior to scanning. Two subjects from this group were scanned two months later and an increased global CBF was measured. These findings were not consistent with similar MDMA-cerebral perfusion studies (e.g.Reneman et al [165]) and the authors suggest that 5-HT_2 receptor densities do not have a significant long-term effect on CBF.

DeWin et al [177] used DSC-MRI to measure differences in relative regional CBV (rrCBV) between novel low-dose MDMA users and MDMA-naive controls. The MDMA group showed significant rrCBV decreases in the putamen and globus pallidus. The authors suggest that decreased rrCBV may reflect long-term vasoconstriction following MDMA use due to changes in the 5-HT regulation of the microvasculature. As the mean period of abstinence before imaging in the study was over four months, this rrCBV effect is classed as a long-term rather than acute effect of MDMA usage.

Chapter 2

Theoeretical Results: A Non-Compartmental Model of Cerebral Perfusion

2.1 Introduction

A new model of cerebral perfusion for ASL will be derived in this section. The model is non-compartmental in nature and considers the ASL signal response to be the result of individual water molecules taking a range of times to traverse the system. The distribution of traversal times is hypothesized to be due to three processes:

1. pseudo-diffusion within the microvasculature [178, 179],
2. exchange of labeled spins between the capillary bed and extravascular water and surrounding cells (osmosis) [180],
3. random diffusion of the labeled spins within both the vascular and extravascular space [181].

The net effect of these processes on an approximately rectangular bolus of labeled spins at the labeling plane in an ASL experiment is the dispersion of that bolus during its transit from the labeling plane to the imaging plane, as depicted in figure 2.1.

A general Langevin equation was chosen as the starting point for the derivation of the non-compartmental model of cerebral perfusion. This type

of equation was first used to describe the trajectory of a small particle immersed in a fluid, undergoing Brownian (or random) motion. In this example the Langevin equation for the particle is comprised of a frictional force term and a random or fluctuating force [182]:

$$m\frac{dv}{dt} = \underbrace{-\zeta v}_{\text{Frictional Force}} + \underbrace{\delta F(t)}_{\text{Random Force}}, \tag{2.1}$$

where m is and v are the mass and velocity of the particle and ζ is the coefficient of friction. The fluctuating force (or noise) term in this case prevents the total force on the particle from decaying to zero and in the case of a particle immersed in a fluid is presumed to come from occasional impacts of the particle with molecules of the surrounding medium. The effects of the fluctuating force can be summarized by its first and second moments as follows [182]:

$$\langle \delta F(t) \rangle = 0, \qquad \text{and} \qquad \langle \delta F(t) \delta F(t') \rangle = 2B\delta(t - t'), \tag{2.2}$$

where B is a measure of the strength of the fluctuating force and the delta function, δ, indicates that there is no correlation between impacts in any distinct time intervals, dt and dt'. The fluctuating force is considered to have a Gaussian distribution determined by the moments in equation 2.2. A Fokker-Planck equation for the noise-averaged distribution of all particles in a given system can be derived from a Langevin equation for a single particle such as equation 2.1 [182].

The Langevin equation chosen as the starting point for the derivation of the non-compartmental model of cerebral perfusion describes the motion of a single particle (or labeled spin) within the vasculature in terms of a directional flow term and a random noise term that takes the three processes above into account. By averaging over all particles in the entire space we arrive at a Fokker-Planck equation that describes the noise-averaged distribution of labeled spins. However, in the case of an ASL experiment, longitudinal relaxation of the labeled spins must also be incorporated into the theoretical formulation. To this end, the derivation of the final Fokker-Planck equation for the non-compartmental model of cerebral perfusion begins with a standard Bloch equation for the magnetization difference between the control and labeled ASL images.

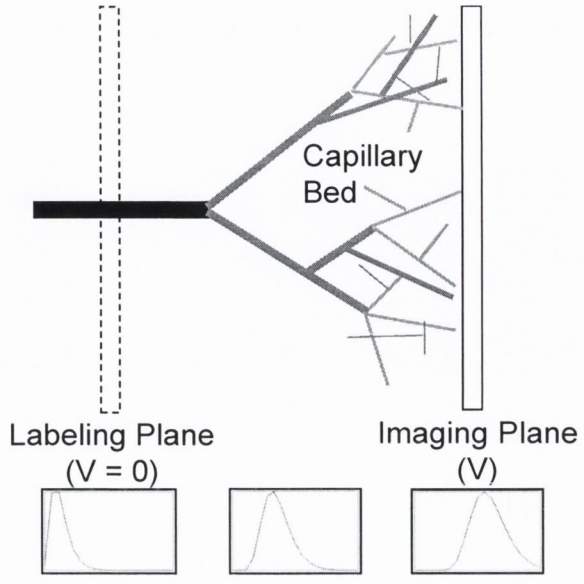

Figure 2.1: Schematic representation of branching of cerebral vasculature between the labeling and imaging plane. The dispersion of an approximately rectangular bolus on traveling from the labeling plane to the imaging plane is depicted.

2.2 Derivation of Fokker-Planck Equation

2.2.1 The Bloch Equation for Longitudinal Relaxation

The T_1 relaxation time of brain water in the absence of flow or exchange between vascular and extravascular water is initially assumed to be a constant throughout the measuring time. With this assumption, the magnetization difference between the control and the labeled image can be expressed using the Bloch equation:

$$\frac{d((M_c(t) - M_l(t)))}{dt} = \frac{(M_c(0) - M_c(t)) - (M_l(0) - M_l(t))}{T_1} \tag{2.3}$$

where $M_{c,l}(t)$ is the concentration of longitudinal magnetization in arbitrary units of an imaging voxel for the control and labeled image respectively and $M_{c,l}(0)$ are these concentrations at equilibrium. Since $M_c(0) = M_l(0)$, equation 2.3 can be simplified to become:

$$\frac{d((M_c(t) - M_l(t)))}{dt} = -\frac{((M_c(t) - M_l(t)))}{T_1}. \tag{2.4}$$

If we consider $M_c(t)$-$M_l(t)$ as the concentration of labeled spins, *c(t)*, the

equation defining the total change in the amount of labeled spins between a control image and a labeled image due to T_1 relaxation is:

$$\frac{dc(t)}{dt} = -\frac{c(t)}{T_1}. \tag{2.5}$$

2.2.2 The Langevin Equation

If flow is defined in units of volume per time, then bulk flow, F, can be described by the mean rate of change of the volume, V, as follows:

$$\langle \frac{dV}{dt} \rangle = F, \tag{2.6}$$

where V is the volume of distributed water or any space into which labeled water can flow between the labeling plane and the imaging plane (depicted in figure 2.1). V consists of both a vascular and extravascular component due to the exchange of water from vessels to the surrounding extravascular space [180][1]. From this definition of the bulk flow, the following general Langevin equation can be assumed:

$$\frac{dV}{dt} = F(V) + \Gamma(V), \tag{2.7}$$

where Γ is a Gaussian noise term with zero mean [178] and F is independent of time, t. The delta correlated second moment of the noise term Γ is given by [182]:

$$\langle \Gamma(t)\Gamma(t') \rangle = 2P\delta(t - t'), \tag{2.8}$$

where P is a function of the volume V and takes into account the magnitude of the random forces acting on a particle as it traverses the vasculature. The first term on the right-hand side of equation 2.7 represents the change in the volume of labeled spins due to bulk flow. The second term represents the random pseudo-diffusion of labeled spins within the microvasculature [178, 179], the exchange of labeled spins from the vascular to the extravascular space [180] and the diffusion of labeled spins within the entire volume.

[1]Refer to sections 2.5 and 2.7 for discussion of the implications of this definition of V

2.2.3 Combining the Langevin and Bloch Equations

Rather than looking for a general solution to equations 2.7 and 2.8, one can look for the probability distribution of the concentration of excited spins, *c(V,t)*, and more specifically the average of this probability distribution over the noise. To solve this problem we start by recognizing that if T_1 relaxation is temporarily neglected, *c(V,t)* is a conserved quantity and the following conservation law can be defined:

$$\int c(V,t)dV = 1. \tag{2.9}$$

When a conservation law such as equation 2.9 is encountered, we expect that the time derivative of the conserved quantity is balanced by the divergence of a flux [182], or a velocity times a density in this case. This leads to the following equation:

$$\frac{\partial c}{\partial t} + \frac{\partial}{\partial V}\left(\frac{dV}{dt}\right)c = 0 \tag{2.10}$$

However, in ASL the relaxation of excited spins, represented by equation 2.5, must be incorporated into the conservationlaw as follows:

$$\frac{\partial c}{\partial t} + \frac{\partial}{\partial V}\left(\frac{dV}{dt}\right)c = -\frac{c}{T_1} \tag{2.11}$$

If the time derivative of the volume in equation 2.11 is replaced by the general Langevin equation in equation 2.7, we get:

$$\frac{\partial c(V,t)}{\partial t} = -\frac{\partial}{\partial V}(F(V)c(V,t) + \Gamma(t)c(V,t)) - \frac{c(V,t)}{T_1}. \tag{2.12}$$

The stochastic differential in equation 2.12 will now be used to derive the Fokker-Planck equation for the noise averaged distribution of labeled spins in an ASL experiment.

2.2.4 Transfer to the Fokker-Planck Equation

The stochastic differential equation in equation 2.12 can be simplified by the introduction of an operator defined as:

$$L\Phi = \frac{\partial}{\partial V}(F(V)\Phi). \tag{2.13}$$

This allows the noise free component of equation 2.12 to be written as:

$$\frac{\partial c(V,t)}{\partial t} = -Lc(V,t) - \frac{c(V,t)}{T_1} = \left(-L - \frac{1}{T_1}\right) c(V,t). \tag{2.14}$$

A symbolic solution to equation 2.14 as an initial value problem is:

$$c(V,t) = e^{\left(-L-\frac{1}{T_1}\right)t} c(V,0). \tag{2.15}$$

If we reincorporate the noise term in equation 2.12, the time derivative of the concentration of labeled spins is given by:

$$\frac{\partial c(V,t)}{\partial t} = \left(-L - \frac{1}{T_1}\right) c(V,t) - \frac{\partial}{\partial V}\Gamma(t)c(V,t). \tag{2.16}$$

Equation 2.15 gives the form of the solution for the first two terms on the right-hand side of equation 2.16. Integration over time leads to the following solution [182]:

$$c(V,t) = e^{\left(-L-\frac{1}{T_1}\right)t} c(V,0) - \int_0^t e^{\left(-L-\frac{1}{T_1}\right)(t-t')} \frac{\partial}{\partial V}\Gamma(t')c(V,t')dt', \tag{2.17}$$

where it should be noted that *c(V,t)* depends on the noise Γ only for times t' that are earlier that t. By substituting equation 2.17 into equation 2.16, a series expansion for c in powers of the noise can be developed:

$$\begin{aligned} \frac{\partial c(V,t)}{\partial t} &= \left(-L - \frac{1}{T_1}\right) c(V,t) - \frac{\partial}{\partial V}\Gamma(t)c(V,0) \\ &+ \frac{\partial}{\partial V}\Gamma(t) \times \int_0^t e^{\left(-L-\frac{1}{T_1}\right)(t-t')} \frac{\partial}{\partial V}\Gamma(t')c(V,t')dt'. \end{aligned} \tag{2.18}$$

The final step in the derivation of the Fokker-Planck equation is to take the average of equation 2.18 over the noise. If we recall the assumptions made about the noise, the term with the single Γ averages to zero. The final term contains two noise factors $\Gamma(t)$ and $\Gamma(t')$. When these two noise factors are paired and equation 2.8 is considered, it can be concluded that the averaging process introduces a factor P and a delta function. The delta function removes the $e^{-L(t-t')}$ term in equation 2.18 and if the operator L is expanded as per its definition in equation 2.13, we arrive at the Fokker-Planck

equation for the noise-averaged distribution of labeled spins:

$$\frac{\partial}{\partial t}\langle c(V,t)\rangle = -\frac{\partial}{\partial V}F(V)\langle c(V,t)\rangle + \frac{\partial}{\partial V}P(V)\frac{\partial}{\partial V}\langle c(V,t)\rangle - \frac{\langle c(V,t)\rangle}{T_1}. \quad (2.19)$$

In this formulation, we assume that the flow F and the perfusion coefficient P are constant with respect to the volume. This allows equation 2.19 to be written in simplified form as the Fokker-Planck equation,

$$\frac{\partial c}{\partial t} = -F\frac{\partial c}{\partial V} + P\frac{\partial^2 c}{\partial V^2} - \frac{c}{T_1} \quad (2.20)$$

This equation incorporates the three factors that affect the concentration of labeled spins within the volume. The first term on the right-hand side of the equation represents transport due to bulk flow, the second term represents pseudo-diffusion, osmosis and free diffusion effects within the microvasculature (discussed above) and the third term represents T_1 relaxation of the labeled spins. The perfusion coefficient P takes the dilution of the labeled magnetization due to the random effects into account and has units similar to a diffusion coefficient ($volume^2/time$). Equation 2.20 will now be solved for specific ASL experiment in which a bolus of a defined duration is labeled at the labeling plane, referred to herein as bolus-tracking ASL (btASL). An additional solution is provided for the saturation CASL experiment in section 2.6 below.

2.3 Bolus-Tracking Arterial Spin Labeling Solution

In order to find a solution to equation 2.20 for the specific case of an ASL experiment with a bolus of defined duration, a boundary-value problem must be solved[2]. The magnetization labeled at the labeling plane, V=0 (where V is being used here as a three dimensional coordinate to denote location in relation to the labeling plane, as depicted in figure 2.1), enters the brain as time progresses. However, at t=0, the concentration of excited spins in the

[2]The solution presented in this section was adapted from the PhD thesis of Dr. Christian Kerskens [44].

brain is zero. This leads to the following set of boundary conditions:

$$\begin{aligned} c(V,t) &= c_0(t) \qquad \text{for} \qquad V = 0 \\ c(V,t) &= 0 \qquad \text{for} \qquad t = 0, V > 0, \end{aligned} \tag{2.21}$$

where V is been used as a coordinate in this instance to denote position in relation to the labeling plane and $c_0(t)$ is the input function. These conditions enable the equation of motion to be solved. Initially we solve the auxiliary problem in which $c_0(t)$ is represented by the delta function $\delta(t)$. The solution to this problem can be found using Laplace's formula [183]. Using this formula, we find a function that satisfies equation 2.20 and also approaches $\delta(t)$ for $V \rightarrow 0$:

$$c(V,t) = \frac{\exp(-t/T_1)}{\sqrt{4\pi P t}} \frac{V}{t} \exp\left(-\frac{(V - Ft)^2}{4Pt}\right). \tag{2.22}$$

This function represents a relaxation function, $m(t)$, multiplied by the tissue response function, $r(V,t)$ where $m(t)$ and $r(V,t)$ are defined as follows:

$$m(t) = \exp\left(\frac{-t}{T_1}\right) \quad \text{and} \quad r(V,t) = \frac{V}{\sqrt{4\pi P t^3}} \exp\left(-\frac{(V - Ft)^2}{4Pt}\right). \tag{2.23}$$

Since the equations are linear, the effects of labeled spins entering the brain at different moments in time are simply additive and therefore the required solution to the Fokker-Planck equation, equation 2.20, with the boundary conditions defined above is:

$$c(V,t) = \int_0^t c_0(t') \frac{\exp(-(t-t')/T_1)}{\sqrt{4\pi P(t-t')}} \frac{V}{(t-t')} \exp\left(-\frac{(V - F(t-t'))^2}{4P(t-t')}\right) dt'. \tag{2.24}$$

The derivation of equation 2.24 from equation 2.20 is described in detail in the appendix, section 2.8, below. The solution for a boundary-value problem as described above allows us to solve for the special case of a rectangular input function or bolus, $c_0(t)$, defined by:

$$c_0(t) = C_0(\Theta(t) - \Theta(t - \tau)), \tag{2.25}$$

where C_0 is the initial concentration of inflowing magnetization at the labeling plane, τ is the inversion pulse duration and $\Theta(t)$ is a rectangular input function defined as $\Theta(t) = 1$ for $t \geq 0$ and $\Theta(t) = 0$ for $t < 0$. Inserting this input function into equation 2.24 gives the following solution to the Fokker-Planck equation for a bolus of labeled spins:

$$c(V,t) = C_0 \int_{t-\tau}^{t} \frac{\exp(-(t-\tau)/T_1)}{\sqrt{4\pi P(t-\tau)}} \frac{V}{(t-\tau)} \exp\left(-\frac{(V - F(t-\tau))^2}{4P(t-\tau)}\right) d\tau. \tag{2.26}$$

By defining the mean transit time, MTT, and a capillary transit time, CTT, as:

$$\text{MTT} = \frac{V}{F}, \qquad \text{CTT} = \frac{P}{F^2}, \tag{2.27}$$

the dependent variables of equation 2.24 and equation 2.26 can be reduced by one. Equation 2.26 becomes:

$$c(V,t) = C_0 \int_{0}^{t} \frac{\exp(-(t-\tau)/T_1)}{\sqrt{4\pi \text{CTT}(t-\tau)}} \frac{\text{MTT}}{(t-\tau)} \exp\left(-\frac{(\text{MTT} - (t-\tau))^2}{4\text{CTT}(t-\tau)}\right) d\tau. \tag{2.28}$$

2.4 Physical Interpretation of Transit Times

If we let $T_1 \rightarrow \infty$, we find that the MTT defined in equation 2.27 is calculated from the first moment of the tissue response function, *r(V,t)*, defined in equation 2.23:

$$\text{MTT} = \frac{\int_0^\infty t \cdot r(V,t)dt}{\int_0^\infty r(V,t)dt} = \frac{V}{F}. \tag{2.29}$$

The MTT represents the average time taken for labeled water to traverse the entire volume (i.e. the time from when spins are labeled at the labeling plane to when they flow out of the imaging plane). The volume, V, in equation 2.29 was defined previously as the volume of distributed water or any space into which labeled water can flow. Due to the exchange of water into and out of the microvasculature, V consists of both and intra- and extravas-

cular component. Previous studies have established that the exchange of water depends on the rate of blood flow [180, 184]. Small animal studies have shown that at high flow rates, the extraction fraction of water is approximately 0.3-0.5, while at lower flow rates this value is closer to 1. Therefore, when the labeled water is imaged at the imaging plane, the measured signal is comprised of contributions from both the intra- and extravascular spaces with the relative proportions of these contributions depending on the flow rate of arterial water. As a result, the MTT defined in equation 2.29 is not purely intravascular in nature as labeled water that has been extracted from the microvasculature also contributes to the concentration-time curves used to quantify MTT.

The CTT defined in equation 2.27 is calculated from the second moment of *r(V,t)*:

$$\mathrm{CTT} = \frac{1}{2}\frac{\int_0^\infty (t - \mathrm{MTT})^2 \cdot r(V,t)dt}{\int_0^\infty t \cdot r(V,t)dt} = \frac{P}{F^2}. \tag{2.30}$$

The CTT is not defined in terms of a specific transit distance but describes the extent to which an initially rectangular bolus of labeled water at the labeling plane has become dispersed when it is measured at the imaging plane. From equation 2.30 it can be seen that the CTT is directly proportional to the perfusion coefficient, P, which was hypothesized in section 2.7 to incorporate the random effects that result in the dispersion of a bolus of labeled spins (such as pseudo-diffusion within the microvasculature and the exchange of water across the capillary walls). For example, if the proportion of water being exchanged across the capillary walls is high (i.e. the water extraction fraction is close to 1), the CTT will be long. The CTT is also inversely proportion to the bulk flow squared (F^2). This inverse relationship is in agreement with the finding of previous studies that the extraction fraction of water decreases with increasing flow rates [180, 184].

2.5 Comparison of the Bolus-Tracking ASL Solution to Existing Theories

Conventional Residue Detection Experiments

The solution to the Fokker-Planck equation for the boundary conditions that describe the btASL solution, equation 2.24, reveals the conventional structure of a residue detection experiment with bolus dispersion [85, 185]. Equation 2.24 can be rewritten as follows:

$$c(V,t) = \int_0^t \underbrace{c_0(t)}_{\text{AIF}} \underbrace{\exp\left(\frac{-(t-\tau)}{T_1}\right)}_{m(t-\tau)} \underbrace{\frac{V}{\sqrt{4\pi P(t-\tau)^3}} \exp\left(-\frac{(V-F(t-\tau))^2}{4P(t-\tau)}\right)}_{r(V,t-\tau)} d\tau. \tag{2.31}$$

From this it can be seen that the solution is equivalent to a convolution described by:

$$c(V,t) = \text{AIF} \otimes r(V,t) \otimes m(t), \tag{2.32}$$

where the arterial input function, AIF, is defined in equation 2.25, *m(t)* is the relaxation function and *r(V,t)* is the residue function, as shown in equation 2.23.

Meier-Zierler Indicator Dilution Theory

The indicator-dilution approach described in section 1.2.2 quantifies the MTT of purely intravascular tracer in terms of the cerebral blood flow and volume (CBF and CBV) [24, 186]. The MTT in this case is calculated from the first moment of the intravascular concentration-time curve (equation 1.13) and is given by:

$$\text{MTT}_{MZ} = \frac{\text{CBV}}{\text{CBF}}, \tag{2.33}$$

and is defined as the mean traversal time of the indicator particles (from P to Q in figure 1.2), where CBV is the intravascular fluid volume and CBF is the constant rate of flow at which fluid enters and exits the system. This relationship is dependent on the following assumptions: (a) the distribution

of traversal times for entering tracer particles does not change with time (i.e. the stationarity of flow), (b) the flow of tracer particles represents the flow of the total fluid, (c) the system has no stagnant pools (i.e. all fluid that enters the system is eventually eliminated). Both (b) and (c) are violated by ASL methods as water is known to be exchanged across the capillary walls [180]. As a result, CBV cannot be measured when water is used as the tracer. Therefore, even though the MTT defined by the btASL solution is calculated from the first moment of the residue function, *r,(V,t)* (equation 2.29) in a manner similar to how the MTT is calculated in the indicator-dilution theory (first moment of the intravascular concentration-time curve, equation 1.13), the theories are not strictly equivalent.

2.6 Additional Solution for a Saturation Experiment

A solution to equation 2.20 may also be found for a CASL experiment where the region of interest (ROI) is saturated with labeled inflowing magnetization[3]. In this case the concentration of labeled spins becomes constant with respect to time and consequently equation 2.20 can be simplified as follows:

$$\frac{\partial^2 c}{\partial V^2} - \frac{F}{P}\frac{\partial c}{\partial V} - \frac{c}{PT_1} = 0. \tag{2.34}$$

The general solution of this equation is of the form:

$$c(V) = Ae^{\lambda_1 V} + Be^{\lambda_2 V}, \tag{2.35}$$

where the coefficients $\lambda_{1,2}$ in equation 2.35 are given as:

$$\lambda_1 = \frac{F}{2P}\left(1 - \sqrt{1 + \frac{4P}{T_1 F^2}}\right), \qquad \lambda_1 = \frac{F}{2P}\left(1 + \sqrt{1 + \frac{4P}{T_1 F^2}}\right). \tag{2.36}$$

The constants A and B are given by the boundary conditions for saturation CASL. First, we expect a minimum concentration for $V \rightarrow \infty$. Secondly, at

[3]The solution presented in this section was adapted from the PhD thesis of Dr. Christian Kerskens [44].

V=0, a constant magnetization C_0 is delivered. With these conditions, we arrive at the solution to equation 2.20 for saturation CASL:

$$c(V) = C_0 \exp\left(\frac{FV}{2P}\left(1 - \sqrt{1 + \frac{4P}{T_1 F^2}}\right)\right). \tag{2.37}$$

When equation 2.37 is rewritten in terms of the MTT and CTT defined in equation 2.27, the number of dependent variables can be reduced by one:

$$c(V) = C_0 \exp\left(\frac{\text{MTT}}{2 \cdot \text{CTT}}\left(1 - \sqrt{1 + \frac{4 \cdot \text{CTT}}{T_1}}\right)\right). \tag{2.38}$$

2.7 Discussion of Theoretical Results

A novel non-compartmental model of cerebral perfusion, based on a Fokker-Planck equation for the distribution of inflowing arterial water in the brain, has been described. Solutions are provided for two types of ASL experiments: btASL and saturation CASL. The model is capable of quantifying two transit times, the MTT and the CTT.

The MTT represents the average time taken for labeled water to traverse the entire volume, V (i.e. the time from when spins are labeled at the labeling plane to when they flow out of the imaging plane), and is calculated from the first moment of the residue function, *r(V,t)* described by equation 2.23. A novel perfusion parameter, the CTT, is defined in equation 2.27. The CTT is shown in equation 2.30 to result from the calculation of the second moment of *r(V,t)*. It has been previously hypothesized that the second moment of tracer concentration-time curve can be used to describe the time taken for a bolus of tracer to be distributed at a ROI [187, 188]. The second moment of concentration-time curves has been used as a quantitative measure of the heterogeneity of the flow pattern of contrast agents within the capillary bed [189]. Also, in pharmacokinetics, the distribution of residence times of boluses of pharmaceutical agents can be assessed by the second moment of concentration-time data [190]. In the case of btASL, the second moment (or CTT) can be used as a quantitative measure of the random processes that result in dispersion of the labeled bolus.

The non-compartmental model considers average parameter values over

the entire volume from the labeling plane to the imaging plane (figure 2.1). The averaging of the parameters becomes apparent in the derivation of the Fokker-Planck equation, equation 2.20. The Langevin equation, equation 2.7, chosen as the starting point for the derivation considers the effects of the system on a single particle. Following the averaging process (section 2.2.4), we arrive at the general Fokker-Planck equation, equation 2.20 for the noise-averaged distribution of labeled spins. With this non-compartmental approach, a complete assessment of the exact mechanisms by which labeled spins are dispersed in the system is not necessary. Instead, the brain is treated as a 'black box' for which an average flow, volume and perfusion coefficient is assumed. As a result, it is not necessary to measure locally defined parameters such as the permeability-surface area product on which compartmental models depend [88, 93]. In addition, it is not necessary to measure the AIF locally as is required when the model-free ASL approach for perfusion quantification is used [96]. The Fokker-Planck equation, equation 2.20, is also one-dimensional in nature and therefore it provides a mathematically simpler solution than would be obtained using an adapted Bloch-Torrey approach, which must be defined in three dimensions.

However, while an average flow rate, volume and perfusion coefficient are considered, it is well established that the T_1 relaxation time varies as a function of tissue and ROI and is also known to decrease following transfer from the capillaries to brain tissue. This change in T_1 has been incorporated into both single [84] and two-compartmental models [89, 92, 93]. The non-compartmental model in its present form only allows for a single, average T_1 value for a given ROI. This T_1 value needs to be measured and ROI-specific values are used when the model is applied to experimental data. In future developments of the theory, it may be possible to incorporate separate T_1 values for the vascular and extravascular compartments.

The theoretical model of cerebral perfusion introduced in this chapter, coupled with the experimental validation of the model (to be described in chapters 3 and 4), has been accepted for publication in the journal of *Physics in Medicine and Biology* [191].

2.8 Appendix: Solution to the Fokker-Planck Equation for the Bolus-Tracking Arterial Spin Labeling Boundary Conditions

Applying the Laplace transformation to the equation of motion, equation 2.20, with respect to t gives:

$$sC(s,V) = -F\frac{\partial C(s,V)}{\partial V} + P\frac{\partial^2 C(s,V)}{\partial V^2} - \frac{C(s,V)}{T_1}, \qquad \text{(A-1)}$$

where $C_0(s)$ is the Laplace transform of $c_0(t)$, $C(0,s)=C_0(s)$ and $C(\infty,s)=0$. The solution to equation A-1 has been found using a similar process to that used in section 2.6:

$$C(V,s) = C_0(s)\exp\left(\frac{FV}{2P} - \frac{V}{2P}\sqrt{F^2 + \frac{4P}{T_1} + 4Ps}\right). \qquad \text{(A-2)}$$

The inverse formula of the Laplace transformation can be written as:

$$c(V,s) = \exp\left(\frac{FV}{2P}\right)\int_{c-i\infty}^{c+i\infty} C_0(s)\exp\left(st - \frac{V}{2P}\sqrt{F^2 + \frac{4P}{T_1} + 4Ps}\right)ds. \qquad \text{(A-3)}$$

Using the substitution $s=s'-F^2/4P-1/T_1$, Eqn. A-3 simifies to:

$$c(V,s) = \exp\left(\frac{FV}{2P} - \frac{F^2}{4P} - \frac{1}{T_1}\right)\int_{c-i\infty}^{c+i\infty} C_0(s)\exp\left(s't - \frac{V\sqrt{s'}}{\sqrt{P}}\right)ds'. \qquad \text{(A-4)}$$

The integral in equation A-4 solves as follows [192]:

$$\int_{c-i\infty}^{c+i\infty} C_0(s)\exp\left(s't - \frac{V\sqrt{s'}}{\sqrt{P}}\right)ds' = \frac{V}{\sqrt{4\pi Pt^3}}\exp\left(-\frac{V^2}{4Pt}\right). \qquad \text{(A-5)}$$

combining equation A-4 and equation A-5 and using the convolution theorem leads to the following solution:

$$c(V,t) = \int_0^t c_0(\tau) \frac{\exp(-(t-\tau)/T_1)}{\sqrt{4\pi P(t-\tau)}} \frac{V}{(t-\tau)} \exp\left(-\frac{(V-F(t-\tau))^2}{4P(t-\tau)}\right) d\tau. \tag{A-6}$$

This solution to the boundary value problem, equation 2.24, allows the special case of a rectangular input function or bolus to be solved, thereby providing the btASL solution that will be used to quantify both the MTT and CTT.

Chapter 3

Materials and Methods

3.1 Magnetic Resonance Imaging Hardware

All imaging experiments were carried out on the 7 Tesla pre-clinical MRI system (Biospec 70/30 Ultra Shield Refrigerated (USR), Bruker Biospin, Ettlingen, Germany) at the Trinity College Institute of Neuroscience (depicted in figure 3.1). A bird-cage linear resonator, optimally tuned to 300.3 MHz, was used for transmission of the ASL inversion pulse and for the excitation pulse in the subsequent image acquisition protocol (section 3.4). The inner diameter and length of the linear resonator were 7.2 cm and 18.6 cm respectively. An actively decoupled, circularly polarized, 20 mm diameter surface coil, designed specifically for rat brain imaging, was used for signal detection. The scanner was equipped with three actively shielded gradient sets (Quasar Dual High Performance Gradient System); a small, medium and large set with maximum gradient strengths of 1000 mT/m, 400 mT/m and 200 mT/m respectively and internal radii of 3.5 cm, 7.2 cm and 15.2 cm respectively.

3.2 Animal Preparation

All experiments were carried out in accordance with the protocols approved by the Trinity College Dublin ethics committee and the Irish Department of Health and Children. Rats were loaded onto a perspex cradle that was custom-built for use with the MRI scanner. Two distinct setups were used:

Figure 3.1: Bruker Biospec 7T 70/30 USR scanner. Image courtesy of Bruker Biospin website.

(a) A setup for non-functional MRI experiments and (b) a setup for functional MRI experiments. Figure 3.2 illustrates the components necessary for both setups, with elements necessary specifically for fMRI experiments shown in red.

3.2.1 Animal Setup for Non-Functional Studies

Results from a validation study and ageing study are presented in chapter 4 and section 6.1 respectively. In both of these studies, rats were anesthetized using isoflurane gas administered via a facemask (1.5 - 2.0% in oxygen, at 1 L/min). A mechanical ventilator (Ugo Basile, Comerio, VA, Italy) was used to deliver adequate inflowing gas to the facemask. Temperature was monitored using a rectal thermometer and maintained using a warming surface controlled by a water pump-driven temperature regulator (SA Instruments Inc., Stony Brook, NY, USA). Respiration and electrocardiograph (ECG) signals were monitored throughout the experiments using custom hardware and software (SA Instruments Inc., Stony Brook, NY, USA).

Results from a MDMA (or "ecstasy") study are presented in section 6.2. In this study, rats were administered either MDMA (20 mg/kg) or 0.89% saline (control) by intraperitoneal injection before imaging. The rats were anesthetized with 0.1 - 0.2 ml of ketamine in combination with 0.1 - 0.2 ml

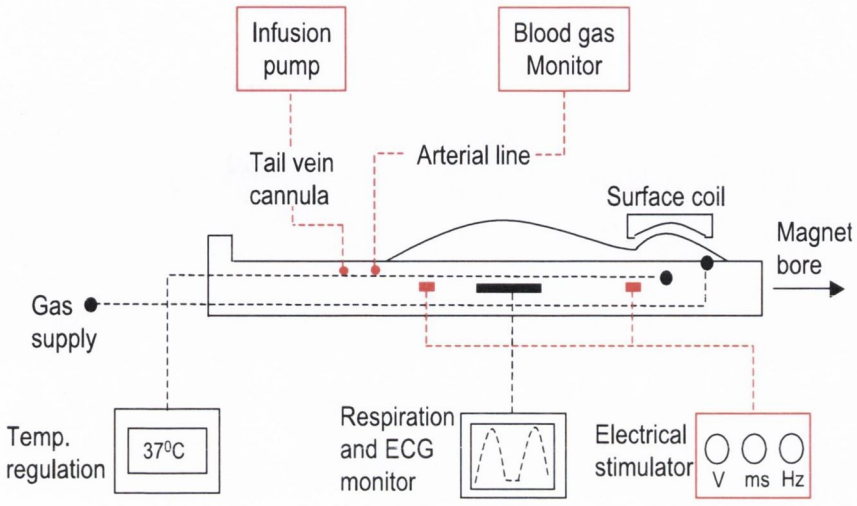

Figure 3.2: Experimental setup for small animal MRI experiments. Elements shown in red are specific to fMRI experiments that require electrical stimulation, close monitoring of pCO_2 and tail vein medetomidine or propofol infusion.

of xylazine. Temperature, ECG and respiration rates were monitored during scanning as described above for the validation and ageing studies.

3.2.2 Animal Setup for Functional Studies

Results from a fMRI study are presented in chapter 5. Each of the elements used for the non-fMRI animal setup (described above in section 3.2.1) were also used during fMRI experiments. However, a number of additional components were also necessary. Firstly, while the rats were initially anaesthetized using isoflurane gas via the facemask, isoflurane was discontinued after 15 - 30 minutes and the rats were switched to one of two anaesthetic agents suitable for fMRI experiments. The results presented in figures 5.1 and 5.2 were acquired in rats that were switched to sedation by continuous infusion of medetomidine (Domitor®, Pfizer) via a cannulated tail vein. A loading dose bolus of 0.035 mg/kg was followed by continuous infusion at 0.1 mg/kg/hr. The results presented in figures 5.5 and 5.6 were acquired in rats that were switched to anaesthesia by propofol (Rapinovert®, Schering-Plough), which was also administered via a cannulated tail vein. A loading bolus of 7.5 mg/kg was followed by continuous infusion at 45 mg/kg/hr.

A square pulse nerve and muscle stimulator (Grass Technologies Inc.,

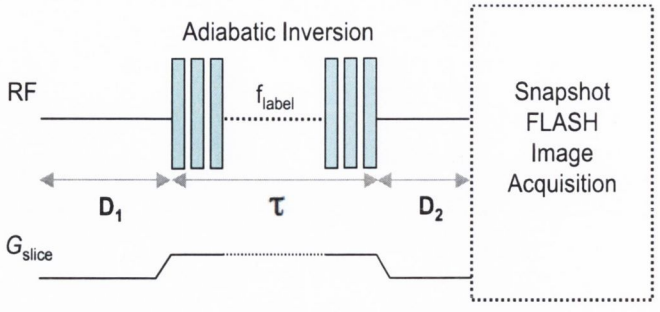

Figure 3.3: Bolus-tracking ASL sequence: Preparation interval containing inversion pulse of duration τ and variable delays D_1 and D_2, followed by Snapshot FLASH acquisition. The inversion pulse was approximated by a series of shorter pulses with durations determined by a user-defined duty cycle.

West Warwick, RI, USA) was used to electrically stimulate the forepaw. The stimulator pulse settings were 3 V, 5 Hz and 5 ms for the medetomidine sedated rats and 10 V, 5Hz and 5 ms for the propofol anaesthetised rats. Stainless steel electrodes were placed between the second and fifth digit of the forepaw. Stimulation resulted in neuronal activation in the S1FL region, at approximately +0.2 mm Bregma, as illustrated in figure 3.4. Stimulation was maintained throughout the labeling phase of the ASL measurements described below in section 3.4. A rest period of 5 minutes followed each stimulation experiment.

Temperature, ECG and respiration rates were monitored as described above for the non-fMRI setup (section 3.2.1). Electrical stimulation of the forepaw resulted in measurable neuronal activation when the respiration rate was in the range of 60 - 80 breaths per minute. The partial pressure of carbon dioxide (pCO_2) was measured at regular intervals during scanning of the propofol anaesthetised animals by taking arterial blood samples of 200 μL from a cannulated artery. The mean $\pm$ standard deviation pCO_2 for the 60 - 80 breaths per minute respiration rate range was 49 $\pm$ 6.7 mmHg. This method of pCO_2 monitoring was not possible in the medetomidine sedated animals due to the vasopressor effects of medetomidine. In these animals, the pCO_2 was measured using a transcutaneous blood gas analyzer (TCM4, Radiometer Copenhagen, Willich, Germany) prior to commencing scanning. Once the pCO_2 and respiration rates were in the suitable range (see above), the rats were transferred to the MRI scanner.

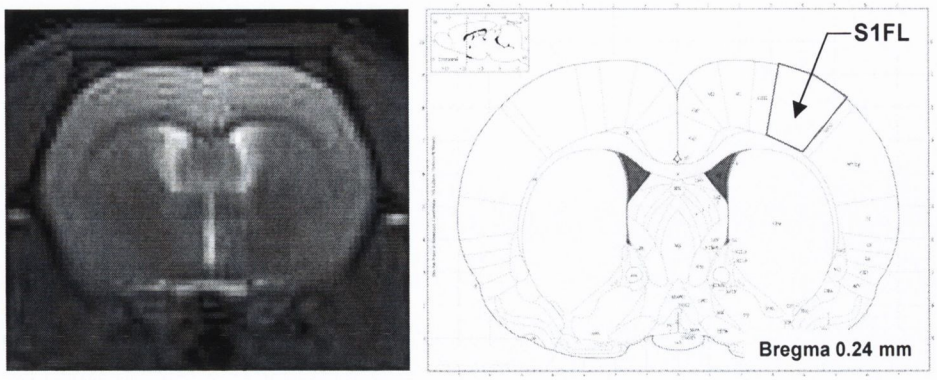

Figure 3.4: High resolution RARE image and corresponding slice from the Rat Brain Atlas [193]. ASL data was acquired following matching of the high resolution image with the Rat Brain Atlas slice containing maximal S1FL coverage.

3.3 Imaging Slice Location

The imaging slice for the ASL and T_1 measurements was chosen by comparing high resolution rapid acquisition with relaxation enhancement (RARE) images [194] with the desired slice in the rat brain atlas [193] (the RARE sequence is described in detail below in sections 3.5 and 3.6.1). For the validation and aging study measurements (chapter 4 and section 6.1 respectively) the imaging slice with optimal hippocampal and cortical coverage was located (-4.0 mm bregma). A slice containing both cortex and striatum (-0.5 mm bregma) was located for the MDMA measurements presented in section 6.2). The slice with optimal somatosensory cortex coverage was located for all fMRI measurements (+0.2 mm bregma) in chapter 5. Figure 3.4 shows a sample RARE image and the corresponding slice in the rat brain atlas for the fMRI experiment.

3.4 Bolus-Tracking Arterial Spin Labeling

A btASL sequence was developed using the Bruker Biospin pulse programming environment (Bruker Biospin, Ettlingen, Germany) to provide perfusion weighted concentration-time curves that allow cerebral perfusion to be quantified by the non-compartmental model for cerebral perfusion described in chapter 2. The sequence consists of a CASL preparation interval followed by a snapshot FLASH image acquisition protocol.

Table 3.1: Variation of D_1, D_2 and τ for a 1.5 s, 2.0 s and 3.0 s bolus.

	1.5 s bolus			2.0 s bolus			3.0 s bolus		
Time-point	D_1	τ	D_2	D_1	τ	D_2	D_1	τ	D_2
1	4.9	0.1	0.0	4.9	0.1	0.0	4.9	0.1	0.0
2	4.5	0.5	0.0	4.5	0.5	0.0	4.5	0.5	0.0
3	4.0	1.0	0.0	4.0	1.0	0.0	4.0	1.0	0.0
4	3.5	1.5	0.0	3.5	1.5	0.0	3.5	1.5	0.0
5	3.0	1.5	0.5	3.0	2.0	0.0	3.0	2.0	0.0
6	2.5	1.5	1.0	2.5	2.0	0.5	2.5	2.5	0.0
7	2.0	1.5	1.5	2.0	2.0	1.0	2.0	3.0	0.0
8	1.5	1.5	2.0	1.5	2.0	1.5	1.5	3.0	0.5
9	1.0	1.5	2.5	1.0	2.0	2.0	1.0	3.0	1.0
10	0.5	1.5	3.0	0.5	2.0	2.5	0.5	3.0	1.5
11	0.0	1.5	3.5	0.0	2.0	3.0	0.0	3.0	2.0

3.4.1 Arterial Spin Labeling Preparation

The 5 s ASL preparation interval contained an adiabatic inversion RF pulse (section 1.3.1) and two variable time delays, D_1 and D_2, as depicted in figure 3.3. The delays D_1 and D_2 and the inversion pulse duration, τ were varied as shown in table 3.1 for bolus durations of 1.5 s, 2.0 s and 3.0 s. The duration of the bolus of labeled inflowing spins is defined by the duration of the inversion pulse, τ. On inspection of table 3.1 it can be seen that τ is less than the ultimate bolus length for the initial time points. This allows the full concentration-time curve to be measured at the ROI in the imaging plane.

For each of the time points in table 3.1, it was necessary to acquire a labeled and control image in order to create perfusion-weighted difference images. Sample labeled, control and perfusion-weighted images are shown in figure 3.5. During acquisition of the labeled image, the principle of flow-driven adiabatic inversion [30] was used to supply inverted inflowing spins to the imaging location. A rectangular pulse with a maximum B_1 amplitude of 120 mG and duration τ was approximated by a ten shorter pulses with durations defined by a duty cycle of 80 % (as illustrated in figure 3.3) in order to reduce demands on the RF amplifier. The RF power of the inversion

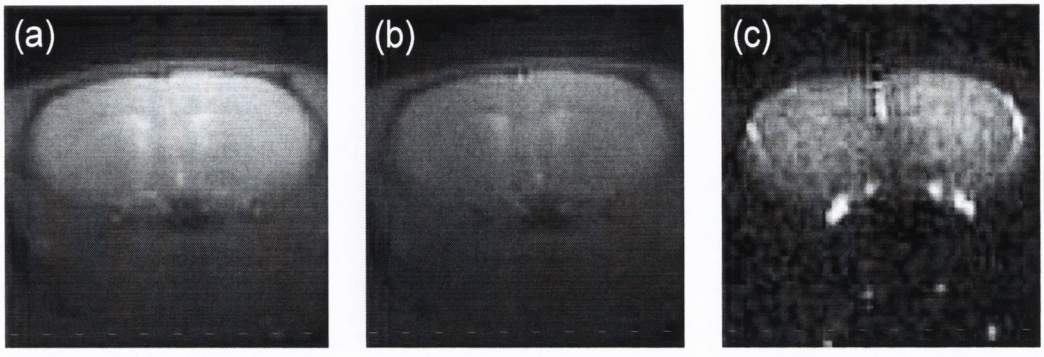

Figure 3.5: Sample ASL images acquired using btASL protocol. (a) Control image (b) Labeled image (c) Difference image.

pulse was set to achieve inversion at the desired location. The pulse had a bandwidth of 2.8 kHz and the gradient strength was set to 14 mT/m to provide an inversion slab thickness of 4.7 mm. The pulse frequency was offset by -12 kHz , resulting in a tagging location 2cm proximal to the imaging slice. A control image with the offset reversed (+12 kHz) was also acquired, in which the inflowing spins were left undisturbed. The labeling and control phases were separated by a 10 s delay to allow the magnetization to return to equilibrium. Corresponding pairs of labeled and control images for each time point in table 3.1 were subtracted to provide time-series perfusion-weighted images, as shown in figures 4.1, 4.2 and 4.3 for bolus lengths of 1.5 s, 2.0 s and 3.0 s respectively.

3.4.2 Fast Low Angle Shot Image Acquisition

The FLASH gradient echo sequence was used to acquire the labeled and control images at the imaging plane. This sequence is based on the principle that small flip angles can be used to provide adequate signal magnitudes that allow the entire k-space evolution to be swept in a short period of time [195]. The contrast provided by FLASH is sensitive to changes in signal amplitude when both the echo time (TE) and repetition time (TR) are short. This property makes the FLASH sequence suitable for the acquisition of perfusion-weighted ASL images.

A diagram of the FLASH sequence and a description of the sequence elements involved is given in figure 3.6. Images were acquired with centric phase encoding, starting at zero phase gradient, maximize the signal

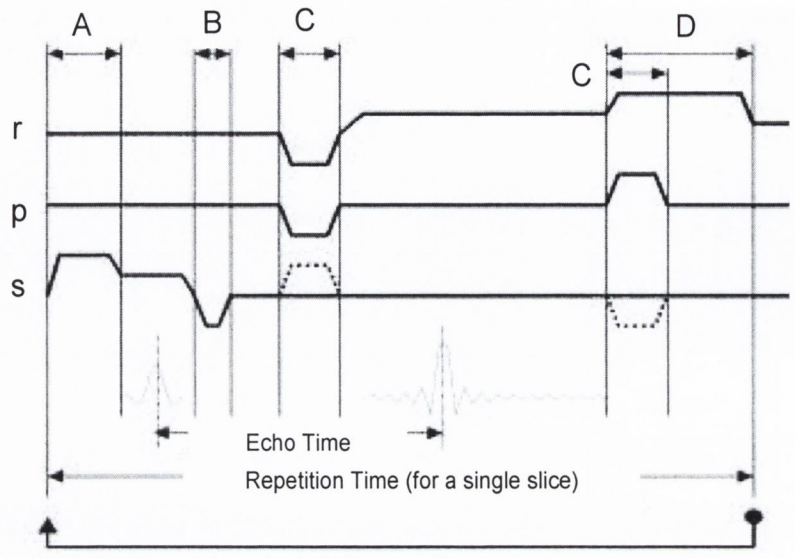

Figure 3.6: Single slice FLASH sequence. Elements: A = slice spoiler gradient, B = slice rephase gradient, C = read dephase and rephase gradients, D = read spoiler gradient. The approximate locations of the RF excitation pulse and the echo are also shown [197].

provided by inflowing labeled spins [196]. The following parameters were used: slice thickness = 2cm, TR = 8.56 ms, TE = 3.04 MS, flip angle = 30^0, field of view = 3.0 $\times$ 3.0 cm, image matrix = 128 $\times$ 64, receiver bandwidth = 50 kHz. The total measurement time for one signal average of the 11 time-points in table 3.1 was 1 minute and 50 seconds. Signal averaging was provided by repeating the measurement NA (number of averages) times (NA=8 for the validation and MDMA studies in chapters 4 and section 6.2 respectively, NA=6 for the fMRI study in chapter 5 and NA=1 for the ageing study in section 6.1).

3.5 T1 Measurement

The rapid acquisition with relaxation enhancement (RARE) sequence [194] with variable repetition time (VTR) was used to generate T_1 maps at the same imaging location as the ASL images for the validation, fMRI, ageing and MDMA studies. The following sequence parameters were used: slice thickness = 2 cm, VTR = 0.3 s, 0.59 s, 0.94 s, 1.40 s, 2.03 s, 3.10 s and 8.00 s, TE = 25.27 ms, field of view = 3.0 $\times$ 3.0, image matrix = 128 $\times$ 64. Multiple

acquisitions with varying TR were acquired to generate saturation recovery series and a standard T_1 saturation fit function (Paravision 4.0, Bruker Biospin, Ettlingen, Germany) was fitted to the saturation recovery series to generate the T_1 maps.

Average ROI-specific T_1 values were calculated for the subsequent curve-fitting procedure (section 3.6.2). For the validation study (chapter 4), the ROI-specific T_1 values were obtained from a subsequent relaxometry study in nine rats of the same type (male Wistar), weight range (350 - 450 g) and age range (4 - 5 monts) as those used in the validation experiments. Average T_1 values of 1.70 s, 1.73 s and 1.63 s were obtained for the cerebral cortex, hippocampus and whole brain ROIs shown in figure 3.7. These values were also applied to the ageing study (section 6.1), as the same ROIs were selected in this study (the implications of the use of these T_1 values for in ageing study are discussed in section 6.1.3). An average T_1 value of 1.74 s was measured for the primary somatosensory cortex forelimb (S1FL) region in the fMRI study (chapter 4). For the MDMA study (section 6.2), average T_1 values of 1.73 s and 1.68 s were measured for the cortical and striatal ROIs respectively.

3.6 Data Analysis

3.6.1 Regions of Interest and Concentration-Time Curves

For the validation, aging and MDMA studies (sections 4.2, 6.1.2 and 6.2.2 respectively), a high resolution image was acquired at the ASL imaging slice using the RARE sequence described in section 3.5, without varying the TR. The following parameters were used for the RARE acquisition: slice thickness = 2 mm, TE =12 ms, TR = 3.134 s, FOV = 3.0 x 3.0 cm, image matrix = 256 x 256. The ImageJ ROI tool (Rasband W.S., Bethesda, MD, USA) was used to select ROIs on the resultant image (figure 3.7). The ROIs were then transferred to ASL time-series datasets acquired by the btASL sequence (section 3.4) and the mean signal intensity within a given ROI for each of the time-points in table 3.1 was calculated and used to form the concentration-time curve for that ROI. Sample concentration-time curves generated in this manner for a whole brain ROI and three bolus durations are shown in fig-

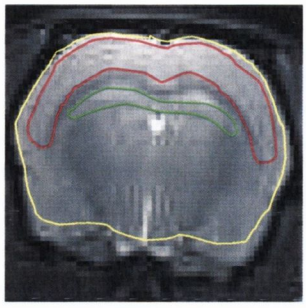

Figure 3.7: High resolution RARE image used for ROI selection. Selected cerebral cortex, hippocampus and whole brain ROIs are applied to ASL images to generate ROI specific concentration-time curves.

ure 3.8.

For the fMRI sudy, ROI selection was carried out directly on the ASL perfusion maps (figures 5.1 and 5.2), as the activated S1FL can be clearly identified on these images. The mean signal intensity within the activated regions during neuronal activation and in the resting state was used to form the concentration-time curves (figures 5.2 and 5.6).

3.6.2 Curve Fitting

Final Fitting Equation

The btASL solution, equation 2.26) to the Fokker-Planck equation (equation 2.20) of the non-compartmental model of cerebral perfusion was re-written as follows to facilitate the curve-fitting procedure:

$$c(V,t) = \frac{c_0}{2}\exp\left(\frac{FV}{2P}\right) \times \left[\operatorname{erfc}\left(\frac{V}{\sqrt{4Pt}} - \sqrt{\left(\frac{F^2}{4P} + \frac{1}{T_1}\right)t}\right) \times \exp\left(-\frac{V}{\sqrt{P}}\sqrt{\frac{F^2}{4P} + \frac{1}{T_1}}\right)\right]_{t=t-\tau}^{t=t}, \quad (3.1)$$

where erfc is the complementary error function and τ is the bolus duration. Equation 3.1 was parameterized in terms of three fitting parameters, A_0, A_1 and A_2 defined as follows:

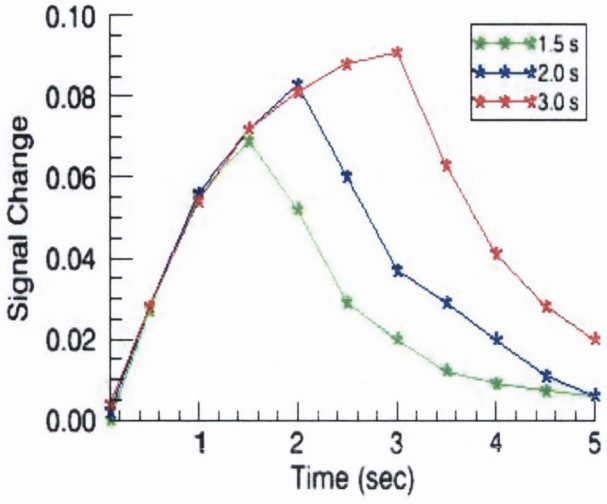

Figure 3.8: Concentration-time curves for a whole brain ROI and 1.5 s, 2.0 s and 3.0 s bolus lengths.

$$A_0 = \frac{c_0}{2}, \qquad A_1 = \frac{FV}{2P}, \qquad A_2 = \frac{F^2}{4P}. \tag{3.2}$$

In terms of these parameters, equation 3.3 becomes:

$$c(V,t) = A_0 \exp(A_1) \times \left[\operatorname{erfc}\left(\frac{1}{2\sqrt{t}} \sqrt{\frac{A_1^2}{A_2}} - \sqrt{(A_2 + R_1)\, t} \right) \times \exp\left(-\sqrt{\frac{A_1^2}{A_2}} \sqrt{A_2 + R_1} \right) \right]_{t=t-\tau}^{t=t}, \tag{3.3}$$

where R_1 is the longitudinal relaxation rate. From the description of the time-points used to generate the concentration-time curves given in table 3.1, it can be seen that for the initial time points, τ is less than the ultimate bolus length. Consequently, for $0 \leq t \leq \tau$, *c(V,t)*, equation 3.3 becomes imaginary due to the presence of t in the square root terms within the error function. As a result, for the subsequent curve fitting procedure, equation 3.3 must be defined in a piecewise continuous manner, where *c(V,t)* is evaluated from $t = 0$ to t for values of t less than τ, and then from $t = t\text{-}\tau$ to t for values of t greater than τ.

Levenberg-Marquardt Curve Fitting Routine

The FindFit curve fitting program provided by Mathematica (Wolfram Research Inc., Version 5.1, Champaign, IL, USA) was used to fit equation 3.3 to the ASL concentration-time curves (section 3.6.1). This program employs the iterative Levenberg-Marquardt method [198, 199] to minimize the sum of the squares of the residuals (or chi-squared, χ^2) between the model and the data. The Levenberg-Marquardt method is commonly applied to the problem of finding the mimimum of a function *F(x)* that is a sum of squares of nonlinear functions [200]:

$$F(x) = \frac{1}{2}\sum_{i=1}^{m}[f_i(x)]^2. \tag{3.4}$$

The minimum of *F(x)* is found by calculating the Jacobian matrix of $f_i(x)$ and searching along the direction of steepest descent. However, unlike the steepest descent and Gauss-Newton methods, the Levenberg-Marquardt method varies the step size of the search as it approaches the minimum and is therefore considered more robust at guarding against returning local rather than global minima, once a good initial estimate of the fitting parameters is provided [201].

Initial Estimates of Fitting Parameters

The parameter A_0 is close to the maximum signal amplitude of the ASL concentration-time curves ($A_0 \sim c_0/2$) and consequently, the amplitude of the experimental concentration-time curves was taken as the initial estimate for this parameter. In order to estimate remaining parameters, A_1 and A_2, a curve description of an experimental concentration-time curve for a 3 s bolus (figure 3.8) was carried out. The error function term in equation 3.3 is equal to zero at the point at half the maximum amplitude [200]. Therefore we can find the following equation for A_1 and A_2 by setting the error function term in equation 3.3 equal to zero:

$$\sqrt{\frac{A_1^2}{4A_2(A_2 + R_1)}} = t, \tag{3.5}$$

where *t* can be measured directly from the curve as the time corresponding

to the half maximum point and R_1 is measured as described in section 3.5. Equation 3.5 has two unknowns, A_1 and A_2, and consequently a second equation is required to solve for A_1 and A_2. The second equation for A_1 and A_2 was obtained by calculating the first derivative of equation 3.3 in Mathematica (Wolfram Research Inc., Version 5.1, Champaign, IL, USA) at the same time point as equation 3.5. The following equation for the slope at this point was obtained:

$$\sqrt{\frac{A_1^2}{A_2}} + 2\sqrt{A_2 + R_1} = \text{slope} \tag{3.6}$$

where the slope can be estimated directly from the curve. Equations 3.5 and 3.6 form a set of two simultaneous equations with two unknowns, A_1 and A_2. When these equations were solved, the values obtained for A_1 and A_2 were 0.64 and 0.18 respectively. Taking the definition of the MTT and CTT in terms of these parameters into account (equation 3.7 below), these values correspond to an MTT of 1.8 s and a CTT of 1.4 s. It can be seen from figure 3.8 that the concentration-time curves for the three bolus lengths follow the same course for the portion of the curve used to find the initial estimate. As a result, the initial estimates were assumed to be the same for all bolus lengths.

Robustness of Curve Fitting Routine

The MTT depends on both A_1 and A_2 (equation 3.7). The initial estimates for the fitting parameters A_1 and A_2 were systematically varied in order to investigate the robustness of the curve fitting routine to variations in the initial estimates. Figure 3.9 shows the variations in the fitted MTT value when the initial estimate for MTT is varied. The fit was performed on a typical 3 s bolus dataset and the initial estimate calculated for the MTT was 1.8 s. It can be seen from this graph that the fitting routine locates approximately the same fitted value of the MTT, MTT_{fit}, when the initial estimate is varied about this initial estimate (mean $\text{MTT}_{fit} \pm$ standard deviation = 1.87 ± 0.05). This suggests that the fit provided by these initial estimates is a global rather than a local minimum. The CTT depends only on A_2 (equation 3.7). The fitted CTT value, CTT_{fit}, demonstrates similar robustness to variations its initial estimate of 1.4 s (mean $\text{CTT}_{fit} \pm$ standard deviation = 1.54 ± 0.08).

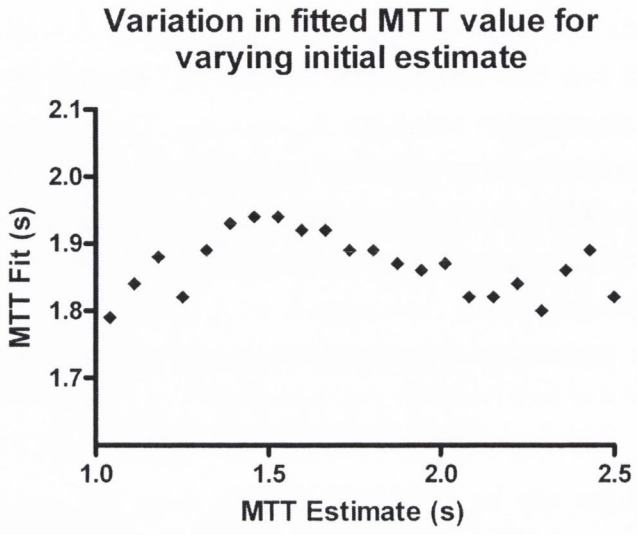

Figure 3.9: Variation in the MTT value calculated by the least squares fit when the initial estimate of the MTT was systematically varied.

3.6.3 Quantification of Perfusion Parameters from Curve Fitting Parameters

From the definition of the MTT and CTT in equation 2.27, it can be seen that these transit times can be calculated directly from the fitting parameters A_1 and A_2 as follows:

$$MTT = \frac{A_1}{2(A_2)} = \frac{V}{F} \quad \text{and} \quad CTT = \frac{1}{4(A_2)} = \frac{P}{F^2}. \tag{3.7}$$

The fitting parameter, A_0, can be used to estimate the relative volume of labeled water at a ROI. The zeroth moment of the tissue response function defined in equation 2.23 is equal to 1:

$$\int_0^\infty r(V,t)dt = 1. \tag{3.8}$$

Therefore, the zeroth moment of the solution for *c(V,t)* given in equation 2.26 is equal to C_0, when T_1 relaxation is neglected. This zeroth moment is a measure of the area under the curve defined by *c(V,t)*, which is assumed in this case to be proportional to the volume of labeled water contributing to *c(V,t)* at the imaging voxel. The fitting parameter A_0 is the value for C_0 estimated by the curve fitting routine. This leads to the following expression:

$$A_0 \sim V_{voxel} \tag{3.9}$$

where V_{voxel} is the volume of labeled water at the imaging voxel. Therefore, A_0 is a measure for the relative volume of labeled water at the imaging voxel (in arbitrary units). As stated earlier in section 2.4, although labeled water is delivered to the capillary bed via inflowing blood, water is not restricted to the blood. At the measurement time a proportion of the labeled water will have been exchanged across the capillary walls [180]. As a result, the parameter A_0 is not a measure of relative cerebral blood volume (rCBV) and will be referred to herein as the relative volume of labeled water (rVLW) at the ROI. Furthermore, it is also possible that for long measurement times and under certain physiological conditions, the total volume of water at the imaging voxel, V_{voxel}, will in fact be equal to the volume of the voxel (this is most likely at low flow rates when the extraction fraction of water is close to 1 and almost all labeled water delivered to the imaging voxel undergoes exchange [180, 184]). When the relationship in equation 3.9 is considered, this limits the usefulness of the rVLW parameter under such conditions.

The signal amplitude obtained at the ROI depends also on the degree of inversion, α_0 (equation 1.15), achieved by the labeling phase of the ASL experiment. As a result, a true representation of rVLW is only obtained when the parameter A_0 is normalized for the degree of inversion. The degree of inversion, α_0, was estimated from the signal magnitude obtained in the left and right middle cerebral arteries (LMCA and RMCA) during the label and control phase of the btASL sequence (location of the MCAs is shown in figure 3.10) as follows:

$$\alpha_0 = \left(\frac{1}{2}\right)\left(\frac{LMCA^l_{max}}{LMCA^c_{max}} + \frac{RMCA^l_{max}}{RMCA^c_{max}}\right), \tag{3.10}$$

where the superscripts l and c refer to the labeled and control images respectively. The final measure of rVLW is then given by:

$$rVLW = \frac{A_0}{\alpha_0}. \tag{3.11}$$

Results for the rVLW calculated using this approach are given below in sections 5.2, 6.1.2 and 6.2.2. Once the MTT, CTT and rVLW have been quan-

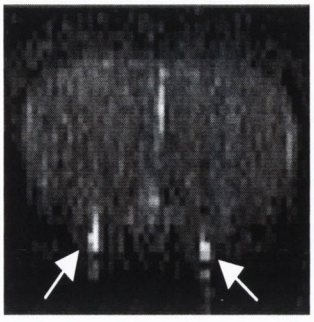

Figure 3.10: ASL perfusion weighted image showing location of middle cerebral arteries (white arrows) used for estimation of the degree of inversion

tified from the curve fitting parameters, the relative change in the average flow rate of labeled water, rFLW, and the perfusion coefficient of labeled water, rPLW, between two groups or two experimental conditions can be calculated from the definitions of the transit times. For example, if MTT, CTT and rVLW are measured in subjects undergoing neuronal activation and then subsequently in the same subjects at rest (as in section 5.2), the change in rFLW can be estimated from the definition of the MTT in section 2.4 as follows:

$$\frac{rFLW_{act}}{rFLW_{ctrl}} = \frac{MTT_{ctrl}}{MTT_{act}} \cdot \frac{rVLW_{act}}{rVLW_{ctrl}}, \tag{3.12}$$

where the subscript *act* refers to the subjects while undergoing neuronal activation and the subscript *ctrl* refers to the same subjects in the resting state. An increase in rFLW during neuronal activation for example (i.e. rFLW_{act} / $\text{rFLW}_{ctrl} > 1$) would correspond to an increase in the average rate at which labeled water is transported through the system (i.e. from the labeling plane to the imaging voxel). Again, as water is not restricted to the vasculature, the rFLW parameter has contributions from both the vascular and extravascular compartments.

Following calculation of the change in rFLW by equation 3.12, the change in the regional perfusion coefficient of labeled water, rPLW, can be calculated from the definition of the CTT in section 2.4 as follows:

$$\frac{rPLW_{act}}{rPLW_{ctrl}} = \frac{CTT_{act}}{CTT_{ctrl}} \cdot \left(\frac{rFLW_{act}}{rFLW_{ctrl}}\right)^2. \tag{3.13}$$

The perfusion coefficient, P, was defined in section 2.7 as representing the

magnitude of the random effects (such as pseudo diffusion within the microvasculature and the exchange of water across the capillary walls) that result in the dispersion of a rectangular bolus of labeled water. As a result, an increase in rPLW during neuronal activation for example (i.e. rPLW_{act} / $\text{rPLW}_{ctrl} > 1$) would correspond to an increase in some or all of these random effects.

Equations 3.12 and 3.13 are given here in the context of the neuronal activation study (chapter 5). The same approach to calculating the change in rFLW and rPLW was used in the validation study for comparing results for varying bolus length (section 4.2.3), in the ageing study when comparing young, middle aged and aged groups (section 6.1.2) and in the MDMA study when comparing the effects of MDMA at varying times post administration (section 6.2.2).

3.6.4 Calculation of Error in Perfusion parameters

The results for MTT, CTT, rVLW, rFLW and rPLW in the results sections of chapters 4, 5 and 6 are quoted in terms of the value calculated from the curve fitting parameters $\pm$ the error in these values. The error was calculated in each case from the standard error (SE) of the fit of equation 3.3 to the experimental data. The SE was calculated from the sum of squared residuals (SSR) and the number of degrees of freedom (DOF) as follows [201]:

$$SE = \sqrt{\frac{SSR}{DOF}} = \sqrt{\frac{\sum_{i=1}^{n}(y_i - \hat{y}_i)^2}{DOF}}, \tag{3.14}$$

where y is the experimental value for each of the eleven points on the curve and $\hat{y}$ is the corresponding value predicted by the curve fitting routine. The number of DOF was equal to 8 (the number of points on the curve, 11, minus the number of fitting parameters, 3). The error in the individual fitting parameters was calculated as the 95% confidence interval of these parameters (1.96$\times$SE). For example, from equation 3.7 it can be seen that the individual error in the parameters A_1 and A_2 contribute to the error in the MTT as follows:

$$\frac{\Delta MTT}{MTT} = \sqrt{\left(\frac{1.96(SE)}{A_1}\right)^2 + \left(\frac{1.96(SE)}{A_2}\right)^2}. \tag{3.15}$$

The error in the CTT and rVLW, which depend on the error in the parameters A_2 and A_0 respectively, were calculated in a similar manner. The error in the rFLW and rPLW were then calculated by applying the principles of Gaussian error propagation.

Chapter 4

Experimental Validation of Non-Compartmental Model of Cerebral Perfusion

4.1 Introduction

The btASL protocol described in section 3.4 was used to acquire time-series perfusion-weighted images from three male Wistar rats (350 - 450 g body weight, 4 - 4.5 months of age). The animals were scanned according to the setup for non-functional studies, described in section 3.2.1. The bolus-tracking solution to the non-compartmental model, equation 3.3, in the form given in equation 3.1, was fitted to experimental data obtained using the methods described in chapter 3. The MTT, CTT and rVLW were quantified from the resultant fitting parameters, as decribed in section 3.6.3. The effect of varying the ROI, bolus length and animal on the these values was investigated by selecting three ROIs (cerebral cortex, hippocampus and whole brain) and three bolus lengths (1.5 s, 2.0 s and 3.0 s) for each animal. The variation in rFLW and rPLW for varying bolus length was also assessed, as described in section 3.6.3.

The experiment in which the variations in the perfusion parameters (MTT, CTT, rVLW, rFLW and rPLW) were assessed for varying bolus length was a used to test the ability of the btASL technique to provide a consistent assessment of cerebral perfusion for constant physiological conditions but varying experimental conditions. Variation of the bolus length has no effect on the

perfusion dynamics of the anaesthetized animals. However, the time-series data obtained using the btASL sequence (figures 4.1, 4.2 and 4.3) as well as the solution used in the curve fitting (equation 3.3) are altered when the bolus duration, τ, is varied. Should the perfusion parameters be found not to vary significantly for varying bolus length, this experiment will demonstrate the ability of the btASL technique to consistently quantify cerebral perfusion when the experimental conditions are varied.

The ROI-specific T_1 values used in the curve fitting were obtained from a subsequent relaxometry study in nine rats of the same type (male Wistar), weight range (350 - 450 g) and age range (4 - 4.5 months) as those used in the btASL validation study. The imaging location was matched to the location used in the btASL measurements and average T_1 values for the cerebral cortex, hippocampus and whole brain ROIs were obtained using the method described in section 3.5.

The aims of this study were: to provide experimental validation for the non-compartmental model of cerebral perfusion, to assess the advantages and shortcomings of the btASL approach in the context of existing techniques and to compare, where possible the results obtained with previously quoted values in the literature.

4.2 Results

4.2.1 Bolus-Tracking Arterial Spin Labeling Datasets

The time-series perfusion-weighted images for animal 1, for bolus-lengths of 1.5 s, 2.0 s and 3.0 s can are shown in figures 4.1, 4.2 and 4.3 respectively. On inspection of these images, the variation in the image number in which the maximum perfusion weighted is obtained for these three bolus lengths can be observed. The maximum perfusion-weighted signal is achieved in figure 4.1 (d) for the 1.5 s bolus, figure 4.2 (e) for the 2.0 s bolus and figure 4.3 (g) for the 3.0 s bolus. These images correspond to time-points 4, 5 and 7 (in table 3.1) for the 1.5 s, 2.0 s and 3.0 s bolus lengths. The corresponding shift in the time at which the concentration time-curves from these image sets reaches a maximum is illustrated in figure 3.8 (for a whole-brain ROI).

4.2.2 Transit Time Results

The least squares fit of equation 3.1 to the concentration-time curves from each of the three animals for three bolus lengths (1.5 s, 2.0 s and 3.0 s) and three ROIs (cerebral cortex, hippocampus and whole-brain) are shown in figures 4.4, 4.5 and 4.6.

The values obtained for the MTT and the CTT for each animal, for each ROI and bolus length are shown in table A.1. The ROI-specific T_1 values calculated using the method described in section 3.5 were 1.7 s, 1.74 s and 1.63 s for the cerebral cortex, hippocampus and whole brain ROIs respectively. The errors in the individual transit times were calculated from the standard error of the curve fitting parameters by applying Guassian error propagation. The average MTT and CTT were 1.83 $\pm$ 0.06 s (mean $\pm$ one standard deviation) and 1.54 $\pm$ 0.08 s respectively for animal 1; 1.76 $\pm$ 0.04 s and 1.43 $\pm$ 0.04 s respectively for animal 2; and 1.68 $\pm$ 0.04 s and 1.32 $\pm$ 0.04 s respectively for animal 3.

The variations in MTT and CTT for varying animal, ROI and bolus length are shown in figure 4.7(a), (b) and (c) respectively. Significant differences in both transit times were found between animal 1 and animal 3 and between animal 2 and animal 3, as shown in figure 4.7(a) (one-way ANOVA with the Bonferroni post hoc test for multiple comparison and the level of significance set to $p \leq 0.05$). A ROI-dependent statistically significant difference was also found for the MTT of the hippocampus compared to the whole brain, as shown in figure 4.7(b). No statistically significant differences in MTT or CTT were found for varying bolus length, as shown in figure 4.7(c).

4.2.3 rVLW, rFLW and rPLW Results

The values obtained for the rVLW for each animal, for each ROI and bolus length are shown in table A.2. The errors in the individual rVLW values were calculated from the standard error of the curve fitting parameters by applying Gaussian error propagation. The average rVLW was 0.13 $\pm$ 0.01 (mean $\pm$ one standard deviation) for animal 1, 0.11 $\pm$ 0.01 for animal 2 and 0.11 $\pm$ 0.01 for animal 3. The variations in the rVLW of each animal for varying ROI and bolus length are shown in figures 4.8 (a) and (b). A ROI-dependent statistically significant difference was found for the rVLW of the

hippocampus compared to the whole brain in animal 3, as shown in figure 4.8(a). No statistically significant differences in rVLW were found for varying bolus length, as shown in figure 4.8(b).

Tables 4.1, 4.2 and 4.3 show the factor by which the rFLW and regional perfusion coefficient, rPLW, change in each ROI when the comparing the average results for the three bolus lengths. Table 4.1 compares the 2.0 s bolus results with the 1.5 s bolus results, table 4.2 compares the 3.0 s bolus results with the 1.5 s results and table 4.3 compares the 3.0 s bolus results with the 2.0 s bolus results. No significant variation in rFLW and rPLW was found for varying bolus length, with a value of 1 (signifying no change in rFLW and rPLW) being within the error in all cases.

Table 4.1: Calculation of the average variation in rFLW and rPLW in the cerebral cortex, hippocampus and whole brain ROIs due to varying bolus length (2.0 s bolus compared to 1.5 s bolus).

ROI	$\frac{MTT_{1.5}}{MTT_{2.0}}$	$\frac{CTT_{2.0}}{CTT_{1.5}}$	$\frac{rVLW_{2.0}}{rVLW_{1.5}}$	$\frac{rFLW_{2.0}}{rFLW_{1.5}}$	$\frac{rPLW_{2.0}}{rPLW_{1.5}}$
Cerebral Cortex	0.99 ± 0.05	0.99 ± 0.11	1.01 ± 0.21	1.01 ± 0.24	1.01 ± 0.26
Hippocampus	0.98 ± 0.05	1.01 ± 0.09	1.02 ± 0.19	1.01 ± 0.19	1.03 ± 0.21
Whole Brain	0.98 ± 0.06	1.01 ± 0.13	0.99 ± 0.14	0.97 ± 0.15	0.95 ± 0.21

Table 4.2: Calculation of the average variation in rFLW and rPLW in the cerebral cortex, hippocampus and whole brain ROIs due to varying bolus length (3.0 s bolus compared to 1.5 s bolus).

ROI	$\frac{MTT_{1.5}}{MTT_{3.0}}$	$\frac{CTT_{3.0}}{CTT_{1.5}}$	$\frac{rVLW_{3.0}}{rVLW_{1.5}}$	$\frac{rFLW_{3.0}}{rFLW_{1.5}}$	$\frac{rPLW_{3.0}}{rPLW_{1.5}}$
Cerebral Cortex	1.01 ± 0.06	0.98 ± 0.12	0.94 ± 0.16	0.95 ± 0.18	0.88 ± 0.23
Hippocampus	0.98 ± 0.05	1.02 ± 0.08	0.98 ± 0.14	0.96 ± 0.15	0.94 ± 0.17
Whole Brain	0.97 ± 0.05	1.04 ± 0.13	0.96 ± 0.13	0.94 ± 0.14	0.91 ± 0.19

Table 4.3: Calculation of the average variation in rFLW and rPLW in the cerebral cortex, hippocampus and whole brain ROIs due to varying bolus length (3.0 s bolus compared to 2.0 s bolus).

ROI	$\frac{MTT_{2.0}}{MTT_{3.0}}$	$\frac{CTT_{3.0}}{CTT_{2.0}}$	$\frac{rVLW_{3.0}}{rVLW_{2.0}}$	$\frac{rFLW_{3.0}}{rFLW_{2.0}}$	$\frac{rPLW_{3.0}}{rPLW_{2.0}}$
Cerebral Cortex	1.01 ± 0.07	0.98 ± 0.13	0.93 ± 0.19	0.94 ± 0.21	0.87 ± 0.26
Hippocampus	0.99 ± 0.05	1.01 ± 0.09	0.96 ± 0.18	0.95 ± 0.18	0.91 ± 0.13
Whole Brain	0.98 ± 0.07	1.03 ± 0.13	0.98 ± 0.10	0.96 ± 0.12	0.95 ± 0.18

4.3 Discussion

The btASL technique was developed by combining the theoretical model of chapter 2 with the experimental methods of chapter 3. In this chapter, the technique was applied to a rat imaging experiment in order to validate the technique and also to assess the variations in the perfusion parameters for varying animal, ROI and bolus length. The least-squares fit results in figures 4.4, 4.5 and 4.4 demonstrate the good agreement between the model and the experimental data. The technique is capable of providing reproducible perfusion parameters that can be of interest in the research and clinical settings.

A number of conclusions can be drawn from the representation of the the data in figure 4.7. Firstly, from figure 4.7 (a) it can be seen that the MTT and CTT can vary for varying animal. This is to be expected as even though animals of the same type, age, gender and body mass were anaesthetised in the same manner for each experiment, physiological variations arising from differing depths of anaesthesia for example, will lead to changes in the quantified parameters. Figure 4.7(b) and (c) illustrates the variation in the transit times for varying ROI and and bolus length respectively. While some ROI-dependent differences in MTT were found, no statistically significant differences in either the MTT or the CTT were found for varying bolus length.

From figures 4.8(a) and (b), it can be concluded that while some ROI-dependent variation in rVLW is possible, the rVLW does not vary significantly for varying bolus length. The changes in rFLW and rPLW for varying bolus length were calculated from the mean MTT, CTT and rVLW for each bolus length, as shown in tables 4.1, 4.2 and 4.3. Neither the rFLW nor rPLW were found to vary significantly for varying bolus length. The finding that the perfusion parameters (MTT, CTT, rVLW, rFLW and rPLW) are not varied significantly when the bolus duration is varied demonstrates that the technique can provide a consistent assessment of cerebral perfusion for constant physiological conditions but varying experimental conditions. It should be noted that this characteristic is not necessarily unique to the btASL technique. Alternative ASL models such as the general kinetic model [85] described in section 1.4.1 can also provide bolus duration-invariant CBF and

transit time measures.

Comparisons between the MTT obtained using the btASL technique and rat brain transit times in the literature are not easily made as the MTT presented herein is unique to the btASL technique and differs fundamentally from previously quoted transit time values. For example, the MTT values quoted by Schockley and LaManna [202] were calculated from analysis of indicator dilution curves generated from bolus injections of an intravascular contrast agent into the right atrium of anaesthetized rats. The curves were measured through a region of the parietal cerebral cortical surface and an MTT of approximately 1.4 seconds was measured under normoxic and normocapnic conditions. The MTT measured by the btASL technique is of the same order of magnitude as these values but a direct comparison is not possible due the differing natures of the measurements. A CASL study aimed at minimizing the transit time sensitivity of ASL measurements of CBF was carried out by Thomas et al [203]. Arterial transit times (defined as the time between the inversion of arterial blood water and its arrival at the imaging slice) in the range of approximately 500 ms were measured in the normal rat brain. This arterial transit time is a component of the MTT measured by the btASL technique but the MTT also includes the time to traverse the imaging voxel.

The error bars in figures 4.7 and 4.8 indicate one standard deviation from the mean. The magnitude of the error in each experiment could be reduced by improving the signal-to-noise ratio (SNR) of the ASL experiment. This can be achieved either through the use of a separate labeling coil, which would remove the contribution to the perfusion-weighted signal by magnetization transfer and provides more efficient labeling, or by employing a more sophisticated preparation method such as the the pseudo CASL sequence (both described in section 1.3.1). The number of signal averages (NSA) can also be increased (NSA = 8 for this study) to improve the SNR, but at the expense of increased scanning time.

The total measurement time for each experiment was approximately 15 minutes. While this scanning time may seem prohibitively long, the protocol duration can be significantly reduced to improve the practicality of the method. The eleven time points in 3.1 were used to measure the entire concentration-time curve, as the aim of this study was to provide proof of concept and validate the theoretical formulation. However, as only three

fitting parameters are necessary to perform the least-squares fit, conceivably four time points would be sufficient to quantify the transit times. This coupled with the use of a separate labeling coil, or the use of the pseudo CASL preparation would greatly reduce the measurement time.

The experimental results presented in this chapter, coupled with the theoretical development of the non-compartmental model of cerebral perfusion described in 2, were published in the journal of *Physics in Medicine in Biology* [191].

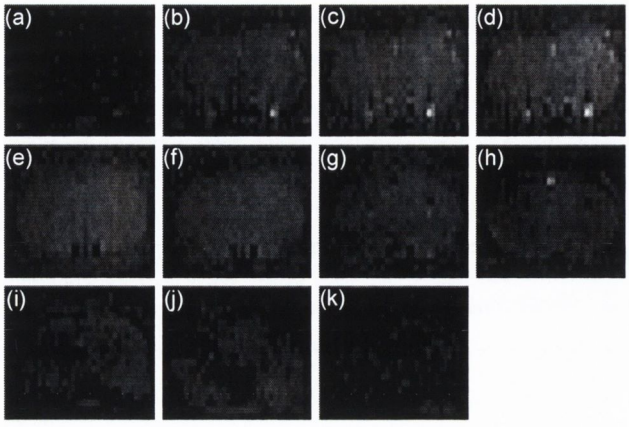

Figure 4.1: ASL perfusion weighted maps with 1.5 s bolus duration. **(a-k)** correspond to time points **(1-11)** in table 3.1.

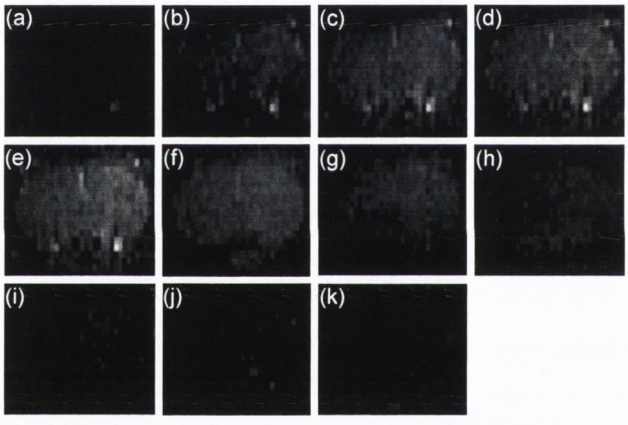

Figure 4.2: ASL perfusion weighted maps with 2 s bolus duration. **(a-k)** correspond to time points **(1-11)** in table 3.1.

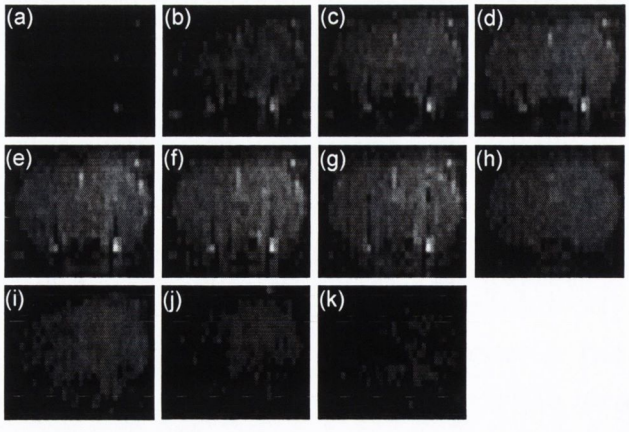

Figure 4.3: ASL perfusion weighted maps with 3 s bolus duration. **(a-k)** correspond to time points **(1-11)** in table 3.1.

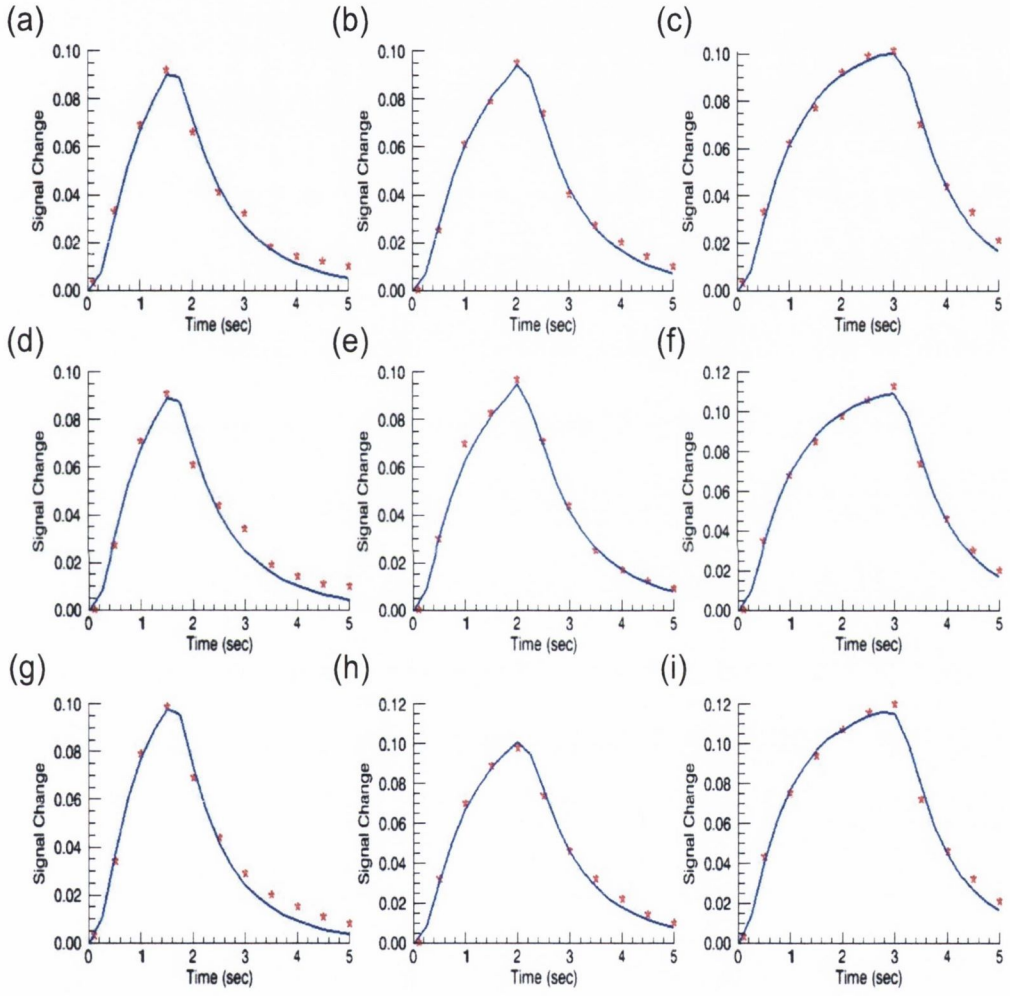

Figure 4.4: Least-squares fit of the model (blue solid line) to the data (red asterisks) for animal 1. **(a,b,c)** 1.5 s, 2.0 s and 3.0 s bolus length for cerebral cortex ROI. **(d,e,f)** 1.5 s, 2.0 s and 3.0 s bolus length for hippocampus ROI. **(g,h,i)** 1.5 s, 2.0 s and 3.0 s bolus length for whole-brain ROI.

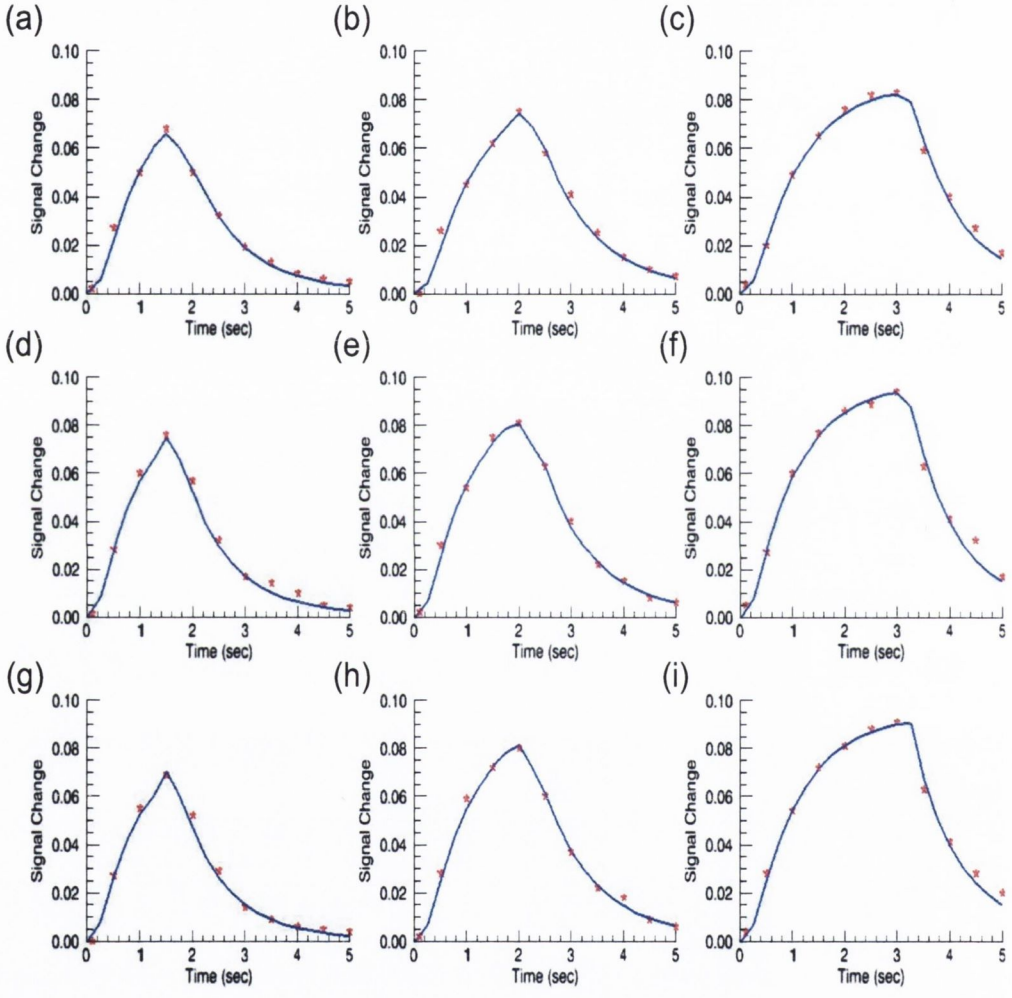

Figure 4.5: Least-squares fit of the model (blue solid line) to the data (red asterisks) for animal 2. **(a,b,c)** 1.5 s, 2.0 s and 3.0 s bolus length for cerebral cortex ROI. **(d,e,f)** 1.5 s, 2.0 s and 3.0 s bolus length for hippocampus ROI. **(g,h,i)** 1.5 s, 2.0 s and 3.0 s bolus length for whole-brain ROI.

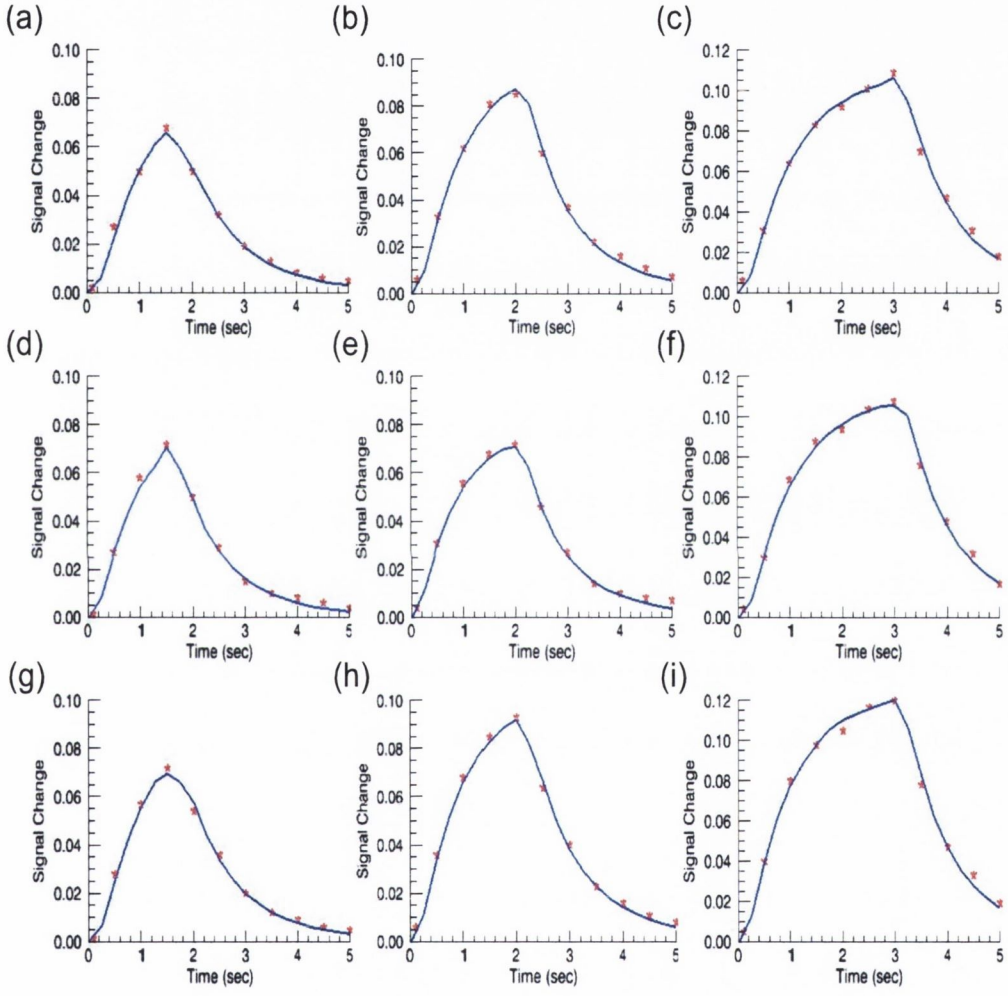

Figure 4.6: Least-squares fit of the model (blue solid line) to the data (red asterisks) for animal 3. **(a,b,c)** 1.5 s, 2.0 s and 3.0 s bolus length for cerebral cortex ROI. **(d,e,f)** 1.5 s, 2.0 s and 3.0 s bolus length for hippocampus ROI. **(g,h,i)** 1.5 s, 2.0 s and 3.0 s bolus length for whole-brain ROI.

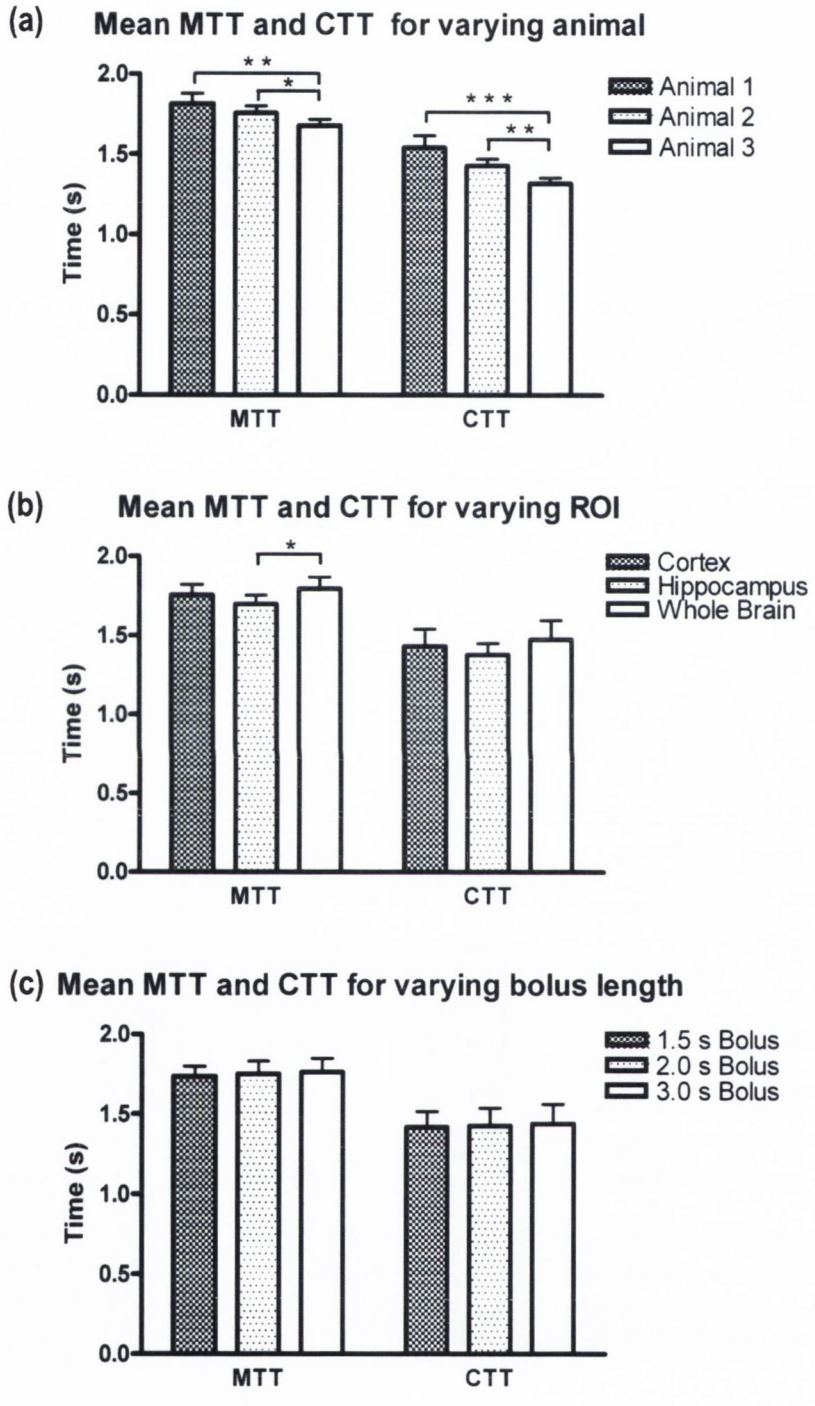

Figure 4.7: Variation in MTT and CTT for varying (a) animal, (b) region of interest and (c) bolus length. Error bars indicate one standard deviation from the mean. A one-way ANOVA was performed to test for statistical significance (*=$p<0.05$, **=$p<0.01$, ***=$p<0.001$).

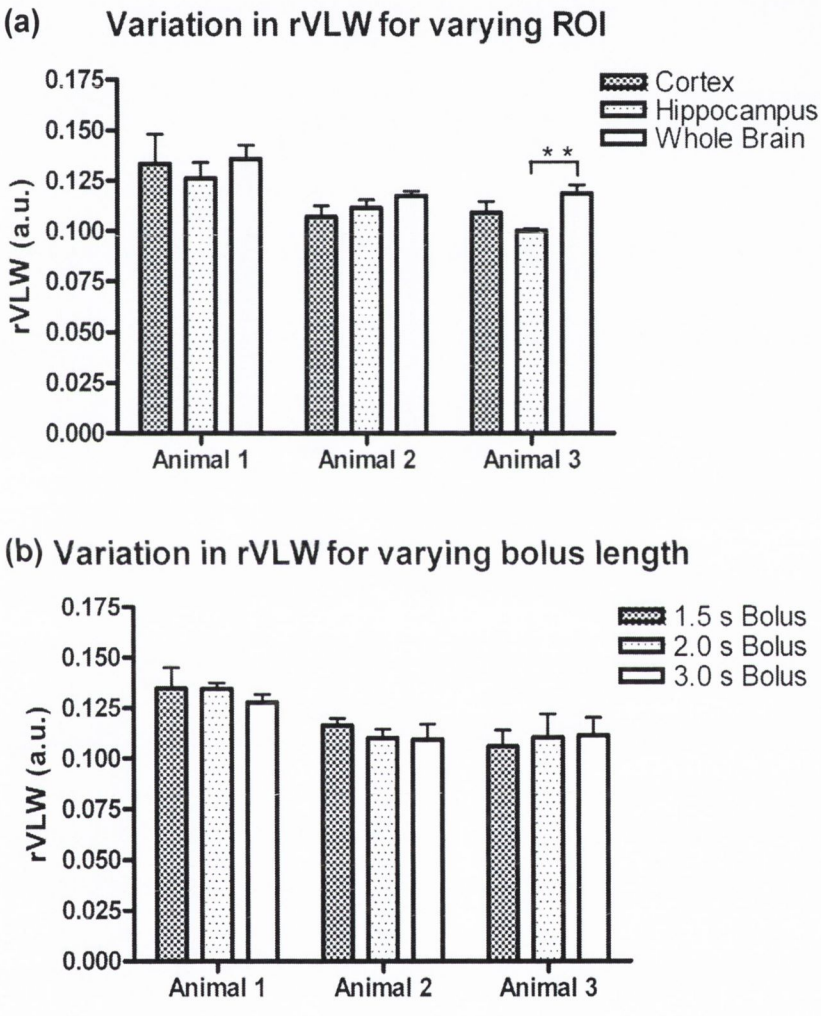

Figure 4.8: Variation in rVLW for each animal for varying (a) ROI and (b) bolus length. Error bars indicate one standard deviation from the mean. A one-way ANOVA was performed to test for statistical significance (**=$p<0.01$).

Chapter 5

Functional MRI with Bolus-Tracking Arterial Spin Labeling

5.1 Introduction

The potential advantages of using ASL fMRI techniques to investigate the haemodynamic response to focal increases in neural activity were described in section 1.5.1. In short, ASL fMRI offers superior long term stability, better spatial localisation of neural activity and most importantly, can provide a quantitative assessment of neural activity in terms of the haemodynamic response. However, the BOLD fMRI technique is still the most widely used fMRI technique in both human and animal fMRI studies. The development of new ASL methods and quantitative models specifically for fMRI applications can enhance the applicability of ASL fMRI to a wide range of fMRI applications.

The aim of this study was to use the btASL technique to measure the changes in the perfusion parameters quantifiable by this technique (MTT, CTT, rVLW, rFLW and rPLW) during increased neural activity in the rat brain. Results are presented from two groups of female Wistar rats (250 - 350 g body weight, 3 - 5 months of age). The first group (n=5) were maintainted under sedation with medetomidine during the fMRI experiments, while the second group (n=5) were under propofol anaesthesia. Electrical stimulation of right forepaw of the medetomidine sedated animals and the left fore-

paw of the propofol sedated animals resulted in increased neural activity[1] in the right and left primary somatosensory cortex forelimb regions (S1FL) respectively (refer to section 3.2.2 for a complete description of the anaesthetics and electrical stimulus). The haemodynamic response to this neural activity was detectable by the btASL technique. The variations in the btASL parameters in the activated S1FL compared to the same region in the resting state were of interest as these variations can provide a novel assessment of the transient haemodynamic changes in an activated brain region.

A comparison of the perfusion parameters (MTT, CTT, rVLW, rFLW and rPLW) obtained in the two groups (medetomidine and propofol) was carried out. The aims of this comparison were: (a) to investigate if the btASL technique was sensitive to any significant differences in the perfusion parameters of the two groups in the resting state and (b) to investigate if any differences measured in the resting state parameters resulted in measurable variations in the haemodynamic response to neuronal activation in the activated region.

5.2 Results

The fMRI results obtained form rats under sedation with medetomidine and under propofol anaesthesia will be presented in sections 5.2.1 and 5.2.2 respectively[2]. A comparison of these results will be given in section 5.2.3.

5.2.1 Medetomidine Results

Variation in Transit Times During Neuronal Activation

The individual MTT and CTT values obtained for the control and activated S1FL regions (figure 5.1) from the fitting parameters of the least-squares fits (figure 5.2) are given in table A.3. Both transit times were found to decrease in all animals during neuronal activation. The MTT decreased on average

[1]The increase in neural activity was confirmed by multi-electrode array data in a parallel study; data courtesy of Karen Griffin.

[2]The medetomidine results in section 5.2.1 were presented via oral presentation at the 24^{th} International Symposium on Cerebral Blood Flow and Metabolism [204] and have been submitted as a full paper to the Journal of Cerebral Blood Flow and Metabolism.

from 1.94 ± 0.18 s (control) to 1.62 ±0.21 s (activation) and the CTT decreased on average from 1.61 ± 0.11 s (control) to 1.31 ± 0.20 s (activation) (errors represent one standard deviation from the mean). These results are illustrated in figure 5.3. A two-tailed paired t test was used to test for statistical significance of the magnitude of the decrease in both transit times. The criterion for statistical significance (p-value) was $p \leq 0.05$. A significant decrease in both transit times during neuronal activation was discovered, with p=0.0012 for the MTT and p=0.0082 for the CTT.

Variation in rVLW, rFLW and rPLW During Neuronal Activation

The individual values obtained for the rVLW for the control and activated S1FL regions are given in table A.4. The rVLW, calculated as per equation 3.11, was found to increase on average from 0.09 ± 0.01 arbitrary units (a.u.) to 0.10 ± 0.01 a.u. This result is illustrated in figure 5.4. A two-tailed paired t test was used to test for statistical significance in the magnitude of the increase in the rVLW. A significant increase in the rVLW in the S1FL region during neuronal activation was discovered, with p=0.0026. The increase in rFLW and rPLW resulting from the measured changes in MTT, CTT and rVLW in the activated S1FL region were calculated using equations 3.12 and 3.13, with the results for each animal presented in table 5.1. The rFLW was found to increase by a factor of 1.35 ± 0.08 on average and the regional perfusion coeffient, rPLW, was found to increase by a factor of 1.48 ± 0.15 during neuronal activation on average.

Table 5.1: Calculation of the increase in rFLW and rPLW in the S1FL region during increased neural activity in animals under sedation by medetomidine

Animal	$\frac{MTT_{ctrl}}{MTT_{act}}$	$\frac{CTT_{act}}{CTT_{ctrl}}$	$\frac{rFLW_{act}}{rFLW_{ctrl}}$	$\frac{rPLW_{act}}{rPLW_{ctrl}}$
1	1.20 ± 0.07	0.69 ± 0.07	1.35 ± 0.17	1.25 ± 0.19
2	1.28 ± 0.10	0.79 ± 0.10	1.44 ± 0.24	1.63 ± 0.26
3	1.12 ± 0.08	0.91 ± 0.08	1.25 ± 0.19	1.43 ± 0.20
4	1.15 ± 0.13	0.89 ± 0.12	1.31 ± 0.29	1.51 ± 0.31
5	1.26 ± 0.11	0.77 ± 0.11	1.43 ± 0.23	1.57 ± 0.26

5.2.2 Propofol Results

Variation in Transit Times During Neuronal Activation

The individual MTT and CTT values obtained for the control and activated S1FL regions (figure 5.5) from the fitting parameters of the least-squares fits (figure 5.6) are given in table A.5. Both transit times were found to decrease in all subjects during neuronal activation. The MTT decreased on average from 1.97 $\pm$ 0.13 s (control) to 1.44 $\pm$0.08 s (activation) and the CTT decreased on average from 1.61 $\pm$ 0.11 s (control) to 1.31 $\pm$ 0.20 s (activation) (errors represent one standard deviation from the mean). These results are illustrated in figure 5.7. A two-tailed paired t test was used to test for statistical significance in the magnitude of the decrease in both transit times. The level for statistical significance (p-value) was set to 0.05. A significant decrease in both transit times during neuronal activation was discovered, with p=0.013 for the MTT and p=0.0096 for the CTT.

Variation in rVLW, rFLW and rPLW During Neuronal Activation

The individual values obtained for the rVLW for the control and activated S1FL regions are given in table A.6. The rVLW, calculated as per equation 3.11, was found to increase on average from 0.11 $\pm$ 0.01 arbitrary units (a.u.) to 0.13 $\pm$ 0.01 a.u. This result is illustrated in figure 5.8. A two-tailed paired t test was used to test for statistical significance in the magnitude of the increase in the rVLW. A significant increase in the rVLW in the S1FL region during neuronal activation was discovered, with p=0.0038. The increase in rFLW and rPLW resulting from the measured changes in MTT, CTT and rVLW in the activated S1FL region were calculated using equations 3.12 and 3.13, with the results for each animal presented in table 5.2. The rFLW was found to increase by a factor of 1.70 $\pm$ 0.16 on average and the regional perfusion coeffient, rPLW, was found to increase by a factor of 2.29 $\pm$ 0.41 on average during neuronal activation.

5.2.3 Comparison of Medetmoidine and Propofol Results

The results in sections 5.2.1 and 5.2.2 for MTT, CTT, rVLW, rFLW and rPLW were compared in order to investigate variations in the haemodynamic re-

Table 5.2: Calculation of the increase in rFLW and rPLW in the S1FL region during increased neural activity in animals under propofol anaesthesia

Animal	$\frac{MTT_{ctrl}}{MTT_{act}}$	$\frac{CTT_{act}}{CTT_{ctrl}}$	$\frac{rFLW_{act}}{rFLW_{ctrl}}$	$\frac{rPLW_{act}}{rPLW_{ctrl}}$
1	1.39 ± 0.12	0.83 ± 0.12	1.59 ± 0.21	2.09 ± 0.24
2	1.46 ± 0.14	0.73 ± 0.13	1.67 ± 0.26	2.04 ± 0.29
3	1.18 ± 0.13	0.98 ± 0.13	1.59 ± 0.24	2.48 ± 0.27
4	1.42 ± 0.20	0.74 ± 0.20	1.98 ± 0.36	2.91 ± 0.41
5	1.40 ± 0.20	0.69 ± 0.19	1.67 ± 0.33	1.92 ± 0.38

sponse to neuronal activation due to the two different anaesthetic agents (medetomidine and propofol). No significant difference was found when the MTT and CTT in both the control and activated state were compared for varying anaesthetic agent, as illustrated in figure 5.9 and 5.10 (MTT_{ctrl}: p=0.7413, MTT_{act}: p=0.1187, CTT_{ctrl}: p=0.0947, CTT_{act}: p=0.4752). A statistically significant difference was discovered when the rVLW in both the control and activated state under propofol anaesthesia and medetomidine sedation were compared ($rVLW_{ctrl}$: p=0.0019, $rVLW_{act}$: p<0.0001), as illustrated in 5.2.1. The magnitude of the increase in rVLW during neuronal activation was greater in the animals under anaesthetia by propofol than those under sedation by medetomidine, as illustrated in figure 5.12. The difference in this increase in rVLW was statistically significant (p=0.0099). The greater increase in rVLW under propofol anaesthesia is accompanied by a greater increase in both the rFLW and regional perfusion coefficient, rPLW (table 5.1 compared to table 5.2). The rFLW and rPLW increased on average by a factor of 1.35 ± 0.08 and 1.48 ± 0.15 respectively in the medetomidine sedated animals and by a factor of 1.67 ± 0.16 and 2.29 ± 0.41 respectively in the propofol anaesthetized animals.

5.3 Discussion

The advent of optical techniques has facilitated the imaging of changes in blood flow dynamics at the cellular scale. For example, through the use of intravenous injections of fluorescent dyes, the vascular topology can be tracked, allowing blood flow velocities in individual vessels to be determ-

ined. These techniques have been applied to to neuronal stimulation studies [205] and can provide information of the cortical haemodynamic response with superior spatio-temporal resolution to fMRI techniques. However, disadvantages such as low penetration depth, scattering and the need to inject fluorescent dyes limits the practicality of these approaches for studies of brain function in large cohorts of healthy or neurologically impaired subjects. As a result, fMRI techniques and in particular BOLD fMRI, are still the foremost tool for the investigation of human sensory, motor and cognitive functions. The potential advantages of ASL fMRI over BOLD fMRI were described in section 1.5.1. The results presented in this chapter describe the application of the btASL technique to two animal models (female Wistar rats under sedation and anaesthesia by medetomidine and propofol respectively). The development of new quantitative ASL fMRI techniques, such as the btASL technique, can enhance the quantitative information from fMRI studies and complement information from existing quantitative approaches.

The functional btASL technique is capable of quantifying the haemodynamic response to neuronal activation in terms of a unique set of perfusion parameters (MTT, CTT, rVLW, rFLW, rPLW). The decrease in the MTT and CTT in all cases coupled with the increase in rVLW corresponds to an increase in both the rFLW and rPLW in the somatosensory cortex of the rat brain during electrical stimulation of the forepaw. Increases in cerebral blood volume (CBV) and cerebral blood flow (CBF) during neuronal activation were reported in section 1.5.1 and have been measured by a variety of MRI [127] and non-MRI techniques such as laser-Doppler flowmetry (LDF) [206, 207], laser speckle contrast imaging (LSCI) [208] and two-photon microscopy [205]. As discussed previously in section 3.6.3, the parameters rVLW and rFLW are not direct measures of CBV and CBF respectively as water is not restricted to the vasculature. However, an increase in CBV can be reasonably expected to result in a greater volume of labeled water both in the vascular space and the surrounding extravascular space (due to exchange), leading to an increase in rVLW. Similarly, an increase in CBF would result in an increase in the average rate at which labeled water is transported through the system (i.e. from the labeling plane to the imaging plane) and lead to an increase in rFLW parameter.

The increase in rVLW during neuronal activation may be due to astrocyte-mediated vasodilatation at the activated region [109], resulting in an increase in the CBV and a concomitant increase in the volume of labeled water (both vascular and extravascular) within the activated region. The increase in rFLW is in agreement with the findings of optical studies that measure an increase in blood velocity during activation [206]. The increase in the regional perfusion coefficient of labeled water, rPLW, during neuronal activation can provide some novel information about the haemodynamic response to neuronal activation. One mechanism that may explain an increase in the parameter rPLW is the so-called capillary recruitment hypothesis [202]. The recruitment of additional capillaries during neuronal activation would lead to increased pseudo diffusion of the bolus of labeled water within the vascular compartment and result in an increase in the parameter rPLW. However, a series of studies have suggested that under resting conditions all cerebral capillaries are continuously perfused with plasma and consequently the recruitment of latent capillaries is not possible [126, 209]. Alternatively, if we consider that rPLW describes the diffusion of the labeled bolus at the ROI, we can hypothesize that an increase in this parameter is due to an increase in the exchange of water from the capillary bed to the surrounding tissue in the activated region.

Both medetomidine and propofol have been previously shown to provide suitable conditions for BOLD fMRI studies in rats [210, 211] and were shown in this study to be also suitable for ASL fMRI studies. The perfusion paramaters of the btASL technique were found to change in a similar manner for both anaesthetics (i.e. MTT and CTT decreased while rVLW, rFLW and rPLW increased). The comparison of the results obtained from the two anaesthetic agents revealed no significant differences in the MTT or the CTT in either the resting state or during neuronal activation. However, the rVLW was significantly higher in the propofol group than in the medetomidine group in both the resting state and during neuronal activation (section 5.2.3). Furthermore, the magnitude of the increase in rVLW during activation was significantly higher in the propofol group than in the medetomidine group. This greater increase in rVLW in the absence of significant differences in MTT and CTT corresponded to a greater increase in rFLW and rPLW in the propofol group. Medetomidine is known to cause

vasoconstriction and result in an overall suppression of global cererbral perfusion [212]. Conversely, propofol is known to stimulate constitutive nitroic oxide (NO) production and therefore causes a global increase in cerebral vasodilatation [213]. This may explain the dampened rVLW, rFLW and rPLW response in the somatosensory cortex of the medetomidine sedated animals compared to the propofol anaesthetized animals. The findings of the comparative study demonstrate that (a) the btASL technique is sensitive to changes in perfusion in the resting state due to the use of different anaesthetic agents and (b) the technique is also sensitive to variations in the magnitude of the haemodynamic response to neuronal activation that may arise due to variations in the resting state perfusion.

The btASL technique has also been applied to an ageing study in the rat brain. The findings of this study demonstrate the sensitivity of the btASL technique to changes in resting state cerebral perfusion with age 6.1.2. When coupled with the neuronal activation results presented here, it can be concluded that the technique holds potential for quantifying changes in the haemodynamic response to neuronal activation in aged and or diseased cohorts. Furthermore, this work represents the first use of medetomidine and propofol in combination with ASL for fMRI of the rat brain. These anaesthetic protocols allow for animal recovery following the following the fMRI experiment. By combining the quantitative btASL fMRI technique with these anaesthetic protocols, the technique is ideal for longitudinal animal fMRI studies of both normal ageing and animal models of age-related diseases.

The application of the btASL technique to the medetomidine fMRI study has been accepted for publication in the *Journal of Cerebral Blood Flow and Metabolism* [214]. A paper on the advantages of using propofol for ASL fMRI of the rat brain is currently in preparation[3].

[3]Griffin K.M. et al, paper in preparation

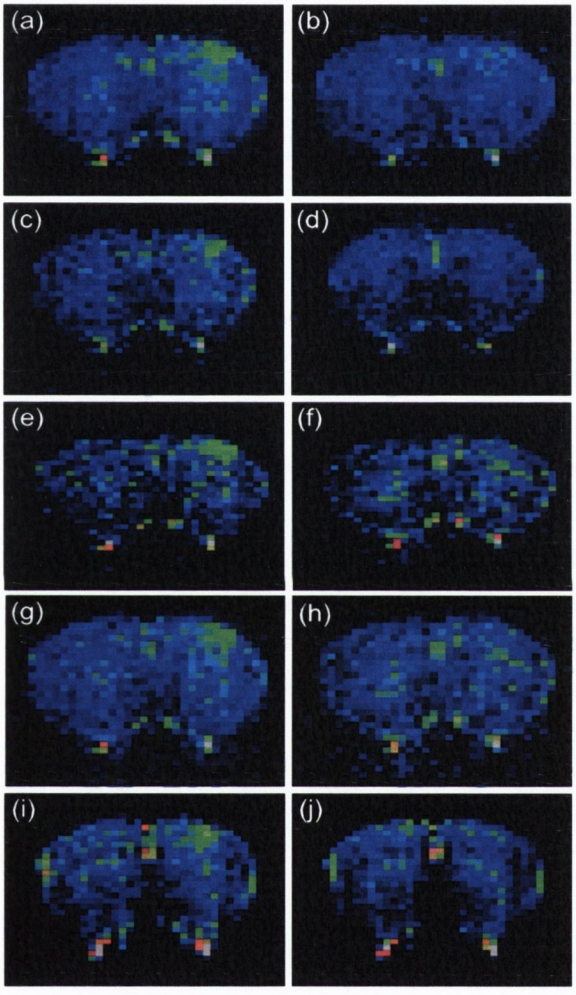

Figure 5.1: ASL difference images resulting from the subtraction of labeled images from control images (arbitrary units of signal intensity). Electrical stimulation of the right forepaw of animals under **medetomidine** sedation resulted in a detectable increase in perfusion in the left S1FL region. **(a,c,e,g,i)**. ASL difference images for animals 1 - 5 during neuronal activation. **(b,d,f,h,j)** ASL difference images for animal 1 - 5 in the resting state.

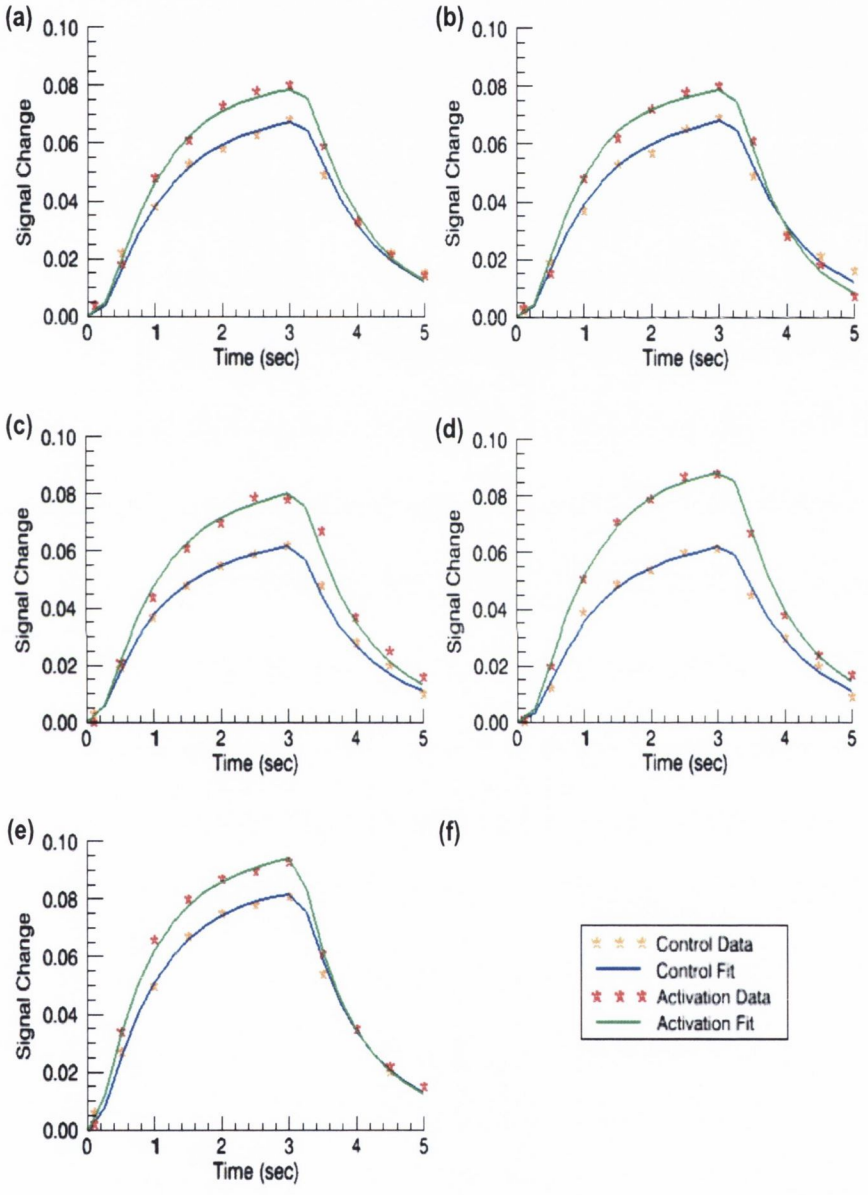

Figure 5.2: **(a-e)** Least-squares fit of the non-compartmental model to ASL data from the left S1FL of animals 1 - 5 respectively, during neuronal activation and in the resting state (control), under **medetomidine** sedation. **(f)** Legend for plots (a-e).

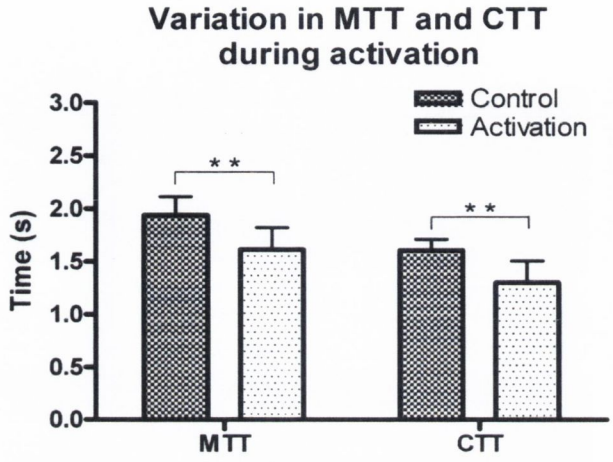

Figure 5.3: Change in MTT and CTT during neuronal activation under medetomidine sedation. A two-tailed paired t test revealed a significant difference in both transit times (MTT: p=0.0012, CTT: p=0.0082).

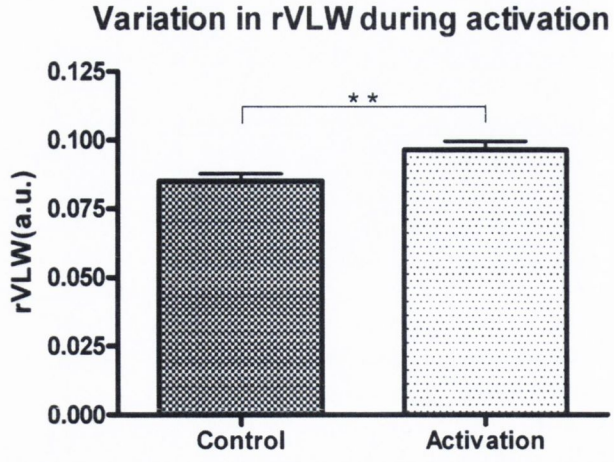

Figure 5.4: Change in rVLW during neuronal activation under medetomidine sedation. A two-tailed paired t test revealed a significant difference in the rVLW (p=0.009).

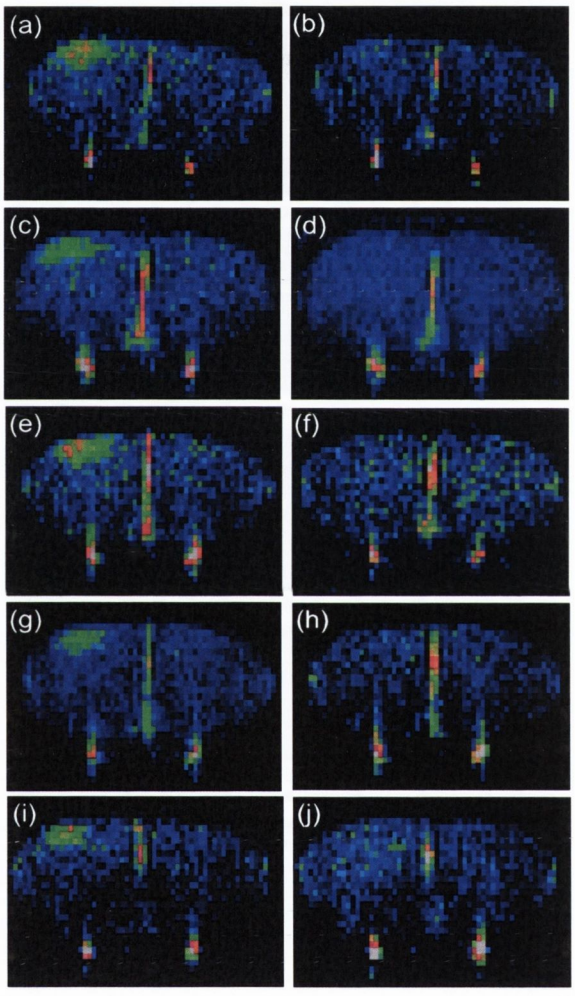

Figure 5.5: ASL difference images resulting from the subtraction of labeled images from control images (arbitrary units of signal intensity). Electrical stimulation of the left forepaw of animals under **propofol** anaesthesia resulted in a detectable increase in perfusion in the right S1FL region. **(a,c,e,g,i)** ASL perfusion maps acquired for animals 1 - 5 during neuronal activation. **(b,d,f,h,j)** ASL perfusion maps acquired for animals 1 - 5 in the resting state.

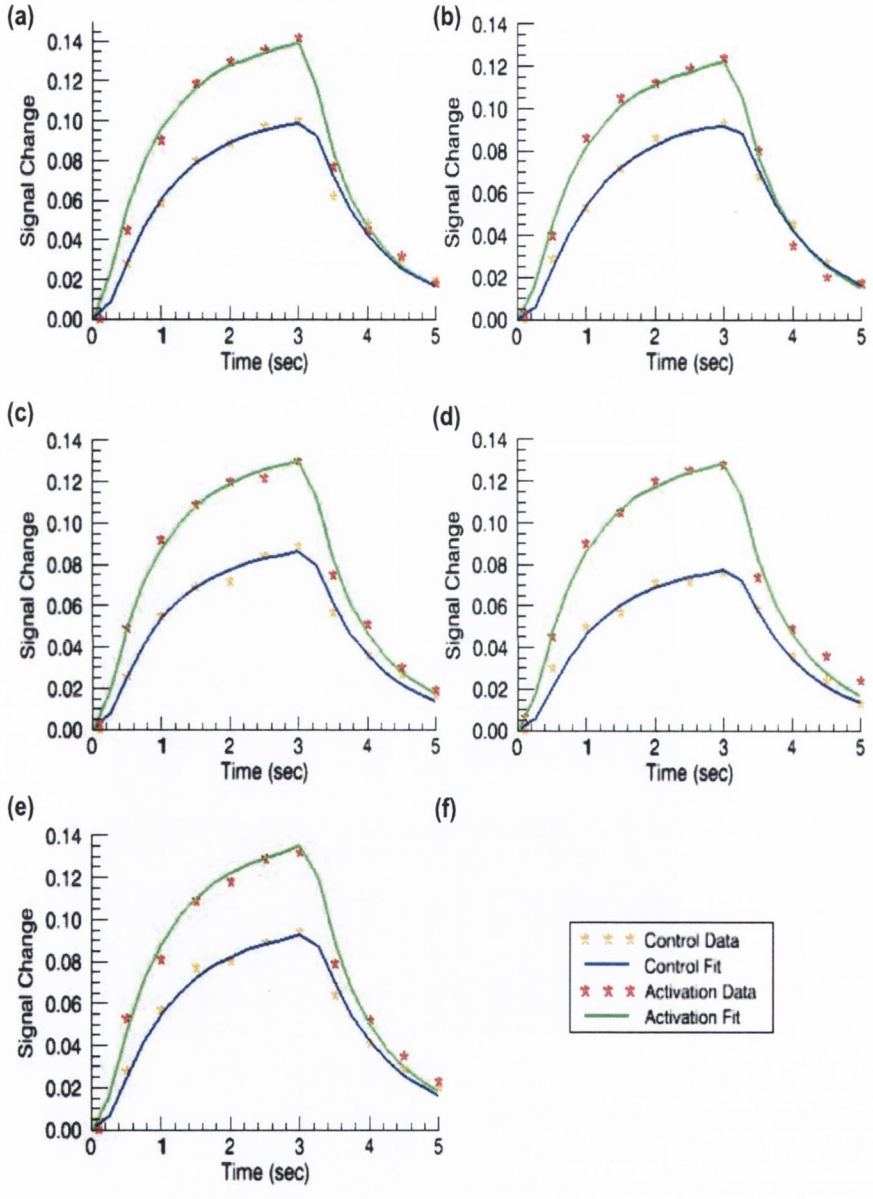

Figure 5.6: **(a-e)** Least-squares fit of the non-compartmental model to ASL data from the right S1FL of animals 1 - 5 respectively, during neuronal activation and in the resting state (control), under **propofol** anaesthesia. **(f)** Legend for plots (a-e).

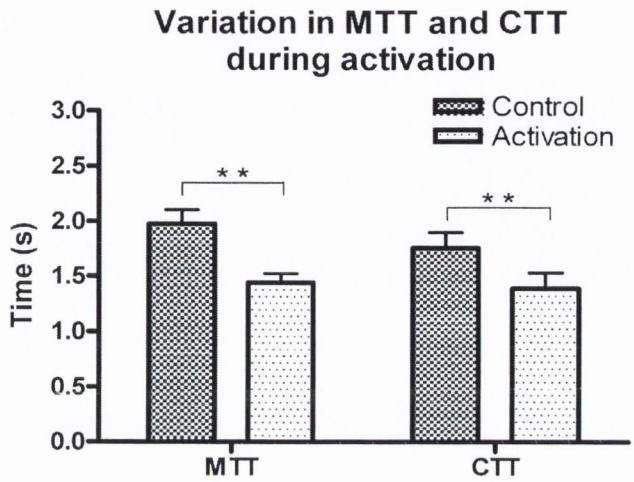

Figure 5.7: Change in MTT and CTT during neuronal activation under propofol anaesthesia. A two-tailed paired t test revealed a significant difference in both transit times (MTT: p=0.0013, CTT: p=0.0214).

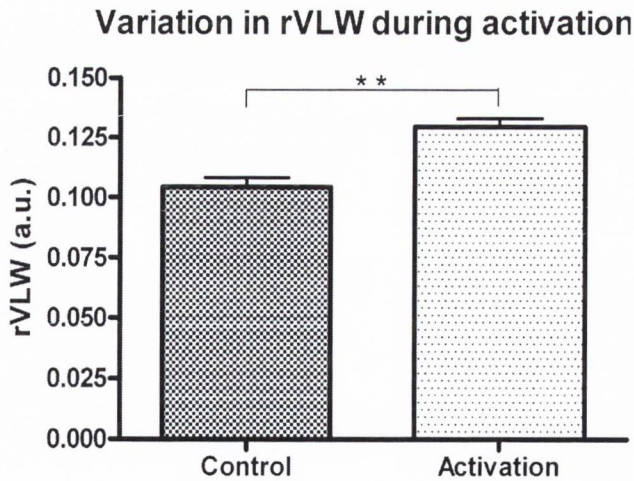

Figure 5.8: Change in rVLW during neuronal activation under propofol anaesthesia. A two-tailed paired t test revealed a significant difference in the rVLW (p=0.0038).

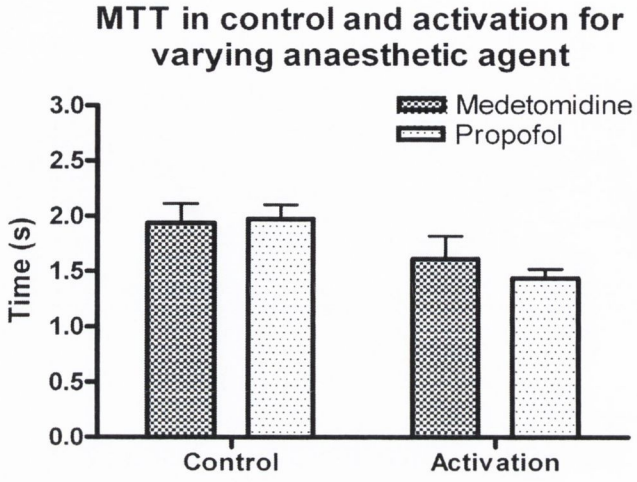

Figure 5.9: Comparison of MTT in resting state (control) and during electrical stimulation of the forepaw (activation) under sedation with medetomidine and anaesthetic by propofol. A two-tailed unpaired t test revealed no significant differences between the MTT in either the control or activation conditions (level of significance: p=0.05).

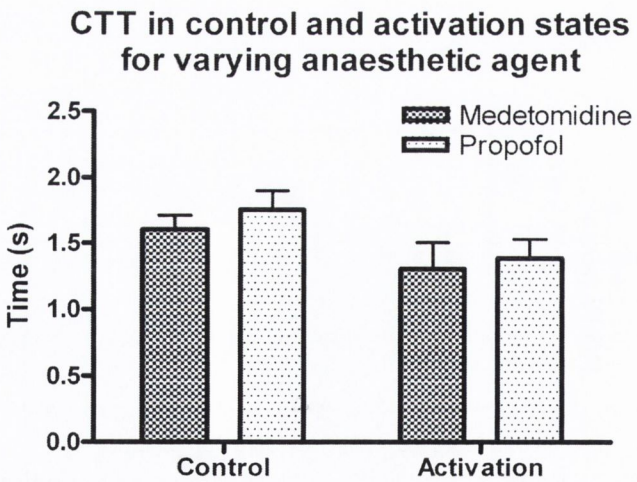

Figure 5.10: Comparison of CTT in resting state (control) and during electrical stimulation of the forepaw (activation) under sedation by medetomidine and anaesthetic by propofol. A two-tailed unpaired t test revealed no significanc differences between the CTT in either the control or activation conditions (level of significance: p=0.05).

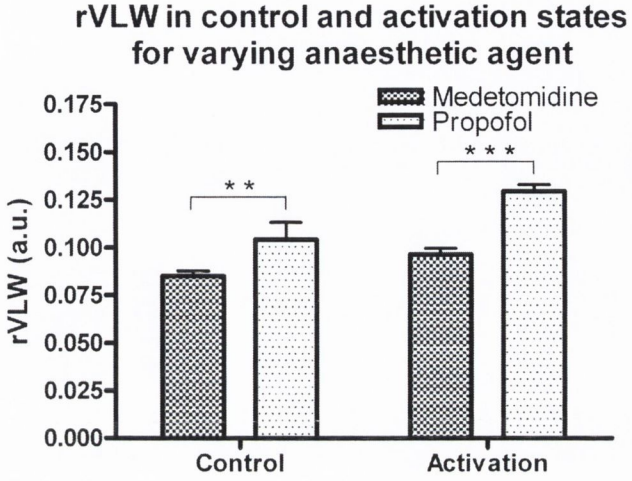

Figure 5.11: Comparison of rVLW in resting state (control) and during electrical stimulation of the forepaw (activation) in animals under sedation with medetomidine and under propofol anaesthesia. A two-tailed unpaired t test revealed that the rVLW under medetomidine sedation was significantly lower than the rVLW under propofol anaesthesia in both the control ($p=0.0019$) and activation ($p<0.0001$) conditions.

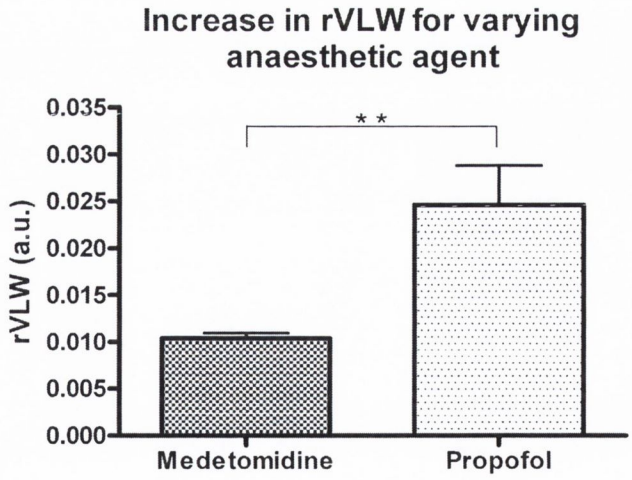

Figure 5.12: Comparison of change in rVLW during neuronal activation under propofol anaesthesia and medetomidine sedation. A two-tailed unpaired t test revealed that the change in rVLW under propofol anaesthesia was significantly higher than the change in rVLW under propofol anaesthesia ($p=0.0099$).

Chapter 6

Additional Bolus-Tracking Arterial Spin Labeling Results

6.1 Ageing Study

6.1.1 Introduction

The structural and functional changes that occur in the cerebrovasculature due to ageing were introduced in section 1.5.2. Age-related effects such as atherosclerosis, decreased microvessel density, increased vessel tortuosity and reduced vessel reactivity have all been attributed to the decline in cerebral perfusion that occurs with normal ageing. Studies using a variety of MRI and non-MRI techniques have reported decreased cerebral perfusion in the sub-cortical, cerebellar and hippocampal regions of both humans and rodents.

The aim of this study was to investigate whether or not the btASL technique is sensitive to age-related changes in cerebral perfusion. Results are presented from three groups of male Wistar rats: young, middle aged and aged (the animal setup for this ageing study is described in section 3.2.1). The young group (n=9) were 3 - 5 months of aged, the middle aged group (n=5) were 12 - 14 months of age and the aged group (n=5) were 22 - 24 months of age. The btASL perfusion parameters (MTT, CTT, rVLW, rFLW and rPLW) were quantified for the cerebral cortex, hippocampus and whole brain ROIs of each animal and the variations in these parameters for varying

age group were examined[1].

6.1.2 Results

Variation in transit times and rVLW with age

The individual MTT, CTT and rVLW values for the cerebral cortex, hippocampus and whole brain ROIs of each subject are given in tables A.7, A.8 and A.9 respectively. A one-way ANOVA test with the Bonferroni post hoc test for multiple comparisons was performed on the MTT, CTT and rVLW values from each ROI to establish if statistically significant differences were present between the young, middle aged and aged groups.

Both the MTT and CTT were found to be significantly higher in the cerebral cortex and hippocampus of the aged group compared to the young and middle aged groups ($p<0.05$). In the cerebral cortex ROI, the average MTTs in the young and middle aged groups were not significantly different at 1.94 ± 0.07 s (all results are presented as the mean $\pm$ one standard deviation) and 1.97 ± 0.05 s respectively, while the average MTT in the aged cerebral cortex was significantly higher at 2.25 ± 0.26 s (young v middle aged: $p>0.05$, young v aged: $p<0.01$, middle aged v aged: $p<0.05$). In the hippocampus ROI, the average MTTs in the young and middle aged groups were not significantly different at 1.95 ± 0.11 s and 1.77 ± 0.16 s respectively, while the average MTT in the aged hippocampus was significantly higher at 2.23 ± 0.20 s (young v middle aged: $p>0.05$, young v aged: $p<0.01$, middle aged v aged: $p<0.001$). The MTT results are presented in figure 6.1.

The average CTTs in the cerebral cortex ROI of the young and middle aged groups were not significantly different at 1.58 ± 0.12 s and 1.56 ± 0.13 s respectively, while the average CTT in the aged hippocampus was significantly higher at 1.94 ± 0.28 s (young v middle aged: $p>0.05$, young v aged: $p<0.01$, middle aged v aged: $p<0.05$). In the hippocampus ROI, the average CTTs in the young and middle aged groups were not significantly different at 1.57 ± 0.17 s and 1.52 ± 0.16 s respectively, while the average CTT in the aged hippocampus was significantly higher at 1.89 ± 0.11 s (young v middle aged: $p>0.05$, young v aged: $p<0.01$, middle aged v aged: $p<0.01$).

[1]The ageing results in section 6.1.2 were presented via oral presentation at both the 17^{th} Annual Meeting of the International Society for Magnetic Resonance in Medicine [215] and the 24^{th} International Symposium on Cerebral Blood Flow and Metabolism [216]

For the whole brain ROI, no significant differences in the transit times was found. The CTT results are presented in figure 6.2. The rVLW did not vary significantly between the groups, as illustrated in figure 6.3.

Variation in rFLW and rPLW with age

The variation in rFLW and rPLW with age was established for the ROIs in which a statistically significant increase in the transit times with age was measured (i.e. young v aged and middle aged v aged, cerebral cortex and hippocampus ROIs). Table 6.1 shows the values obtained for the change in rFLW and rPLW when the aged group was compared to the young group (calculated using equations 3.12 and 3.13) and table 6.2 shows the values obtained when the aged group was compared to the middle aged group. The standard deviation in these values was calculated by from the individual standard deviations of the contributing parameters in equations 3.12 and 3.13.

The factor by which the rFLW decreased with age was calculated as 0.76 $\pm$ 0.21 (all results are presented as the mean $\pm$ one standard deviation) and 0.84 $\pm$ 0.24 for the cerebral cortex and hippocampus ROIs respectively, when the aged group was compared with the young group (table 6.1). When the aged group was compared to the middle aged group, this factor was calculated as 0.89 $\pm$ 0.21 and 0.88 $\pm$ 0.22 for the cerebral cortex and hippocampus ROIs respectively (table 6.2).

The regional perfusion coefficient, rPLW, decreased by a factor of 0.72 $\pm$ 0.31 and 0.85 $\pm$ 0.31 for the cerebral cortex and hippocampus ROIs respectively, in the aged group compared to the young group (table 6.1). When the aged group was compared to the middle aged group, the factor by which rPLW decreased with age was calculated as 0.97 $\pm$ 0.29 and 0.95 $\pm$ 0.28 for the cerebral cortex and hippocampus ROIs respectively (table 6.2).

6.1.3 Discussion

The findings of this ageing study demonstrate the sensitivity of the btASL technique to age-related changes in cerebral perfusion. The significant increase in both the MTT and CTT in the cortex and hippocampes of the aged group compared to the young and middle aged groups, in the absence of a

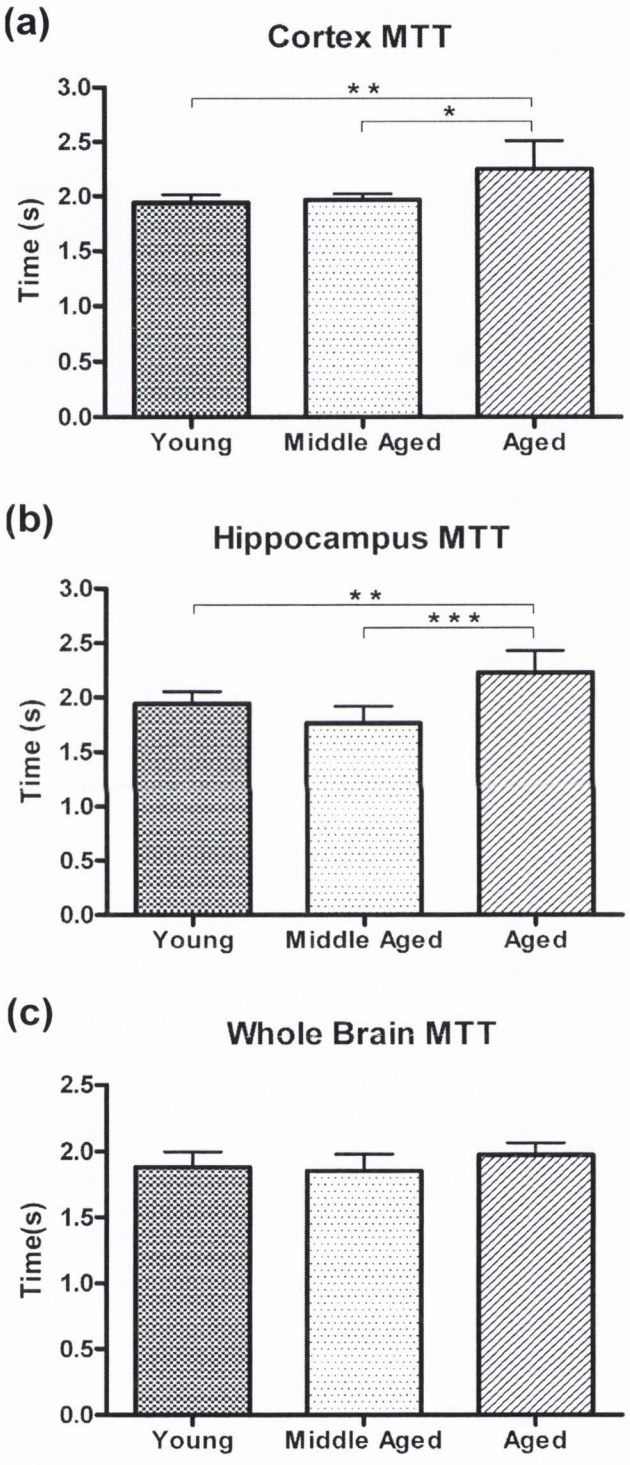

Figure 6.1: Variation in MTT with age within (a) the cerebral cortex, (b) the hippocampus and (c) the whole brain. A one-way ANOVA was performed to test for statistical significance between the young (n=9), middle aged (n=5) and aged (n-5) groups (*=$p<0.05$, **=$p<0.01$, ***=$p<0.001$).

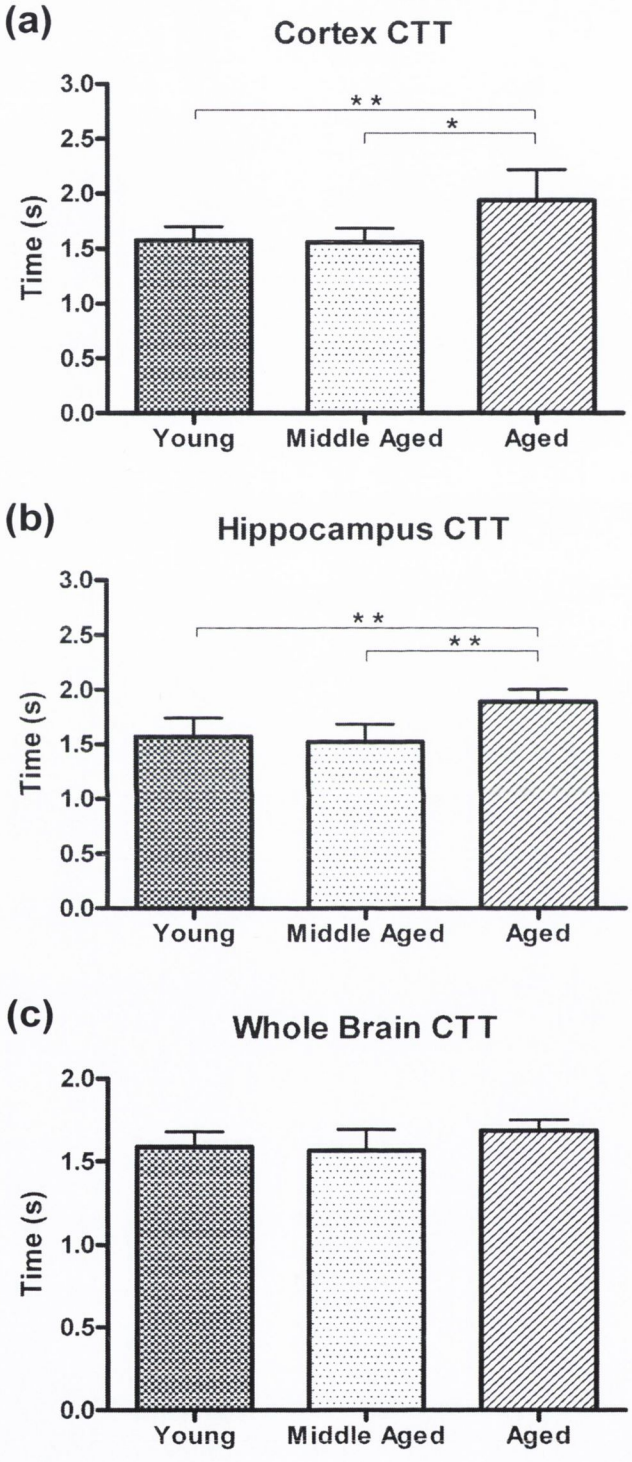

Figure 6.2: Variation in CTT with age within (a) the cerebral cortex, (b) the hippocampus and (c) the whole brain. A one-way ANOVA was performed to test for statistical significance between the young (n=9), middle aged (n=5) and aged (n=5) groups (*=$p<0.05$, **=$p<0.01$).

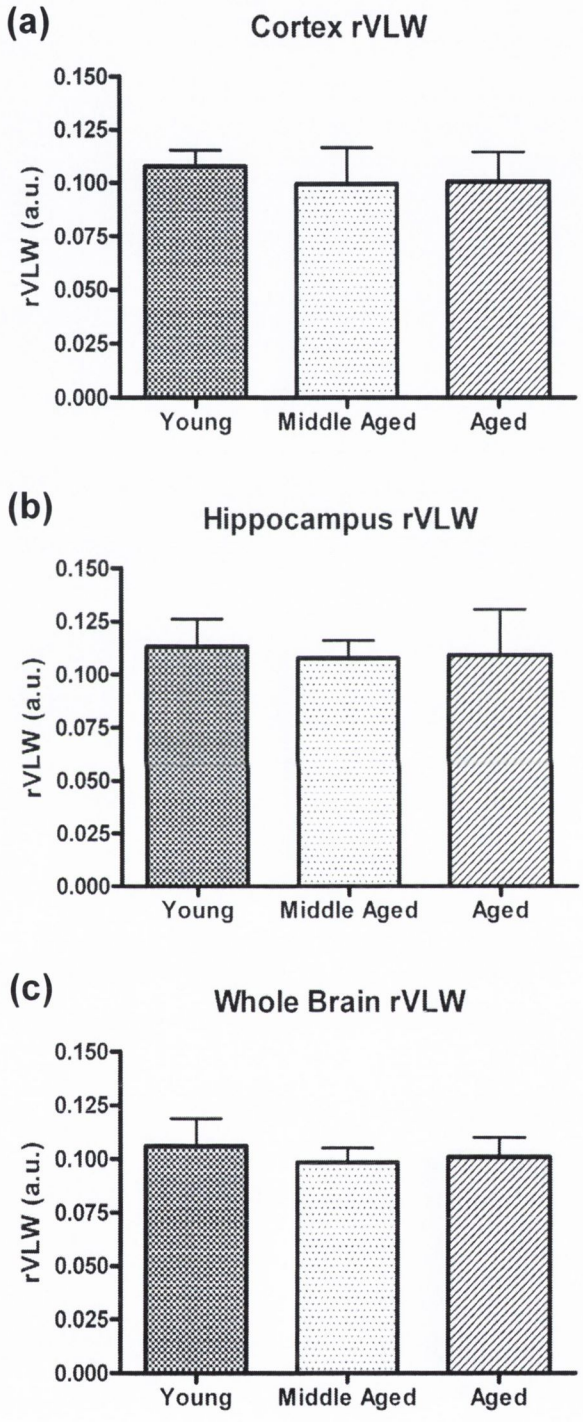

Figure 6.3: Variation in rVLW with age within (a) the cerebral cortex, (b) the hippocampus and (c) the whole brain. A one-way ANOVA was performed to test for statistical significance between the young (n=9), middle aged (n=5) and aged (n=5) groups. There were no significant differences between any of the groups.

Table 6.1: Calculation of the change in rFLW and rPLW in the cerebral cortex and hippocampus due to ageing. The mean MTT, CTT and rVLW of the **aged** (A) and **young** (Y) groups are used to calculate the change in rFLW and rPLW in this case.

ROI	$\frac{MTT_Y}{MTT_A}$	$\frac{CTT_A}{CTT_Y}$	$\frac{rVLW_A}{rVLW_Y}$	$\frac{rFLW_A}{rFLW_Y}$	$\frac{rPLW_A}{rPLW_Y}$
Cerebral Cortex	0.86 ± 0.12	1.23 ± 0.16	0.89 ± 0.19	0.76 ± 0.21	0.72 ± 0.31
Hippocampus	0.87 ± 0.11	1.20 ± 0.12	0.97 ± 0.23	0.84 ± 0.24	0.85 ± 0.31

Table 6.2: Calculation of the change in rFLW and rPLW in the cerebral cortex and hippocampus due to ageing. The mean MTT, CTT and rVLW of the **aged** (A) and **middle aged** (MA) groups are used to calculate the change in rFLW and rPLW in this case.

ROI	$\frac{MTT_{MA}}{MTT_A}$	$\frac{CTT_A}{CTT_{MA}}$	$\frac{rVLW_A}{rVLW_{MA}}$	$\frac{rFLW_A}{rFLW_{MA}}$	$\frac{rPLW_A}{rPLW_{MA}}$
Cerebral Cortex	0.88 ± 0.12	1.24 ± 0.16	1.01 ± 0.22	0.89 ± 0.21	0.97 ± 0.29
Hippocampus	0.79 ± 0.13	1.24 ± 0.12	1.11 ± 0.23	0.88 ± 0.22	0.95 ± 0.28

significant difference in the rVLW, corresponds to a decrease in both rFLW and rPLW within these regions. The absence of significant differences in the MTT, CTT and rVLW for the whole brain ROI indicate that the age-related decline in cerebral perfusion is region-specific as opposed to global in nature.

Regional decreases in CBF have been reported previously in studies using PET [154, 155], SPECT [157, 158] and ASL [153, 161, 160] techniques. As discussed previously (section 3.6.3), this rFLW parameter is not equivalent to CBF as it also consists of an extravascular component (due to water exchange). However, a decrease in the CBF would be expected to result in a decrease in the average rate at which labeled water is transported through the system (i.e. from the labeling plane to the imaging plane) and this in turn would be expected to lead to a decrease in rFLW. The age-related decrease in rFLW measured by the btASL technique may therefore be indicative of a decrease in CBF in the affected regions.

The perfusion parameter, P, is unique to the btASL technique and can provide a novel insight into changes in the microvasculature due to ageing. In the derivation of the non-compartmental model of cerebral perfusion (chapter 2), it was hypothesized that P takes into account the dilution of the bolus of labeled spins due to three random effects: pseudo diffusion within the microvasculature, the exchange of water between the capillary

bed and the surrounding tissue (osmosis) and random diffusion of labeled spins within both of these compartments. If we assume that the random diffusion component is unlikely to change due to ageing (as core body temperature was maintained at physiological levels in all experiments), the decrease in rPLW measured in the aged group can be presumed to be due to either a decrease in the exchange of water (functional change) or a decrease in pseudo diffusion due to reduced microvessel density in the cortex and hippocampus (structural change) [148, 150]. The rVLW parameter measured by the btASL technique is not equivalent to a purely intravascular measure of CBV (as discussed previously in section 3.6.3). However, a regional change in CBV would be expected to lead to a resultant change in the rVLW at that region. No significant differences in rVLW were measured in this study and consequently, variations in CBV are unlikely. This in turn implies that a structural vascular change is unlikely and therefore, the most likely reason for a region-specific decrease in P due to ageing is a reduction in the exchange of water from the capillary bed to the surrounding tissue.

The results also indicate that the variations in the perfusion parameters over time are non-linear, i.e. no significant differences in the transit times were found between the young and aged group but both transit times were significantly lower in these two groups compared to the aged group. The findings of Biagi et al [161] support the idea that the decline in cerebral perfusion with ageing is non-linear. However, in this study it was found that CBF decline in both grey and white matter of humans occurred primarily up to the age of approximately 30 years, while the results presented here suggest that cerebral perfusion decline in the rat brain occurs primarily from middle age onwards.

While the results presented are in agreement with previous findings in the literature, a number of improvements need to be made to this ageing study before it can be concluded that the measured differences are purely due to age-related changes in cerebral perfusion. While the animals were both age- and gender-matched, the reproducibility of the technique should be established by performing repeat measurements in selected animals from each group [160]. In addition, neither partial pressure of carbon dioxide (pCO_2) nor blood pressure (BP) measurements were possible at the time of the experiment. A cross-group comparison of these physiological paramet-

ers would allow the effects of the anaesthetic agent on the different groups and possible changes in BP with age to be ruled in or out as possible sources of the measured differences. Furthermore, the ASL data in this study was acquired without signal averaging (NA=1) and as a result, large regions of interest encompassing the entire cerebral cortex and hippocampus were necessary to compensate for the low SNR. In future experiments, signal average would allow sub-cortical and hippocampal regions to be selected.

The changes in rat brain T_1 relaxation times with age are not well known. In human relaxometry studies, an increase in T_1 with age is generally reported [217], although a decrease in T_1 up to early adulthood has also been suggested [218]. The region-specific T_1 values used in this ageing study were obtained from a parallel relaxometry study using young male Wistar rats that were matched in age, weight and gender to the young group in this ageing study. Therefore, in the context of the ageing study results it is important to establish what effect an increase in T_1 in the middle aged or aged groups would have on the transit time results. This consequences of this potential source of error is discussed in detail in chapter 7.

Notwithstanding the shortcomings of the presented ageing results, the sensitivity of the btASL technique to age-related changes in cerebral perfusion has potential for future applications. For example, cerebral hypoperfusion has been reported in animal models of Alzheimer's disease (AD) compared to age-matched controls [219]. Longitudinal tracking of the rate of cerebral perfusion decline in AD models and normally aged animals with the btASL technique may provide insight into when deviations between these groups occur. Also, by combining the fMRI techniques in chapter 5 with an ageing study, variations in the haemodynamic response to neural activity due to healthy or diseased ageing may be elucidated.

6.2 MDMA Study

6.2.1 Introduction

A description of the acute and long-term cerebrovascular effects of MDMA usage was given in section 1.5.3. The mechanism by which MDMA might effect these changes is not clear and the longer-term effects of MDMA on

the cerebrovasculature are yet to be fully elucidated [168]. Animal studies suggesting that MDMA administration may produce long-lasting or even permanent brain changes have led researchers to better understand the consequences for MDMA use for humans (for a review, see [220]). None of the perfusion studies outlined in section 1.5.3 use ASL techniques to measure the short and long-term variations in cerebral perfusion that arise as a direct result of MDMA usage. The non-invasive nature of ASL coupled with its suitability for longitudinal rodent studies, make it an ideal tool for tracking these cerebral perfusion changes in the same animals from the time of MDMA injection onwards.

The results from a btASL study of the short term effects of MDMA on cerebral perfusion in the rat brain are presented. Results are presented from three groups of male Wistar rats. Group 1 (n=4) and group 2 (n=5) were injected with boluses of saline (0.89%) and MDMA (20 mg/kg) respectively and scanned 3 hours post-injection. Group 3 (n=5) were injected with a bolus of MDMA (20 mg/kg) and scanned 24 hours post-injection. The animal setup for this experiment is described in section 3.2.1. The btASL perfusion parameters (MTT, CTT, rVLW, rFLW and rPLW) were quantified for the cerebral cortex, striatum and whole brain ROIs of each animal and the variations in these parameters across the three groups were examined[2].

6.2.2 Results

Variation in transit times and rVLW following MDMA administration

The individual MTT, CTT and rVLW values for the right and left cortex and striatum ROIs are given in tables A.10, A.11, A.12 and A.13 respectively. A one-way ANOVA test with the Bonferroni post hoc test for multiple comparisons was performed on the MTT, CTT and rVLW values from each ROI to establish if statistically significant differences were present between the control group and the MDMA treatment groups imaged 3 and 24 hours following drug administration. The results of the ANOVA analyses revealed a trend towards significant differences between the control and 3 hour group

[2]This study was part of a collaboration with fellow PhD candidate Jennifer Rouine. The surgical preparation and MDMA administration was performed by Jennifer and the btASL technique was applied as part of the MRI protocol. As a result, the MDMA results presented herein may be presented in the future as part of the Jennifer's PhD thesis

for the MTT and CTT of the cortical ROIs, with a significant difference reported for the right cortex MTT ($p<0.05$). As a result, a two-tailed unpaired t-test was performed on the MTT, CTT and rVLW results of the control, 3 hour and 24 hour groups for all ROIs.

The two-tailed unpaired t-test revealed that the MTT and CTT were significantly decreased in both the right and left cortex ROIs in the 3 hour group compared to the control group (the level of significance was set to $p<0.05$). In the right cortex ROI, the average MTT decreased significantly from 1.93 ± 0.04 s (mean $\pm$ one standard deviation) in the control group to 1.58 ± 0.18 s in the 3 hour group ($p=0.0072$). The CTT decreased significantly from 1.56 ± 0.08 s to 1.29 ± 0.09 s ($p=0.0025$). In the left cortex ROI, the average MTT decreased significantly from 1.89 ± 0.10 s in the control group to 1.56 ± 0.16 s in the 3 hour group ($p=0.0102$). The CTT decreased significantly from 1.56 ± 0.14 s to 1.28 ± 0.07 s ($p=0.0045$). These results are illustrated in figures 6.4(a) and 6.5(a). It can also be seen from these histograms there was a return to control transit times 24 hours following MDMA administration, although this effect was not at the level of statistical significance.

No statistically significant differences were found when the transit times from the right and left striatum ROIs of each group were compared ($p>0.05$ for all comparisons), as illustrated in figures 6.4(b) and 6.5(b). Figure 6.6 illustrates the rVLW for each ROI for the control, 3 hour and 24 hour groups. It can be seen from these histograms that the rVLW trends towards an increase in the 3 hour group compared to the control and 24 hour groups, although this effect was not at the level of statistical significance.

Variation in rFLW and rPLW following MDMA intake

The variation in rFLW and the regional perfusion coefficient, rPLW, was calculated (using equations 3.12 and 3.13) for the ROIs that yielded a statistically significant decrease in the transit times when the 3 hour group was compared to the control group (i.e. left and right cerebral cortex). As discussed above, the statistically significant differences were only present when the 3 hour group was compared to the control group using a two-tailed paired t-test. However, the variation in rFLW and rPLW between the 3 hour group and the 24 hour group was also calculated, due to the tendency of the transit

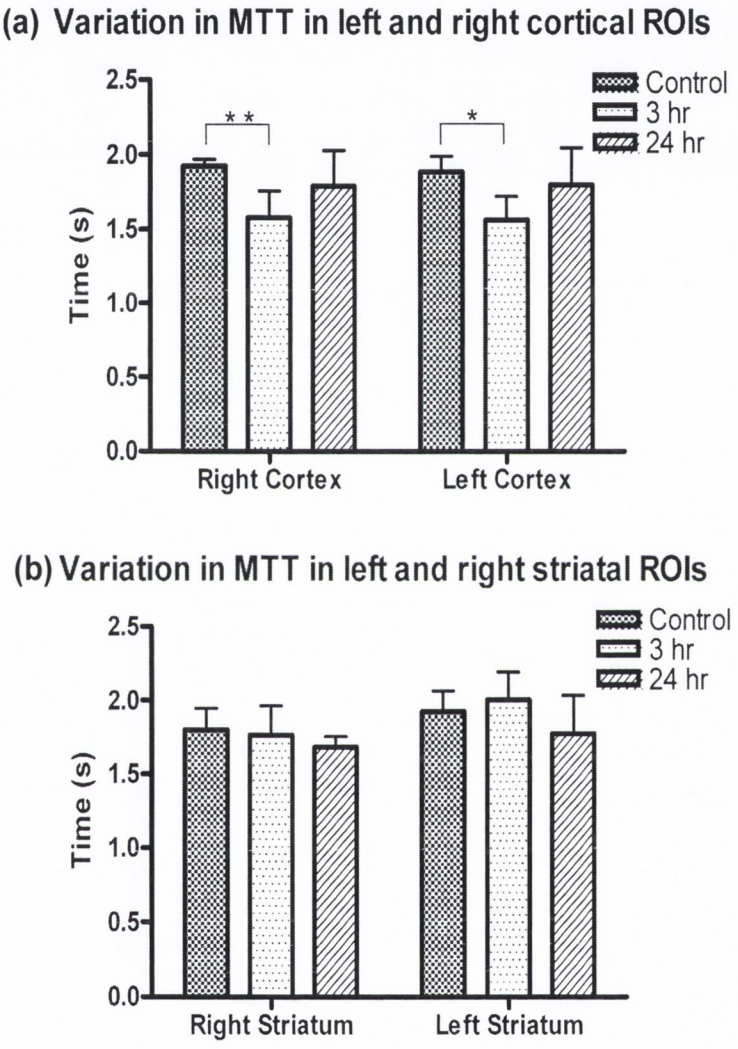

Figure 6.4: Variation in MTT 3 and 24 hours following MDMA administration in (a) right and left cortical ROIs and (b) right and left striatal ROIs. A two-tailed unpaired t-test revealed significant differences between the control and 3 hour groups for the MTT of the right and left cortex ($p=0.0072$ for right cortex and $p=0.0102$ for right cortex). No significant differences were found for the striatal ROIs.

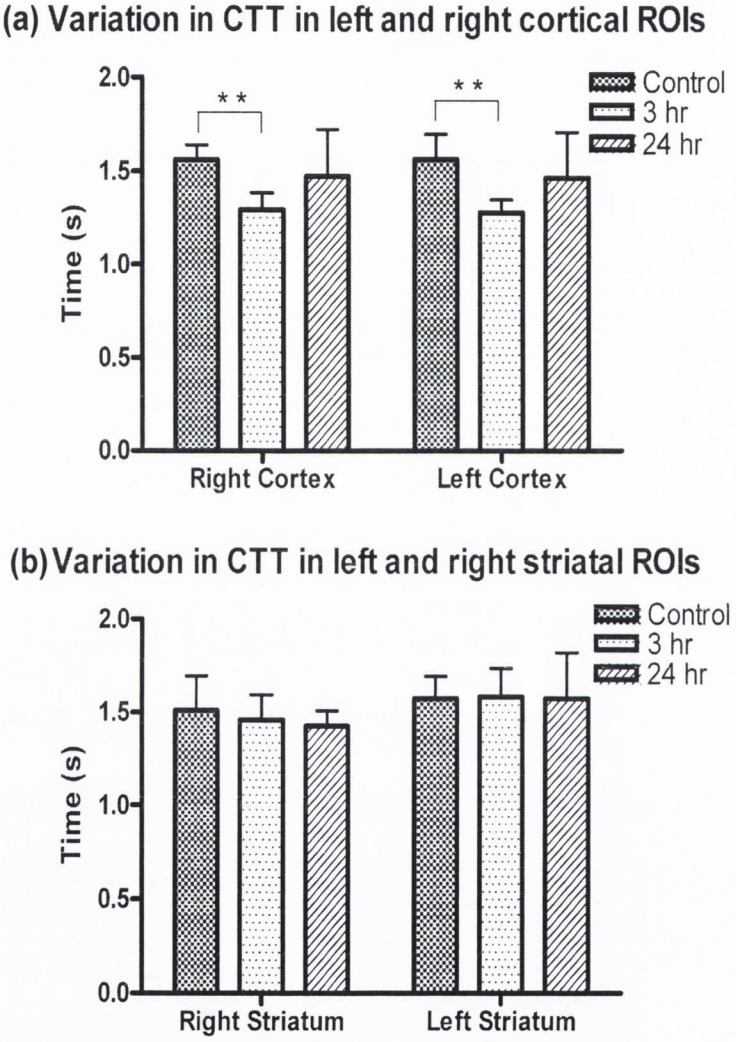

Figure 6.5: Variation in CTT 3 and 24 hours following MDMA administration in (a) right and left cortical ROIs and (b) right and left striatal ROIs. A two-tailed unpaired t-test revealed significant differences between the control and 3 hour groups for the CTT of the left and right cortex ($p=0.0025$ for right cortex and $p=0.0045$ for left cortex). No significant differences were found for the striatal ROIs.

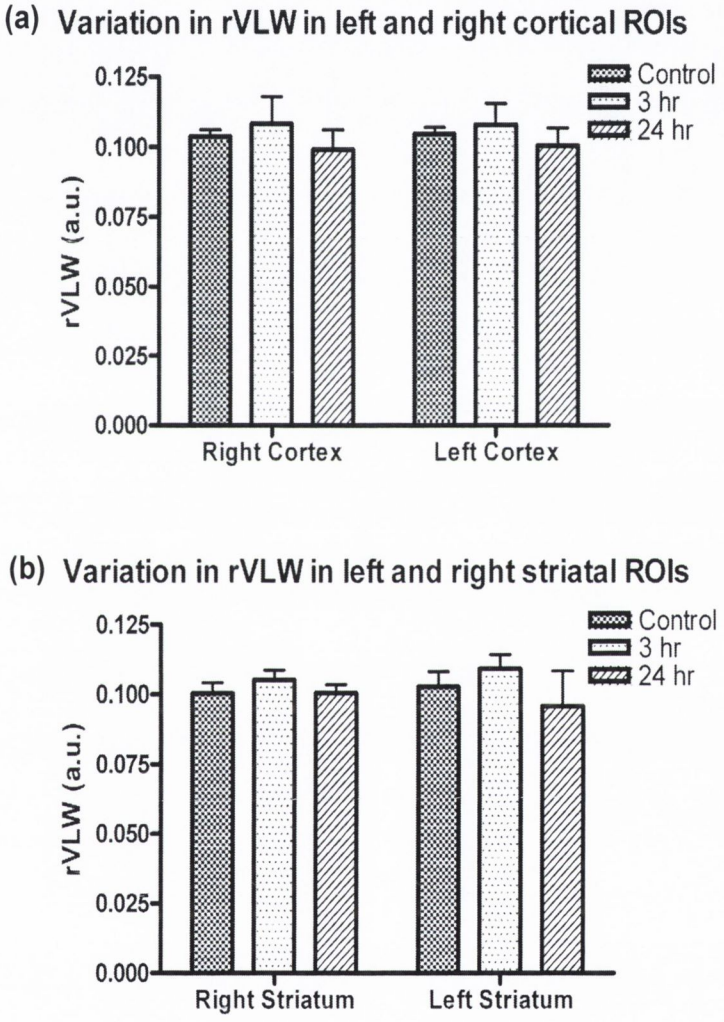

Figure 6.6: Variation in rVLW 3 and 24 hours following MDMA administration in (a) right and left cortical ROIs and (b) right and left striatal ROIs. A two-tailed unpaired t-test failed to reveal statistically significant differences in the rVLW.

times to return to the control values at the 24 hour time point (figures 6.4(a) and 6.5(b)). The results are presented in tables 6.3 and 6.4.

The rFLW increased by a factor of 1.27 ± 0.15 in the right cortex ROI of the 3 hour group compared to the same ROI of the control group and by a factor of 1.25 ± 0.14 in the left cortex ROI. The regional perfusion coefficient, rPLW, increased by a factor of 1.33 ± 0.15 in the right cortex ROI of the 3 hour group compared to the control group and by a factor of 1.29 ± 0.15 in the left cortex ROI (table 6.3). When the 3 hour group was compared to the 24 hour group, the rFLW was found to be a factor of 1.24 ± 0.21 higher in the right cortex ROI and a factor of 1.24 ± 0.19 higher in the left cortex ROI. The perfusion coefficient, rPLW, was a factor of 1.35 ± 0.12 times higher in the right cortex ROI of the 3 hour group compared to the 24 hour group and 1.34 ± 0.24 time higher in the left cortex ROI (table 6.4).

Table 6.3: Calculation of the change in rFLW and rPLW in the right and left cerebral cortex ROIs due to MDMA administration by comparing the 3 hour group to the control group.

ROI	$\frac{MTT_{ctrl}}{MTT_{3hr}}$	$\frac{CTT_{3hr}}{CTT_{ctrl}}$	$\frac{rVLW_{3hr}}{rVLW_{ctrl}}$	$\frac{rFLW_{3hr}}{rFLW_{ctrl}}$	$\frac{rPLW_{3hr}}{rPLW_{ctrl}}$
Right Cortex	1.22 ± 0.12	0.82 ± 0.09	1.04 ± 0.09	1.27 ± 0.15	1.33 ± 0.15
Left Cortex	1.21 ± 0.12	0.83 ± 0.10	1.03 ± 0.07	1.25 ± 0.14	1.29 ± 0.15

Table 6.4: Calculation of the change in rFLW and rPLW in the right and left cerebral cortex ROIs due to MDMA administration by comparing the 3 hour group to the 24 hour group.

ROI	$\frac{MTT_{24hr}}{MTT_{3hr}}$	$\frac{CTT_{3hr}}{CTT_{24hr}}$	$\frac{rVLW_{3hr}}{rVLW_{24hr}}$	$\frac{rFLW_{3hr}}{rFLW_{24hr}}$	$\frac{rPLW_{3hr}}{rPLW_{24hr}}$
Right Cortex	1.13 ± 0.18	0.88 ± 0.19	1.09 ± 0.11	1.24 ± 0.21	1.35 ± 0.21
Left Cortex	1.15 ± 0.17	0.87 ± 0.18	1.08 ± 0.09	1.24 ± 0.20	1.34 ± 0.24

Variation in temperature following MDMA intake

The temperatures of the animals in the control, 3 hour and 24 hour groups were monitored at half-hour intervals in the three hours following injection of the saline and MDMA boluses respectively. The 3 hour and 24 hour groups received identical treatments, the only difference between these two groups being the time post-injection at which they were scanned. As a result, temperature readings from these two groups were combined to form an

MDMA group for comparison with the control group. Figure 6.7 shows the difference in the temperatures of these groups over this time period. The temperature of the MDMA group was significantly elevated from the 0.5 hour time-point onwards ($p<0.01$) when compared to the control group.

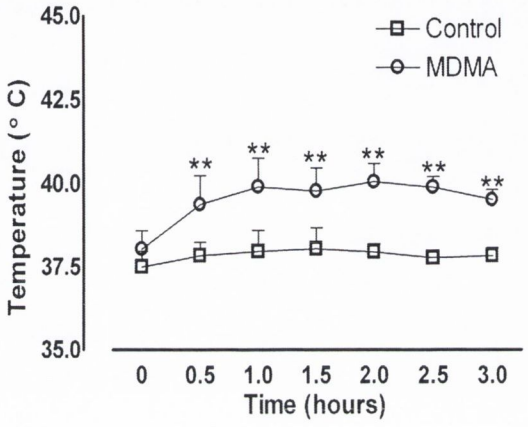

Figure 6.7: Variation in body temperature of control and MDMA animals in the first 3 hours following saline and MDMA administration respectively (**=$p<0.01$).

6.2.3 Discussion

The findings of the MDMA study demonstrate the sensitivity of the btASL technique to transient changes in perfusion of the rat brain due to the MDMA administration. The significant decrease in cortical MTT and CTT in the 3 hour group compared to the control group, in the absence of a significant difference in the rVLW, corresponds to an increase in both rFLW and rPLW in the 3 hour group compared to the controls. The absence of significant differences in the MTT and CTT in the striatum indicate that the perfusion response to MDMA is region-specific.

The trend towards a return to the baseline MTT and CTT values of the control group in the group that were scanned 24 hours post MDMA administration (evident in figures 6.4(a) and 6.5(a)) indicates that the decreases measured in the cortical transit times and the corresponding increase rFLW and rPLW are transient in nature and arise due to acute exposure to MDMA. This result is in agreement with previous findings in the literature [162, 168], where transient increases in CBF in cortical regions of the rat brain have been linked to a loss of autoregulatory capacity following MDMA-induced

hypertension. This mechanism is a possible explanation for the transient increase in rFLW presented here but blood pressure monitoring was not possible during the MRI experiments. A parallel MDMA-blood pressure study would be necessary to verify compromised autoregulation. As discussed previously in section 3.6.3, the rFLW parameter measured by the btASL technique is not equivalent to purely intravascular CBF as it also consists of an extravascular component (due to water exchange). However, a transient increase in CBF would be expected to lead to an increase in the rate at which labeled water is transported through the vasculature and a concomitant increase in the rFLW parameter.

The temperature measurements presented in figure 6.7 verified that the MDMA was active in both groups that were administered the drug. The mean temperature in these groups was significantly elevated in the three hours following the MDMA challenge, indicating a hyperthermic response to MDMA that correlates to the increase in rFLW measured at the 3 hour time point. A correlation between MDMA-induced hyperthermia and focal increases in CBF was previously reported by Rosa-Neto et al [221] in a PET study of MDMA-evoked changes in the pig brain.

The increase in the regional perfusion coefficient, rPLW, at the 3 hour time point can provide some additional information on MDMA-induced changes in the microvasculature. As previously described in section 6.1.3, this coefficient has been hypothesized to account for effects such as pseudo diffusion due to the tortuosity of the microvasculature, osmosis and water diffusion in the vascular and extravascular compartments. As discussed previously (section 3.6.3), the rVLW parameter measured by the btASL technique is not equivalent to a purely intravascular measure of CBV. However, a regional change in CBV would be expected to lead to a resultant change in the the volume of labeled water at that region (rVLW). No significant differences in rVLW were measured in this study and consequently, variations in CBV are unlikely. This in turn implies that a structural vascular change is unlikely and therefore the pseudo-diffusion component of P is unlikely to have changed. The increase in rPLW can therefore be hypothesized to be either due to increased water diffusion or an increase in the exchange of water from the capillary bed to the surrounding tissue. The former is a possible consequence of the elevated temperature in the MDMA group at

the 3 hour time point, as an increase in temperature results in an increase in the diffusion coefficient of fluids [182]. The latter is also possible as it has been established, through measurements of local cerebral glucose utilization ($LCMR_{glu}$), that MDMA administration correlates with acute increases in metabolic demand [168]. A transient increase in water exchange may be an indicator for this increase in metabolic demand.

The findings presented demonstrate the potential of the btASL technique for future studies investigating the cerebrovascular effects of MDMA. Close monitoring of BP during the acute phase can establish if autoregulation is in fact transiently altered. Furthermore, cerebral perfusion was only monitored twice following MDMA administration (after 3 and 24 hours). More frequent sampling within this phase may establish the complete pattern of cerebral perfusion changes. Also, a longitudinal btASL study may be used to investigate if short term increases in cerebral perfusion become deficits in the long term as predicted by the chronic MDMA studies described in section 1.5.3.

Chapter 7

Discussion

7.1 Summary

A new technique for the quantification of cerebral perfusion, termed bolus-tracking arterial spin labeling (btASL), has been developed by combining the non-compartmental model of cerebral perfusion (chapter 2) with an ASL imaging technique (section 3.4). The technique provides an assessment of cerebral perfusion in terms of the following set of parameters: MTT, CTT, rVLW, rFLW and rPLW and is sensitive to changes in these parameters under varying physiological conditions. The MTT and CTT parameters were described in section 2.4 and the rVLW, rFLW and rPLW parameters were described in section 3.6.3. However, at this point, a summary of the parameter definitions is necessary.

The mean transit time (MTT) is calculated from the first moment of the tissue response function. It is defined as the average time taken for labeled water to traverse the entire volume of distributed water, V (i.e. the time from when spins are labeled at the labeling plane to when they flow out of the imaging plane). From equation 2.29 (MTT=V/F) it can be seen that the MTT will increase with increasing V and decrease with increasing average flow rate, F (i.e. if the volume, V, into which labeled water can flow increases, the average time taken to traverse V will increase whereas if the average flow rate increases, the time taken to traverse the volume, V, decreases).

The capillary transit time (CTT) parameter is calculated from the second moment of the tissue response function. This transit time is not defined in

terms of a specific transit distance but describes the extent to which an initially rectangular bolus of labeled water at the labeling plane has become dispersed when it is measured at the imaging plane. From equation 2.30 ($CTT=P/F^2$) it can be seen that the CTT is directly proportional to the perfusion coefficient, P, where P is thought to incorporate the random processes that act on a particle as it traverses the vasculature. The inverse relationship between CTT and the square of the average flow, F, indicates that as F increases, the dispersive effects of the P term are lessened and the CTT is decreased.

The relative volume of labeled water (rVLW) is an estimate for the volume of labeled water at the imaging voxel (equation 3.9). Water is known to undergo exchange between the vascular and extravascular spaces in the capillary bed with the degree of exchange [180] and as a result, the rVLW is not a measure of cerebral blood volume (CBV). However, if the CBV in a region increases, the amount of labeled water at that region would be expected to increase and lead to a concomitant increase in rVLW.

Once the MTT, CTT and rVLW have been quantified from the curve fitting parameters, the relative change in the average flow rate of labeled water, rFLW, and the perfusion coefficient of labeled water, rPLW, between two groups (e.g. aged v young) or two physiological conditions (e.g. resting state v neuronal activation) can be calculated from the definitions of the transit times (equations 3.12 and 3.13). The rFLW parameter represents a relative change in the average rate at which labeled water is transported through the volume, V. Again, as water is not restricted to the vasculature, the rFLW parameter has contributions from both the vascular and extravascular compartments and is therefore not a direct measure of cerebral blood flow (CBF). However, if the CBF in a region increases, the average rate at which labeled water is transported through that region would increase and an increase in the rFLW would be expected. Finally, the rPLW parameter represents a relative change in the random effects (such as pseudo diffusion within the microvasculature and the exchange of water across the capillary walls) that result in the dispersion of a rectangular bolus of labeled water as it flows through the volume, V.

In chapter 4, significant differences in the MTT, CTT and rVLW and consequent changes in rFLW and rPLW were detected for varying animal

and ROI. The absence of significant differences in the perfusion parameters for varying bolus length indicate that the btASL technique is capable of providing consistent perfusion parameters when the physiological conditions remain constant but the experimental conditions are varied. In the fMRI study, the MTT and CTT were found to decrease significantly during neuronal activation while the rVLW increased significantly. A corresponding increase in rFLW and rPLW was calculated. The greater increase in rVLW in the propofol anaesthetised animals compared to the medetomidine sedated animals indicate the sensitivity of the btASL technique to variations in the magnitude of the haemodynamic response to neuronal activation. The ageing study revealed an age-related significant increase in the MTT and CTT in the absence of a change in rVLW. A corresponding decrease in rFLW and rPLW with age were calculated. The MDMA study demonstrates the sensitivity of the btASL technique to pharmacologically induced changes in cerebral perfusion. A significant decrease in the MTT and CTT was recorded in animals scanned 3 hours post MDMA administration compared to vehicle treated controls, while the rVLW did not change significantly. In this case, a corresponding increase in rFLW and rPlw was calculated for the MDMA group.

The non-compartmental model is fundamentally different from compartmental models of cerebral perfusion. The Fokker-Planck equation of the non-compartmental model describes the rate of change of the concentration of labeled water within the entire volume, V, when a bolus of labeled water flows from the labeling plane (carotid artery) to the imaging plane (capillary bed/brain tissue). Global or average parameters for the flow rate, F, and the perfusion coefficient, P are used to describe the motion of the labeled water. As a result, a complete assessment of the exact mechanisms by which labeled water is distributed within the volume is not required and it is therefore not necessary to measure locally defined parameters such as the permeability surface-area (PS) product on which two-compartmental models depend [89, 93]. In addition, the measurement of the local arterial input function, which is required for techniques such as the model-free ASL approach [1] and DSC-MRI [26], is not necessary for a quantitative assessment of cerebral perfusion.

However, due to the global nature of the parameters in the theoretical

formulation of the btASL technique, the technique is only capable of quantifying absolute transit times (MTT and CTT), while the remaining parameters (rVLW, rFLW and rPLW) are estimates for relative changes between groups or physiological conditions. As a result, the quantification of absolute CBF values is not possible. This is a considerable disadvantage of the btASL technique as the CBF is generally quantified in units of ml/gram of tissue/min (or ml/100 ml of tissue/min) by alternative ASL models such as the general kinetic model [85], the two-compartmental model [93] and the model-free approach [96].

Furthermore, as labeled water is not restricted to the vasculature, the parameters of the btASL technique are each composed of intra- and extravascular contributions. The degree to which extravascular water contributes to these parameters is not characterized by the btASL technique in its current form. Alternative ASL models are more sensitive to the effects of capillary/tissue water exchange parameters quantified by these models. For example, the general kinetic model [85] analyzes the effect of the exchange of water on the relaxation time of a labeled bolus and the resultant errors in CBF quantification. The two-compartmental model [93] describes the blood-brain system in terms of a vascular and extravascular compartment and uses the permeability surface-area product (PS) to model the exchange of water between the compartments. In future developments of the btASL technique, the intra- and extravascular components of the signal used to generate the ASL concentration-time curves may be separated through the use of diffusion-sensitized measurements [180] and the relative contributions of intra- and extravascular labeled water on the btASL parameters may be evaluated.

In the two-compartmental approach, separate T_1 values are used for the vascular and extravascular compartments, to account for the time spent by labeled water in blood before exchange to the tissue occurs [93]. The non-compartmental model in its present form only allows for a single, average T_1, measured for each ROI. Signal from both blood and tissue (grey and white matter) contribute to this average T_1 value. However, in future developments of the non-compartmental model, it may be possible to introduce separate T_1 values for blood and tissue.

The effect of an inaccurate T_1 value on the MTT and CTT quantified by

the btASL technique can been assessed by the introduction of an error term, Δr_1, into equation 2.26, the solution to the non-compartmental model for the boundary conditions of the btASL experiment. Δr_1 represents the difference between the measured ROI-specific relaxation rate used in the least squares fit, R_1, and the optimum or true relaxation rate, ${R_1}^r$:

$$R_1 = R_1^r \pm \Delta r_1. \tag{7.1}$$

The resultant change in the MTT and CTT due to this error term can be calculated as:

$$MTT_{new} = \frac{MTT_{old}}{\sqrt{1 \pm \frac{\Delta r_1}{F^2/P}}} = \frac{MTT_{old}}{\sqrt{1 \pm 4\Delta r_1 \cdot CTT_{old}}}, \tag{7.2}$$

$$CTT_{new} = \frac{CTT_{old}}{\left(1 \pm \frac{\Delta r_1}{F^2/P}\right)} = \frac{CTT_{old}}{(1 \pm 4\Delta r_1 \cdot CTT_{old})} \tag{7.3}$$

where MTT_{old} and CTT_{old} are the original MTT and CTT values and MTT_{new} and CTT_{new} are these values corrected for the Δr_1 term. It can be seen from equations 7.2 and 7.3 that if the measured T_1 is less than the optimum value, then both the MTT and CTT are underestimated and conversely, if the measured T_1 is greater than the optimum value, both the MTT and CTT are overestimated. An inaccurate T_1 value can therefore have an effect on the results obtained by the btASL technique. For example, the results of the ageing study presented in section 6.1 were obtained using the same ROI-specific T_1 values for the young, middle aged and aged groups. While the variation in T_1 in the rat brain with age is not well known, it has been suggested from human studies that T_1 increases with age [217]. If T_1 increases with age, the measured increase in MTT and CTT in the aged group, reported in section 6.1.2, would in fact be greater, if corrected for the error in T_1.

The bolus-tracking ASL sequence used for all experiments and described in detail in section 3.4 uses continuous RF pulses of 1.5 s, 2.0 s and 3.0 s duration in combination with a gradient in the direction of flow to invert arterial spins by the principle of flow-driven adiabatic inversion. By varying the delays and the duration of the labeling pulse within the ASL preparation interval (figure 3.3), the entire concentration-time curve at the imaging plane was measured. The use of a single coil to provide these long lasting inver-

sion pulses is known to produce magnetization transfer (MT) effects that cause saturation of the macromolecular pool at the imaging plane and result in a reduced signal from the free water pool in the tissue of interest (section 1.3.1). Due to the antisymmetrical nature of the MT/frequency curve, the use of distal labeling during the control experiment of the btASL sequence does not fully compensate for MT and a systematic error in the perfusion parameters of the btASL technique results. The development of a dedicated labeling coil [50, 51] for the btASL technique would remove the contribution of MT to the btASL signal. However, due to technical difficulties and budgetary limitations, a dedicated labeling coil has not yet been implemented. Alternatively, a more sophisticated labeling scheme such as the double adiabatic inversion (DAI) scheme [49] or the pseudo CASL approach [56, 57] could be used to minimize the MT effects. These approaches would also facilitate multi-slice ASL imaging.

The snapshot FLASH sequence used to acquire the labeled and control images at the imaging plane was described in section 3.4.2. The echo time (TE) and repetition time (TR) were minimized to provide optimum sensitivity to the signal amplitude changes resulting from inflowing inverted magnetization. The use of an EPI acquisition [222] instead of the FLASH approach may provide a number of advantages. Firstly, as the EPI sequence is a single excitation sequence, the amplitude change due to inflowing inverted magnetization may be larger. Furthermore, the use of single-shot double-echo EPI sequence [223] would facilitate the simultaneous measurement of the ASL and BOLD signal [68, 139], as discussed in section 1.5.1. However, while an implementation of the btASL technique with EPI image acquisition was attempted, the EPI artefacts at 7 Tesla were a major disadvantage of this approach and consequently, the FLASH sequence was used for all experiments.

7.1.1 Further Validation and Testing

As described above, the MTT and CTT were unaltered when the bolus length was varied in the validation study, while changes in both the MTT and CTT were recorded in the fMRI, ageing and MDMA studies. The fractional change in both the MTT and CTT was calculated for each of these experiments and the change in CTT was plotted against the change in MTT

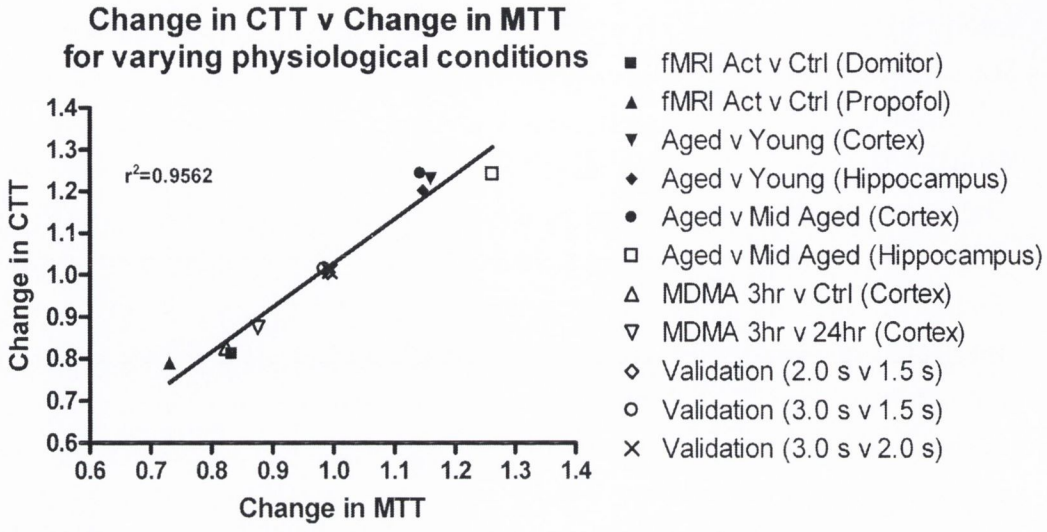

Figure 7.1: Fractional change in CTT plotted against fractional change in MTT for all experimental conditions. The data points represent the mean change in the MTT and CTT for each experiment (error bars have been omitted for clarity). A linear correlation was found, with r^2=0.9562, slope=1.059 $\pm$ 0.076 and y-intercept=-0.031 $\pm$ 0.076 respectively.

for all experiments. The fractional change in MTT and CTT were found to be highly correlated (r^2=0.96), as illustrated in figure 7.1. Furthermore, the slope of the linear regression in figure 7.1 is approximately equal to 1. When the definitions of MTT and CTT from equations 2.29 and 2.30 are considered, the following relationship can be proposed:

$$\frac{\Delta CTT}{\Delta MTT} = \frac{\Delta P}{\Delta F} \cdot \frac{\Delta F}{\Delta V} \approx 1. \tag{7.4}$$

Equation 7.4 may describe a constant relationship between the parameters of the btASL technique. However, this cannot be verified without further testing of the fit of the model to the data. Such a highly correlated linear relationship between the MTT and CTT leads to misgivings that the model may be in fact be over-fitting the data and is therefore unable to independently quantify the two parameters. The final fitting equation used in the curve fitting routine can be rewritten in terms of the MTT and CTT as follows:

$$c(V,t) = \frac{c_0}{2}\exp\left(\frac{MTT}{2CTT}\right) \times \left[\text{erfc}\left(\frac{MTT}{\sqrt{4CTT.t}} - \sqrt{\left(\frac{1}{4CTT} + \frac{1}{T_1}\right)t}\right) \times \exp\left(-\frac{MTT}{\sqrt{CTT}}\sqrt{\frac{1}{4CTT} + \frac{1}{T_1}}\right)\right]_{t=t-\tau}^{t=t} \quad (7.5)$$

This equation demonstrates the dependence of the solution on both transit times and might be used to simulate the effect varying one of the transit times has on the other transit time. For example, the MTT could be systematically incremented and the resultant effect on the CTT established. If the model can fit these parameters independently, variations in the MTT will not necessarily impact on the CTT. This simulation must be carried out before any conclusions (such as equation 7.4) can be reached about the linear relationship between the fractional change in MTT and CTT.

While the solution to the non-compartment model given by equation 7.5 appears to fit the btASL data reliably and provided consistent transit time values for varying bolus length (chapter 4), this experiment alone does not provide complete validation of the btASL technique and further validation is required. For example, the goodness of model fit should be compared to an accepted ASL model such as the general kinetic model [85] that may also provide arrival time measured that are invariant to bolus duration (section 1.4.1).

A number of additional experiments are also necessary to provide further validation and a clearer understanding of the perfusion parameters of the btASL technique. For example, in the first quantitative ASL experiments by Williams et al [13], the partial pressure of carbon dioxide (pCO_2) was altered by adding various amounts of CO_2 to the gas mixture of anaesthetized rats. A linear relationship between CBF and pCO_2 was established. An experiment investigating the changes in the parameters of the btASL technique with varying pCO_2 levels would improve the understanding of the parameters. A comparison with changes in CBF measured by a standard ASL model would also be beneficial.

The fMRI results presented in chapter 5 appear to demonstrate reproducible variations in the btASL parameters during neuronal activation. However, the actual relationship between the perfusion parameters and neural

activity has not yet been established and additional experiments are required. For example, a micro-electrode array experiment can be used to measure the electrophysiological response to systematic variations in the parameters of the electrical stimulus used for forepaw stimulation (voltage, frequency and/or duration). A subsequent btASL study in which the stimulus is varied in the same manner would allow the variations of the perfusion parameters for varying stimuli to be compared to the electrophysiological response. Furthermore, a comparison between a standard BOLD fMRI protocol and the btASL technique under these conditions may be used to investigate if the potential advantages of ASL fMRI over BOLD fMRI (section 1.5.1) are valid for btASL.

7.2 Conclusions and perspectives

The findings of the btASL technique presented herein demonstrate the potential the technique holds for future developments and applications in the field of neuroscience. Imaging techniques that are capable of quantifying changes in cerebral persuion that occur due to both normal and diseased ageing are of great interest to the neuroscience community as they can provide a useful insight into changes in the functional cerebrovascular system with age [224]. The sensitivity of the btASL technique to differences in the haemodynamic response to neuronal activation under varying conditions was demonstrated in section 5.2.3. These results hold potential for future fMRI applications, particularly when the age related changes in resting cerebral perfusion presented in section 6.1 are also taken into account. A btASL fMRI study comparing the haemodynamic response to neuronal activation in young and healthy aged animals may provide a novel quantitative assessment of the variations in this response with age. The development of reliable experimental methods for animal fMRI (described in section 3.2.2) facilitates future longitudinal btASL fMRI studies. For example, through the use of transgenic mouse [225] or rat [226] models of Alzheimer's disease (AD), changes in the haemodynamic response to neuronal activation due to the progression of the disease can be tracked over time in the same animal and the variations in the parameters quantified by the btASL technique would be of interest.

The results of the MDMA study demonstrate the suitability of the btASL technique for studying perfusion-altering pharmaceutical agents. The finding of this study was that the increase in the rFLW and rPLW in the acute phase following administration of the drug was most likely due to a transient increase in both temperature (hyperthermia) and blood pressure (hypertension). Therefore, future btASL studies on the effects of recreational drugs such as cocaine, which is also known to alter brain haemodynamics [227], may be of interest. Furthermore, the measured differences in the medetomidine and propofol results of the fMRI study were concluded to be due in part to the vasopressor and vasodilatation effects of the respective drugs. This finding demonstrates the potential usefulness of btASL for the assessment of the vasodilatation and vasoconstriction effects of various anaesthetic agents on the microvasculature.

In summary, a novel approach to quantifying cerebral perfusion, btASL, has been developed and used to quantify changes in cerebral perfusion under varying physiological conditions. While further validation and testing of the technique (section 7.1.1) as well as future developments of both the non-compartmental model and the ASL method (section 7.1) are required, the findings presented demonstrate the potential of btASL to provide interesting results in future applications in the field of neuroscience.

Appendix A

Data Tables

Table A.1: **Validation study transit times.** MTT and CTT obtained from least-squares fit of the theoretical model to data from the cerebral cortex (CC), hippocampus (HC) and whole brain (WB) of three male Wistar rats.

Animal	ROI	Bolus (s)	MTT (s)	CTT (s)
1	CC	1.5	1.78 ± 0.26	1.48 ± 0.21
1	CC	2.0	1.78 ± 0.17	1.45 ± 0.13
1	CC	3.0	1.72 ± 0.28	1.40 ± 0.22
1	HC	1.5	1.69 ± 0.17	1.36 ± 0.13
1	HC	2.0	1.74 ± 0.22	1.40 ± 0.17
1	HC	3.0	1.73 ± 0.23	1.38 ± 0.21
1	WB	1.5	1.79 ± 0.21	1.45 ± 0.17
1	WB	2.0	1.78 ± 0.19	1.45 ± 0.15
1	WB	3.0	1.81 ± 0.15	1.48 ± 0.12
2	CC	1.5	1.81 ± 0.20	1.51 ± 0.16
2	CC	2.0	1.83 ± 0.25	1.55 ± 0.21
2	CC	3.0	1.86 ± 0.17	1.57 ± 0.14
2	HC	1.5	1.73 ± 0.26	1.43 ± 0.21
2	HC	2.0	1.74 ± 0.23	1.45 ± 0.18
2	HC	3.0	1.77 ± 0.22	1.49 ± 0.17
2	WB	1.5	1.80 ± 0.33	1.58 ± 0.28
2	WB	2.0	1.89 ± 0.32	1.61 ± 0.27
2	WB	3.0	1.91 ± 0.33	1.66 ± 0.28
3	CC	1.5	1.70 ± 0.24	1.34 ± 0.18
3	CC	2.0	1.69 ± 0.13	1.32 ± 0.10
3	CC	3.0	1.67 ± 0.17	1.27 ± 0.13
3	HC	1.5	1.63 ± 0.21	1.29 ± 0.16
3	HC	2.0	1.63 ± 0.24	1.28 ± 0.18
3	HC	3.0	1.65 ± 0.16	1.31 ± 0.12
3	WB	1.5	1.71 ± 0.07	1.32 ± 0.15
3	WB	2.0	1.70 ± 0.26	1.33 ± 0.19
3	WB	3.0	1.74 ± 0.21	1.40 ± 0.17

Table A.2: **Validation study rVLW**. Calculation of rVLW from A_0 fitting parameter (normalised by degree of inversion, α) from least-squares fit of the theoretical model to data for the cerebral cortex (CC), hippocampus (HC) and whole brain (WB) of three male Wistar rats.

Animal	ROI	Bolus (s)	A_0	α	rVLW (a.u.)
1	CC	1.5	0.12 ± 0.02	0.85 ± 0.02	0.14 ± 0.04
1	CC	2.0	0.13 ± 0.02	0.88 ± 0.01	0.15 ± 0.03
1	CC	3.0	0.11 ± 0.01	0.92 ± 0.01	0.12 ± 0.02
1	HC	1.5	0.10 ± 0.03	0.85 ± 0.02	0.12 ± 0.05
1	HC	2.0	0.12 ± 0.02	0.88 ± 0.01	0.14 ± 0.03
1	HC	3.0	0.11 ± 0.02	0.92 ± 0.01	0.12 ± 0.03
1	WB	1.5	0.12 ± 0.03	0.85 ± 0.02	0.14 ± 0.05
1	WB	2.0	0.12 ± 0.03	0.88 ± 0.01	0.13 ± 0.04
1	WB	3.0	0.12 ± 0.03	0.92 ± 0.01	0.13 ± 0.04
2	CC	1.5	0.10 ± 0.02	0.86 ± 0.02	0.11 ± 0.04
2	CC	2.0	0.10 ± 0.02	0.91 ± 0.04	0.10 ± 0.05
2	CC	3.0	0.09 ± 0.03	0.87 ± 0.02	0.10 ± 0.05
2	HC	1.5	0.10 ± 0.02	0.86 ± 0.02	0.12 ± 0.04
2	HC	2.0	0.10 ± 0.02	0.91 ± 0.04	0.11 ± 0.03
2	HC	3.0	0.09 ± 0.03	0.87 ± 0.02	0.11 ± 0.04
2	WB	1.5	0.10 ± 0.02	0.86 ± 0.02	0.12 ± 0.04
2	WB	2.0	0.10 ± 0.02	0.91 ± 0.04	0.12 ± 0.05
2	WB	3.0	0.10 ± 0.01	0.87 ± 0.02	0.12 ± 0.03
3	CC	1.5	0.10 ± 0.03	0.92 ± 0.02	0.10 ± 0.05
3	CC	2.0	0.09 ± 0.01	0.87 ± 0.03	0.11 ± 0.04
3	CC	3.0	0.10 ± 0.02	0.88 ± 0.01	0.12 ± 0.03
3	HC	1.5	0.09 ± 0.02	0.92 ± 0.02	0.10 ± 0.04
3	HC	2.0	0.09 ± 0.03	0.87 ± 0.03	0.10 ± 0.05
3	HC	3.0	0.09 ± 0.02	0.88 ± 0.01	0.10 ± 0.03
3	WB	1.5	0.11 ± 0.01	0.92 ± 0.02	0.12 ± 0.03
3	WB	2.0	0.11 ± 0.03	0.87 ± 0.03	0.12 ± 0.05
3	WB	3.0	0.10 ± 0.02	0.88 ± 0.01	0.12 ± 0.03

Table A.3: **fMRI study medetomidine transit times**. MTT and CTT in the S1FL region measured during resting state (ctrl) and electrical stimulation of the forepaw(act) under medetomidine sedation.

Animal	MTT_{ctrl} (s)	CTT_{ctrl} (s)	MTT_{act} (s)	CTT_{act} (s)
1	1.98 ± 0.12	1.53 ± 0.09	1.64 ± 0.06	1.05 ± 0.04
2	1.95 ± 0.14	1.48 ± 0.10	1.52 ± 0.10	1.17 ± 0.08
3	2.20 ± 0.12	1.71 ± 0.09	1.97 ± 0.13	1.56 ± 0.10
4	1.74 ± 0.18	1.61 ± 0.16	1.51 ± 0.11	1.43 ± 0.10
5	1.83 ± 0.13	1.71 ± 0.12	1.45 ± 0.13	1.32 ± 0.17

Table A.4: **fMRI study medetomidine rVLW**. Calculation of the increase in rVLW in the S1FL region during neuronal activation of the S1FL region under medetomidine sedation.

Animal	Amp_{ctrl}	Amp_{act}	α_{ctrl}	α_{act}	$\frac{rVLW_{act}}{rVLW_{ctrl}}$
1	0.08 ± 0.01	0.09 ± 0.01	0.87 ± 0.05	0.91 ± 0.04	1.12 ± 0.16
2	0.08 ± 0.01	0.09 ± 0.01	0.91 ± 0.02	0.92 ± 0.05	1.12 ± 0.22
3	0.07 ± 0.01	0.08 ± 0.01	0.85 ± 0.03	0.85 ± 0.04	0.12 ± 0.17
4	0.07 ± 0.02	0.09 ± 0.01	0.84 ± 0.09	0.87 ± 0.06	0.13 ± 0.26
5	0.09 ± 0.01	0.09 ± 0.02	0.96 ± 0.04	0.94 ± 0.07	0.13 ± 0.20

Table A.5: **fMRI study propofol transit times**. MTT and CTT in the S1FL region measured during resting state (ctrl) and electrical stimulation of the forepaw(act) under propofol anaesthesia.

Animal	MTT_{ctrl} (s)	CTT_{ctrl} (s)	MTT_{act} (s)	CTT_{act} (s)
1	1.88 ± 0.15	1.68 ± 0.13	1.35 ± 0.13	1.40 ± 0.12
2	1.98 ± 0.19	1.65 ± 0.15	1.36 ± 0.14	1.21 ± 0.12
3	1.81 ± 0.19	1.63 ± 0.17	1.53 ± 0.12	1.60 ± 0.12
4	2.10 ± 0.37	1.90 ± 0.33	1.48 ± 0.16	1.41 ± 0.14
5	2.09 ± 0.29	1.92 ± 0.26	1.49 ± 0.21	1.32 ± 0.18

Table A.6: **fMRI study propofol rVLW**.Calculation of the increase in rVLW in the S1FL region during neuronal activation under propofol anaesthesia

Animal	Amp_{ctrl}	Amp_{act}	α_{ctrl}	α_{act}	$\frac{rVLW_{act}}{rVLW_{ctrl}}$
1	0.10 ± 0.01	0.12 ± 0.02	0.94 ± 0.04	0.93 ± 0.05	1.14 ± 0.17
2	0.10 ± 0.01	0.12 ± 0.02	0.93 ± 0.03	0.94 ± 0.03	1.15 ± 0.22
3	0.09 ± 0.02	0.12 ± 0.01	0.93 ± 0.05	0.92 ± 0.05	1.34 ± 0.20
4	0.09 ± 0.02	0.12 ± 0.02	0.91 ± 0.06	0.91 ± 0.04	1.39 ± 0.29
5	0.10 ± 0.02	0.13 ± 0.03	0.93 ± 0.06	0.90 ± 0.04	1.19 ± 0.27

Table A.7: **Aging study transit times and rVLW for the cerebral cortex ROI.** MTT, CTT, amplitude, degree of inversion (α) and rVLW for the cerebral cortex ROI of young (Y), middle aged (MA) and aged (A) groups.

Animal	MTT (s)	CTT (s)	Amplitude	α	rVLW
Y1	1.99 ± 0.31	1.63 ± 0.25	0.09 ± 0.02	0.94 ± 0.06	0.10 ± 0.02
Y2	2.05 ± 0.22	1.50 ± 0.16	0.09 ± 0.02	0.88 ± 0.04	0.11 ± 0.05
Y3	2.01 ± 0.38	1.68 ± 0.31	0.10 ± 0.03	0.92 ± 0.01	0.11 ± 0.03
Y4	1.97 ± 0.28	1.74 ± 0.24	0.09 ± 0.02	0.76 ± 0.04	0.12 ± 0.06
Y5	1.81 ± 0.17	1.40 ± 0.12	0.12 ± 0.02	0.95 ± 0.02	0.12 ± 0.04
Y6	1.91 ± 0.38	1.44 ± 0.27	0.10 ± 0.03	0.92 ± 0.03	0.10 ± 0.04
Y7	1.93 ± 0.19	1.70 ± 0.16	0.09 ± 0.01	0.94 ± 0.06	0.10 ± 0.04
Y8	1.93 ± 0.38	1.64 ± 0.32	0.12 ± 0.03	0.93 ± 0.02	0.13 ± 0.03
Y9	1.88 ± 0.25	1.48 ± 0.19	0.12 ± 0.02	0.87 ± 0.04	0.14 ± 0.05
MA1	1.98 ± 0.31	1.77 ± 0.27	0.08 ± 0.02	0.93 ± 0.02	0.09 ± 0.04
MA2	1.94 ± 0.34	1.56 ± 0.27	0.07 ± 0.02	0.92 ± 0.04	0.08 ± 0.05
MA3	1.95 ± 0.31	1.53 ± 0.24	0.09 ± 0.03	0.78 ± 0.02	0.11 ± 0.03
MA4	1.92 ± 0.22	1.44 ± 0.16	0.10 ± 0.02	0.87 ± 0.02	0.12 ± 0.03
MA5	2.06 ± 0.20	1.49 ± 0.14	0.10 ± 0.01	0.95 ± 0.03	0.10 ± 0.04
A1	2.67 ± 0.40	2.37 ± 0.26	0.08 ± 0.01	0.97 ± 0.01	0.08 ± 0.02
A2	2.16 ± 0.26	1.68 ± 0.20	0.09 ± 0.02	0.94 ± 0.02	0.10 ± 0.03
A3	2.09 ± 0.24	1.80 ± 0.20	0.11 ± 0.02	0.90 ± 0.04	0.12 ± 0.05
A4	2.02 ± 0.35	1.79 ± 0.25	0.10 ± 0.02	0.89 ± 0.02	0.11 ± 0.03
A5	2.32 ± 0.35	2.06 ± 0.23	0.09 ± 0.01	0.95 ± 0.02	0.09 ± 0.03

Table A.8: **Aging study transit times and rVLW for the hippocampus ROI**. MTT, CTT, amplitude, degree of inversion (α) and rVLW for the hippocampus ROI of young (Y), middle aged (MA) and aged (A) groups.

Animal	MTT (s)	CTT (s)	Amplitude	α	rVLW
Y1	1.92 ± 0.21	1.69 ± 0.18	0.09 ± 0.02	0.94 ± 0.06	0.10 ± 0.05
Y2	2.00 ± 0.21	1.46 ± 0.15	0.10 ± 0.02	0.88 ± 0.04	0.11 ± 0.04
Y3	1.75 ± 0.26	1.40 ± 0.20	0.10 ± 0.03	0.92 ± 0.01	0.11 ± 0.04
Y4	2.07 ± 0.24	1.76 ± 0.20	0.08 ± 0.02	0.76 ± 0.04	0.11 ± 0.05
Y5	2.09 ± 0.32	1.88 ± 0.28	0.13 ± 0.02	0.95 ± 0.02	0.13 ± 0.04
Y6	1.94 ± 0.34	1.46 ± 0.25	0.10 ± 0.03	0.92 ± 0.03	0.11 ± 0.05
Y7	1.83 ± 0.19	1.44 ± 0.15	0.10 ± 0.02	0.94 ± 0.06	0.10 ± 0.04
Y8	1.90 ± 0.29	1.43 ± 0.21	0.11 ± 0.03	0.93 ± 0.02	0.12 ± 0.03
Y9	2.00 ± 0.34	1.60 ± 0.26	0.12 ± 0.03	0.87 ± 0.04	0.13 ± 0.04
MA1	1.54 ± 0.14	1.36 ± 0.13	0.09 ± 0.02	0.93 ± 0.02	0.10 ± 0.04
MA2	1.81 ± 0.33	1.40 ± 0.25	0.08 ± 0.03	0.92 ± 0.04	0.09 ± 0.05
MA3	1.88 ± 0.36	1.69 ± 0.32	0.09 ± 0.03	0.78 ± 0.02	0.12 ± 0.04
MA4	1.68 ± 0.20	1.45 ± 0.17	0.09 ± 0.02	0.87 ± 0.02	0.10 ± 0.03
MA5	1.92 ± 0.19	1.70 ± 0.16	0.09 ± 0.01	0.95 ± 0.03	0.09 ± 0.03
A1	2.19 ± 0.34	1.75 ± 0.26	0.08 ± 0.02	0.97 ± 0.01	0.09 ± 0.02
A2	2.03 ± 0.28	1.89 ± 0.25	0.10 ± 0.02	0.94 ± 0.02	0.11 ± 0.03
A3	2.53 ± 0.33	2.01 ± 0.25	0.13 ± 0.02	0.90 ± 0.04	0.14 ± 0.04
A4	2.09 ± 0.37	1.80 ± 0.31	0.10 ± 0.02	0.89 ± 0.02	0.11 ± 0.03
A5	2.30 ± 0.29	1.98 ± 0.25	0.09 ± 0.02	0.95 ± 0.02	0.10 ± 0.03

Table A.9: **Aging study transit times and rVLW for the whole brain ROI.** MTT, CTT, amplitude, degree of inversion (α) and rVLW for the whole brain ROI of young (Y), middle aged (MA) and aged (A) groups.

Animal	MTT (s)	CTT (s)	Amplitude	α	rVLW
Y1	1.92 ± 0.25	1.58 ± 0.20	0.09 ± 0.02	0.10 ± 0.06	0.10 ± 0.03
Y2	1.95 ± 0.18	1.46 ± 0.13	0.11 ± 0.02	0.13 ± 0.04	0.13 ± 0.04
Y3	2.09 ± 0.32	1.73 ± 0.26	0.10 ± 0.02	0.11 ± 0.01	0.11 ± 0.03
Y4	1.93 ± 0.18	1.68 ± 0.15	0.09 ± 0.01	0.12 ± 0.04	0.12 ± 0.03
Y5	1.81 ± 0.14	1.55 ± 0.11	0.13 ± 0.01	0.13 ± 0.02	0.13 ± 0.04
Y6	1.86 ± 0.31	1.56 ± 0.25	0.11 ± 0.03	0.12 ± 0.03	0.12 ± 0.05
Y7	1.69 ± 0.15	1.50 ± 0.12	0.09 ± 0.01	0.10 ± 0.06	0.10 ± 0.03
Y8	1.76 ± 0.25	1.56 ± 0.21	0.12 ± 0.02	0.13 ± 0.02	0.13 ± 0.03
Y9	1.93 ± 0.24	1.68 ± 0.20	0.12 ± 0.02	0.14 ± 0.04	0.14 ± 0.04
MA1	1.73 ± 0.21	1.46 ± 0.17	0.09 ± 0.02	0.10 ± 0.02	0.10 ± 0.03
MA2	2.06 ± 0.26	1.71 ± 0.21	0.09 ± 0.02	0.10 ± 0.04	0.10 ± 0.04
MA3	1.83 ± 0.27	1.63 ± 0.23	0.11 ± 0.02	0.14 ± 0.02	0.14 ± 0.03
MA4	1.82 ± 0.17	1.40 ± 0.12	0.09 ± 0.02	0.11 ± 0.02	0.11 ± 0.03
MA5	1.84 ± 0.19	1.62 ± 0.17	0.10 ± 0.02	0.10 ± 0.03	0.10 ± 0.04
A1	2.03 ± 0.32	1.75 ± 0.27	0.09 ± 0.02	0.09 ± 0.01	0.09 ± 0.02
A2	1.89 ± 0.18	1.70 ± 0.16	0.11 ± 0.01	0.11 ± 0.02	0.11 ± 0.02
A3	1.93 ± 0.16	1.67 ± 0.13	0.11 ± 0.01	0.12 ± 0.04	0.12 ± 0.04
A4	1.92 ± 0.20	1.58 ± 0.16	0.11 ± 0.02	0.12 ± 0.02	0.12 ± 0.03
A5	2.11 ± 0.32	1.72 ± 0.25	0.09 ± 0.02	0.01 ± 0.02	0.10 ± 0.02

Table A.10: **MDMA study transit times and rVLW for the right cerebral cortex ROI.** MTT, CTT, amplitude, degree of inversion (α) and rVLW for the right cerebral cortex ROI of each animal in the control (ctrl), 3 hour post MDMA administration (3hr) and 24 hr post MDMA administration (24hr) groups.

Animal	MTT (s)	CTT (s)	Amplitude	α	rVLW
Ctrl 1	1.09 ± 0.16	1.48 ± 0.12	0.10 ± 0.01	0.94 ± 0.02	0.10 ± 0.02
Ctrl 2	1.97 ± 0.29	1.67 ± 0.24	0.10 ± 0.02	0.95 ± 0.03	0.11 ± 0.04
Ctrl 3	1.96 ± 0.32	1.54 ± 0.24	0.10 ± 0.03	0.94 ± 0.01	0.11 ± 0.03
Ctrl 4	1.88 ± 0.21	1.56 ± 0.17	0.09 ± 0.02	0.93 ± 0.01	0.10 ± 0.02
3hr 1	1.80 ± 0.25	1.42 ± 0.19	0.12 ± 0.02	0.94 ± 0.01	0.12 ± 0.02
3hr 2	1.43 ± 0.09	1.23 ± 0.07	0.09 ± 0.01	0.93 ± 0.02	0.10 ± 0.03
3hr 3	1.75 ± 0.19	1.36 ± 0.15	0.10 ± 0.02	0.95 ± 0.03	0.10 ± 0.04
3hr 4	1.43 ± 0.17	1.22 ± 0.14	0.10 ± 0.02	0.92 ± 0.04	0.11 ± 0.05
3hr 5	1.49 ± 0.08	1.24 ± 0.06	0.10 ± 0.01	0.93 ± 0.03	0.11 ± 0.02
24hr 1	1.55 ± 0.13	1.28 ± 0.10	0.09 ± 0.02	0.92 ± 0.02	0.10 ± 0.03
24hr 2	1.84 ± 0.31	1.47 ± 0.24	0.09 ± 0.03	0.94 ± 0.01	0.10 ± 0.03
24hr 3	1.61 ± 0.17	1.31 ± 0.14	0.10 ± 0.02	0.95 ± 0.03	0.10 ± 0.04
24hr 4	2.16 ± 0.23	1.90 ± 0.20	0.08 ± 0.01	0.92 ± 0.04	0.09 ± 0.03
24hr 5	1.78 ± 0.19	1.40 ± 0.14	0.10 ± 0.02	0.92 ± 0.03	0.11 ± 0.05

Table A.11: **MDMA study transit times and rVLW for the left cerebral cortex ROI.** MTT, CTT, amplitude, degree of inversion (α) and rVLW for the left cerebral cortex ROI of each animal in the control (ctrl), 3 hour post MDMA administration (3hr) and 24 hr post MDMA administration (24hr) groups.

Animal	MTT (s)	CTT (s)	Amplitude	α	rVLW
Ctrl 1	2.03 ± 0.28	1.69 ± 0.22	0.10 ± 0.02	0.94 ± 0.02	0.10 ± 0.03
Ctrl 2	1.80 ± 0.17	1.43 ± 0.13	0.10 ± 0.02	0.95 ± 0.03	0.11 ±0.04
Ctrl 3	1.83 ± 0.15	1.47 ± 0.12	0.10 ± 0.02	0.94 ± 0.01	0.11 ±0.02
Ctrl 4	1.88 ± 0.31	1.67 ± 0.26	0.10 ± 0.03	0.93 ± 0.01	0.10 ±0.03
3hr 1	1.82 ± 0.19	1.39 ± 0.14	0.11 ± 0.02	0.94 ± 0.01	0.12 ±0.02
3hr 2	1.45 ± 0.07	1.23 ± 0.06	0.09 ± 0.01	0.93 ± 0.02	0.10 ±0.03
3hr 3	1.59 ± 0.10	1.29 ± 0.08	0.10 ± 0.01	0.95 ± 0.03	0.10 ±0.03
3hr 4	1.42 ± 0.14	1.21 ± 0.12	0.10 ± 0.02	0.92 ± 0.04	0.11 ±0.04
3hr 5	1.54 ± 0.21	1.26 ± 0.16	0.11 ± 0.03	0.93 ± 0.03	0.12 ±0.05
24hr 1	1.75 ± 0.24	1.38 ± 0.18	0.10 ± 0.03	0.92 ± 0.02	0.11 ±0.04
24hr 2	1.55 ± 0.23	1.28 ± 0.18	0.09 ± 0.03	0.94 ± 0.01	0.10 ±0.03
24hr 3	1.81 ± 0.17	1.45 ± 0.13	0.10 ± 0.02	0.95 ± 0.03	0.10 ±0.04
24hr 4	2.21 ± 0.30	1.89 ± 0.25	0.08 ± 0.02	0.92 ± 0.04	0.09 ±0.04
24hr 5	1.67 ± 0.20	1.34 ± 0.15	0.09 ± 0.02	0.92 ± 0.03	0.10 ± 0.04

Table A.12: **MDMA study transit times and rVLW for the right striatum ROI.** MTT, CTT, amplitude, degree of inversion (α) and rVLW for the right striatum ROI of each animal in the control (ctrl), 3 hour post MDMA administration (3hr) and 24 hr post MDMA administration (24hr) groups.

Animal	MTT (s)	CTT (s)	Amplitude	α	rVLW
Ctrl 1	1.71 ± 0.15	1.34 ± 0.11	0.10 ± 0.02	0.94 ± 0.02	0.11 ± 0.03
Ctrl 2	2.02 ± 0.26	1.77 ± 0.22	0.09 ± 0.02	0.95 ± 0.03	0.10 ± 0.04
Ctrl 3	1.75 ± 0.12	1.43 ± 0.01	0.10 ± 0.01	0.94 ± 0.01	0.10 ± 0.02
Ctrl 4	1.73 ± 0.19	1.50 ± 0.16	0.09 ± 0.02	0.93 ± 0.01	0.10 ± 0.02
3hr 1	1.76 ± 0.11	1.50 ± 0.09	0.10 ± 0.01	0.94 ± 0.01	0.10 ± 0.02
3hr 2	1.75 ± 0.18	1.43 ± 0.14	0.10 ± 0.02	0.93 ± 0.02	0.10 ± 0.03
3hr 3	1.73 ± 0.26	1.51 ± 0.22	0.10 ± 0.03	0.95 ± 0.03	0.10 ± 0.05
3hr 4	1.49 ± 0.16	1.26 ± 0.12	0.10 ± 0.02	0.92 ± 0.04	0.11 ± 0.05
3hr 5	2.07 ± 0.19	1.62 ± 0.14	0.10 ± 0.02	0.93 ± 0.03	0.11 ± 0.04
24hr 1	1.70 ± 0.13	1.31 ± 0.09	0.09 ± 0.02	0.92 ± 0.02	0.11 ± 0.03
24hr 2	1.73 ± 0.17	1.50 ± 0.14	0.09 ± 0.02	0.94 ± 0.01	0.10 ± 0.02
24hr 3	1.55 ± 0.21	1.39 ± 0.18	0.10 ± 0.03	0.95 ± 0.03	0.10 ± 0.04
24hr 4	1.73 ± 0.27	1.50 ± 0.23	0.09 ± 0.03	0.92 ± 0.04	0.10 ± 0.05
24hr 5	1.70 ± 0.22	1.44 ± 0.18	0.10 ± 0.02	0.92 ± 0.03	0.10 ± 0.04

Table A.13: **MDMA study transit times and rVLW for the left striatum ROI.** MTT, CTT, amplitude, degree of inversion ($/alpha$) and rVLW for the left striatum ROI of each animal in the control (ctrl), 3 hour post MDMA administration (3hr) and 24 hr post MDMA administration (24hr) groups.

Animal	MTT (s)	CTT (s)	Amplitude	α	rVLW
Ctrl 1	1.92 ± 0.18	1.46 ± 0.13	0.10 ± 0.02	0.94 ± 0.02	0.11 ± 0.03
Ctrl 2	1.94 ± 0.13	1.59 ± 0.10	0.10 ± 0.01	0.95 ± 0.03	0.10 ± 0.03
Ctrl 3	1.75 ± 0.21	1.50 ± 0.18	0.09 ± 0.02	0.94 ± 0.01	0.10 ± 0.02
Ctrl 4	2.10 ± 0.26	1.73 ± 0.21	0.10 ± 0.02	0.93 ± 0.01	0.10 ± 0.02
3hr 1	1.84 ± 0.15	1.43 ± 0.11	0.11 ± 0.02	0.94 ± 0.01	0.12 ± 0.02
3hr 2	2.11 ± 0.35	1.58 ± 0.26	0.10 ± 0.03	0.93 ± 0.02	0.11 ± 0.04
3hr 3	2.29 ± 0.37	1.84 ± 0.29	0.10 ± 0.02	0.95 ± 0.03	0.10 ± 0.04
3hr 4	1.88 ± 0.28	1.52 ± 0.22	0.10 ± 0.03	0.92 ± 0.04	0.11 ± 0.05
3hr 5	1.90 ± 0.21	1.54 ± 0.17	0.10 ± 0.02	0.93 ± 0.03	0.11 ± 0.04
24hr 1	1.37 ± 0.10	1.19 ± 0.08	0.10 ± 0.02	0.92 ± 0.02	0.11 ± 0.03
24hr 2	1.84 ± 0.25	1.69 ± 0.22	0.09 ± 0.02	0.94 ± 0.01	0.10 ± 0.02
24hr 3	1.77 ± 0.29	1.53 ± 0.24	0.09 ± 0.03	0.95 ± 0.03	0.10 ± 0.04
24hr 4	2.09 ± 0.38	1.86 ± 0.33	0.07 ± 0.03	0.92 ± 0.04	0.08 ± 0.03
24hr 5	1.81 ± 0.26	1.59 ± 0.22	0.09 ± 0.02	0.92 ± 0.03	0.10 ± 0.04

Bibliography

[1] E. T. Petersen, I. Zimine, Y. C. Ho, and X. Golay. Non-invasive measurement of perfusion: a critical review of arterial spin labelling techniques. *Br J Radiol*, 79:688–701, 2006.

[2] B. A. Bell. A history of the study of the cerebral circulation and the measurement of cerebral blood flow. *Neurosurgery*, 14:238–246, 1984.

[3] M. Wintermark, M. Sesay, E. Barbier, K. Borbly, W. P. Dillon, J. D. Eastwood, T. C. Glenn, C. B. Grandin, S. Pedraza, J. F. Soustiel, T. Nariai, G. Zaharchuk, J. M. Caill, V. Dousset, and H. Yonas. Comparative overview of brain perfusion imaging techniques. *J Neuroradiol*, 32:294–314, 2005.

[4] M. D. Stern. In vivo evaluation of microcirculation by coherent light scattering. *Nature*, 254:56–58, 1975.

[5] W. Denk, J. H. Strickler, and W. W. Webb. Two-photon laser scanning fluorescence microscopy. *Science*, 248:73–76, 1990.

[6] JD Briers and S. Webster. Laser speckle contrast analysis (LASCA): a nonscanning, full-field technique for monitoring capillary blood flow. *J Biomed Opt*, 1:174, 1996.

[7] P. Herscovitch, J. Markham, and M. E. Raichle. Brain blood flow measured with intravenous H2(15)O. I. Theory and error analysis. *J Nucl Med*, 24:782–789, 1983.

[8] W. D. Obrist, H. K. Thompson, C. H. King, and H. S. Wang. Determination of regional cerebral blood flow by inhalation of 133-Xenon. *Circ Res*, 20:124–135, 1967.

[9] F. Kelcz, S. K. Hilal, P. Hartwell, and P. M. Joseph. Computed tomographic measurement of the xenon brain-blood partition coefficient and implications for regional cerebral blood flow: a preliminary report. *Radiology*, 127:385–392, 1978.

[10] J. D. Eastwood, M. H. Lev, and J. M. Provenzale. Perfusion CT with iodinated contrast material. *AJR Am J Roentgenol*, 180:3–12, 2003.

[11] P. W. Leopold, A. A. Shandall, P. Feustel, J. D. Corson, D. M. Shah, A. J. Popp, J. B. Fortune, R. P. Leather, and A. M. Karmody. Duplex scanning of the internal carotid artery: an assessment of cerebral blood flow. *Br J Surg*, 74:630–633, 1987.

[12] B. R. Rosen, J. W. Belliveau, J. M. Vevea, and T. J. Brady. Perfusion imaging with NMR contrast agents. *Magn Reson Med*, 14:249–265, 1990.

[13] D. S. Williams, J. A. Detre, J. S. Leigh, and A. P. Koretsky. Magnetic resonance imaging of perfusion using spin inversion of arterial water. *Proc. Natl. Acad. Sci. U.S.A.*, 89:212–216, 1992.

[14] J. A. Detre, J. S. Leigh, D. S. Williams, and A. P. Koretsky. Perfusion imaging. *Magn Reson Med*, 23:37–45, 1992.

[15] J. F. Soustiel, E. Levy, M. Zaaroor, R. Bibi, S. Lukaschuk, and D. Manor. A new angle-independent Doppler ultrasonic device for assessment of blood flow volume in the extracranial internal carotid artery. *J Ultrasound Med*, 21:1405–1412, 2002.

[16] G. K. Aguirre, J. A. Detre, E. Zarahn, and D. C. Alsop. Experimental design and the relative sensitivity of BOLD and perfusion fMRI. *Neuroimage*, 15:488–500, 2002.

[17] G. G. Brown, L. T. Eyler Zorrilla, B. Georgy, S. S. Kindermann, E. C. Wong, and R. B. Buxton. BOLD and perfusion response to finger-thumb apposition after acetazolamide administration: differential relationship to global perfusion. *J Cereb Blood Flow Metab*, 23:829–837, 2003.

[18] C. B. Grandin. Assessment of brain perfusion with MRI: methodology and application to acute stroke. *Neuroradiology*, 45:755–766, 2003.

[19] B. M. Ances, M. L. McGarvey, J. M. Abrahams, J. A. Maldjian, D. C. Alsop, E. L. Zager, and J. A. Detre. Continuous arterial spin labeled perfusion magnetic resonance imaging in patients before and after carotid endarterectomy. *J Neuroimaging*, 14:133–138, 2004.

[20] D. C. Alsop, J. A. Detre, and M. Grossman. Assessment of cerebral blood flow in Alzheimer's disease by spin-labeled magnetic resonance imaging. *Ann Neurol*, 47:93–100, 2000.

[21] S. Lui, L. M. Parkes, X. Huang, K. Zou, R. C. Chan, H. Yang, L. Zou, D. Li, H. Tang, T. Zhang, X. Li, Y. Wei, L. Chen, X. Sun, G. J. Kemp, and Q. Y. Gong. Depressive disorders: focally altered cerebral perfusion measured with arterial spin-labeling MR imaging. *Radiology*, 251:476–484, 2009.

[22] A. C. Silva, S. G. Kim, and M. Garwood. Imaging blood flow in brain tumors using arterial spin labeling. *Magn Reson Med*, 44:169–173, 2000.

[23] S. S. Kety and C. F. Schmidt. The nitrous oxide method for the quantitative determination of cerebral blood flow in man; theory, procedure and normal values. *J Clin Invest*, 27:476–483, 1948.

[24] P. Meier and K. L. Zierler. On the theory of the indicator-dilution method for measurement of blood flow and volume. *J Appl Physiol*, 6:731–744, 1954.

[25] G. N. Stewart. Researches on the Circulation Time in Organs and on the Influences which affect it: Parts I.-III. *J Physiol (Lond)*, 15:1–89, 1893.

[26] L. Østergaard, R. M. Weisskoff, D. A. Chesler, C. Gyldensted, and B. R. Rosen. High resolution measurement of cerebral blood flow using intravascular tracer bolus passages. Part I: Mathematical approach and statistical analysis. *Magn Reson Med*, 36:715–725, 1996.

[27] K. K. Kwong, J. W. Belliveau, D. A. Chesler, I. E. Goldberg, R. M. Weisskoff, B. P. Poncelet, D. N. Kennedy, B. E. Hoppel, M. S. Cohen, and R. Turner. Dynamic magnetic resonance imaging of human brain activity during primary sensory stimulation. *Proc Natl Acad Sci USA.*, 89:5675–5679, 1992.

[28] E. L. Barbier, L. Lamalle, and M. Dcorps. Methodology of brain perfusion imaging. *J Magn Reson Imaging*, 13:496–520, 2001.

[29] F. Calamante, D. L. Thomas, G. S. Pell, J. Wiersma, and R. Turner. Measuring cerebral blood flow using magnetic resonance imaging techniques. *J Cereb Blood Flow Metab*, 19:701–735, 1999.

[30] W. T. Dixon, L. N. Du, D. D. Faul, M. Gado, and S. Rossnick. Projection angiograms of blood labeled by adiabatic fast passage. *Magn Reson Med*, 3:454–462, 1986.

[31] A Abragam. *The Principles of Nuclear Magnetism*. Oxford: Clarendon Press, 1961.

[32] W. Zhang, D. S. Williams, and A. P. Koretsky. Measurement of rat brain perfusion by NMR using spin labeling of arterial water: in vivo determination of the degree of spin labeling. *Magn Reson Med*, 29:416–421, 1993.

[33] L. Maccotta, J. A. Detre, and D. C. Alsop. The efficiency of adiabatic inversion for perfusion imaging by arterial spin labeling. *NMR Biomed*, 10:216–221, 1997.

[34] J. F. Utting, D. L. Thomas, D. G. Gadian, and R. J. Ordidge. Velocity-driven adiabatic fast passage for arterial spin labeling: results from a computer model. *Magn Reson Med*, 49:398–401, 2003.

[35] L. Hernandez-Garcia, D. P. Lewis, B. Moffat, and C. A. Branch. Magnetization transfer effects on the efficiency of flow-driven adiabatic fast passage inversion of arterial blood. *NMR Biomed*, 20:733–742, 2007.

[36] W. Zhang, D. S. Williams, J. A. Detre, and A. P. Koretsky. Measurement of brain perfusion by volume-localized NMR spectroscopy using inversion of arterial water spins: accounting for transit time and cross-relaxation. *Magn Reson Med*, 25:362–371, 1992.

[37] M.A. Bernstein. *Handbook of MRI Pulse Sequences*. Oxford: Academic Press, 2004.

[38] D. A. Roberts, J. A. Detre, L. Bolinger, E. K. Insko, and J. S. Leigh. Quantitative magnetic resonance imaging of human brain perfusion at 1.5 T using steady-state inversion of arterial water. *Proc Natl Acad Sci USA*, 91:33–37, 1994.

[39] F. Q. Ye, J. J. Pekar, P. Jezzard, J. Duyn, J. A. Frank, and A. C. McLaughlin. Perfusion imaging of the human brain at 1.5 T using a single-shot EPI spin tagging approach. *Magn Reson Med*, 36:217–224, 1996.

[40] C. M. Kerskens, M. Hoehn-Berlage, B. Schmitz, E. Busch, C. Bock, M. L. Gyngell, and K. A. Hossmann. Ultrafast perfusion-weighted MRI of functional brain activation in rats during forepaw stimulation: comparison with T2 -weighted MRI. *NMR Biomed*, 9:20–23, 1996.

[41] D.G. Norris. Adiabatic radiofrequency pulse forms in biomedical nuclear magnetic resonance. *Conc Magn Reson*, 14:89–101, 2002.

[42] M.E. Haacke, R.W. Brown, M.R. Thompson, and R. Venkatesan. *Magnetic Resonance Imaging: Physical Principles and Sequence Design*. Wiley, 1999.

[43] AI Zhernovoy. On Fast Adiabatic Passage in Nuclear Magnetic Resonance. *Phys Status Solidi B*, 74(1), 1976.

[44] C.M. Kerskens. *Development of theoretical and experimental methods to measure brain perfusion with magnetic resonance tomography*. PhD thesis, Max Planck Institute, Cologne, 1997.

[45] S. D. Wolff and R. S. Balaban. Magnetization transfer contrast (MTC) and tissue water proton relaxation in vivo. *Magn Reson Med*, 10:135–144, 1989.

[46] R. I. Grossman, J. M. Gomori, K. N. Ramer, F. J. Lexa, and M. D. Schnall. Magnetization transfer: theory and clinical applications in neuroradiology. *Radiographics*, 14:279–290, 1994.

[47] R. M. Henkelman, X. Huang, Q. S. Xiang, G. J. Stanisz, S. D. Swanson, and M. J. Bronskill. Quantitative interpretation of magnetization transfer. *Magn Reson Med*, 29:759–766, 1993.

[48] J. Pekar, P. Jezzard, D. A. Roberts, J. S. Leigh, J. A. Frank, and A. C. McLaughlin. Perfusion imaging with compensation for asymmetric magnetization transfer effects. *Magn Reson Med*, 35:70–79, 1996.

[49] D. C. Alsop and J. A. Detre. Multisection cerebral blood flow MR imaging with continuous arterial spin labeling. *Radiology*, 208:410–416, 1998.

[50] A. C. Silva, W. Zhang, D. S. Williams, and A. P. Koretsky. Multi-slice MRI of rat brain perfusion during amphetamine stimulation using arterial spin labeling. *Magn Reson Med*, 33:209–214, 1995.

[51] W. Zhang, A. C. Silva, D. S. Williams, and A. P. Koretsky. NMR measurement of perfusion using arterial spin labeling without saturation of macromolecular spins. *Magn Reson Med*, 33:370–376, 1995.

[52] G. Zaharchuk, P. J. Ledden, K. K. Kwong, T. G. Reese, B. R. Rosen, and L. L. Wald. Multislice perfusion and perfusion territory imaging in humans with separate label and image coils. *Magn Reson Med*, 41:1093–1098, 1999.

[53] T. Mildner, R. Trampel, H. E. Mller, A. SchŁfer, C. J. Wiggins, and D. G. Norris. Functional perfusion imaging using continuous arterial spin labeling with separate labeling and imaging coils at 3 T. *Magn Reson Med*, 49:791–795, 2003.

[54] F. F. Paiva, A. Tanns, S. L. Talagala, and A. C. Silva. Arterial spin labeling of cerebral perfusion territories using a separate labeling coil. *J Magn Reson Imaging*, 27:970–977, 2008.

[55] R. R. Edelman, B. Siewert, D. G. Darby, V. Thangaraj, A. C. Nobre, M. M. Mesulam, and S. Warach. Qualitative mapping of cerebral blood flow and functional localization with echo-planar MR imaging and signal targeting with alternating radio frequency. *Radiology*, 192:513–520, 1994.

[56] A. C. Silva and S. G. Kim. Pseudo-continuous arterial spin labeling technique for measuring CBF dynamics with high temporal resolution. *Magn Reson Med*, 42:425–429, 1999.

[57] L. Hernandez-Garcia, G. R. Lee, A. L. Vazquez, and D. C. Noll. Fast, pseudo-continuous arterial spin labeling for functional imaging using a two-coil system. *Magn Reson Med*, 51:577–585, 2004.

[58] D. C. Alsop. The sensitivity of low flip angle RARE imaging. *Magn Reson Med*, 37:176–184, 1997.

[59] DM Garcia, C. De Bazelaire, and D. Alsop. Pseudo-continuous flow driven adiabatic inversion for arterial spin labeling. In *Proc Int Soc Magn Reson Med*, page 37, 2005.

[60] R. Werner, K. Alfke, T. Schaeffter, A. Nabavi, H. M. Mehdorn, and O. Jansen. Brain perfusion territory imaging applying oblique-plane arterial spin labeling with a standard send/receive head coil. *Magn Reson Med*, 52:1443–1447, 2004.

[61] J. A. Detre, W. Zhang, D. A. Roberts, A. C. Silva, D. S. Williams, D. J. Grandis, A. P. Koretsky, and J. S. Leigh. Tissue specific perfusion imaging using arterial spin labeling. *NMR Biomed*, 7:75–82, 1994.

[62] E. C. Wong, R. B. Buxton, and L. R. Frank. Quantitative imaging of perfusion using a single subtraction (QUIPSS and QUIPSS II). *Magn Reson Med*, 39:702–708, 1998.

[63] R. R. Edelman and Q. Chen. EPISTAR MRI: multislice mapping of cerebral blood flow. *Magn Reson Med*, 40:800–805, 1998.

[64] P. Mansfield, R. Coxon, and P. Glover. Echo-planar imaging of the brain at 3.0 T: first normal volunteer results. *J Comput Assist Tomogr*, 18:339–343, 1994.

[65] Q. Chen, B. Siewert, B. M. Bly, S. Warach, and R. R. Edelman. STAR-HASTE: perfusion imaging without magnetic susceptibility artifact. *Magn Reson Med*, 38:404–408, 1997.

[66] X. Golay, M. Stuber, K. P. Pruessmann, D. Meier, and P. Boesiger. Transfer insensitive labeling technique (TILT): application to multislice functional perfusion imaging. *J Magn Reson Imaging*, 9:454–461, 1999.

[67] K. P. Pruessmann, X. Golay, M. Stuber, M. B. Scheidegger, and P. Boesiger. RF pulse concatenation for spatially selective inversion. *J Magn Reson*, 146:58–65, 2000.

[68] E. C. Wong, R. B. Buxton, and L. R. Frank. Implementation of quantitative perfusion imaging techniques for functional brain mapping using pulsed arterial spin labeling. *NMR Biomed*, 10:237–249, 1997.

[69] X. Golay, E. T. Petersen, and F. Hui. Pulsed star labeling of arterial regions (PULSAR): a robust regional perfusion technique for high field imaging. *Magn Reson Med*, 53:15–21, 2005.

[70] R. J. Ogg, P. B. Kingsley, and J. S. Taylor. WET, a T1- and B1-insensitive water-suppression method for in vivo localized 1H NMR spectroscopy. *J Magn Reson B*, 104:1–10, 1994.

[71] K. K. Kwong, D. A. Chesler, R. M. Weisskoff, K. M. Donahue, T. L. Davis, L. Ostergaard, T. A. Campbell, and B. R. Rosen. MR perfusion studies with T1-weighted echo planar imaging. *Magn Reson Med*, 34:878–887, 1995.

[72] S. G. Kim. Quantification of relative cerebral blood flow change by flow-sensitive alternating inversion recovery (FAIR) technique: application to functional mapping. *Magn Reson Med*, 34:293–301, 1995.

[73] D. G. Nishimura, A. Macovski, J. M. Pauly, and S. M. Conolly. MR angiography by selective inversion recovery. *Magn Reson Med*, 4:193–202, 1987.

[74] C. Schwarzbauer and W. Heinke. BASE imaging: a new spin labeling technique for measuring absolute perfusion changes. *Magn Reson Med*, 39:717–722, 1998.

[75] VM Mai, J. Knight-Scott, DF Kallmes, W. Marx, W. Cail, J. Christopher, and S. Berr. Quantification of steady-state perfusion rates using flow-sensitive alternating inversion recovery with an extra radiofrequency pulse (FAIRER). In *Proc Intl Soc Magn Reson Med*, page 1215, 1996.

[76] V. M. Mai and S. S. Berr. MR perfusion imaging of pulmonary parenchyma using pulsed arterial spin labeling techniques: FAIRER and FAIR. *J Magn Reson Imaging*, 9:483–487, 1999.

[77] W. M. Luh, E. C. Wong, P. A. Bandettini, and J. S. Hyde. QUIPSS II with thin-slice TI1 periodic saturation: a method for improving accuracy of quantitative perfusion imaging using pulsed arterial spin labeling. *Magn Reson Med*, 41:1246–1254, 1999.

[78] E. C. Wong, M. Cronin, W. C. Wu, B. Inglis, L. R. Frank, and T. T. Liu. Velocity-selective arterial spin labeling. *Magn Reson Med*, 55:1334–1341, 2006.

[79] D. G. Norris and C. Schwarzbauer. Velocity selective radiofrequency pulse trains. *J Magn Reson*, 137:231–236, 1999.

[80] W. C. Wu and E. C. Wong. Intravascular effect in velocity-selective arterial spin labeling: the choice of inflow time and cutoff velocity. *Neuroimage*, 32:122–128, 2006.

[81] W. C. Wu and E. C. Wong. Feasibility of velocity selective arterial spin labeling in functional MRI. *J Cereb Blood Flow Metab*, 27:831–838, 2007.

[82] X. Golay, E. T. Petersen, I. Zimine, and T. C. Lim. Arterial Spin Labeling: a one-stop-shop for measurement of brain perfusion in the clinical settings. *Conf Proc IEEE Eng Med Biol Soc*, 2007:4320–4323, 2007.

[83] B. Eklf, N. A. Lassen, L. Nilsson, K. Norberg, B. K. Siesj, and P. Torlf. Regional cerebral blood flow in the rat measured by the tissue sampling technique; a critical evaluation using four indicators C14-antipyrine, C14-ethanol H3-water and xenon. *Acta Physiol Scand*, 91:1–10, 1974.

[84] F. Calamante, S. R. Williams, N. van Bruggen, K. K. Kwong, and R. Turner. A model for quantification of perfusion in pulsed labelling techniques. *NMR Biomed*, 9:79–83, 1996.

[85] R. B. Buxton, L. R. Frank, E. C. Wong, B. Siewert, S. Warach, and R. R. Edelman. A general kinetic model for quantitative perfusion imaging with arterial spin labeling. *Magn Reson Med*, 40:383–396, 1998.

[86] L. M. Parkes. Quantification of cerebral perfusion using arterial spin labeling: two-compartment models. *J Magn Reson Imaging*, 22:732–736, 2005.

[87] J. R. Ewing, Y. Cao, and J. Fenstermacher. Single-coil arterial spin-tagging for estimating cerebral blood flow as viewed from the capillary: relative contributions of intra- and extravascular signal. *Magn Reson Med*, 46:465–475, 2001.

[88] D. C. Alsop and J. A. Detre. Reduced transit-time sensitivity in non-invasive magnetic resonance imaging of human cerebral blood flow. *J Cereb Blood Flow Metab*, 16:1236–1249, 1996.

[89] K. S. St Lawrence, J. A. Frank, and A. C. McLaughlin. Effect of restricted water exchange on cerebral blood flow values calculated with arterial spin tagging: a theoretical investigation. *Magn Reson Med*, 44:440–449, 2000.

[90] O. B. Paulson, M. M. Hertz, T. G. Bolwig, and N. A. Lassen. Filtration and diffusion of water across the blood-brain barrier in man. *Microvasc Res*, 13:113–124, 1977.

[91] P. Herscovitch, M. E. Raichle, M. R. Kilbourn, and M. J. Welch. Positron emission tomographic measurement of cerebral blood flow and permeability-surface area product of water using [15O]water and [11C]butanol. *J Cereb Blood Flow Metab*, 7:527–542, 1987.

[92] J. Zhou, D. A. Wilson, J. A. Ulatowski, R. J. Traystman, and P. C. van Zijl. Two-compartment exchange model for perfusion quantification using arterial spin tagging. *J Cereb Blood Flow Metab*, 21:440–455, 2001.

[93] L. M. Parkes and P. S. Tofts. Improved accuracy of human cerebral blood perfusion measurements using arterial spin labeling: accounting for capillary water permeability. *Magn Reson Med*, 48:27–41, 2002.

[94] A. C. Zappe, J. Reichold, C. Burger, B. Weber, A. Buck, J. Pfeuffer, and N. K. Logothetis. Quantification of cerebral blood flow in nonhuman primates using arterial spin labeling and a two-compartment model. *Magn Reson Imaging*, 25:775–783, 2007.

[95] J. P. Carr, D. L. Buckley, J. Tessier, and G. J. Parker. What levels of precision are achievable for quantification of perfusion and capillary permeability surface area product using ASL? *Magn Reson Med*, 58:281–289, 2007.

[96] E. T. Petersen, T. Lim, and X. Golay. Model-free arterial spin labeling quantification approach for perfusion MRI. *Magn Reson Med*, 55:219–232, 2006.

[97] F. Q. Ye, V. S. Mattay, P. Jezzard, J. A. Frank, D. R. Weinberger, and A. C. McLaughlin. Correction for vascular artifacts in cerebral blood flow values measured by using arterial spin tagging techniques. *Magn Reson Med*, 37:226–235, 1997.

[98] P. Gowland and P. Mansfield. Accurate measurement of T1 in vivo in less than 3 seconds using echo-planar imaging. *Magn Reson Med*, 30:351–354, 1993.

[99] E. L. Barbier, A. C. Silva, S. G. Kim, and A. P. Koretsky. Perfusion imaging using dynamic arterial spin labeling (DASL). *Magn Reson Med*, 45:1021–1029, 2001.

[100] L. Knutsson, D. van Westen, E. T. Petersen, K. M. Bloch, S. Holts, F. Sthlberg, and R. Wirestam. Absolute quantification of cerebral blood flow: correlation between dynamic susceptibility contrast MRI and model-free arterial spin labeling. *Magn Reson Imaging*, 2009.

[101] Y. C. Ho, E. T. Petersen, and X. Golay. Measuring arterial and tissue responses to functional challenges using arterial spin labeling. *Neuroimage*, 2009.

[102] J. Wang, D. C. Alsop, H. K. Song, J. A. Maldjian, K. Tang, A. E. Salvucci, and J. A. Detre. Arterial transit time imaging with flow encoding arterial spin tagging (FEAST). *Magn Reson Med*, 50:599–607, 2003.

[103] J. A. Detre, D. C. Alsop, L. R. Vives, L. Maccotta, J. W. Teener, and E. C. Raps. Noninvasive MRI evaluation of cerebral blood flow in cerebrovascular disease. *Neurology*, 50:633–641, 1998.

[104] J. Hrabe and D. P. Lewis. Two analytical solutions for a model of pulsed arterial spin labeling with randomized blood arrival times. *J Magn Reson*, 167:49–55, 2004.

[105] S. S. KETY. The theory and applications of the exchange of inert gas at the lungs and tissues. *Pharmacol Rev*, 3:1–41, 1951.

[106] D. A. Roberts, R. Rizi, R. E. Lenkinski, and J. S. Leigh. Magnetic resonance imaging of the brain: blood partition coefficient for water: application to spin-tagging measurement of perfusion. *J Magn Reson Imaging*, 6:363–366, 1996.

[107] C. S. Roy and C. S. Sherrington. On the Regulation of the Blood-supply of the Brain. *J Physiol (Lond)*, 11:85–158, 1890.

[108] E. Leniger-Follert and K. A. Hossmann. Simultaneous measurements of microflow and evoked potentials in the somatomotor cortex of the cat brain during specific sensory activation. *Pflugers Arch*, 380:85–89, 1979.

[109] H. Girouard and C. Iadecola. Neurovascular coupling in the normal brain and in hypertension, stroke, and Alzheimer disease. *J Appl Physiol*, 100:328–335, Jan 2006.

[110] R. D. Hoge, J. Atkinson, B. Gill, G. R. Crelier, S. Marrett, and G. B. Pike. Linear coupling between cerebral blood flow and oxygen consumption in activated human cortex. *Proc. Natl. Acad. Sci. U.S.A.*, 96:9403–9408, 1999.

[111] D. Attwell and C. Iadecola. The neural basis of functional brain imaging signals. *Trends Neurosci.*, 25:621–625, 2002.

[112] C. Mathiesen, K. Caesar, N. Akgren, and M. Lauritzen. Modification of activity-dependent increases of cerebral blood flow by excitatory synaptic activity and spikes in rat cerebellar cortex. *J. Physiol. (Lond.)*, 512 (Pt 2):555–566, 1998.

[113] N. K. Logothetis, J. Pauls, M. Augath, T. Trinath, and A. Oeltermann. Neurophysiological investigation of the basis of the fMRI signal. *Nature*, 412:150–157, 2001.

[114] H. L. Xu, L. Mao, S. Ye, C. Paisansathan, F. Vetri, and D. A. Pelligrino. Astrocytes are a key conduit for upstream signaling of vasodilation during cerebral cortical neuronal activation in vivo. *Am J Physiol Heart Circ Physiol*, 294:H622–632, 2008.

[115] B. N. Pasley and R. D. Freeman. Neurovascular coupling. *Scholarpedia*, 3(3):5340, 2008.

[116] S. Ogawa, T. M. Lee, A. S. Nayak, and P. Glynn. Oxygenation-sensitive contrast in magnetic resonance image of rodent brain at high magnetic fields. *Magn Reson Med*, 14:68–78, 1990.

[117] S. Ogawa and T. M. Lee. Magnetic resonance imaging of blood vessels at high fields: in vivo and in vitro measurements and image simulation. *Magn Reson Med*, 16:9–18, 1990.

[118] P. A. Bandettini, E. C. Wong, R. S. Hinks, R. S. Tikofsky, and J. S. Hyde. Time course EPI of human brain function during task activation. *Magn Reson Med*, 25:390–397, 1992.

[119] S. Ogawa, D. W. Tank, R. Menon, J. M. Ellermann, S. G. Kim, H. Merkle, and K. Ugurbil. Intrinsic signal changes accompanying sensory stimulation: functional brain mapping with magnetic resonance imaging. *Proc Natl Acad Sci USA*, 89:5951–5955, 1992.

[120] N. K. Logothetis and J. Pfeuffer. On the nature of the BOLD fMRI contrast mechanism. *Magn Reson Imaging*, 22:1517–1531, 2004.

[121] P. T. Fox and M. E. Raichle. Focal physiological uncoupling of cerebral blood flow and oxidative metabolism during somatosensory stimulation in human subjects. *Proc Natl Acad Sci USA*, 83:1140–1144, 1986.

[122] E. Yacoub, A. Shmuel, J. Pfeuffer, P. F. Van De Moortele, G. Adriany, K. Ugurbil, and X. Hu. Investigation of the initial dip in fMRI at 7 Tesla. *NMR Biomed*, 14:408–412, 2001.

[123] J. B. Mandeville, J. J. Marota, C. Ayata, M. A. Moskowitz, R. M. Weisskoff, and B. R. Rosen. MRI measurement of the temporal evolution of relative CMRO(2) during rat forepaw stimulation. *Magn Reson Med*, pages 944–951, 1999.

[124] H. Lu, X. Golay, J. J. Pekar, and P. C. Van Zijl. Sustained poststimulus elevation in cerebral oxygen utilization after vascular recovery. *J Cereb Blood Flow Metab*, 24:764–770, 2004.

[125] R. B. Buxton and L. R. Frank. A model for the coupling between cerebral blood flow and oxygen metabolism during neural stimulation. *J Cereb Blood Flow Metab*, 17:64–72, 1997.

[126] U. Gbel, B. Klein, H. Schrck, and W. Kuschinsky. Lack of capillary recruitment in the brains of awake rats during hypercapnia. *J Cereb Blood Flow Metab*, 9:491–499, 1989.

[127] T. Q. Li, T. N. Haefelin, B. Chan, A. Kastrup, T. Jonsson, G. H. Glover, and M. E. Moseley. Assessment of hemodynamic response during focal neural activity in human using bolus tracking, arterial spin labeling and BOLD techniques. *Neuroimage*, 12:442–451, 2000.

[128] F. Hyder, R. G. Shulman, and D. L. Rothman. A model for the regulation of cerebral oxygen delivery. *J Appl Physiol*, 85:554–564, 1998.

[129] T. L. Davis, K. K. Kwong, R. M. Weisskoff, and B. R. Rosen. Calibrated functional MRI: mapping the dynamics of oxidative metabolism. *Proc Natl Acad Sci USA*, 95:1834–1839, 1998.

[130] R. D. Hoge, J. Atkinson, B. Gill, G. R. Crelier, S. Marrett, and G. B. Pike. Investigation of BOLD signal dependence on cerebral blood flow and oxygen consumption: the deoxyhemoglobin dilution model. *Magn Reson Med*, 42:849–863, 1999.

[131] D. P. Bulte, K. Drescher, and P. Jezzard. Comparison of hypercapnia-based calibration techniques for measurement of cerebral oxygen metabolism with MRI. *Magn Reson Med*, 61:391–398, 2009.

[132] M. D'Esposito, L. Y. Deouell, and A. Gazzaley. Alterations in the BOLD fMRI signal with ageing and disease: a challenge for neuroimaging. *Nat Rev Neurosci*, 4:863–872, 2003.

[133] C. Hock, K. Villringer, F. Mller-Spahn, R. Wenzel, H. Heekeren, S. Schuh-Hofer, M. Hofmann, S. Minoshima, M. Schwaiger, U. Dirnagl, and A. Villringer. Decrease in parietal cerebral hemoglobin oxygenation during performance of a verbal fluency task in patients with Alzheimer's disease monitored by means of near-infrared spectroscopy (NIRS)–correlation with simultaneous rCBF-PET measurements. *Brain Res*, 755:293–303, 1997.

[134] B. Siewert, B. M. Bly, G. Schlaug, D. G. Darby, V. Thangaraj, S. Warach, and R. R. Edelman. Comparison of the BOLD- and EPISTAR-technique for functional brain imaging by using signal detection theory. *Magn Reson Med*, 36:249–255, 1996.

[135] S. G. Kim and K. Ugurbil. Comparison of blood oxygenation and cerebral blood flow effects in fMRI: estimation of relative oxygen consumption change. *Magn Reson Med*, 38:59–65, 1997.

[136] T. Q. Duong, D. S. Kim, K. Ugurbil, and S. G. Kim. Localized cerebral blood flow response at submillimeter columnar resolution. *Proc Natl Acad Sci USA*, 98:10904–10909, 2001.

[137] M. E. Raichle, J. O. Eichling, M. G. Straatmann, M. J. Welch, K. B. Larson, and M. M. Ter-Pogossian. Blood-brain barrier permeability of 11C-labeled alcohols and 15O-labeled water. *Am J Physiol*, 230:543–552, 1976.

[138] S. G. Kim, N. V. Tsekos, and J. Ashe. Multi-slice perfusion-based functional MRI using the FAIR technique: comparison of CBF and BOLD effects. *NMR Biomed*, 10:191–196, 1997.

[139] J. Wang, G. K. Aguirre, D. Y. Kimberg, A. C. Roc, L. Li, and J. A. Detre. Arterial spin labeling perfusion fMRI with very low task frequency. *Magn Reson Med*, 49:796–802, 2003.

[140] J. Wang, D. C. Alsop, L. Li, J. Listerud, J. B. Gonzalez-At, M. D. Schnall, and J. A. Detre. Comparison of quantitative perfusion imaging using arterial spin labeling at 1.5 and 4.0 Tesla. *Magn Reson Med*, 48:242–254, 2002.

[141] J. J. Chen, M. Wieckowska, E. Meyer, and G. B. Pike. Cerebral Blood Flow Measurement Using fMRI and PET: A Cross-Validation Study. *Int J Biomed Imaging*, 2008:516359, 2008.

[142] L. Ostergaard, P. Johannsen, P. Hst-Poulsen, P. Vestergaard-Poulsen, H. Asboe, A. D. Gee, S. B. Hansen, G. E. Cold, A. Gjedde, and C. Gyldensted. Cerebral blood flow measurements by magnetic resonance imaging bolus tracking: comparison with [(15)O]H2O positron emission tomography in humans. *J Cereb Blood Flow Metab*, 18:935–940, 1998.

[143] E. Farkas and P. G. Luiten. Cerebral microvascular pathology in aging and Alzheimer's disease. *Prog Neurobiol*, 64:575–611, 2001.

[144] S. Nagasawa, H. Handa, A. Okumura, Y. Naruo, K. Moritake, and K. Hayashi. Mechanical properties of human cerebral arteries. Part 1: Effects of age and vascular smooth muscle activation. *Surg Neurol*, 12:297–304, 1979.

[145] N. Masawa, Y. Yoshida, T. Yamada, T. Joshita, S. Sato, and B. Mihara. Morphometry of structural preservation of tunica media in aged and hypertensive human intracerebral arteries. *Stroke*, 25:122–127, 1994.

[146] C.A. Knox, R.D. Yates, I. Chen, and P.M. Klara. Effects of aging on the structural and permeability characteristics of cerebrovasculature in normotensive and hypertensive strains of rats. *Acta Neuropathologica*, 51(1):1–13, 1980.

[147] W. B. Abernethy, M. A. Bell, M. Morris, and D. M. Moody. Microvascular density of the human paraventricular nucleus decreases with aging but not hypertension. *Exp Neurol*, 121:270–274, Jun 1993.

[148] M. A. Bell and M. J. Ball. Morphometric comparison of hippocampal microvasculature in ageing and demented people: diameters and densities. *Acta Neuropathol*, 53:299–318, 1981.

[149] M. A. Bell and M. J. Ball. Neuritic plaques and vessels of visual cortex in aging and Alzheimer's dementia. *Neurobiol Aging*, 11:359–370, 1990.

[150] C. M. Wenn and D. L. Newman. Arterial tortuosity. *Australas Phys Eng Sci Med*, 13:67–70, 1990.

[151] K. Tamaki, M. Nakai, T. Yokota, and J. Ogata. Effects of aging and chronic hypertension on cerebral blood flow and cerebrovascular CO2 reactivity in the rat. *Gerontology*, 41:11–17, 1995.

[152] H. Ito, I. Kanno, M. Ibaraki, and J. Hatazawa. Effect of aging on cerebral vascular response to Paco2 changes in humans as measured by positron emission tomography. *J Cereb Blood Flow Metab*, 22:997–1003, 2002.

[153] M. Mitschelen, P. Garteiser, B. A. Carnes, J. A. Farley, S. Doblas, J. H. Demoe, J. P. Warrington, H. Yan, M. M. Nicolle, R. Towner, and W. E. Sonntag. Basal and hypercapnia-altered cerebrovascular perfusion predict mild cognitive impairment in aging rodents. *Neuroscience*, 2009.

[154] P. Pantano, J. C. Baron, P. Lebrun-Grandi, N. Duquesnoy, M. G. Bousser, and D. Comar. Regional cerebral blood flow and oxygen consumption in human aging. *Stroke*, 15:635–641, 1984.

[155] K. L. Leenders, D. Perani, A. A. Lammertsma, J. D. Heather, P. Buckingham, M. J. Healy, J. M. Gibbs, R. J. Wise, J. Hatazawa, and S. Herold. Cerebral blood flow, blood volume and oxygen utilization. Normal values and effect of age. *Brain*, 113 (Pt 1):27–47, 1990.

[156] A. J. Martin, K. J. Friston, J. G. Colebatch, and R. S. Frackowiak. Decreases in regional cerebral blood flow with normal aging. *J Cereb Blood Flow Metab*, 11:684–689, 1991.

[157] J. S. Meyer, N. Ishihara, V. D. Deshmukh, H. Naritomi, F. Sakai, M. C. Hsu, and P. Pollack. Improved method for noninvasive measurement of regional cerebral blood flow by 133Xenon inhalation. Part I: description of method and normal values obtained in healthy volunteers. *Stroke*, 9:195–205, 1978.

[158] H. Kato, T. Yoshikawa, N. Oku, M. Imaizumi, M. Takasawa, Y. Kimura, K. Kajimoto, M. Tanaka, K. Kitagawa, M. Hori, and J. Hatazawa. Statistical parametric analysis of cerebral blood flow in vascular dementia with small-vessel disease using Tc-HMPAO SPECT. *Cerebrovasc Dis*, 26:556–562, 2008.

[159] J. Krejza, Z. Mariak, J. Walecki, P. Szydlik, J. Lewko, and A. Ustymowicz. Transcranial color Doppler sonography of basal cerebral arteries in 182 healthy subjects: age and sex variability and normal reference values for blood flow parameters. *AJR Am J Roentgenol*, 172:213–218, 1999.

[160] L. M. Parkes, W. Rashid, D. T. Chard, and P. S. Tofts. Normal cerebral perfusion measurements using arterial spin labeling: reproducibility, stability, and age and gender effects. *Magn Reson Med*, 51:736–743, 2004.

[161] L. Biagi, A. Abbruzzese, M. C. Bianchi, D. C. Alsop, A. Del Guerra, and M. Tosetti. Age dependence of cerebral perfusion assessed by magnetic resonance continuous arterial spin labeling. *J Magn Reson Imaging*, 25:696–702, 2007.

[162] P. A. Kelly, I. M. Ritchie, M. Sangra, M. J. Cursham, E. M. Dickson, B. Kelly, F. P. Neilson, M. J. Reidy, and M. C. Stevens. Hyperaemia in rat neocortex produced by acute exposure to methylenedioxymethamphetamine. *Brain Res*, 665:315–318, 1994.

[163] F. X. Vollenweider, A. Gamma, M. Liechti, and T. Huber. Psychological and cardiovascular effects and short-term sequelae of MDMA ("ecstasy") in MDMA-nave healthy volunteers. *Neuropsychopharmacol*, 19:241–251, 1998.

[164] L. A. Badon, A. Hicks, K. Lord, B. A. Ogden, S. Meleg-Smith, and K. J. Varner. Changes in cardiovascular responsiveness and cardiotoxicity elicited during binge administration of Ecstasy. *J Pharmacol Exp Ther*, 302:898–907, 2002.

[165] L. Reneman, J. B. Habraken, C. B. Majoie, J. Booij, and G. J. den Heeten. MDMA ("Ecstasy") and its association with cerebrovascular

accidents: preliminary findings. *AJNR Am J Neuroradiol*, 21:1001–1007, 2000.

[166] A. W. McEvoy, N. D. Kitchen, and D. G. Thomas. Intracerebral haemorrhage and drug abuse in young adults. *Br J Neurosurg*, 14:449–454, 2000.

[167] A. R. Green, A. J. Cross, and G. M. Goodwin. Review of the pharmacology and clinical pharmacology of 3,4-methylenedioxymethamphetamine (MDMA or "Ecstasy"). *Psychopharmacol (Berl)*, 119:247–260, 1995.

[168] L. Ferrington, E. Kirilly, D. E. McBean, H. J. Olverman, G. Bagdy, and P. A. Kelly. Persistent cerebrovascular effects of MDMA and acute responses to the drug. *Eur J Neurosci*, 24:509–519, 2006.

[169] R. L. Cowan, D. M. Roberts, and J. M. Joers. Neuroimaging in human MDMA (Ecstasy) users. *Ann N Y Acad Sci*, 1139:291–298, 2008.

[170] A. A. Parsons. 5-HT receptors in human and animal cerebrovasculature. *Trends Pharmacol Sci*, 12, 1991.

[171] Z. Cohen, G. Bonvento, P. Lacombe, and E. Hamel. Serotonin in the regulation of brain microcirculation. *Prog Neurobiol*, 50:335–362, 1996.

[172] L. Quate, D. E. McBean, I. M. Ritchie, H. J. Olverman, and P. A. Kelly. Acute methylenedioxymethamphetamine administration: effects on local cerebral blood flow and glucose utilisation in the Dark Agouti rat. *Psychopharmacol (Berl)*, 173:287–295, 2004.

[173] R. L. Cowan. Neuroimaging research in human MDMA users: a review. *Psychopharmacol (Berl)*, 189:539–556, 2007.

[174] O. Sakurada, C. Kennedy, J. Jehle, J. D. Brown, G. L. Carbin, and L. Sokoloff. Measurement of local cerebral blood flow with iodo [14C] antipyrine. *Am J Physiol*, 234:59–66, 1978.

[175] O. B. Paulson, S. Strandgaard, and L. Edvinsson. Cerebral autoregulation. *Cerebrovasc Brain Metab Rev*, 2:161–192, 1990.

[176] L. Chang, C. S. Grob, T. Ernst, L. Itti, F. S. Mishkin, R. Jose-Melchor, and R. E. Poland. Effect of ecstasy [3,4-methylenedioxymethamphetamine (MDMA)] on cerebral blood flow: a co-registered SPECT and MRI study. *Psychiatry Res*, 98:15–28, 2000.

[177] M. M. de Win, G. Jager, J. Booij, L. Reneman, T. Schilt, C. Lavini, S. D. Olabarriaga, G. J. den Heeten, and W. van den Brink. Sustained effects of ecstasy on the human brain: a prospective neuroimaging study in novel users. *Brain*, 131:2936–2945, 2008.

[178] W. T. Coffey. *The Langevin Equation: With Applications to Stochastic Problems in Physics, Chemistry and Electrical Engineering*. Singapore : World Scientific, 1996.

[179] T. Kim and S. G. Kim. Quantification of cerebral arterial blood volume using arterial spin labeling with intravoxel incoherent motion-sensitive gradients. *Magn Reson Med*, 55:1047–1057, 2006.

[180] A. C. Silva, D. S. Williams, and A. P. Koretsky. Evidence for the exchange of arterial spin-labeled water with tissue water in rat brain from diffusion-sensitized measurements of perfusion. *Magn Reson Med*, 38:232–237, 1997.

[181] L. L. Latour, K. Svoboda, P. P. Mitra, and C. H. Sotak. Time-dependent diffusion of water in a biological model system. *Proc Natl Acad Sci USA*, 91:1229–1233, 1994.

[182] R Zwanzig. *Non Equilibrium Statstical Mechanics*. Oxford : Oxford University Press, 2001.

[183] L.C. Evans. *Partial Differential Equations*. Providence: American Mathematical Society, 1998.

[184] G. Zaharchuk, A. A. Bogdanov, J. J. Marota, M. Shimizu-Sasamata, R. M. Weisskoff, K. K. Kwong, B. G. Jenkins, R. Weissleder, and B. R. Rosen. Continuous assessment of perfusion by tagging including volume and water extraction (CAPTIVE): a steady-state contrast

agent technique for measuring blood flow, relative blood volume fraction, and the water extraction fraction. *Magn Reson Med*, 40:666–678, 1998.

[185] F. Calamante, D. G. Gadian, and A. Connelly. Delay and dispersion effects in dynamic susceptibility contrast MRI: simulations using singular value decomposition. *Magn Reson Med*, 44:466–473, 2000.

[186] K.L. Zierler. Theoretical basis of indicator-dilution methods for measuring flow and volume. *Circ Res*, 10(3):393–407, 1962.

[187] G. T. Gobbel, C. E. Cann, and J. R. Fike. Measurement of regional cerebral blood flow using ultrafast computed tomography. Theoretical aspects. *Stroke*, 22:768–771, 1991.

[188] R. M. Weisskoff, D. Chesler, J. L. Boxerman, and B. R. Rosen. Pitfalls in MR measurement of tissue blood flow with intravascular tracers: which mean transit time? *Magn Reson Med*, 29:553–558, 1993.

[189] Y. Tomita, M. Tomita, I. Schiszler, T. Amano, N. Tanahashi, M. Kobari, H. Takeda, M. Ohtomo, and Y. Fukuuchi. Moment analysis of microflow histogram in focal ischemic lesion to evaluate microvascular derangement after small pial arterial occlusion in rats. *J Cereb Blood Flow Metab*, 22:663–669, 2002.

[190] R. D. Purves. Numerical estimation of the noncompartmental pharmacokinetic parameters variance and coefficient of variation of residence times. *J Pharm Sci*, 83:202–205, 1994.

[191] M. E. Kelly, C. W. Blau, and C. M. Kerskens. Bolus-tracking arterial spin labelling: theoretical and experimental results. *Phys Med Biol*, 54:1235–1251, 2009.

[192] J. Kevorkian. *Partial Differential Equations: Analytical Solution Techniques*. Berlin: Springer, 2000.

[193] G Paxinos and C. Watson. *The Rat Brain in Stereotaxic Coordinates*. Burlington: Academic Press, 2005.

[194] J. Hennig, A. Nauerth, and H. Friedburg. RARE imaging: a fast imaging method for clinical MR. *Magn Reson Med*, 3:823–833, 1986.

[195] J. Frahm, A. Haase, and D. Matthaei. Rapid NMR imaging of dynamic processes using the FLASH technique. *Magn Reson Med*, 3:321–327, 1986.

[196] A. E. Holsinger and S. J. Riederer. The importance of phase-encoding order in ultra-short TR snapshot MR imaging. *Magn Reson Med*, 16:481–488, 1990.

[197] Bruker Biospin. *Users Manual (Method Description)*. Bruker Biospin, 2006.

[198] K. Levenberg. A method for the solution of certain non-linear problems in least squares. *Q Appl Math*, 2:164–168, 1944.

[199] D. Marquardt. An algorithm for least-squares estimation of nonlinear parameters. *J SIAM Appl Math*, 11:431–441, 1963.

[200] E.W. Weisstein. Levenberg-marquardt method. From *Mathworld*-A Wolfram Web Resource. `http://www.fermentas.com/techinfo/nucleicacids/maplambda.htm`, 2008.

[201] P.R. Bevington and D.K. Robinson. *Data Reduction and Error Analysis for the Physical Sciences (2d ed.; New York*. McGraw-Hill, 1992.

[202] R. P. Shockley and J. C. LaManna. Determination of rat cerebral cortical blood volume changes by capillary mean transit time analysis during hypoxia, hypercapnia and hyperventilation. *Brain Res*, 454:170–178, 1988.

[203] D. L. Thomas, M. F. Lythgoe, L. van der Weerd, R. J. Ordidge, and D. G. Gadian. Regional variation of cerebral blood flow and arterial transit time in the normal and hypoperfused rat brain measured using continuous arterial spin labeling MRI. *J Cereb Blood Flow Metab*, 26:274–282, 2006.

[204] M. E. Kelly, C. W. Blau, O. L. Gobbo, K. M. Griffin, J . F. X. Jones, and C. M. Kerskens. Functional bolus-tracking arterial spin labeling;

a new approach to quantitative fMRI. In *Proc Int Soc Cereb Blood Flow Metab*, page 48, 2009.

[205] E. M. Hillman, A. Devor, M. B. Bouchard, A. K. Dunn, G. W. Krauss, J. Skoch, B. J. Bacskai, A. M. Dale, and D. A. Boas. Depth-resolved optical imaging and microscopy of vascular compartment dynamics during somatosensory stimulation. *Neuroimage*, 35:89–104, 2007.

[206] M. Jones, J. Berwick, D. Johnston, and J. Mayhew. Concurrent optical imaging spectroscopy and laser-Doppler flowmetry: the relationship between blood flow, oxygenation, and volume in rodent barrel cortex. *Neuroimage*, 13:1002–1015, 2001.

[207] P. Enager, H. Piilgaard, N. Offenhauser, A. Kocharyan, P. Fernandes, E. Hamel, and M. Lauritzen. Pathway-specific variations in neurovascular and neurometabolic coupling in rat primary somatosensory cortex. *J Cereb Blood Flow Metab*, 29:976–986, 2009.

[208] G. Royl, C. Leithner, H. Sellien, J. P. Mller, D. Megow, N. Offenhauser, J. Steinbrink, M. Kohl-Bareis, U. Dirnagl, and U. Lindauer. Functional imaging with laser speckle contrast analysis: vascular compartment analysis and correlation with laser Doppler flowmetry and somatosensory evoked potentials. *Brain Res*, 1121:95–103, 2006.

[209] A. Villringer, A. Them, U. Lindauer, K. EinhŁupl, and U. Dirnagl. Capillary perfusion of the rat brain cortex. An in vivo confocal microscopy study. *Circ Res*, 75:55–62, 1994.

[210] R. Weber, P. Ramos-Cabrer, D. Wiedermann, N. van Camp, and M. Hoehn. A fully noninvasive and robust experimental protocol for longitudinal fMRI studies in the rat. *Neuroimage*, 29:1303–1310, 2006.

[211] K. M. Lahti, C. F. Ferris, F. Li, C. H. Sotak, and J. A. King. Comparison of evoked cortical activity in conscious and propofol-anesthetized rats using functional MRI. *Magn Reson Med*, 41:412–416, 1999.

[212] P. Ganjoo, N. E. Farber, A. Hudetz, J. J. Smith, E. Samso, J. P. Kampine, and W. T. Schmeling. In vivo effects of dexmedetomidine on laser-Doppler flow and pial arteriolar diameter. *Anesthesiology*, 88:429–439, 1998.

[213] I. Vasileiou, T. Xanthos, E. Koudouna, D. Perrea, C. Klonaris, A. Katsargyris, and L. Papadimitriou. Propofol: A review of its non- anaesthetic effects. *Eur J Pharmacol*, Jan 2009.

[214] M. E. Kelly, C. W. Blau, K. M. Griffin, O. L. Gobbo, J. F. Jones, and C. M. Kerskens. Quantitative functional magnetic resonance imaging of brain activity using bolus-tracking arterial spin labeling. *J Cereb Blood Flow Metab*, Epub ahead of print, 2010.

[215] M. E. Kelly, C. W. Blau, R. Bechara, M. A. Lynch, and C. M. Kerskens. Bolus-tracking arterial spin labeling; A new marker for age and age related neurological diseases. In *Proc Int Soc Magn Reson Med*, page 144, 2009.

[216] M. E. Kelly, C. W. Blau, R. Bechara, M. A. Lynch, and C. M. Kerskens. FBolus-tracking arterial spin labeling; A new marker for age and age related neurological diseases. In *Proc Int Soc Cereb Blood Flow Metab*, page 45, 2009.

[217] R. G. Steen, S. A. Gronemeyer, and J. S. Taylor. Age-related changes in proton T1 values of normal human brain. *J Magn Reson Imaging*, 5:43–48, 1995.

[218] S. Cho, D. Jones, W. E. Reddick, R. J. Ogg, and R. G. Steen. Establishing norms for age-related changes in proton T1 of human brain tissue in vivo. *Magn Reson Imaging*, 15:1133–1143, 1997.

[219] C. Weidensteiner, F. Metzger, A. Bruns, B. Bohrmann, B. Kuennecke, and M. von Kienlin. Cortical hypoperfusion in the B6.PS2APP mouse model for Alzheimer's disease: comprehensive phenotyping of vascular and tissular parameters by MRI. *Magn Reson Med*, 62:35–45, 2009.

[220] A. R. Green. MDMA: fact and fallacy, and the need to increase knowledge in both the scientific and popular press. *Psychopharmacol (Berl)*, 173:231–233, 2004.

[221] P. Rosa-Neto, A. K. Olsen, A. Gjedde, H. Watanabe, and P. Cumming. MDMA-evoked changes in cerebral blood flow in living porcine brain: correlation with hyperthermia. *Synapse*, 53:214–221, 2004.

[222] P. Mansfield, AA Maudsley, and T. Baines. Fast scan proton density imaging by NMR. *J Phys E*, 9(4):271–278, 1976.

[223] P. Bornert and D. Jensen. Single-shot-double-echo EPI. *Magn Reson Imaging*, 12:1033–1038, 1994.

[224] K. Restom, K. J. Bangen, M. W. Bondi, J. E. Perthen, and T. T. Liu. Cerebral blood flow and BOLD responses to a memory encoding task: a comparison between healthy young and elderly adults. *Neuroimage*, 37:430–439, 2007.

[225] Y. S. Mineur, D. McLoughlin, W. E. Crusio, and F. Sluyter. Genetic mouse models of Alzheimer's disease. *Neural Plast*, 12:299–310, 2005.

[226] L. Liu, I. J. Orozco, E. Planel, Y. Wen, A. Bretteville, P. Krishnamurthy, L. Wang, M. Herman, H. Figueroa, W. H. Yu, O. Arancio, and K. Duff. A transgenic rat that develops Alzheimer's disease-like amyloid pathology, deficits in synaptic plasticity and cognitive impairment. *Neurobiol Dis*, 31:46–57, 2008.

[227] K. F. Schmidt, M. Febo, Q. Shen, F. Luo, K. M. Sicard, C. F. Ferris, E. A. Stein, and T. Q. Duong. Hemodynamic and metabolic changes induced by cocaine in anesthetized rat observed with multimodal functional MRI. *Psychopharmacol (Berl)*, 185:479–486, 2006.